APPROXIMATE TRANSFER FUNCTIONS FOR
FLEXIBLE-BOOSTER-AND-AUTOPILOT ANALYSIS

DAVID R. LUKENS
ALFRED F. SCHMITT
GEORGE T. BROUCEK

CONVAIR (ASTRONAUTICS) DIVISION
GENERAL DYNAMICS CORPORATION
SAN DIEGO, CALIFORNIA

CONVAIR REPORT No. AE 61-0198
FLIGHT CONTROL LABORATORY
CONTRACT No. AF 33(616)-7037

APRIL 1961

AERONAUTICAL SYSTEMS DIVISION

NOTICES

ERRATA

Page 11, Equation 2-2, denominator should read

$$s \left(s^2 + \frac{F_\alpha + T_c}{MV} \; s - \mu_\alpha \right)$$

Page 22, Equation 2-15, should read

$$\text{where} \qquad A_i \equiv \frac{\sigma_{xG}^{(i)} \; T_c}{m_i \; \mu_\delta}$$

Page 98, Equation 4-29, should read

$$\frac{\ddot{H}_G}{\delta} = (x_{CG} - x_T) K_i \quad (\text{etc.})$$

where

$$A_i = \frac{I \; \sigma_{xG}^{(i)} \; \phi_{xT}^{(i)}}{m_i (x_{CG} - x_T)}$$

Page 101, Equation 4-35, the following may be added:

$$\text{also} \qquad \frac{\ddot{s}}{\ddot{s}_G} = \frac{\mu_\alpha - \frac{F_\alpha}{MV} \; s}{s^2 + \frac{T + F_\alpha}{MV} \; s - \mu_\alpha}$$

Page A-14, list of symbols should read

$$\eta_1 \quad \text{wave height for first sloshing mode} \approx 0.84 \; a \left| \Gamma_p \, (\text{max}) \right|$$

Page B-39, Equation B-4, should read

$$Q_v = \frac{-x_s \; C_s}{\sqrt{2}} \; \sqrt{\left| P_s - P_R - P_L \, \text{sgn} \, x_s \right|} \; \text{sgn} \, (P_s - P_R - P_L \, \text{sgn} \, x_s)$$

Equation B-6, should read

$$-i_v = K_{J} (\delta_c - \delta_F) = K_{J} \, \delta_\epsilon$$

Page B-40, Equation B-9, should read

$$Q_V = -i_{veq} \, K_V \, \cdots \cdots \, etc$$

Equation B-10, should read

$$i_{veq} = -K_a \, (\delta_c - \delta_F) + K_s \, P_{13}$$

$$= -K_a \, (\delta_c - \delta) \, \cdots \, etc.$$

Page B-43, equation immediately preceding paragraph B4-2-8 should read:

$$G_{NL} = C_V + \frac{4}{\pi} \, \frac{C_B}{\omega \bar{\delta}}$$

Page B-46, Equation B-27, the second parenthesis of the numerator should read:

$$(\tau_F \, s^2 + K_2 \, s + K_3)$$

Also the definition of K2 should read

$$K_2 = \frac{\tau_F \, K_c}{\left(\dfrac{V_T}{4B} + \dfrac{A^2}{K_m} \right)} \, \left(\frac{AR \, K_s}{K_a} + \frac{A^2}{K_m} \right) + 1$$

Page C-17, Figure C-5, should be drawn

APPROXIMATE TRANSFER FUNCTIONS FOR FLEXIBLE-BOOSTER-AND-AUTOPILOT ANALYSIS

DAVID R. LUKENS
ALFRED F. SCHMITT
GEORGE T. BROUCEK

CONVAIR (ASTRONAUTICS) DIVISION
GENERAL DYNAMICS CORPORATION
SAN DIEGO, CALIFORNIA

APRIL 1961

FOREWORD

This report was prepared under Air Force Contract No. AF33(616)-7037 by the Convair (Astronautics) Division of General Dynamics Corporation, San Diego, California. The contract was initiated under Project No. 8219, Task No. 82158 and was administered under the Direction of the Flight Control Laboratory, Aerospace Mechanics Branch with Mr. H. M. Davis and Lt. R. L. Swaim acting successively as project engineer.

The project was carried out by the Dynamics Group of the Convair (Astronautics) Division of General Dynamics Corporation, with the major portion of the study conducted by Mr. David R. Lukens, project leader, Dr. A. F. Schmitt, supervisor, and Mr. George T. Broucek. Convair-Astronautics personnel assisting in the study were: Mr. J. W. Evans, Mr. F. I. Backus, and Mr. R. G. Norell.

ABSTRACT

This report summarizes sufficient information to enable a practicing engineer to understand and analyze the phenomena associated with a flexible-booster-and-autopilot analysis. Simplifications and approximations are given for all phases of synthesis and analysis, and the limitations of the simplified solutions are discussed in detail.

The development of methods for synthesis and analysis of flexible boosters is presented in several stages--from simple linear techniques useful for predesign or preliminary design analysis, up to the complex forms requiring computer solutions, which may be used to verify the adequacy of the final flexible-booster-and-autopilot configuration.

The methods of synthesis and analysis are presented with three major limitations: 1) A linear airframe is assumed, 2) The aerodynamic surfaces (wings) are assumed to be small and relatively rigid, and 3) The aerodynamics are represented by a simple quasi-steady model. These limitations will not restrict the usefulness of the results for most classes of flexible boosters.

The results of the work indicate that accurate solutions for most nonwinged flexible boosters can be achieved by simple root-locus techniques involving linearized equations. The cases where more advanced techniques are necessary, and the equations and methods for a more comprehensive analysis are also presented.

PUBLICATION REVIEW

This report has been reviewed and is approved.

FOR THE COMMANDER:

C. B. Westbrook
Chief, Aerospace Mechanics Branch
Flight Control Laboratory

TABLE OF CONTENTS

TABLE OF CONTENTS (CONT.)

TABLE OF CONTENTS (CONT.)

TABLE OF CONTENTS (CONT.)

TABLE OF CONTENTS (CONT.)

TABLE OF CONTENTS (CONT.)

LIST OF ILLUSTRATIONS

LIST OF ILLUSTRATIONS (CONT.)

LIST OF ILLUSTRATIONS (CONT.)

LIST OF ILLUSTRATIONS (CONT.)

LIST OF ILLUSTRATIONS (CONT.)

LIST OF ILLUSTRATIONS (CONT.)

LIST OF ILLUSTRATIONS (CONT.)

LIST OF ILLUSTRATIONS (CONT.)

LIST OF TABLES

LIST OF SYMBOLS

SECTION 1

INTRODUCTION

1.1 GENERAL

Booster flexibility is recognized as a problem causing adverse effects upon vehicle loading and stability because the bending modes couple with elements of the missile control system. The effects upon loading, particularly air-loading, may be traced to local increases in the angle of attack as a result of vehicle flexing. Such increases lead to additional deflections and loads. Convair-Astronautics' experience has shown that increases in structural loading due to gusts may range from a few percent on early ICBM's to as much as five to ten percent on multistage space booster vehicles having a large slenderness ratio.

Elastic coupling with the control system usually arises because of modal pickup by the sensors. These elastic modes are due to additional degrees of freedom which appear as parallel blocks to the rigid body when the missile transfer function is derived. If these modes are within the control system bandwidth, or within several octaves of the control frequency, then accurate transfer function determination is necessary so that the modes may be gain- and/or phase-stabilized. Phase stabilization has been necessary for the fundamental bending mode on all Atlas program vehicles.

1.2 PURPOSE OF REPORT

It is the intent of this report to present the basic concepts and techniques needed by engineers to understand the principles and techniques used in the analysis and synthesis of a large flexible booster with autopilot control. This report presents the methods of applied mechanics, servo theory, and aerodynamics which are felt to be most applicable to this analysis. The presentation is made in a manner so as to provide an approach to the problem which will be based solely upon the laws of mechanics. The results presented will therefore be directly applicable to new aerodynamic methods which improve upon the quasi-steady aerodynamics used in this report.

The type of flexible boosters considered will have no modes of operation in which flight is not basically sustained by propulsive thrust; therefore, no wings are required on the vehicle. Small tail fins may be used to provide stability, although the stability problems may usually be solved by thrust-vector control alone. The equations and simplifications presented in this report will therefore assume that the external aerodynamic surfaces are small enough and stiff enough so that their analysis does not require the use of additional degrees of freedom.

If a winged payload is affixed, it is likewise assumed to be sufficiently rigid that the payload's own elastic modes need not be coupled to those of the vehicle.

The class of vehicles analyzed are, by intent, built with a high degree of inertial and elastic symmetry. The asymmetric configurational aspects, which do occur, result in very minor aerodynamic and inertial coupling effects between control planes. These effects are so small that analysis of planar motions is permitted in almost all instances.

In the development of transfer functions the modal or normal coordinate representation is used whenever possible. Thus, it is possible to apply direct simplifications to the analysis of the rigid-body, sloshing, and elastic modes, without having to recalculate the booster parameters or rewrite the equations of motion. The simplifications presented make use of describing functions for significant nonlinearities and can be used to predict system stability and to show the existence of stable and unstable limit cycles. The role of detailed computer simulations of the complete system of equations for final system proofing and special studies, is described.

The airframe of a booster may be assembled by the bolting (or other nonhomogeneous fastening) of several sections (stages) to make up the complete booster vehicle. This assembly leads to nonlinear elastic properties for the airframe which are not amendable to the analytical techniques presented in this report. However, during flight the steady loads on the vehicle (longitudinal thrust and air loads) are usually sufficient to preload the structure and to hold it in a linear range for small elastic oscillations such as would be encountered in a stable configuration. The methods presented in this report are therefore limited to a linear, or linearized, airframe and will be adequate for most classes of flexible boosters.

1.3 MATERIAL COVERED

Sections 2 and 3 contain the background material for using the methods of analysis and simplification, as well as a comprehensive derivation of the equations of motion used. The equations and analytical techniques cover the booster airframe plus related elastic motion, propellant sloshing forces and moments, and the autopilot and control system. Sections 4 and 5 contain methods of approximation and simplifications of the flexible booster and autopilot, and a comparison of these simplifications with the complete analysis. Section 6 gives comparisons of analytic results with flight and captive test data.

The appendices give related data not directly involved in the simplification and analysis of the flexible booster but nevertheless necessary for the analysis of flexible booster and autopilot coupling. Appendix A gives the preparation of the basic data necessary to describe the airframe, the mass and related inertial, propellant sloshing, the elastic properties (modes), and the aerodynamic coefficients. Appendix B describes the missile autopilot and control subsystems. Appendix C discusses several miscellaneous related topics, i.e., spin-stabilized vehicles and payloads, solid propellant grain motion, and the effect of mass flow and internal damping on rigid-body and modal solutions.

SECTION 2

SURVEY OF BOOSTER SYNTHESIS AND ANALYSIS
TECHNIQUES

SYMBOLS USED IN SECTION 2

Symbol	Definition	Units
BM	bending moment	ft lbs
C_N/α	aerodynamic normal force coefficient per unit angle of attack	1/rad
EI_{xn}	flexural rigidity at station n along the longitudinal axis	lb-ft^2
F	force	lbs
F_α	aerodynamic force coefficient in the pitch plane	lbs/rad
I	reduced moment of inertia in pitch (see Appendix A1-5)	slug ft^2
K_A	position gyro gain factor	rad δ/rad Θ
K_c	hydraulic actuator gain factor	(rad/sec) δ/rad δ_c
K_ℓ	spring constant for ℓ^{th} propellant sloshing mass	lbs/ft
K_R	rate gyro gain factor	rad δ_c/(rad/sec) Θ
K_α	α-loop feedback gain factor	rad δ_c/rad α
ℓ_a	aerodynamic moment arm	ft
ℓ_c	rocket engine moment arm	ft
ℓ_p	moment arm of sloshing mass (pendulum)	ft
L_p	sloshing analogy pendulum length	ft
$\mathscr{M}_i$	generalized mass for the ith mode	slugs
M	moment (also, vehicle mass)	lb-ft (slugs)
M_i	discrete (lumped) mass at station i	slugs
q	aerodynamic pressure (q $= \rho V^2/2$)	lbs/ft^2
q_i	generalized displacement of the ith mode	ft
r	radius of gyration (Equation 2-9)	ft
s	Laplace operator (s $= \sigma + j\omega$)	1/sec
S	vehicle reference area	ft^2
t	time	sec
T_c	control engine thrust	lbs

SYMBOLS USED IN SECTION 2 (Continued)

Symbol	Definition	Units
T_L	load torque	ft-lbs
V	vehicle velocity	ft/sec
x, y, z	vehicle coordinates referenced from center of gravity	ft
X_{CG}	center of gravity position along longitudinal axis	ft
X_{CP}	center of pressure position along longitudinal axis	ft
X_p	location of pendulum attach point on longitudinal axis	ft
Y_ℓ	lateral displacement of ℓth sloshing mass (spring mass analogy)	ft
$\ddot{Z}$	acceleration along the Z axis	ft/sec^2
α	angle of attack in pitch plane	rad
α_{gust}	angle of attack due to a gust	rad
α_T	vehicle acceleration along its longitudinal axis	ft/sec^2
β	angle of attack in yaw plane	rad
γ	flight path angle	rad
Γ	propellant pendulum angle (pendulum analogy)	rad
δ	rocket engine gimbal angle	rad
ζ	damping ratio	N.D.*
Θ	vehicle pitching angle	rad
μ_α	aerodynamic effectiveness parameter defined in Equation 2-2	$1/sec^2$
μ_δ	control engine effectiveness parameter defined in Equation 2-2	$1/sec^2$
σ	standard deviation as used in probability	N.D.
$\sigma_{xn}^{(i)}$	normalized slope of the ith mode at station n along the longitudinal axis	rad/ft
$\phi_{xn}^{(i)}$	normalized deflection of the ith mode at station n along the longitudinal axis	ft/ft
ω	natural frequency	1/sec
ω_c, ω_{cn}	frequencies of engine hydraulic actuator transfer functions	1/sec

Note: Throughout this report no distinction is made in notation between a real time function and a transformed function of the complex frequency, $s = \sigma + j\omega$. The differential equations are given as time functions, but the equations otherwise are generally written as transformed equations, as is always evident by the presence of the variable s.

---

*Non-dimensional

2.1 BASIC CONCEPTS*

In the normal evolution of a large flexible-booster design, a considerable number of feasibility studies are undertaken in the preliminary design phase to determine the payload capability and mode of operation of the booster for different missions. These studies may be of varying degrees of sophistication in the extent to which they consider propulsion characteristics, "g" field, aerodynamic properties, etc. Almost invariably, however, they employ the common approximation of studying the motion of a point-mass under the previously mentioned forces, assuming that the booster can be steered perfectly to produce flight along the desired trajectories. These studies are sufficient to define quite closely the nominal trajectory and flight characteristics of the system. After the preliminary studies have outlined the capabilities of a properly controlled and guided vehicle, it becomes the task of the guidance and control system to realize these capabilities.

The overall task of system analysis is of such complexity that many tools of analysis have to be applied in order to obtain satisfactory solutions to the problems. Thus, both manual and complex computer studies are employed at various stages. One recognizes that during early phases of flexible-missile-and-autopilot analysis there exists an economic and logical requirement to reduce the use of computers. For the early phase of the investigations the overall problem must be simplified in order to emphasize the main parameters and their interrelation for the system under study. To attempt to study all phases of this analysis through the use of computers would not only be too costly but would also limit the inventiveness and creativity of the engineer for formulating novel concepts. After the main parameters and distinguishing features of the problem have been roughed out, the complete system should be progressively analyzed with computer techniques through an iterative procedure of synthesis and analysis.

In the determination of approximate transfer functions of a large flexible missile, it is assumed that what is sought is the simplest transfer function which will adequately describe the system under study in the realm of signal frequency and amplitude. It is also desired that the approximate transfer function may be obtained with a minimum of effort on the part of the person studying the system. To determine which type of transfer function will be best suited for approximate studies, it is necessary to look at both the analytic models and the mathematical methods available for their analyses. In the following discussion, it is assumed that the reader is familiar with the basic theory and techniques in the solution of feedback control problems. The tools used in the majority of the analyses will be those employing system transfer functions of the complex frequency, $s = \sigma + j\omega$. The root-locus method of analyzing the closed-loop response, based upon the open loop transfer function, will be used for most graphic presentations.

In this section a brief survey of the booster control system synthesis and analysis process is given to provide a background against which the usefulness and appropriateness of the transfer functions, and their simplification given in succeeding chapters, may be judged.

2.2 STABILITY TECHNIQUES

To enable guidance of a vehicle, it must be possible to control its attitude. The problem of attitude control will also determine, in part, the loads imposed upon the vehicle by its environment. The control problems may be considered as uncoupled from the guidance problems for many of the large flexible boosters. It is felt that this assumption is justified for the class of vehicles to which this study is applicable, as the control and elastic oscillations have periods that are several orders of magnitude shorter than those of the guidance modes. If the guidance and control systems are coupled (for hardware, energy management, or other considerations), then the problem cannot be simplified to the extent of an uncoupled system. The equations and techniques presented are correct, however, and fully applicable to these systems, even though all of the simplifications recommended may not be usable.

The major parameters and mode of operation of the booster must be understood before an attitude control system can be studied. The following paragraphs summarize these factors.

The booster vehicle's mission is to lift the upper stages and payload through the earth's atmosphere, imparting to them a desired velocity vector. To accomplish this mission in an efficient manner, a mode of operation is devised which capitalizes on the presence of large propulsive forces and on very low maneuver requirements. In addition, the flight plan is tailored so as to minimize aerodynamic loading and thus permit a low structural

---

*References 1 and 2 have been drawn up in preparation of subsections 2.1 through 2.4.

weight in both booster and upper stages. The vehicle is launched vertically to minimize launcher requirements and to permit the vehicle to complete its initial rise without placing large-lateral-stabilizing-load requirements on the control system. Shortly after lift-off, the vehicle is turned (pitches over) from a vertical flight path to a zero-lift (zero-angle-of-attack) flight trajectory. Using this flight plan, the vehicle assumes an intentional angle of attack at low dynamic pressures during the brief transitional pitch-over. Thereafter, an attempt is made to fly a trajectory in which the turning rate is equal to the flight-path turn rate so as to obtain a zero angle of attack. Obviously, atmospheric inputs of winds (steady profiles and gusts) will produce some unintended loadings which the control system must cope with. However, intentional vehicle maneuvering is kept at an absolute minimum.

Special flight operations, such as staging, can impose severe control problems if conducted at high dynamic pressures. These operations are, therefore, generally deferred until the vehicle has left the atmosphere or, at least, the region of high dynamic pressure. The control problems posed by such an operation concern the stability of rigid-body motions; a specialized and complex kinematic-dynamic-autopilot simulation is required for system analysis. Elastic mode coupling problems are not considered in such a situation, due to the fact that complex transient conditions pertain at these times, while the vehicle configuration is being varied and control gains and forces (propulsive and hydraulic) are changing rapidly.

2.2.1 <u>Equations and System Block Diagrams.</u>* For purposes of the primary study of the vehicle and control system, it is satisfactory to consider the vehicle as being rigid. This assumption simplifies visualization of the effect of basic vehicle and control parameters. Such an assumption implies that the control frequencies will be kept sufficiently low so that their separation from frequencies of other major degrees of freedom (propellant sloshing and elastic modes) is reasonably great.

Only planar motion of the vehicle will be assumed in the present discussion, the equations of motion and the vehicle's control system being treated as uncoupled, insofar as the vehicle's three axes of rotation are concerned. The three-axes coupled equations are given in Section 3. The class of booster vehicles considered will not have large wings, will be very nearly symmetrical, and will execute no rapid maneuvers. Therefore, the coupling between control planes will be very small, and the planar motion assumption should be adequate. To fix ideas, the analysis is conducted for the vehicle's pitching plane (longitudinal mode) but is also representative of yaw plane analyses.

Figure 2-1 shows the parameters employed. The vehicle is assumed to be aerodynamically unstable (center of pressure ahead of center of gravity) and to employ thrust-vector control for attitude stabilization. Perturbation angles away from a reference trajectory are shown. This reference trajectory is the zero lift path, having a steady-state turn rate, $\dot{\theta}_o$, so adjusted as to cancel the transverse gravitational acceleration.
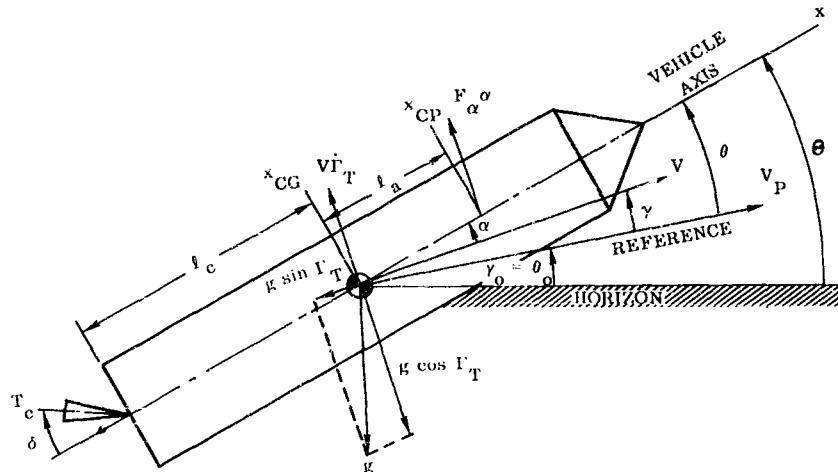
Figure 2-1. Rigid Vehicle Control Parameters

*The equations of motion derived in this section are quite simple and are only adequate to illustrate gross effects. The reader is referred to Sections 3 and 4 for more comprehensive equations.

The equations of motion (small δ and α angles assumed) are:

$$\Sigma F_{\substack{along \\ path}} = M\dot{V} = T_c - D - Mg \sin \Gamma_T$$

$$\Sigma F_{\substack{normal \\ to\ path}} = MV\dot{\Gamma}_T = F_\alpha \alpha - T_c (\delta - \alpha) - Mg \cos \Gamma_T \qquad (2\text{-}1)$$

$$\Sigma M_{CG} = I\ddot{\Theta} = T_c \ell_c \delta + F_\alpha \ell_a \alpha$$

Here, F_α is the aerodynamic normal force per unit angle of attack, and D is the drag force. In writing Equations 2-1 certain lesser aerodynamic coefficients have been omitted, their effects being negligible.

In solving Equations 2-1 the first equation will be considered as uncoupled from the others, by assuming the drag is not a function of the angle of attack. Thus, the forward velocity is unperturbed by attitude changes. This assumption removes any consideration of a "phugoid" mode. It is justified on the basis that: 1) aerodynamic drag is a small force relative to the propulsive and inertial forces and, hence, its perturbations have a negligible effect on velocity history; and 2) the system analyzed is one of accelerated motion, having no steady-state flight condition in which a low-frequency "phugoid" mode can manifest itself.

The initial unperturbed state of the system is one involving flight along a zero-lift path, for which $\dot{\gamma}_o = \dot{\Theta}_o = -\dfrac{g \cos \gamma_o}{V}$ and $\alpha_o = 0$.

Now let:

$$\Gamma_T = \gamma_o + \gamma$$

$$\Theta = \Theta_o + \Theta$$

$$\alpha = \alpha$$

Substituting into the last two of Equations 2-1, one obtains:

$$MV(\dot{\gamma}_o + \dot{\gamma}) = F_\alpha \alpha - T_c (\delta - \alpha) - Mg \cos (\gamma_o + \gamma)$$

$$I\ddot{\Theta} = T_c \ell_c \delta + F_\alpha \alpha \ell_a$$

Cancelling $MV\dot{\gamma}_o = -Mg \cos \gamma_o$, one gets:

$$MV\dot{\gamma} = F_\alpha \alpha - T_c (\delta - \alpha) + Mg \sin \gamma_o \cdot \gamma$$

$$I\ddot{\Theta} = T_c \ell_c \delta + F_\alpha \ell_a \alpha \qquad (2\text{-}1a)$$

The term $Mg \sin \gamma_o \cdot \gamma$ represents the motion of the vehicle relative to an accelerated reference system (the earth and its atmosphere). It is commonly omitted for attitude stability studies of ballistic boosters, since the effects of the flight-path ⎯ coupling into attitude stability (through aerodynamic force perturbations) are minor. If this term is omitted, and if one uses $\Theta = \gamma + \alpha$, Equations 2-1a may be solved to yield:

$$\frac{\Theta}{\delta} = \mu_\delta \frac{s + \dfrac{T_c}{MV} + \dfrac{F_\alpha}{MV} \dfrac{\left(\ell_c + \ell_a\right)}{\ell_c}}{s\left(s^2 + \dfrac{F_\alpha + T_c}{MV} - \mu_\alpha\right)} \qquad (2\text{-}2)$$

where $\mu_\delta = T_c \ell_c / I$ is the control effectiveness parameter, and $\mu_\alpha = F_\alpha \ell_a / I$ is the measure of aerodynamic instability. These parameters have the units of (seconds)$^{-2}$, and give the angular-acceleration per unit-thrust-vector deflection and per unit-angle-of-attack, respectively. (For an aerodynamically stable aircraft, μ_α is the square of the short period mode natural frequency.)

At launch, or out of the atmosphere, when the dynamic pressure is low ($F_\alpha \longrightarrow 0$) Equation 2-2 simplifies to:

$$\frac{\theta}{\delta} = \frac{\mu_\delta}{s^2} \quad . \tag{2-3}$$

At another extreme, when the velocity is very high ($V \longrightarrow \infty$), one has:

$$\frac{\theta}{\delta} = \frac{\mu_\delta}{s^2 - \mu_\alpha} \quad . \tag{2-4}$$

For a vehicle of the class being studied here, one finds that Equation 2-4 is a good approximation whenever the aerodynamic instability is sufficiently great to necessitate its inclusion. The other terms of Equation 2-2 which are omitted thereby only lead to a dipole of small residue (pole-zero grouped closely together), having little influence on this problem.

Physically, the approximation is that $\theta = \alpha$, a satisfactory assumption for a massive vehicle whose transverse forces are low by design intent.

2.2.2 Autopilot and Control System Equations. To discuss the methods used in a preliminary analysis of a flexible booster and control system, it will be advantageous to choose a particular control system. This assumption will not exclude other control configurations from the methods used because the discussion will be kept general. The advantage gained will be that sample root-locus plots can be sketched from representative numerical substitutions into the equations representing the example control system.

The control system described will be for one axis of vehicle rotation only. Figures 2-2 and 2-3 show a block diagram of the attitude control system. A gyro provides attitude reference, a deviation from which results in an error signal which yields a thrust-vector gimbaling command. It is assumed that thrust-vector positioning is achieved by gimbaling the rocket engine thrust chambers--a popular solution. The response of the thrust-chamber positioning servo is represented by a first order lag. Sufficient lead will have to be provided in the control loop to stabilize the system. The necessary lead may be provided by either a lead compensation network or by insertion of a rate gyro; the latter solution is assumed herein.
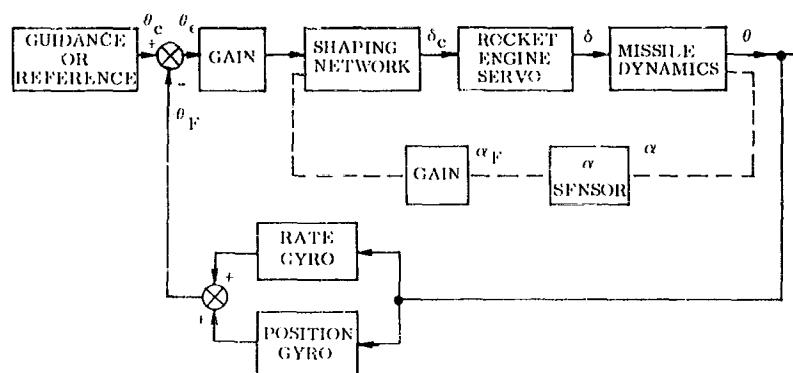
Figure 2-2. Basic Elements of the Control System to be Discussed
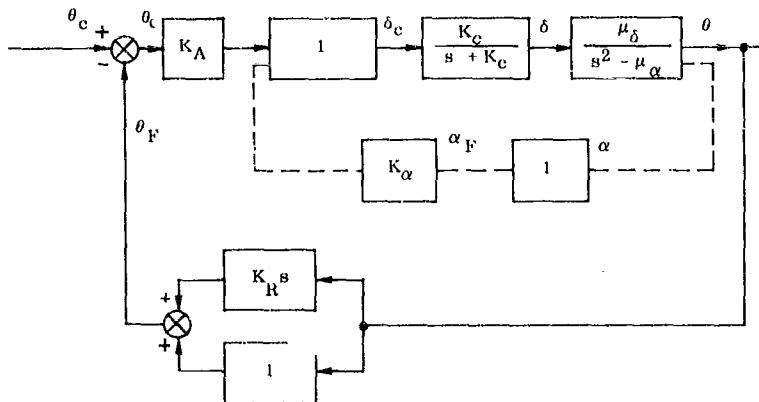
Figure 2-3. Approximations Used for Preliminary Analysis

An aerodynamically stable vehicle is one which responds to angles of attack by turning into the velocity vector so as to reduce the angle of attack. The aerodynamically unstable vehicle can be given a degree of synthetic aerodynamic stability by sensing angle-of-attack variations as they develop and by commanding the engine to gimbal so as to turn the vehicle into the velocity vector. Thus, the inner feedback loop (shown dashed) with gain, K_α, induces such a stability.

Angle-of-attack feedback has the potential advantage of relieving aerodynamic loads on the vehicle, since it moves the vehicle so as to reduce the angle of attack as it develops. Some of the disadvantages of this additional feedback loop lie in the increase in complexity (and attendant decrease in reliability) and in the introduction of additional higher-order degrees of freedom in the angle-of-attack sensor, which can lead to further stability problems. An additional shortcoming of the system lies in the erratic or uncertain behavior of this loop at low dynamic pressures (near launch or outside the atmosphere), possibly necessitating some compensation by gain changes in the outer position loop. It is assumed that α feedback is not used in the system under study, although the principles discussed apply equally well to such a system.

2.2.3 <u>Preliminary Gain Choice.</u> It is desired at this time to make a preliminary selection of system gains so as to provide working values for subsequent discussion. There are three gains at the designer's disposal: K_c, K_A, and K_R. The characteristic equation for the system of Figures 2-2 and 2-3 is:

$$s^3 + K_c s^2 + [K_A K_c K_R \mu_\delta - \mu_\alpha] s + K_c (K_A \mu_\delta - \mu_\alpha) = 0 . \qquad (2-5)$$

A brief study of this equation by use of Routh's criteria yields two simple inviolate criteria for stability, viz.:

$$K_A \mu_\delta > \mu_\alpha \quad \text{and} \quad 1/K_R < K_c .$$

The first of these criteria may be characterized as the static stability criterion; it stipulates that the restoring moment per unit attitude change must be greater than the upsetting moment. The second criterion is a dynamic stability requirement to yield positive damping; it states that the lead from the rate gyro must be greater than the lag from the engine servo. Within these bounds the designer may select many suitable gain combinations. However, experience with this class of systems and vehicles requires that one look ahead and foresee problem areas which may further restrict the choice of gains. Therefore, before proceeding with a choice of gains, it is appropriate to detail some of these problem areas so that they may be weighed in subsequent discussions.

a.   The engine-thrust-chamber-gimbaling time-constant, $1/K_c$, cannot be reduced indefinitely because of practical power and structural limitations. While a small time-constant may be desirable to reduce the amount of lead necessary in stabilizing the system, the practical problems associated with providing high accelerations and velocities to a massive thrust chamber and of stabilizing the necessarily high-gain servo loop, will result in a compromised upper limit to K_c.

b. Vehicle response to transients, particularly gust inputs, must be considered if system loads are to be limited to within the capability of a light-weight structure. The control system, without angle-of-attack feedback, does not respond to a gust until a change in vehicle attitude has occurred. This attitude change, in the case of the aerodynamically unstable vehicle, is always in a direction which increases the angle of attack, the gust thereby overshooting the imposed value. The vehicle's gust response is strongly dependent upon the system's transient response. A tight system, having a rapid response with good damping, therefore, leads to small gust overshoots.

c. Stability of the system when higher order terms (other degrees of freedom) are included must be considered in selecting gains, these being particularly significant in limiting the upper values of the gains. A number of these problems will be considered below, in relation to additions to the basic system equations and modifications to the root-locus plots. Briefly, some of these additions are: 1) inclusion of propellant sloshing modes, 2) addition of vehicle body bending modes, 3) inclusion of higher order terms in the engine-thrust-chamber-servo-loop transfer function and in the transfer functions of the reference gyros, and 4) the insertion of additional shaping and filtering networks within the autopilot as required to stabilize these new terms.

To select some tentative gains we can assume the roots of the characteristic equation are of the form:

$$(s + \rho)(s^2 + 2\zeta\omega s + \omega^2) = 0 \tag{2-6}$$

i.e., an oscillatory mode (a pair of complex poles) plus an exponential decay (real pole). If Equation 2-6 is expanded and the results compared term by term with Equation 2-5, one finds:

$$K_c = 2\zeta\omega + \rho$$

$$K_A K_c K_R \mu_\delta - \mu_\alpha = \omega^2 + 2\zeta\omega\rho \tag{2-7}$$

$$K_c(K_A \mu_\delta - \mu_\alpha) = \rho\omega^2 \quad .$$

Equations 2-7 permit a choice of the gains for a given μ_δ and μ_α, provided one can rationally select ρ, ω, and ζ.

To make this selection, one can be guided by considerations from the problem areas enumerated above. Specifically:

a. A fast, well-damped transient response is desired,

b. K_c should be kept reasonably low,

c. The overall gains should be kept low so as not to excite higher modes (body bending in particular).

These requirements are conflicting, of course. However, one can begin with an observation, based upon experience, that a separation ratio of at least four to one between the rigid-body-mode and first-body-bending-mode frequencies will relieve problem c, above. This simple rule-of-thumb will often provide a basis for the choice of ω, since the first-body-bending frequency will have been previously established by the configuration.

From a study of transients for systems with the pole configuration of Equation 2-6 (Reference 3, pp. 37-43), it is known that a good, well-damped transient will result from choosing $\zeta = 0.3$ and $\rho = \omega$.

The value of K_c which results from the above calculations should be examined from two points of view. First, the value should be reasonable as it affects the thrust-chamber-servo-system requirements — a separate study in itself. Second, K_c should not be too low, inasmuch as the complete gust transient response contains a zero at K_c; too low a value of K_c will adversely affect the gust overshoot. As a general rule, if K_c exceeds twice the value of ρ, the influence of the zero on the gust transient will be slight.

The first approximation gains chosen in the above manner should form a satisfactory basis for more elaborate analysis. Before proceeding to a root locus presentation and to the study of additional degrees of freedom, it is important to discuss one other prime factor. The properties of this vehicle — its inertial, aerodynamic, and

14

propulsive parameters — vary over wide ranges through the boost phase. Moreover, many of the higher order effects to be discussed below change in relative importance as the flight progresses. Consequently, it is understood that the tentative gain selection just described, when carried out for a specific time of flight, may require different adjustments for different flight times when analyzed further. Such a result may lead to the necessity for programmed gain changes. It is reasonable to carry out the preliminary gain selection for conditions at the time of maximum dynamic pressure (usually in the mid-portion of the boost phase), on the basis that these are mean conditions of a sort and will lead to suitable working values for studies through the entire phase. It is quite possible that gains so chosen may prove satisfactory without time programming, thus leading to the simplest, most reliable system.

2.2.4 <u>Root Locus Studies: Rigid Vehicle.</u> To permit plotting root loci, numerical data will be introduced at this point. For convenience all data is expressed here nondimensionally, using the first-body bending-mode period $(1/\omega_1)$ as the unit of time.

At maximum dynamic pressure, data taken from the feasibility phase studies show that the vehicle studied has:

$$\mu_\delta = 0.012\ \omega_1^2 \qquad \text{and} \qquad \mu_\alpha = 0.0067\ \omega_1^2 \ .$$

Following a rule-of-thumb given earlier, we let the control frequency be less than one-quarter of ω_1. Let $\omega = 0.2\ \omega_1$ and set this also equal to ρ. Let $\zeta = 0.3$. Equations 2-7 now yield:

$$K_c = 0.32\ \omega_1$$

$$K_A = 2.65$$

$$K_R = 7/\omega_1 \ .$$

With these data the root locus for the control system of Figures 2-2 and 2-3 has been drawn in Figure 2-4, showing the operating point for the above gains.

$$\frac{\theta_F}{\theta_\epsilon} = \frac{K_A K_c K_R \mu_\delta \left(s + \dfrac{1}{K_R}\right)}{(s + K_c)(s^2 - \mu_\alpha)}$$

$$\sqrt{\mu_\alpha} = 0.082\ \omega_1$$

$$K_R = \frac{7}{\omega_1}$$

$$K_c = 0.32\ \omega_1$$

$$\mu_\delta = 0.012\ \omega_1^2$$

CLOSED LOOP ROOTS
(OPERATING POINTS)
FOR $K_A = 2.65$
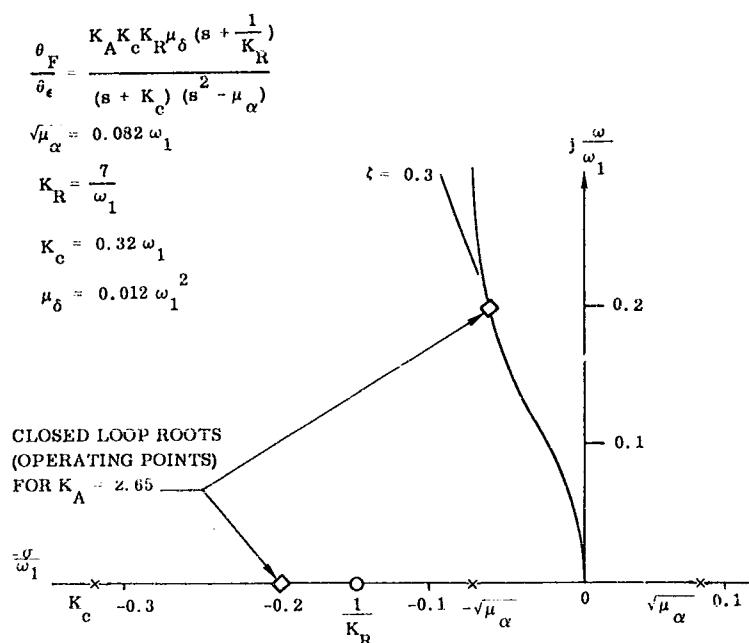
Figure 2-4. Root Locus for System of Figures 2-2 and 2-3, Using Preliminary Gains

Considering also the problem of changing vehicle properties, we will check the operating point root locations for the gains chosen above at conditions near launch and near the time of booster staging. At both of these times dynamic pressure is low, so that $\mu_\alpha \approx 0$. Since engine thrust increases somewhat with altitude (as the back pressure from the atmosphere decreases) and vehicle moment of inertia decreases with flight, the control effectiveness parameter, μ_δ, will vary over a modest range. For the vehicle studied:

$$\mu_{\delta \text{(launch)}} = 0.0068 \, \omega_1^2 \text{ and}$$

$$\mu_{\delta \text{(staging)}} = 0.020 \, \omega_1^2 \quad .$$

Assuming all autopilot gains are kept constant, Figure 2-5 shows the root loci and operating points for the beginning and end of this boost phase. Also shown (dashed) is a locus of the operating points as they vary over the boost phase due to changes in both μ_δ and μ_α.

$$K_A = 2.65$$
$$K_c = 0.32 \, \omega_1$$
$$K_R = \frac{7}{\omega_1}$$
$$\mu_\delta \text{ LAUNCH} = 0.0068 \, \omega_1^2$$
$$\mu_\delta \text{ STAGING} = 0.020 \, \omega_1$$
——— ROOT LOCUS FOR $\mu_\alpha = 0$
— — — LOCUS OF OPERATING POINTS FOR $K_A = 2.65$
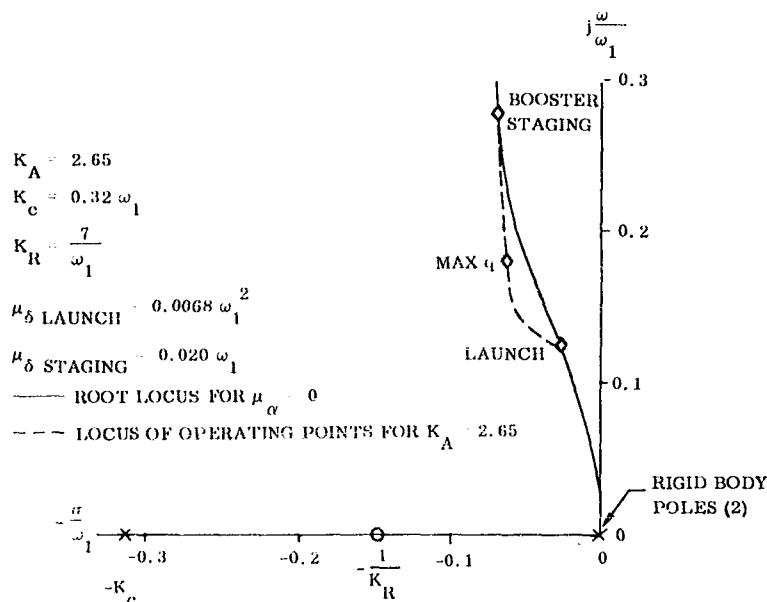
Figure 2-5. Root Locus for $\mu_\alpha = 0$

By inspection of the loci of Figure 2-5 it would be concluded that the preliminary gains chosen would be satisfactory for use throughout the boost phase, at least insofar as the rigid-body stability is concerned. Such a constant gain autopilot is highly desirable from a reliability standpoint.

2.2.5 Root Locus Studies: Propellant Modes Included. One of the important stability problems in the attitude control of large liquid-fueled vehicles is that of the control of sloshing modes of the internal propellants. An attitude-sensing control system, such as that proposed here, couples the rigid-body and sloshing modes quite strongly, under some circumstances often producing a divergent mode. Since the inherent damping in a tank of fluid varies inversely with tank diameter, these propellant modes are only very lightly damped in large vehicles. Thus, the energy imparted to the propellants by the vehicle motion is but slowly dissipated, and sloshing-control system modes may build up to destructive amplitudes unless properly treated.

In Appendix A, Paragraph A-3, it is shown that the problem of propellant sloshing in a cylindrical tank can be treated satisfactorily by the substitution of a mechanical analogy for the fluid. The analogy consists of a rigid mass, plus a series of harmonic oscillators (spring masses or pendulums) — one for each fluid mode. The mechanical system duplicates the fluid's response and the resultant forces and moments on the tank. In practical control problems, only the first propellant mode of each tank is treated, the higher modes producing negligible contributions.

The usual liquid-fueled booster has a multiplicity of tanks — two per stage. The transfer functions for such a system are unwieldy when treated by algebraic solution. Treatment of such a system will, therefore, be reserved for solution by machine computation. It is instructive, however, to begin with the more modest problem of a single tank in order to discover some features of the problems.

Figure 2-6 shows the basic vehicle, with the addition of a simple pendulum representing the sloshing propellants of the first fluid mode. The "rigid" (non-sloshing) portion of the mechanical analogy is lumped in with the vehicle's structure in computing an effective center of gravity, mass, and moment of inertia. The appropriate parameters for the sloshing analogy, as a function of tank proportions, are given in Appendix A, Paragraph A-3.
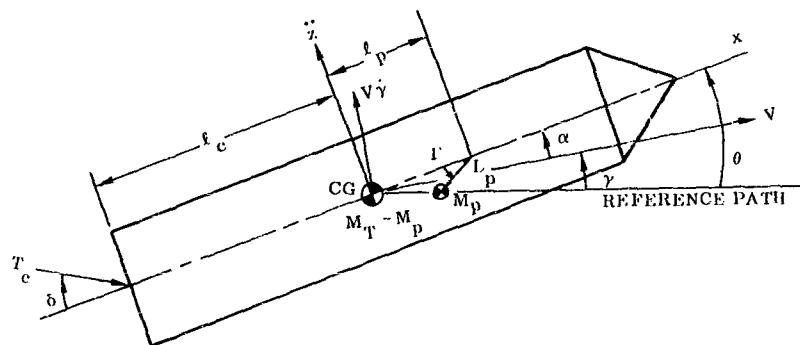
Figure 2-6. Sloshing Model

The equations of motion become:

$$\Sigma M_{CG} = I\ddot{\theta} = T_c \ell_c \delta - M_p \alpha_T \ell_p \Gamma$$

$$\Sigma F_{\substack{norm. \\ path}} = MV\dot{\gamma} = -T_c(\delta - \alpha) - M_p \alpha_T (\Gamma + \alpha)$$

$$(s^2 + \omega_p^2)\Gamma = \frac{1}{L_p}\left[\frac{\Sigma F_z}{M} + \left(\ell_p - L_p\right)\ddot{\theta}\right].$$

(2-8)

where $\omega_p^2 = \alpha_T/L_p$ and $\alpha_T = T-D/M_{total}$ is the absolute longitudinal acceleration of the vehicle, this being the parameter affecting the tension in the pendulum rod. $(M_{total} = M + M_p)$.

In writing Equations 2-8, we have omitted the aerodynamic effects. While the influence of the aerodynamic forces on sloshing is not necessarily small at all times of flight, it develops that the sloshing problem seldom becomes acute until the vehicle's propellant mass has burned down considerably. By this time the dynamic pressure will have fallen off to a point where these aerodynamic forces are small. The pendulum is shown responding to the absolute transverse acceleration at the pendulum mass station, the force summation indicated being the summation of all real forces transverse to the missile's logitudinal axis. (Gravitational attractions do not displace the pendulum.) Setting:

$$\Sigma F_z = -\left(T_c \delta + M_p \alpha_T l'\right),$$

one sees that the first and last equations of Equations 2-8 are uncoupled from the flight-path equation (the result of assuming no aerodynamic effects).

Hence one finds, by simple substitution, that:

$$\frac{\Theta}{\delta} = \frac{\mu_\delta}{s^2} \frac{s^2 + \omega_p'^2 + \dfrac{M_p}{M} \dfrac{\alpha_T}{L_p} \dfrac{l_p}{l_c}}{s^2 + \omega_p'^2 + \dfrac{M_p}{M} \dfrac{\alpha_T}{L_p} \dfrac{l_p}{l_c} \dfrac{(l_p - L_p) l_c}{r^2}} \tag{2-9}$$

where

$$\omega_p'^2 = \frac{\alpha_T}{L_p}\left(1 + \frac{M_p}{M}\right) \quad \text{and} \quad r^2 = I/M.$$

A comparison of Equations 2-9 and 2-3 reveals that the addition of the harmonic oscillator has introduced a pair of pole-zero dipoles on the imaginary axis. The presence of the very small fluid damping (omitted in the equations) would shift these points slightly into the left-hand half of the s-plane. A study of root loci for the closed-loop autopilot system may be made using this transfer function. Figure 2-7 shows a typical result for one of the main tanks of a booster vehicle.
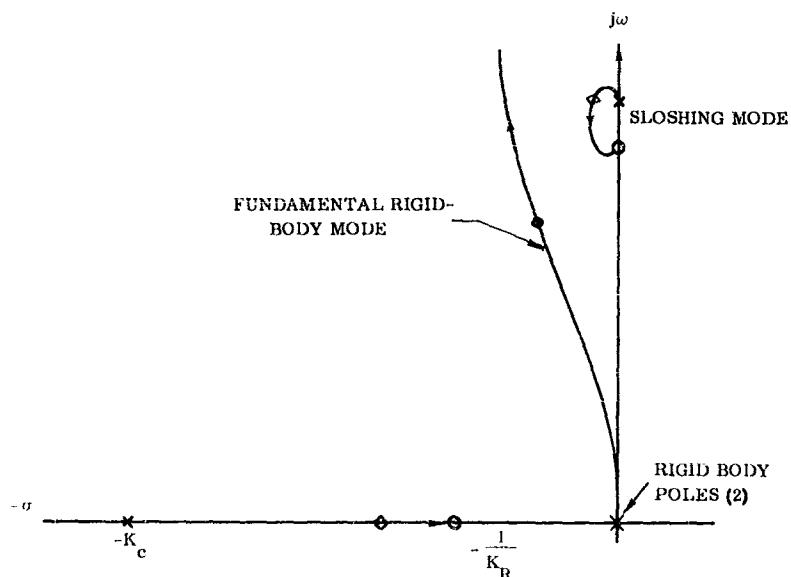
Figure 2-7. Typical Root Loci for Booster Vehicle with Single Tank of Sloshing Propellant

2.2.6 Detailed Root Locus Studies: Multi-Tank Vehicle. For purposes of studying more carefully the variations in roots of the significant modes (modes within the range of control frequencies), it is convenient to employ a digital computer, particularly when the equations become quite numerous and strongly coupled. The digital routine should be capable of extracting the roots directly from the equations when they are written as a set of simultaneous differential equations in all the variables. The homogeneous equations of motion (independent variables such as gust inputs set equal to zero) will usually have the matrix form:

$$\left| [A] s^2 + [B] s + [C] \right| \left| q_i \right| = 0$$

where the q_i elements are the problem variables, and the A, B, and C matrices contain the system parameters (constant for a given instant of flight).

It is most efficient, in terms of machine time, to extract the roots of the equation for $K_A = 0$ and $K_A \rightarrow \infty$, obtaining thereby the open-loop poles and zeroes (respectively) and then to employ a separate digital routine using these poles and zeroes as inputs to generate the root locus. The variety of methods which may be programmed to accomplish these calculations is so great as to preclude any discussion here.

Figure 2-8 shows machine-generated root loci for a two-tank booster vehicle, computed at one time instant of boost phase flight. The variables considered were the rigid-body degrees of freedom and the sloshing of propellants in the two main tanks. One tank's roots are seen to be slightly unstable for the assumed case of zero damping.
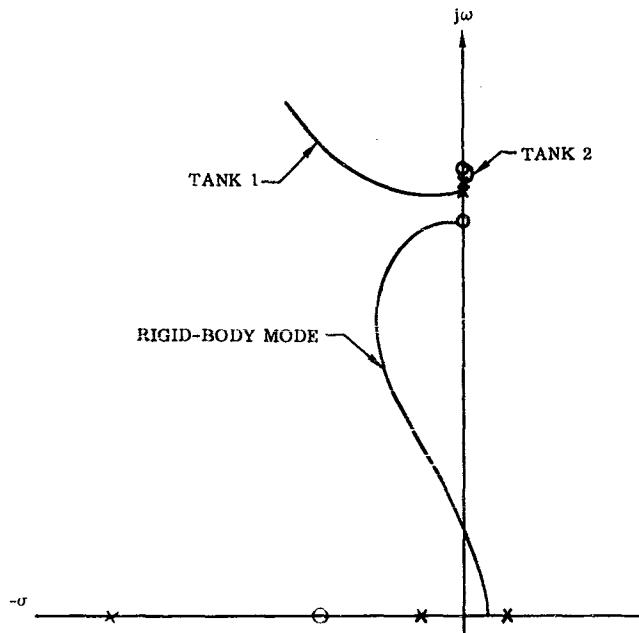
Figure 2-8. Root Loci for Booster Vehicle with Two Propellant Tanks

Since propellant modes can be controlled by mechanical baffles to provide damping, it is common to defer further study of the sloshing problem until other problem areas (such as bending stability) have been investigated.

2.2.7 Root Locus Studies: Body Bending Included. The problem of closed-loop stability of the flexible missile was mentioned earlier in connection with phenomena which will establish an upper limit on the autopilot gains. The attitude gyros sense missile body bending modes in addition to rigid-body attitude changes, and these modal contributions provide a gimbaling command to the thrust chambers. Since the thrust vector movement, in turn,

excites body bending modes, a closed loop is formed which can lead to a divergent oscillation at the bending frequency, if excessive gains and incorrect phasing are employed.

Figure 2-9 shows the parameters used in a simple one-mode analysis for moderate frequencies, i.e., frequencies at which thrust chamber lateral inertial forces are small relative to the gimbaling thrust vector's transverse component.
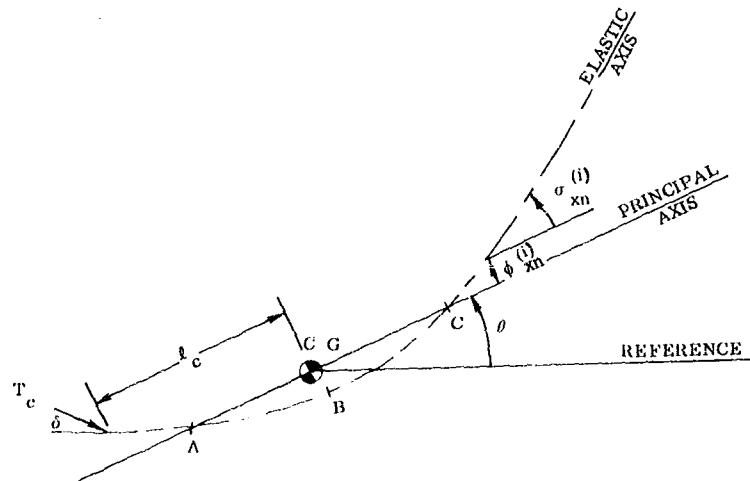
Figure 2-9. Vehicle with One Elastic Mode

The equations of motion for rigid-body attitude and the first bending mode are:

$$\left. \begin{array}{l} Is^2 O = T_c \ell_c (\delta - \sigma_{xT}^{(i)} q_i) - T_c \phi_{xT}^{(i)} q_i \\[2em] (s^2 + 2\zeta_i \omega_i s + \omega_i^2) q_i = -\dfrac{T_c \phi_{xT}^{(i)}}{\mathcal{M}_i} \delta \end{array} \right\} (i) = 1 \qquad (2\text{-}10)$$

where $\sigma_{xT}^{(i)}$ and $\phi_{xT}^{(i)}$ are the normalized modal slope and deflections, respectively, at the engine station (subscript "T"). The mode normal coordinate is q_i and ζ_i, ω_i, and $\mathcal{M}_i$ are the mode damping, frequency and generalized mass, respectively.

Because the gyro package senses the total attitude at the gyro station, the expression, $O_G = \Theta + \sigma_{xG}^{(i)} q_i$, can be written. Here $\sigma_{xG}^{(i)}$ is the normalized mode slope (positive nose up) at the gryo station. Schematically, the block diagram could be drawn as in Figure 2-10.
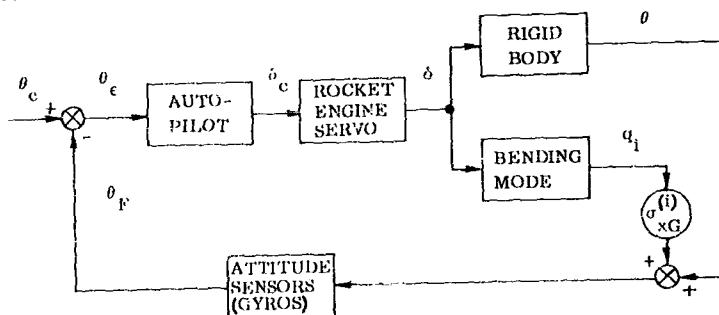
Figure 2-10. Block Diagram of Control System Including One Elastic Mode

If these additional relationships are incorporated, the open loop transfer function becomes:

$$\frac{\Theta_F}{\Theta_\epsilon} = K_A K_R K_c \mu_\delta \left(1 - \frac{T_c \phi_{xT}^{(i)} \sigma_{xG}^{(i)}}{\mathcal{M}_i \mu_\delta}\right) \frac{s + {}^{1/}K_R}{(s + K_c) s^2}$$

$$\frac{s^2 + \left(\dfrac{2\zeta_i \omega_i}{1 - \dfrac{T_c \phi_{xT}^{(i)} \sigma_{xG}^{(i)}}{\mathcal{M}_i \mu_\delta}}\right) s + \dfrac{\omega_i^2 + \dfrac{\sigma_{xT}^{(i)} T_c \phi_{xT}^{(i)}}{\mathcal{M}_i} + \dfrac{(\phi_{xT}^{(i)})^2 T_c}{\mathcal{M}_i \ell_c}}{1 - \dfrac{T_c \phi_{xT}^{(i)} \sigma_{xG}^{(i)}}{\mathcal{M}_i \mu_\delta}}}{s^2 + 2\zeta_i \omega_i s + \omega_i^2} \qquad (2\text{-}11)$$

A comparison between Equation 2-11 and the open-loop transfer function for Figures 2-2 and 2-3 (Ref. Figure 2-4) reveals that the addition of the mode has affected the gain as well as introduced a pole-zero doublet. One may show that in order for such a dipole to yield a loop of stable roots, the bending mode zero should be less than (below) the pole (see Figure 2-7). Thus, an inspection of the equation reveals that it is desirable to locate the gyro on the aft portion of the vehicle, (behind the antinode) where $\sigma_{xG}^{(i)}$ is negative. It must be added, however, that this simple conclusion applies only to modes of moderate frequency (probably only the fundamental) and to the simple low-order autopilot of Figure 2-11. A more elaborate study will be required to provide a reasonable assurance of stable operation when higher frequency modes are considered.
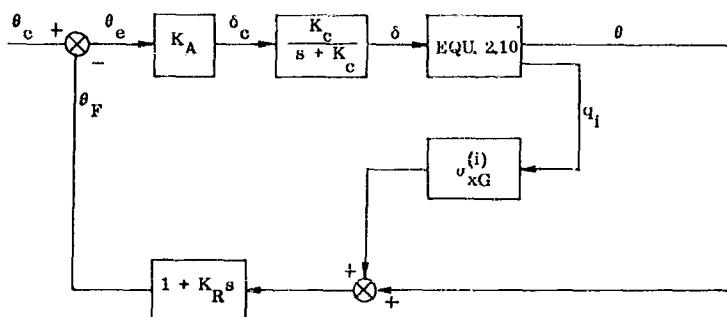
Figure 2-11. Approximations Used for Preliminary Analysis of Control System Including One Elastic Mode

2.2.8 Detailed Root Locus Studies: Higher-Order Elastic Mode Analysis. Even a planar analysis of an elastic vehicle leads to complex equations when numerous modes of motion and system degrees of freedom are to be accounted for. Large analog computer simulations were used for the early studies of such large boosters as Navaho and Atlas. The use of the analog computer permitted the inclusion of many modes, aerodynamic and propellant slosh forces, and the nonlinear characteristics of the servo actuator. As more was learned about the problem it became apparent that the system could be analyzed adequately in separate parts, i.e., the elastic modes examined one mode at a time, and the rigid-body and sloshing modes examined independently from elastic motion.

For the analysis of the coupling of the control system with the elastic motions, the following simplifications were found to be suitable to adapt the analysis for manual techniques. Such analysis yields good results for preliminary design and may, under certain conditions, be acceptable for determining final configuration. The limitations upon this method are explained in later chapters.

In the first simplification only one elastic mode is considered at a time. This step is permissible because the elastic modes are orthogonal and couple only through the aerodynamic forces, rocket engine control forces (through the autopilot), and fuel sloshing modes. The frequency separation between modes and the highly tuned nature of each mode (low damping) make this coupling negligible (see Section 4).

In calculating the characteristics of the modes, the vehicle mass and inertial properties are computed with the engine mass and rigid portion of the propellants included (see Appendix A). This technique provides maximum uncoupling of the modal coordinates.

The second simplification neglects the effects of aerodynamics. This assumption generally is satisfactory at all times for a ballistic booster with a nonwinged payload. For analysis of a winged booster or payload, aerodynamics will have to be included at certain times of flight. The effect of aerodynamics on stability can be estimated by computing the apparent frequency change of the mode brought about by the generalized aerodynamic forcing function. If the frequency does not change more than a few percent the effects of aerodynamics are safely ignored.

In the third simplification, a linear rocket engine servo (as derived in Appendix B-4) is used. The technique used to linearize the nonlinear equations is given in Appendix B-4. By using gains for several engine amplitudes the presence of stable and unstable limit cycles can be predicted.

For the block diagram of the control system and missile, including an elastic mode, two parallel blocks will be used to represent the missile dynamics – one for rigid motion (Θ/δ) and the other for elastic motion (q_i/δ). This block diagram is given in Figure 2-10.

The equations which will be used to replace Equations 2-10 for vehicle dynamics are derived by addition of engine chamber inertial terms. They are: $I_R s^2 \delta$ and $M_R \ell_R R s^2 \delta$, respectively. Hence:

(Rigid Body):

$$I s^2 \Theta = \ell_c \left[T_c + \left(M_R \ell_R + \frac{I_R}{\ell_c} \right) s^2 \right] \delta - T_c \left(\ell_c \sigma_{xT}^{(i)} + \phi_{xT}^{(i)} \right) q_i \tag{2-12}$$

(Bending Mode):

$$(s^2 + 2\zeta_i \omega_i s + \omega_i^2) q_i = -\frac{1}{\mathcal{m}_i} \phi_{xT}^{(i)} \left[T_c + \left(M_R \ell_R - I_R \frac{\sigma_{xT}^{(i)}}{\phi_{xT}^{(i)}} \right) s^2 \right] \delta . \tag{2-13}$$

For the engine servo one uses the equation:

$$(s^3 + 2\zeta_{cn} \omega_{cn} s^2 + \omega_{cn}^2 s + K_c \omega_c^2) \delta = K_c \omega_c^2 \delta_c . \tag{2-14}$$

Combining these equations in the control system of Figure 2-10 gives the following open-loop transfer function.

$$\frac{\Theta_F}{\Theta_\epsilon} = \frac{K_A K_c K_R \omega_c^2 \ell_c (M_R \ell_R - I_R \sigma_{xT}^{(i)})}{I [\text{filter}] [\text{gyro dynamics}] \quad s^2}$$

$$\frac{\left(1 - \frac{\sigma_{xG}^{(i)} T_c}{\mathcal{m}_i \mu_\delta} \right) \left(s + \frac{1}{K_R} \right) \left(s^2 + \frac{T_c}{M_R \ell_R - I_R \sigma_{xT}^{(i)}} \right)}{s^3 + 2\zeta_{cn} \omega_{cn} s^2 + \omega_{cn}^2 s + K_c \omega_c^2}$$

$$\frac{\left(s^2 + \frac{2\zeta_i \omega_i}{1 - \Lambda_i} s + \frac{\omega_i^2 + \frac{T_c}{\mathcal{m}_i} \left(\sigma_{xT}^{(i)} + \frac{1}{\ell_c} \right)}{1 - \Lambda_i} \right)}{s^2 + 2\zeta_i \omega_i s + \omega_i^2} \tag{2-15}$$

where $\Lambda_i \equiv 1 - \frac{\sigma_{kG}^{(i)} T_c}{\mathcal{m}_i \mu_\delta}$

In writing Equation 2-15 the second order terms describing the effect of rocket engine inertia on the rigid body motion have been approximated in favor of factoring out a simple expression for the "tail-wags-dog" zero. Also, we have used the convention $\phi_{xT}^{(i)} \equiv 1$.

The so-called "tail-wags-dog" (TWD) zero appears in Equation 2-15. This zero occurs at the frequency at which the transverse inertia forces resulting from the gimbaling of the rocket engine chamber cancel the thrust forces resulting from the chamber's angular deflection. Thus, at frequencies below the TWD zero the thrust forces will determine the phase of the resulting force, while the inertia forces will determine the resultant force-vector phase at frequencies above the TWD zero. Therefore, there will be a 180-degree phase shift in force output as the frequency crosses the override point.

In writing Equation 2-15 the rate and position gyros, if both are used, were restricted to the same location on the missile. The equations and simplifications which can be used when this assumption is invalid are given in Section 4.

With Equation 2-15 one may continue to use the root-locus technique for simplified analysis. This is one of the best methods available for linear systems, giving a good visual indication of the effect of one mode and/or element upon the other. In addition, the root-locus technique gives a direct indication of the damping of the system. Figure 2-12 shows a representative root-locus pole-zero configuration for Equation 2-15.
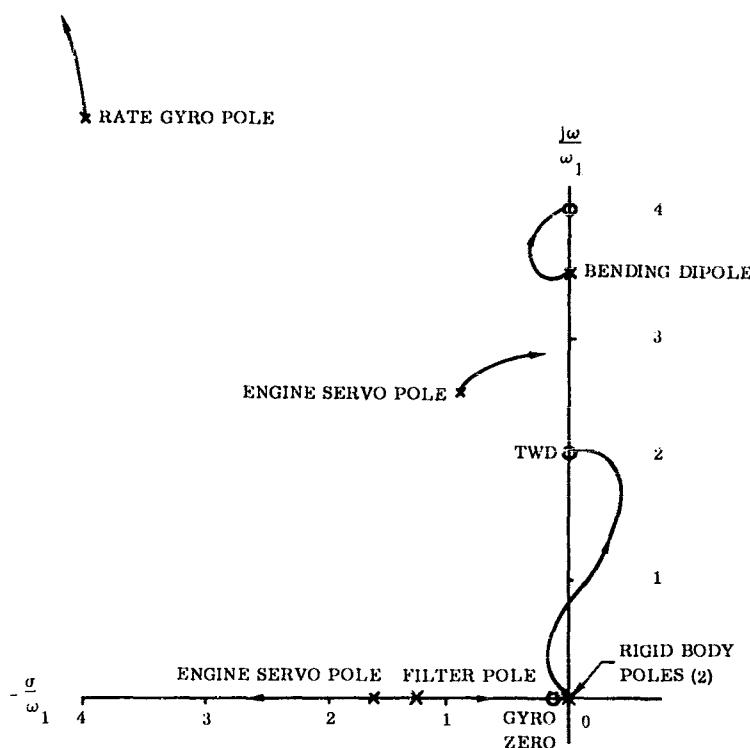
Figure 2-12. Representative Root-Locus for Pole-Zero Configurations for Equation 2-15

The effect of higher order elements such as those poles due to the rate gyro roll-off characteristics can be illustrated at this point. The relatively high frequency body bending mode in Figure 2-12 would be affected by the rate gyro poles. This effect can be shown by measuring the phase-angle contribution of these poles from the

elastic mode pole. For a low frequency mode, on the other hand, the phase contribution of the gyro poles will be negligible.

As a linear approximation is used to represent the nonlinear actuator, the engine servo pole configuration will only be applicable to one engine amplitude and frequency of oscillation (see Appendix B-4). A change in amplitude would cause a shift in the position of the actuator roots. This shift would cause a gain change and angular rotation in the locus from the elastic pole. A typical change in locus with amplitude is shown in Figure 2-13.
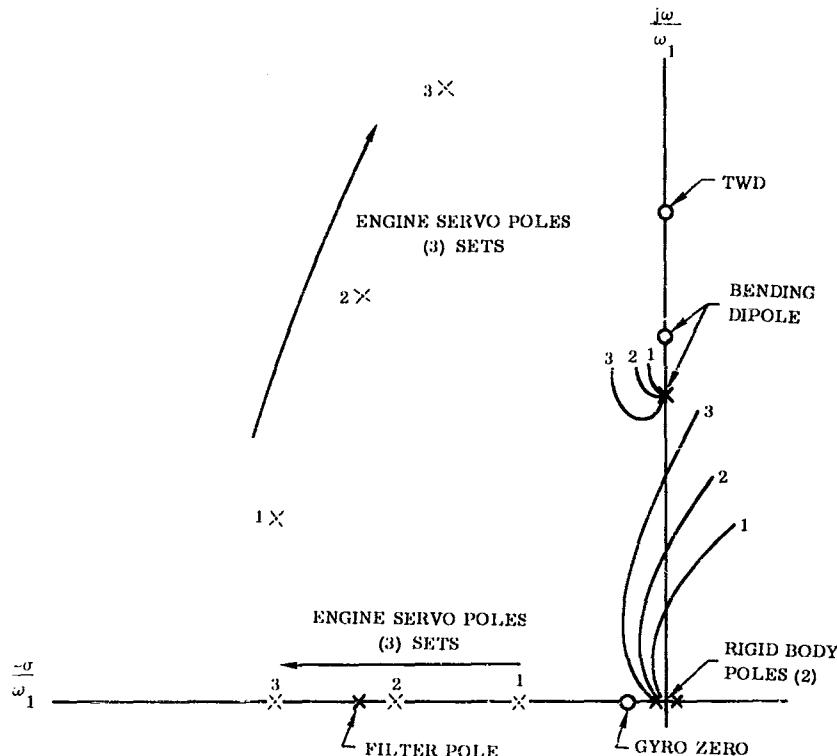
Figure 2-13. Engine Servo Poles for the Three Different Signal Amplitudes and the Resulting Three Different Departure Loci

The results of the locus of Figure 2-13 can be expressed in three ways: a constant amplitude locus (conventional gain locus), a constant gain locus, or a family of gain and amplitude loci. These representations would appear as shown in Figures 2-14 through 2-16.
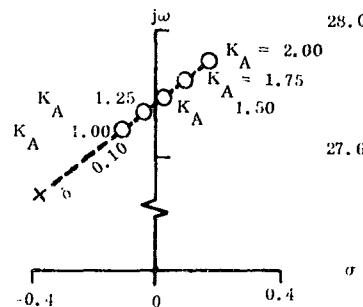
Figure 2-14. Constant Amplitude Locus
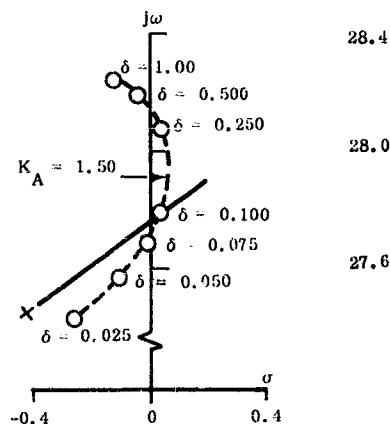
Figure 2-15. Constant-Gain Locus

Although Figures 2-12 through 2-16 represent a simplification, they are very useful in analysis of the effects of elastic motion. The roots illustrated above can be easily handled by manual techniques. One effect which has
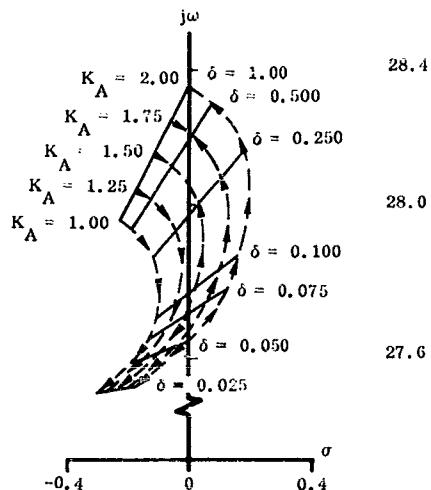
Figure 2-16. Family of Constant-Gain vs. Constant-Amplitude Loci

been omitted is that of the dynamics of the displacement gyro. The relative unimportance of the displacement gyro, its gain, and its characteristics may be seen from the fact that the $1/K_R$ zero is practically at the origin, and hence is almost cancelled by a pole there, insofar as its appearance from the region of the bending dipole is concerned.

Figure 2-17 illustrates the importance of the angle of departure from the bending pole in the analysis of the stability of the system. By manipulating the parameters related to the filter (position and number of poles and zeros), one can obtain any desired angle of departure from the bending pole. For example, the addition of a lag filter is quite often used to phase-stabilize the lower frequency modes. However, this results in a deterioration of the rigid-body locus, as shown in Figure 2-17.
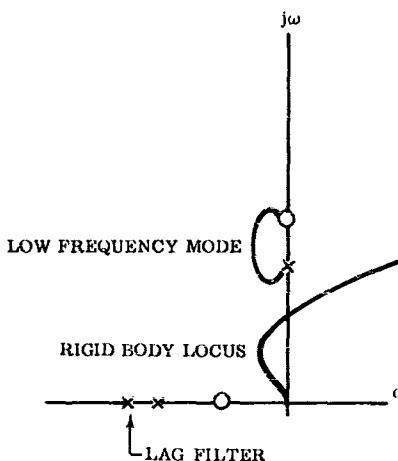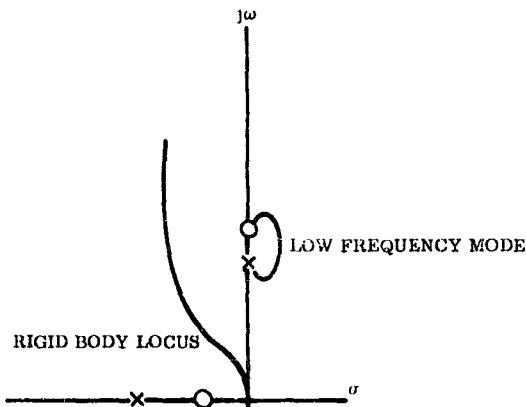
Figure 2-17. Deterioration of the Rigid-Body Locus as a Result
of Lag-Stabilization of Low Frequency Mode

The preceding discussion indicates that at any time the control system analyst could provide a stable control system bending mode configuration by the addition of proper phase compensation. This approach, however, is not always feasible in practice. First, there will be many dipoles, each one representing a different mode. Thus, a simple filter which stabilizes one mode may make another unstable, thereby requiring a more elaborate filter design. In addition to the multiplicity of dipoles, each dipole will move in the course of the flight. This would correspond to an increase in the frequency of the modes as the propellants are expended. The frequency range covered by a higher mode (e.g., the third or fourth) over the course of a stage of flight might be very great. In addition, the mode shapes change, often altering the sense (sign) of a modal slope seen at a gyro station.

It is therefore impractical to try to achieve a stable angle of departure for all poles throughout flight by filtering only. Thus, structural damping (modal damping) must be relied upon in practical control systems to help in gain-stabilizing certain modes. While for many configurations the angle of departure of closed-loop roots from the pole might be toward the right half of the s-plane, the combination of structural damping and control system

attenuation will be sufficient to give a stable operating point. The general philosophy is to attempt to control the angle of departure (phase-stabilize) the low frequency modes while depending on the structural damping and control system "roll off" to gain-stabilize the high frequency modes.

The use of structural damping to stabilize the low frequency modes is inadvisable due to the small amount of damping available. This damping has been found to vary from 1/4 percent critical, for a large, structurally clean configuration which is full of propellants, to 2 percent for conventional built-up construction when the tanks are empty. This damping will generally be higher for the high frequency modes*. Curves illustrating the damping for several configurations of a large booster are given in Section 6.

The preceding technique gives a simple method for the preliminary analysis of flexible booster-autopilot elastic coupling. The answers are correct under the assumptions made and give insight into phenomena which may occur when a more complete analysis is undertaken. The results obtained are useful for predesign studies on autopilots for flexible booster configurations and will be adequate for final configuration and gains for a large class of boosters (see Sections 4 and 5).

2.3 DETAILED COMPUTER STUDIES

In addition to the simple linear and describing function results, analog and digital computer solutions of the complete system of equations are often used. The analog solutions may be used to give final verification of the solution of the elastic, rigid body, and slosh equations. With present analog equipment one can simulate (practically) up to five elastic modes plus the slosh analogies. A block diagram of the control system missile dynamics and the elastic modes, plus the rate and position sensor dynamics for such a system of equations is shown in Figure 2-18. The use of an analog computer makes it possible to simulate more extensive nonlinearities such as a complete servo actuator and intentional control nonlinearities (limits, thresholds, digital sampling-and-hold, etc.). The computer allows all significant degrees of freedom to be included at the same time, this giving a final verification of freedom from instabilities arising because of unexpected coupling between the various modes and because of the nonlinearities.

Early analog studies were used to obtain elastic missile stability boundaries, which are plots of gyro location versus maximum allowable gain for stability. Each boundary represents one particular flight time. A typical stability boundary plot for several flight times is shown in Figure 2-19.

The elastic modes change frequency and configuration as propellants are expended. On a root locus system they have the effect of moving the bending dipole up along the $j\omega$ axis. In the stability boundary obtained from the analog this effect shows up as a change in permissible gain and a shift of the boundary along the missile. This shift reduces the available area in which the sensors can be placed.

The stability boundary gives an accurate representation of the gains which can be used at various times of flight but does not give information necessary for complete confidence in the result. This is true because small changes in phase, such as could occur with changes in time and other parameters, may alter the angle of departure from the elastic pole and drastically change the gains allowable for stable operation. For instance, if the angle of departure from the elastic pole were parallel to the $j\omega$ axis, the allowable gain could be appreciably reduced by a rotation of this angle a few degrees towards the $j\omega$ axis. Thus, even a minor interpolation or change in operating characteristics could alter the nature of the results seriously.

The best method of synthesis and analysis of a quasi-linear booster control system appears to be through the use of modified root-locus techniques (as described in Subsection 2.2.8) to determine the gains and filter configurations. These techniques may be elaborated to consider suspected coupling between modes due to a small frequency separation and/or significant generalized forces. Such elaboration is made by employing a general, digital-root extraction routine such as described in Subsection 2.2.6, along with as many modes of the system as necessary.

The degree to which such a result can be utilized without analog verification is dependent upon the accuracy with which the system's nonlinearities-both unintentional and intentional - can be represented. One fruitful usage of

---

*This observation is in contradiction to the classical structural damping property but rests upon the fact that a portion of the damping is from coulomb friction and propellants.
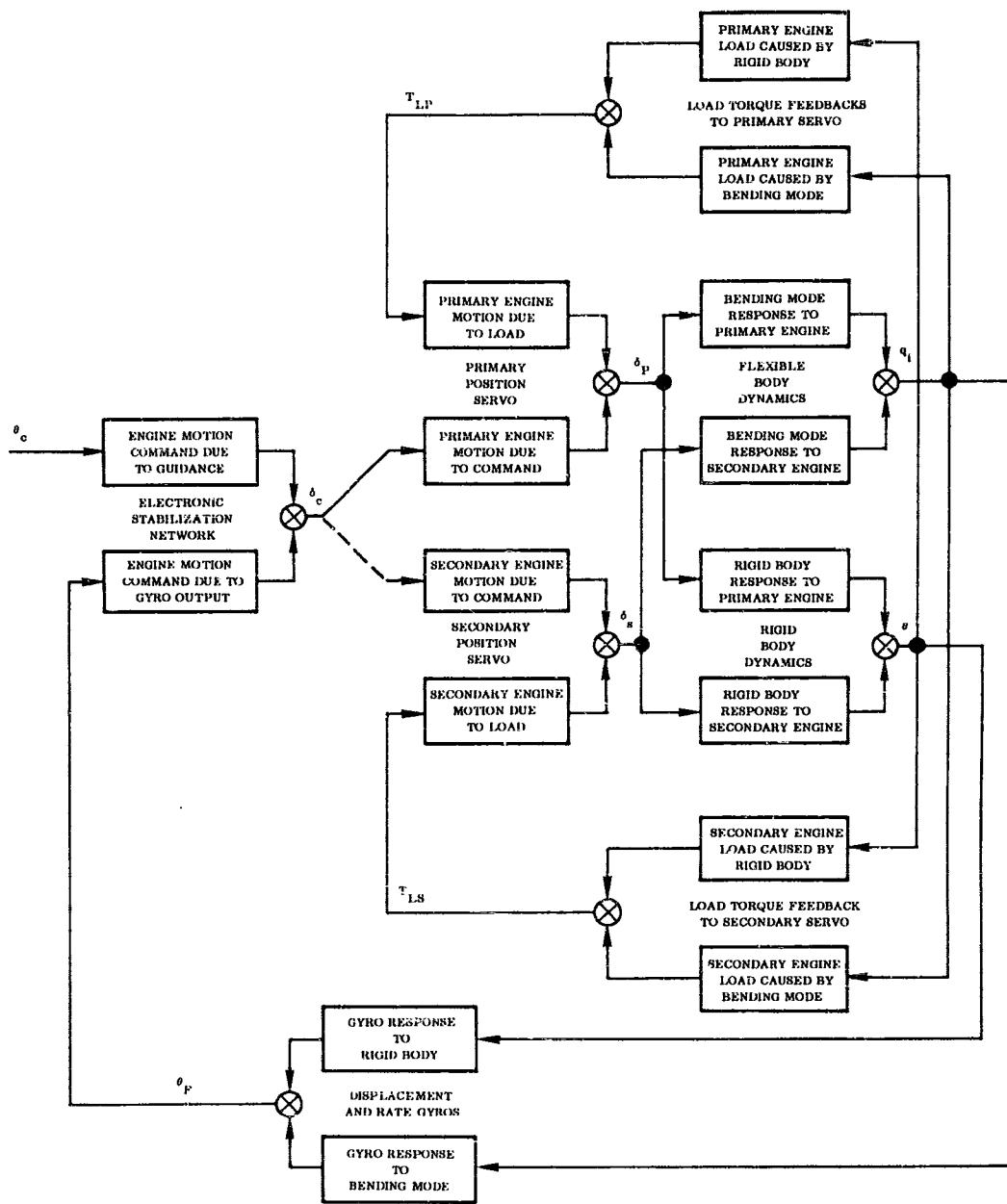
Figure 2-18. Single-Plane Attitude-Control System for a Flexible-Bodied Vehicle: Simplified Block Diagram
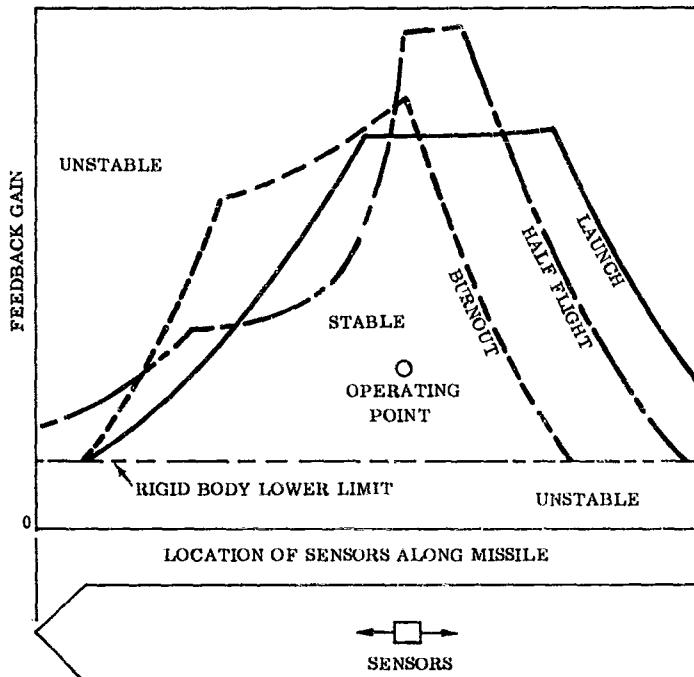
Figure 2-19. Typical Stability Boundary Plot for Several Flight Times

the analog might be to provide a measure of the accuracy of the digital results by running a test problem as a standard, against which digital predictions may be gaged. In this way the necessity for mounting a full-scale analog effort, with its attendant equipment complexity problems, may be obviated.

On the other hand, the use of the massive computer simulation for a final proofing of the complete missile system does have several advantages. One advantage is that all terms which affect solution accuracy, including strong nonlinearities, can be simulated, and the results cannot be questioned on the basis of an excessive number of simplifying assumptions. Thus, one increases the confidence level by verifying the results of other studies. Finally, the simulation yields transient results under various inputs and provides data concerning local histories of body loads. The determination of loads is discussed below.

2.4 TIME-VARYING STUDIES

Time-varying studies constitute the most complete simulation and analysis which can be applied to the flight of a missile. A mathematical model which changes with time is the only comprehensive representation that can be used for the lower frequency modes of a vehicle expending propellants and flying through a varying environment. The effect of the change of parameters can then be evaluated and the differences from fixed time studies shown.

The time-varying nature of the studies gives rise to additional transfers of energy which are not present in fixed-coefficient studies. This transfer arises from changes in longitudinal acceleration upon propellant sloshing, aerodynamic forces, mass and inertial changes, and changes in the elastic properties. Of the preceding items, changes in elastic properties are usually not included in the time-varying analysis. This omission is acceptable because the time-varying solution is usually conducted to analyze the rigid-body and sloshing coupling between the pitch, yaw, and roll planes; there normally is a great frequency spread between these modes and the elastic modes.

Conversely, time-varying solutions are not usually used in the analysis of elastic modes. The bending-mode equations are of such nature that a theory for the time-varying case which can be practically implemented does not exist. The partial differential equations of the elastic motion are too cumbersome to handle, and the modal simplifications can only be made for time-fixed configurations. The time-fixed analysis is satisfactorily accurate, however, since modal periods are short and parameters vary slowly.

The design of an autopilot demands that the system be stable at all conditions of flight. Using the time-slice approach, system stability is demonstrated at selected times. There is small possibility of elastic instabilities in a system that passes through a number of stable points in which the parameters vary only slightly from point to point. Thus, by analyzing a number of points during the flight the stability between these discrete points can be correctly inferred.

Both single-plane and three-axis studies are used in time-varying analyses. The single-plane analysis will always be simpler than the three-axis analysis and, therefore, should be used whenever it can give satisfactory results. One such study area concerns the effect of the continuing increase in acceleration on propellant sloshing amplitudes. This increasing acceleration has the effect of reducing slightly the amplitude at any given time. As the acceleration is increased, the same energy can be contained in an oscillation of slightly less amplitude. In a related study, the build-up of sloshing due to system inputs is simulated. All expected atmospheric disturbances during flight are simulated to provide the most accurate means of predicting the maximum slosh angles which are to be expected. The effect of this maximum slosh amplitude on loads and control capability can be evaluated. The damping provided by mechanical baffles – one common method of slosh control – is a function of the amplitude of slosh (see Appendix A-3). The effect of this nonlinear damping on fluid slosh history during flight can be analyzed only by a time-varying solution.

The effect of the cumulative flight history upon aerodynamic loadings may also be analyzed in this simulation. Vehicle initial conditions, angle of attack, angular velocity, and control deflection all have an effect on the response to aerodynamic disturbances such as wind profile, shear, shear reversal, and gusts.

With the time-varying simulation a number of tests of performance quality may be made which are not possible with fixed-coefficient studies. Primarily, these studies consist of a complete launch-to-staging (burnout for a single stage vehicle) simulation to observe the behavior of the vehicle and control system during launch, transition-turn off the vertical, and flight through various wind profiles and gusts. The implications of the instability in the forward propellant tanks and the amount of damping which must be added to the tank may be examined. In one vehicle, for instance, it was found possible to allow a slight degree of propellant-mode instability up to about $t = 0.7\ T_s$ (T_s = time of staging) without adding propellant damping baffles. After $t = 0.7\ T_s$, it was found necessary to add baffles. (A baffle is "added" at a certain time-of-flight by locating it in the propellant tank such that the free surface of the liquid arrives at the baffle station just shortly before the damping is needed. Baffle damping is only effective when the baffle is close to the liquid's free surface.)

There are some problem areas where all three control axes must be simulated and the vehicle given six degrees of rigid-body freedom. Some of these problem areas are:

a. Circular sloshing (swirling propellants), in which the propellant may oscillate in two orthogonal planes with varying phase and amplitude relations. It should be noted also that propellants tend to slosh in inertial planes about which the vehicle may roll.

b. Center-of-gravity offset and product-of-inertia coupling.

c. Coupling through the control system due to cross-talk between control channels or due to poor tracking between chambers of a multi-engine configuration. Cross-talk may be caused from electrical pickup between control channels or from unwanted signals "seen" by the sensors (e.g., a rate gyro is sensitive to accelerations about its output axis).

2.5 LOAD STUDIES

The problem of load determination and transient response is a necessary part of the flexible-booster autopilot analysis since the matter of maximum bending moments imposed on the structure is critical to the success of the booster system being analyzed. An unnecessary increase in the bending moments which the structure must sustain will result in an unnecessary increase in the structural weight. An indication of the maximum angle of attack that the control system must balance will also be evaluated. As the classes of vehicles considered will

usually be aerodynamically unstable, the rocket engine control moment available must be greater than the aerodynamic overturning moment at the maximum expected angles of attack and dynamic pressures. Thus, the load analysis will also lead to a verification that the control moment available is adequate for the task.

The determination of the loads imposed on the structure can be determined in three, progressively refined studies: 1) rigid body (steady-state), 2) in-flight rigid body, and 3) in-flight elastic body. Each of these methods will be used at some time during the design study from preliminary to detailed final analysis. The three methods will be discussed, and the stage of the analysis under which each is applicable will be outlined.

2.5.1 Steady-State Loads. The simplest method is that of rigid body steady-state load determination. This method is usually used during early predesign studies to give a rough estimate of the loads which the airframe structure will be required to carry. The method is particularly well suited to rapid parametric studies wherein comparative data is desired on the relative load carrying requirements of several configurations. It is also the only method which may be used independently of the nature of the flight control system characteristics, i.e., it does not make use of an autopilot. The major shortcoming of the steady-state analysis is that it requires engineering judgment and experience to obtain quantitative load data and to make allowances for dynamic overshoot effects.

The method used for steady-state analysis is derived as follows. Assume that the missile has a steady-state angle of attack. This angle of attack determines the aerodynamic forces and moments (see Figure 2-20).
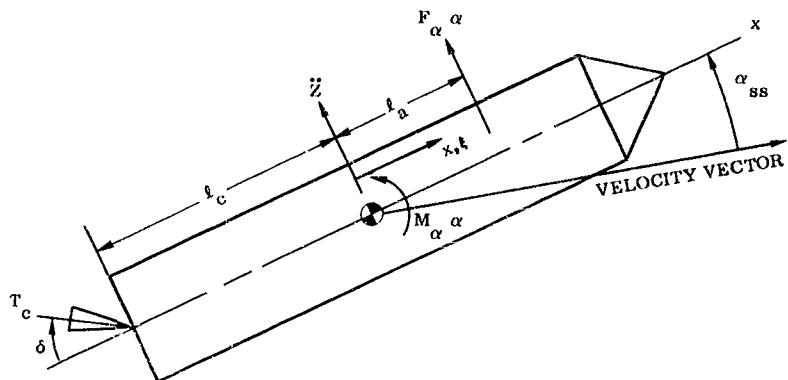
Figure 2-20. Model Used for Rigid-Body "Steady-State" Angle of Attack

Let

$$F_\alpha = q\,S \int_{tail}^{nose} \frac{\partial C_N/\alpha}{\partial x}\ dx \ \text{and}\ M_\alpha = F_\alpha \ell_a = q S \int_{tail}^{nose} \frac{\partial C_N/\alpha}{\partial x}\ (x - x_{CG})\, dx.$$

The control force required to trim the aerodynamic moment is then determined:*

$$\Sigma\ M_\theta = 0 = M_\alpha \alpha + T_c \ell_c \sin \delta. \tag{2-16}$$

The equation for the summation of lateral forces can be written:*

$$\Sigma\ F_Z = F_\alpha \alpha - T_c \sin \delta. \tag{2-17}$$

_____

* Equations 2-16, 2-17 were written for one control force only. If more than one control or propulsive force is present they must all be included in moment and force equations.

This force causes a lateral acceleration of the vehicle as shown below:

$$\ddot{Z} = \frac{\Sigma F_Z}{M_T} \quad \text{where} \quad M_T = \int_{tail}^{nose} m(x)\, dx \quad \text{and } m(x) \text{ is the mass per unit length.}$$

The bending moment at any point along the vehicle can now be determined by summing moments from the nose. Thus, the moment at station X_n equals:

$$M\Big|_{x = x_n} = -\ddot{Z} \int_{x_n}^{nose} m(\xi)(\xi - x_n)\, d\xi + \alpha q \beta \int_{x_n}^{nose} \frac{\partial C_N/\alpha}{\partial x}(\xi - x_n)\, d\xi.$$

Here the auxiliary variable, ξ, has been introduced for convenience. The preceding equation was written as an integral equation. The solution will usually be accomplished by a summation of discrete elements in the actual analysis.

The integral in the preceding equation gives the value of the bending moment at any station along the vehicle. It may be seen that the loading is proportional to both angle of attack and dynamic pressure, q. The required dynamic pressure can be obtained from trajectory data. The preliminary trajectories are usually sufficiently accurate for determining this value of "q" to be used for load calculations.

The maximum bending moment for an actual vehicle will occur at some general position along the missile. Thus, the bending moment must be calculated at various selected points and an interpolation made. This can be represented by a graph showing bending moment per unit angle of attack, per unit q versus station number. Figure 2-21 gives a typical curve of bending moment for a steady state α along the vehicle length at a particular time and dynamic pressure. A number of such plots will have to be made for different times of flight. The use of these curves requires estimates of flight conditions (angle of attack and dynamic pressure) at various times of flight so that the absolute magnitude of the bending moment at each section of the booster can be determined.
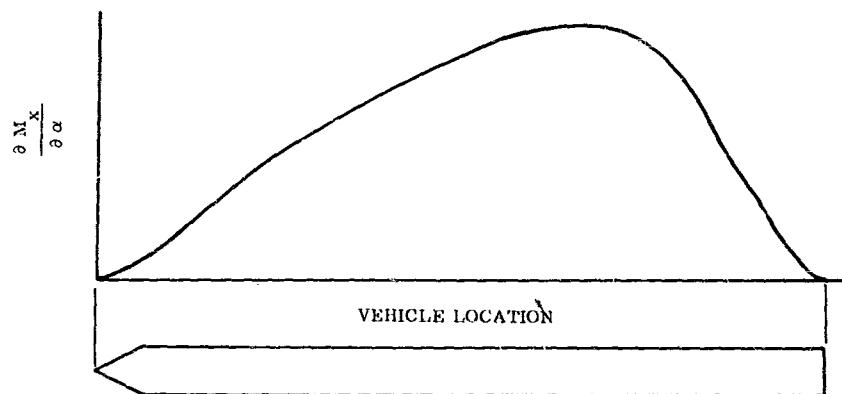
Figure 2-21. Bending Moment for Steady-State Angle of Attack

The maximum angle of attack to be considered in load determination presents a more serious problem. The various contributions to the total angle of attack must be assayed and their sum used to obtain the vehicle loading. First, the angle of attack history due to the reasonable steady wind profile (shear reversal peak not included) is obtained from trajectory calculations which are made with an instantaneously balancing control engine (no autopilot required as yet).

In addition to the load imposed on the structure by the wind profile, short-period wind disturbances such as shear layers and gusts also affect loads. These disturbances exist mostly at altitudes below 100,000 feet, which is also the region of high dynamic pressure. Allowance for these loads must also be included in structural capability. An estimate of the angle of attack accompanying a sharp-edged gust is readily had as $\alpha_{gust} = \tan^{-1}\frac{V_g}{V}$, where V_g is the gust velocity component normal to the vehicle, whose velocity is V. A further empirical

allowance must be made at this point for an anticipated dynamic gust overshoot — ranging from 20 to 50 percent on typical aerodynamically unstable boost vehicles — which occurs because of the finite time of response of actual control systems.

The total air load then consists of that due to the steady wind profile, plus that due either to a gust or to shear layers (shear reversal peak). The last two events appear to be mutually exclusive and rarely will occur simultaneously. The gust usually imposes the greatest load upon the system; however, the loading imposed by both gust and reversal should be evaluated.

The wind profile (horizontal wind velocity versus altitude) velocities and wind shear and gust velocities have a probability value associated with them. These probability data are available in the literature (Refs. 4, 5, and 14 in the Bibliography). Figures 2-22, 2-23, and 2-24 give typical wind profiles and wind shear and gust intensity data. These curves are representative of the most severe conditions existing over the North American
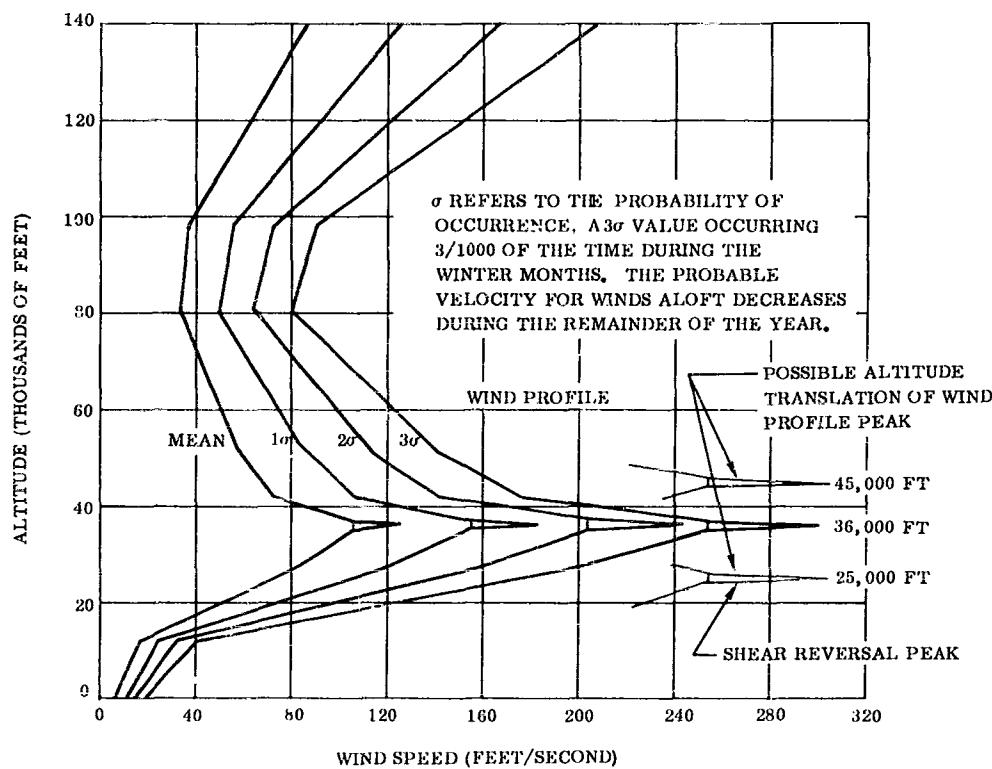
Figure 2-22. Maximum Predicted Wind Velocity Over the North American Continent

Continent at any time during the year. Less severe criteria can usually be chosen if a particular location and direction are known; also, reductions can sometimes be made if it is known that the vehicle will fly during a particular time of the year.

A detailed statistical analysis of the effect on vehicle loads of winds aloft is being performed by Hobbs (Reference 14). The initial results of this study indicate that the loads which would be obtained using the methods outlined in this section are non-conservative for vehicles smaller than an Atlas (actual loads could be slightly in excess of predicted loads). There exists some doubt, however, as to the accuracy of the methods used in the reduction of the balloon-sounding data which was used for these studies. Further studies have indicated that the

σ REFERS TO THE PROBABILITY
OF OCCURRENCE, A 3σ VALUE
OCCURRING 3/1000 OF THE TIME
DURING THE WINTER MONTHS.

WIND SHEAR (FEET/SECOND/1000 FEET)
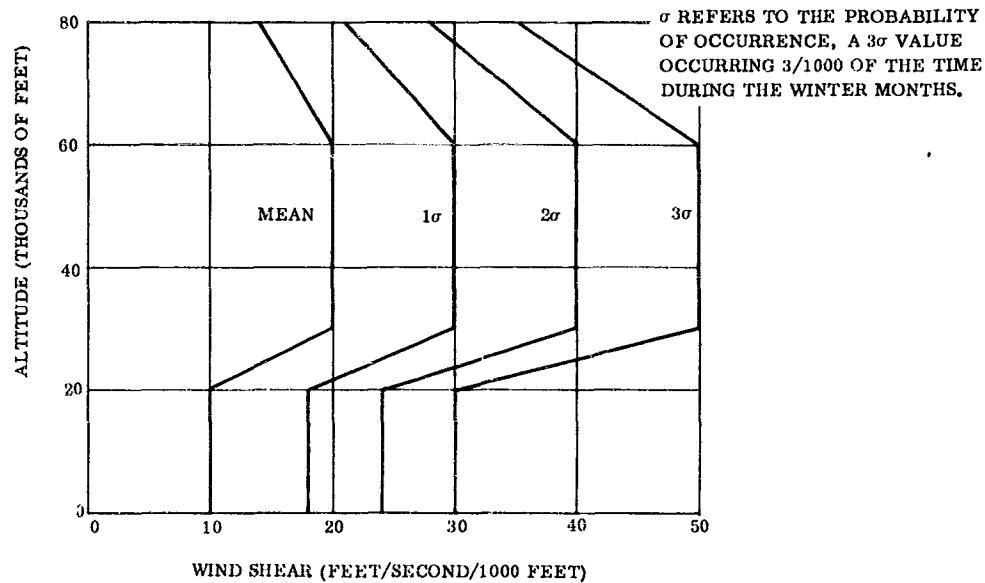
Figure 2-23. Variation of Wind Shear Intensities Versus Altitude for Various Probabilities
of Occurrence Over the North American Continent

σ REFERS TO THE PROBABILITY OF OCCURRENCE,
A 3σ VALUE OCCURRING 3/1000 OF THE TIME DURING
THE WINTER MONTHS. GUSTS USUALLY REFER TO
DISTURBANCES HAVING OCCURRENCE TIMES OF LESS
THAN 2 SECONDS. THOSE OCCURRING OVER PERIODS
IN EXCESS OF 2 SECONDS ARE CLASSED AS SHEARS
FOR BALLISTIC BOOST VEHICLES.

TRUE GUST INTENSITY (FEET/SECOND)
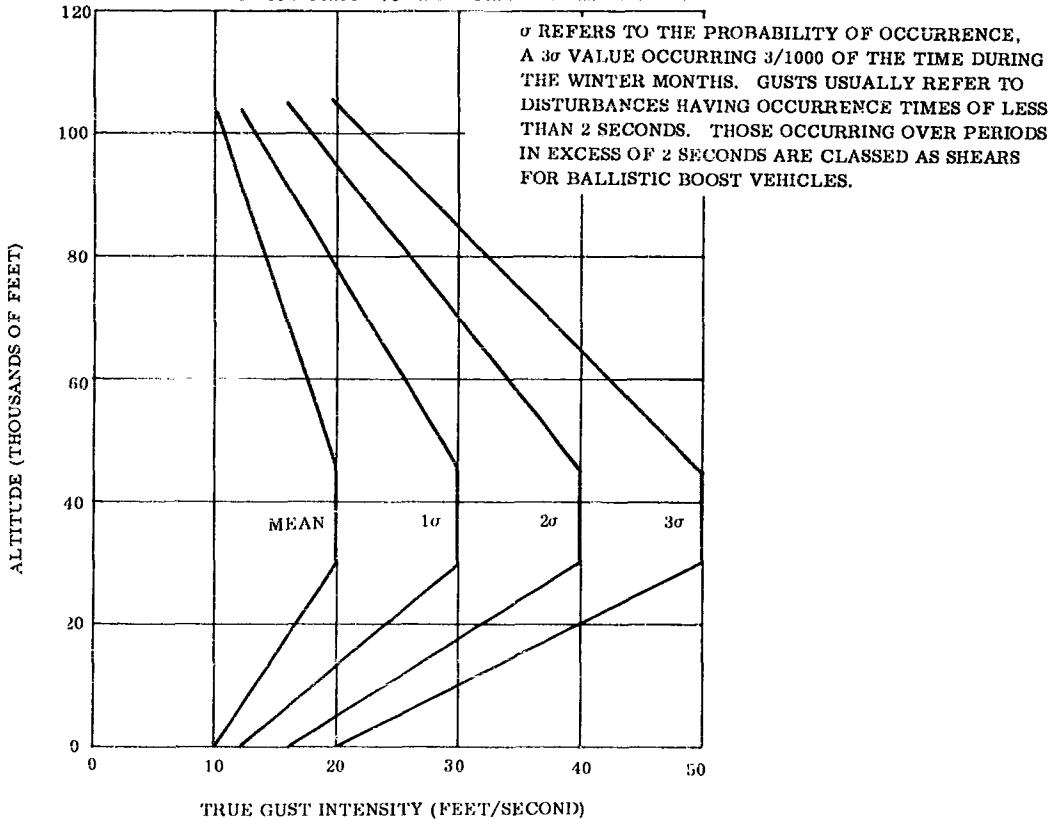
Figure 2-24. Variation of Gust Intensities Versus Altitude for Various Probabilities of Occurrence
Over the North American Continent (Gust Shapes are Versine Types)

wind loads as predicted in Reference 14 are too severe and that the method explained in this section will give as accurate a result as any discrete method. The further studies also indicate that for vehicles of Atlas-size, the loads predicted using the methods of this section will be conservative.

2.5.2 In-Flight Rigid-Body Bending Moment. The design of the autopilot cannot be made without giving attention to the loads imposed on the air-frame by the environment and the manner in which they are affected by the control-system response. In this next, more elaborate loads study an active control system is simulated, so that dynamic response of the vehicle may be observed. The equations of motion of the vehicle with autopilot are written as usual. Equations comparable to those of Subsection 2.5.1 (but including angular acceleration effects) are also added to yield the bending moments at various stations as linear functions of two flight parameters:

$$BM_{x_n} = BM_{\delta_n}(\delta) + BM_{\alpha_n}(\alpha)$$

where the coefficients BM_{δ_n} and BM_{α_n} are functions of x along the vehicle body and are also functions of flight time, as outlined below:

$$BM_{\delta_n} = \frac{T_c}{M_T} \sum_i^{x_n} M_i (\xi_i - x_n) - \mu_\delta \sum_i^{x_n} M_i (\xi_i - x_n)^2 - \mu_\delta (x_n - x_{CG}) \sum_i^{x_n} M_i (\xi_i - x_n)$$

$$BM_{\alpha_n} = \sum_i^{x_n} (C_N/\alpha)_i (\xi_i - x_n) qS - \sum_i^{x_n} M_i (\xi_i - x_n) \frac{F_\alpha}{M_T}$$

$$- \mu_\alpha \sum_i^{x_n} M_i (\xi_i - x_n)^2 - \mu_\alpha (x_n - x_{CG}) \sum_i^{x_n} M_i (\xi_i - x_n).$$

The steady-state bending moment can be obtained directly from the simulation used. The next step is to analyze the effect of the autopilot on loads. A curve of maximum bending moment for a gust or shear input may be plotted for various values of control system gain (K_A). A typical plot of the results for an aerodynamically unstable vehicle is given in Figure 2-25.
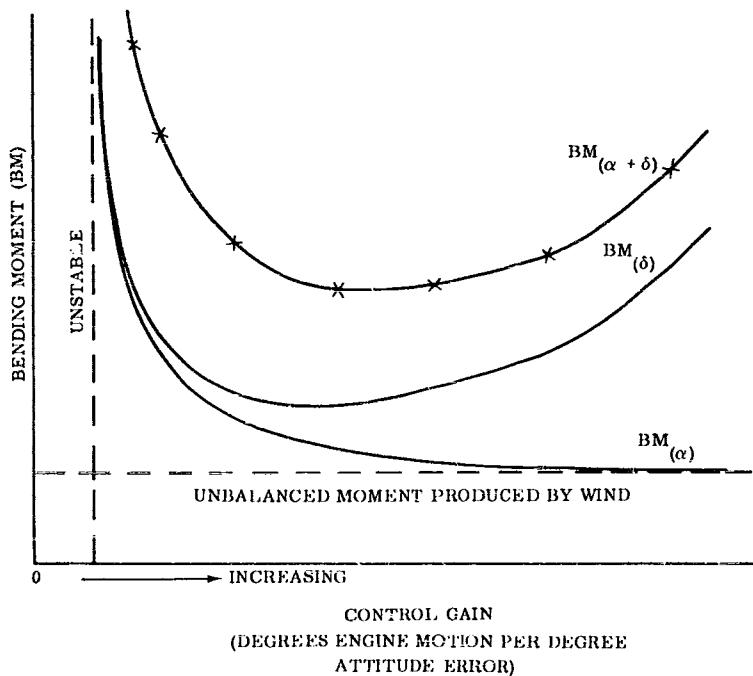
Figure 2-25. Steady State Rigid-Body Bending Moment for Increasing Autopilot Gains

The loads in Figure 2-25 have a simple physical explanation. The bending moment due to aerodynamics (α) can be thought of as going to infinity at low values of K_A, since the vehicle, being unstable, will tumble. At intermediate gains the control system will allow some overshoot due to control sluggishness. This overshoot will go to zero at an infinitely high gain, thus reducing the bending moment due to aerodynamics to that of the steady-state value for high values of K_A. For the bending moment due to the rocket engine (δ) the converse is true for high values of K_A. The higher the gain the farther the engine will gimbal for the same attitude disturbance. Thus, for increasing values of K_A the bending moment due to the rocket engine (δ) will increase. Figure 2-25 also shows a curve of the total bending moment, $BM(\alpha + \delta)$. The optimum point for gain, as far as loads are concerned, can be taken from this minimum point on the curve.

2.5.3 In-Flight Elastic Vehicle Bending Moment. The preceding rigid-vehicle study may be sufficiently accurate for many applications. The increase in loading due to elastic deflections is small for the types of vehicles presently flown. This increase is only significant under gust or shear reversal responses and will run from a few percent on a present-day ICBM to five to 10 percent on multistage satellite vehicles having a large slenderness ratio. When an analysis of the elastic flexing on the flexible booster is considered important, the following method can be used to evaluate this loading.

In calculating the loads due to elastic motion, an analysis technique which can determine transient response must be used. This restriction will usually imply that a large digital or analog computer simulation must be used. This simulation would use a flow diagram similar to that of Figure 2-18.

Once the transient response to a particular input has been determined, there are two methods which may be used to calculate the bending moment. The first of these is the mode-displacement method and the second is the mode-acceleration method.

In the mode-displacement method the following equation is used for calculation of the transient bending moment at station "x_n":

$$BM_{xn} = EI_{xn} \sum_{i=1}^{n} \frac{d^2 \phi^{(i)}}{d x_n^2} q_i$$

where n = number of modes used and $\dfrac{d^2 \phi^{(i)}}{d x_n^2}$ is the normalized curvature of the ith mode at station x_n.

The mode-deflection method is theoretically correct for calculation of the bending moment only if all modes are used. In practice, the answer is obtained by using no more than five modes, with three being a more representative number. For this limited number of modes the mode displacement method can introduce certain inaccuracies into the result. These inaccuracies arise because the flexible booster will, in general, have a highly discontinuous mass distribution. The modal solution tends to smooth out these discontinuities and can give results which are substantially in error in certain areas. To give a more accurate answer with fewer modes the mode acceleration method is usually used.

In the mode-acceleration method the transient bending moment at station "x_n" is given by a static summation of moments, working from the nose of the vehicle back to a given station. The equations follow:

$$BM_{xn} = \sum_{j} \left\{ - M_{xj} \left(\sum_{i} \phi_{xn}^{(i)} \ddot{q}_i + (x_j - x_{CG}) \ddot{\theta} + \ddot{z} \right) + \right.$$

$$qS (C_N/\alpha)_{xj} \left[(\alpha_{gust} + \alpha) + \sum_{i} \sigma_{xn}^{(i)} q_i - \right.$$

$$\left. \left. \frac{1}{V} \sum_{i} \phi_{xn}^{(i)} \dot{q}_i - \frac{1}{V} (x_j - x_{CG}) \dot{\theta} \right] \right\} (x_j - x_n) + \sum_{\ell} K_\ell Y_\ell (x_\ell - x_n)$$

where j = index of stations forward of X_n
ℓ index of propellant sloshing tank
i = modal index
n = station index.

Here $\ddot{Z}$ is the lateral acceleration of the center of gravity of the reduced mass (with sloshing propellants removed) of the vehicle under the action of air loads, thrust vector forces, and sloshing propellant forces.

The mode-acceleration method will give more accurate results than the mode-displacement method, in that it will converge to the desired value with fewer modes. As the elastic contribution is usually small compared to that from the rigid body and rigid body overshoot, the use of one mode by the mode acceleration method is usually sufficiently accurate for the determination of bending moments on the structure.

In addition to the bending moment it may be necessary to determine the lateral acceleration at various stations on the missile. This acceleration environment is needed for design of equipment and mountings, and may be computed using the same simulation used in determination of bending moments. The transient lateral acceleration at station X_n is given by the equation:

$$\ddot{z}_{xn} = \left[\ddot{z}_{CG} + (x_n - x_{CG})\,\ddot{\theta} + \sum_{i=1}^{r} \phi_{xn}^{(i)}\,\ddot{q}_i \right].$$

This discussion completes the information usually obtained during transient analysis of the flexible booster.

SECTION 3

SYSTEM EQUATIONS OF MOTION

SYMBOLS USED IN SECTION 3

Symbol	Definition	Units
C_D	aerodynamic drag coefficient	N.D.*
$\bar{C}_f$	linearized gimbal friction	lb-ft-sec/rad
C_{nm}	flexibility influence coefficient for an unrestrained beam	ft/lb
$C_{N/\alpha}$	aerodynamic normal force coefficient per unit angle of attack in pitch plane	1/rad
$(C_{N/\alpha})_{xn}$	local aerodynamics normal force coefficient per unit angle of attack at station n along the longitudinal axis	1/rad
$C_{N/\beta}$	aerodynamic normal force coefficient per unit angle of attack in yaw plane	1/rad
$EIxn$	flexural rigidity at station n along the longitudinal axis	lb ft^2
Fx,y,z	total force acting along the x, y or z axis	lbs
g	acceleration due to gravity	ft/sec^2
I	reduced moment of inertia (see Appendix A1-5)	slug ft^2
I_{Ok}	moment of inertia (pitch or yaw) of kth engine about its own c.g.	slug ft^2
K_ℓ	spring constant for sloshing mass in ℓ^{th} propellant sloshing tank	lbs/ft
ℓ	sloshing propellant index	N.D.
ℓ_{P_ℓ}	moment arm of sloshing mass in ℓ^{th} propellant sloshing tank	ft
ℓ_{R_k}	moment arm of kth rocket engine measured from its gimbal point to its center of gravity	ft
L,M,N	moments about the x,y or z axis respectively	ft lbs
$m(x)$	running mass along the longitudinal axis	slugs/ft
$\mathcal{M}_i$	generalized mass of the ith mode	slugs
M_{c_ℓ}	sloshing moment coefficient for the ℓth propellant sloshing tank	slug ft
M_{i_ℓ}	sloshing mass (1st mode) of ℓth propellant sloshing tank	slugs
M_n	"lumped" mass at station n	slugs
M_o	reduced vehicle mass	slugs
M_{R_k}	mass of kth rocket engine	slugs
M_T	total mass of vehicle	slugs

* Non-dimensional

SYMBOLS USED IN SECTION 3 (Continued)

Symbol	Definition	Units
P	aerodynamic force parameter, $= qS$	lbs
P,Q,R	angular rotation rates about the x, y, and z axis respectively	rad/sec
q	aerodynamic pressure ($q = \rho V^2/2$)	lbs/ft^2
q_i	generalized displacement of ith mode	ft
Ql	generalized force acting on the ith mode	lbs
S or S_{REF}	vehicle reference area	ft^2
t	time	sec
T	thrust	lbs
U,V,W	velocity along the x, y, and z axis respectively	ft/sec
$u_n(t)$	"lumped" displacement as a function of time	ft
u(x,t)	transverse displacement of longitudinal axis	ft
$W_n(t)$	"lumped" loading as a function of time	lbs
w(x,t)	transverse loading along longitudinal axis	lbs/ft
x,y,z	vehicle coordinate system	ft
X,Y,Z	component forces along x, y, and z axis	lbs
Y_ℓ	lateral displacement of sloshing mass in ℓ^{th} sloshing propellant tank (spring mass analogy)	ft
α, β	aerodynamic angles of attack in the pitch and yaw planes respectively	rad
α_T	vehicle longitudinal acceleration	ft/sec^2
α_{xn}	local angle of attack at station n along the longitudinal axis	rad
Γ	sloshing pendulum angle (pendulum analogy)	rad
δ	angle between rocket engine thrust vector and vehicle elastic axis at gimbal point; includes elastic deformation of engine position servo and actuation within the servo itself	rad
δ'_k	angle between thrust vector and elastic mode at the kth rocket engine CG due to actuation within the positioning servo	rad
ζ_i	damping ratio for the ith mode	N.D.
ζ_ℓ	damping ratio for the ℓth sloshing propellant tank	N.D.
Θ, ψ, ϕ	rotation angles defined in Figure 3-5	rad
ρ	radius of gyration	ft

SYMBOLS USED IN SECTION 3 (Continued)

Symbol	Definition	Units
$\sigma_x^{(i)}$	normalized slope of the ith mode along the longitudinal axis	rad/ft
$\sigma_x^{(j)}$	normalized slope of the jth mode along the longitudinal axis	rad/ft
$\sigma_{xn}^{(\bar{z})}$	normalized rigid body plunging mode slope at station n along the longitudinal axis	rad/ft
$\sigma_{xn}^{(O)}$	normalized pitching mode slope at station n along the longitudinal axis	N.D.
$\sigma_{xT}^{(i)}$	normalized slope for the ith mode at station T (rocket engine gimbal point) along the longitudinal axis	rad/ft
$\phi_{xe_k}^{(i)}$	normalized deflection of the ith mode at station c (rocket engine center of gravity) along the longitudinal axis for the kth engine	ft/ft
$\phi_{xn}^{(i)}$	normalized deflection of the ith mode at station n along the longitudinal axis	ft/ft
$\phi_{xn}^{(j)}$	normalized deflection of the jth mode at station n along the longitudinal axis	ft/ft
$\phi_{xn}^{(\bar{z})}$	normalized deflection of the rigid body plunging mode at station n along the longitudinal axis	ft/ft
$\phi_{xn}^{(\Theta)}$	normalized deflection of the pitching mode at station n along the longitudinal axis	ft/rad
$\phi_{xT}^{(i)}$	normalized deflection of the ith mode at station T (rocket engine gimbal point) along the longitudinal axis	ft/ft
ω_i	natural frequency of the ith mode	1/sec
ω_ℓ	natural frequency of slosh for the ℓth propellant sloshing tank	1/sec

Aerodynamic Coefficients (N.D.)

$$C_{N/\beta}, \quad C_{y/P}, \quad C_{y/R}, \quad C_{y/\delta_\psi}$$

$$C_{N/\alpha}, \quad C_{z/P}, \quad C_{z/Q}, \quad C_{z/\delta_\theta}$$

$$C_{\ell/\beta}, \quad C_{\ell/P}, \quad C_{\ell/R}, \quad C_{\ell/\delta_\phi}$$

$$C_{m/\alpha}, \quad C_{m/P}, \quad C_{m/Q}, \quad C_{m/\delta_\theta}$$

$$C_{n/\beta}, \quad C_{n/P}, \quad C_{n/R}, \quad C_{n/\delta_\psi}$$

NOTE: These coefficients are defined to represent the aerodynamic forces or moments per unit value of a variable producing the effect. Thus, $C_{z/Q}$ represents (in nondimensional form) the force in the z-direction per unit angular pitching rate, Q.

Matrix Notation

$\lfloor \ \rfloor$ column matrix

$\lceil \ \rfloor$ diagonal matrix

$\lceil \ \rceil$ square matrix
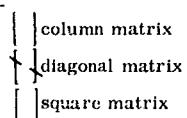
3.1 BASIC PRINCIPLES

Certain characteristics of the ballistic booster distinguish this class of vehicle from the lift-sustained vehicle. The ballistic booster is built with a high degree of structural (and hence inertial) symmetry. This symmetry in many cases goes beyond the plane symmetry of the lifting vehicle, extending almost to pure axial symmetry. The control axes nearly coincide with the principal inertial axes. Thus, inertial coupling effects between motions about the control axes are small. The external configuration is nearly symmetric as it affects aerodynamic properties, leading to negligible aerodynamic cross effects (lateral-directional coupling). The control configuration will rarely employ active aerodynamic surfaces, but will depend primarily upon reaction-jet control. For those configurations which depend upon a degree of aerodynamic control in the region of high dynamic pressure, the vehicle configuration is still such as to result in very small aerodynamic cross-coupling effects between control channels.

The three-axes coupled equations of motion of the ballistic booster are given in Subsection 3.5, where these coupling effects are discussed further. It is sufficient at this point of development to say that the cross-couplings are minor enough for this class of vehicle to permit very extensive and detailed control analyses of plane motions; these analyses are highly satisfactory for purposes of control system design.

It should be stated further that such coupling effects between vehicle axes as do exist are only of significance for studies of the lower frequency (rigid-body) modes and are of lesser importance in studying closed-loop servoelastic stability of the control system. Since the main thesis of this report is the analysis of elastic autopilot coupling effects, the greatest emphasis is placed here on the equations for plane motion of a flexible booster. These plane motion analyses are applicable to either the pitch-, yaw-, or roll-control planes but for uniformity of presentation are illustrated here for the pitch plane alone. In general, the roll control system for this class of vehicle is not a high performance control loop, and hence, elastic coupling problems in roll will rarely occur. Thus, the pitch and yaw planes are the control planes of greatest interest and are those to which the following analysis is pointed.

For purposes of analysis the mathematical model of the missile system under consideration in this study is basically the same for all vehicles, regardless of the external configuration of the missile system. Although one may have configurations ranging in size from a sounding rocket to a large space probe with tandem tanks, parallel tanks, winged payloads, etc.; the main body of the missile structure may be represented adequately as a loaded beam in all cases. It may be necessary to represent the missile as a split, "branch" beam for certain configurations; but the modal solutions of all the configurations will be of identical form, yielding modal frequencies, masses, and mode shapes for all portions of the beam.

Two approaches to writing the equations of motion may be taken. If the system is looked upon as a continuous medium having an infinite number of degrees of freedom, one is led to a differential equation representation of the problem. On the other hand one may take a lumped parameter model leading to a finite (but large) number of degrees of freedom, the equations being written most conveniently in matrix form.

In either case, to reduce the problem to a reasonable number of degrees of freedom, a modal solution approach is employed. In this approach the system's deflected shape under forced motion is represented by the superposition of a restricted number of selected functional shapes (modes). The shapes of these modes are chosen such that, in proper combination, one may expect to represent accurately the system's deflected form. For reasons of computational expediency (and for their physical appeal) one often uses orthogonal modes as computed for the free vibrations of the system. These "normal modes" lead to equations having no inertial or elastic coupling terms. Lacking a set of truly orthogonal modes, the analyst may employ completely arbitrary mode shapes ("assumed modes"), or as a better compromise, some mode shapes computed in the presence of certain artificial constraints which are applied for convenience ("artificially uncoupled modes"). These modes are explained in the following paragraphs.

Modes which are computed for the complete system with no artificial constraints applied are called "normal modes". In the resulting equations of motion for the system, these modes are completely uncoupled elastically and inertially. However, in the calculation of these modes the analyst accounts for all of the physical coupling between elements of the system. Hence, historically (and unfortunately), these modes came to be known as "coupled modes".

Modes which are computed for the system in the presence of some artificial mathematical constraints (applied usually for computational ease) are called "artificially uncoupled modes". For example, the missile body-bending

modes are often computed with the sloshing portion of the liquid propellants removed. Correspondingly, the liquid propellant mode is computed for a rigid (fixed) tank. These two modes, computed in this artificially un-coupled manner, are then coupled together analytically in writing the equations of motion. They will therefore have elastic and inertial coupling terms between them in the equations of motion.

Modes are sometimes used which have assumed, arbitrary shapes; these modes will have the greatest elastic and inertial coupling in the equations of motion. Such functions may be used if analytic evaluations of certain elements in the equations (most often integral terms) are greatly expedited by the use of a series of closed form (standard) functions (polynomials, harmonic functions, etc.). There may also be reason to suspect (on physical grounds) that some such function may actually better describe the system's deflected shape than do the normal modes. This might be the case on an aeroelastic calculation for a thin lifting surface where it is felt that aero-dynamic forces, rather than inertial forces, are dominant in distorting the wing. Since for the ballistic booster it is clear that elastic, inertial, and propulsive forces are dominant, use of arbitrary modes is seldom made; the system's deflected shape is unquestionably better described by normal modes or (second best) by certain ar-tificially uncoupled modes.

In the following paragraphs, equations of motion for the vehicle treated as a loaded elastic beam are derived by both the differential equation and lumped parameter approaches. In each case one is led to a modal formulation of the problem of forced motion. Finally, a rather complete set of equations of forced motion for a flexible booster with autopilot is written in a format suitable for use with either orthogonal normal modes or with certain classes of artificially uncoupled modes.

3.2 DIFFERENTIAL EQUATION PROBLEM FORMULATION

The plane elastic motion of the continuous system of Figure 3-1 is described by the partial differential equations for forced small amplitude vibrations of a "free-free" (floating) beam.*

$$m(x) \frac{\partial^2 u}{\partial t^2} + \frac{\partial^2}{\partial x^2} \left[EI(x) \frac{\partial^2 u}{\partial x^2} \right] = w(x, t) \qquad (3-1)$$
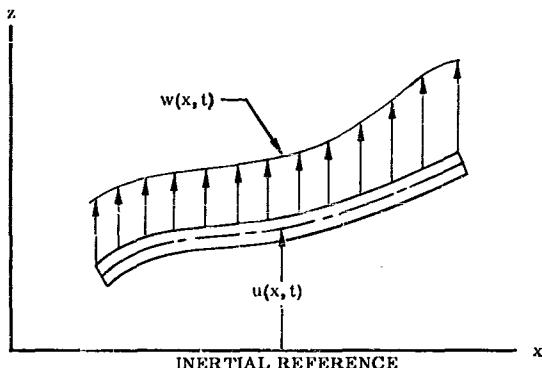
Figure 3-1. Elastic Beam Coordinates of a Continuous System

3.2.1 Free Vibrations of System. The solution to the free vibration problem (w = o) for this beam is obtained by the method of separation of variables, i.e., by assuming a solution of the form:

$$u(x, t) = U(x) \cdot T(t)$$

The spatial functions $U(x)$ are found to be the system's normal modes of vibration (eigenfunctions) which are de-pendent upon the geometric boundary conditions (method of support or constraint of the beam). Associated with each of these modes is a characteristic parameter (eigenvalue), ω_i, its natural frequency. The time functions, $T(t)$, are found to be harmonic functions of the circular frequency ω_i.

* Shear deformation displacements and rotary inertial terms are omitted here for simplicity, see pp. 67, 68 of Reference 6. Their inclusion in the general solution is discussed later.

An infinite series of these functions is necessary to satisfy the general boundary conditions in time (initial conditions) and to describe thereby the time history of free vibratory motion. Thus, one writes:

$$u(x,t) = \sum_{i=1}^{\infty} \left[A_i \sin \omega_i t + B_i \cos \omega_i t \right] \phi_{(x)}^{(i)}$$

where the $\phi_{(x)}^{(i)}$'s are the normal modes. In computing the coefficients, A_i and B_i, from the given initial conditions, advantage is taken of the modes' property of <u>weighted</u> orthogonality, viz.:

$$\int_0^L m(x) \, \phi_{(x)}^{(i)} \, \phi_{(x)}^{(j)} \, dx = \begin{cases} 0 & i \neq j \\ \mathcal{M}_i & i = j \end{cases} \qquad (3-2)$$

Note that the absolute magnitude of $\mathcal{M}_i$ as defined here is dependent upon the scale selected for the mode shapes, $\phi_{(x)}^{(i)}$, since these are functions giving only relative amplitudes. Selecting a particular scale for these is the process known as <u>normalizing</u>.

3.2.2 Forced Motions of System.

A Fourier series of normal mode functions is used to represent the deflection:

$$u(x,t) = \sum_{i=1}^{\infty} q_i(t) \cdot \phi_{(x)}^{(i)} \qquad (3-3)$$

where the $q_i(t)$'s are functions of time to be determined and are called <u>normal coordinates</u>. If Equation 3-3 is substituted into Equation 3-1 and the result is multiplied by $\phi_{(x)}^{(i)}$ and integrated over the length of the beam, one obtains a series of simultaneous equations of the following generic form:

$$\ddot{q}_i + \omega_i^2 \, q_i = \frac{Q_i(t)}{\mathcal{M}_i} \, . \qquad (3-4)$$

Here advantage has been taken of the modal orthogonality property, and we have defined:

$$Q_i(t) = \int_0^L w(x,t) \cdot \phi_{(x)}^{(i)} \, dx$$

as the generalized force acting on the ith mode. The generalized mass of this mode is given by:

$$\mathcal{M}_i = \int_0^L m(x) \left[\phi_{(x)}^{(i)} \right]^2 \, dx.$$

Also, the natural frequency is defined by:

$$\omega_i^2 = \frac{1}{\mathcal{M}_i} \int_0^L \frac{d^2}{dx^2} \left[EI(x) \, \frac{d^2 \phi_{(x)}^{(i)}}{dx^2} \right] \phi^{(i)}(x) \, dx.$$

No inertial or elastic coupling terms appear between the coordinates. It follows that the normal coordinates (modes) couple only through any dependence of the forcing function, $w(x,t)$ upon the motions themselves, i.e., if $w = w(x, t, u, \dot{u})$. The "external" forcing functions used in an elastic missile simulation are:

a. <u>Aerodynamic Forces</u>

b. <u>Rocket Engine Thrust Forces</u>

c. <u>Engine Control-Servo Inertial Forces</u>

d. <u>Propellant Sloshing Forces</u>

Quasi-static aerodynamics are most commonly used, employing local lift coefficients along the body and local angles of attack induced by body deflections and deflection rates. Both in-phase and damping terms are thereby generated. Methods which can be used to approximate the aerodynamic forces are given in Appendix A5.

For an unwinged ballistic booster the aerodynamic forces (which do depend upon the displacements) are small in comparison to the elastic, inertial, and propulsive forces. These, therefore, provide negligible modal coupling. The other significant source of coupling is through the control forces (autopilot) which respond to sensed motions. These modal frequencies are, however, always (by intent) well above the control system bandwidth; hence, their signals receive great attenuation. Consequently, it is only harmonic or quasi-harmonic motion at or near the resonant frequency of a given mode which can achieve sufficient magnification to be sustained by control forces (and then only if the phase is correct). The control system then provides negligible elastic modal coupling.

In practical applications a beam will possess some dissipative forces which provide damping. This dissipative energy is usually small in comparison to the elastic and kinetic energies; thus, the lower eigenvalues and eigenfunctions are negligibly affected. These effects are discussed in detail in Appendix C3. This dissipative force can be approximated by adding a small viscous damping term to Equation (3-4):

$$\ddot{q}_i + 2\,\zeta_i\,\omega_i\,\dot{q}_i + \omega_i^2\,q_i = \frac{Qi(t)}{\mathcal{M}_i}$$

This damping does not affect the calculations of the normal modes nor does it couple them together.

Values of ζ_i have been determined by experiment. The use of an equivalent viscous damping term in place of a combination of structural damping, coulomb damping, and true viscous effects is acceptable because of its small magnitude (1/4 to 2 percent of critical) and because of the near-harmonic nature of the motion being investigated for stability. Typical curves of damping for various tank configurations and propellant loading conditions are given in Section 6.

Finally, we note that the missile in free flight is an unrestrained, "floating" beam. For such a case it is convenient to introduce two rigid body modes: translation and rotation of the principal inertial axis through the center of mass. These modes have zero frequency. The elastic deflections in this case become simply the deflections measured relative to this principal axis. This technique is employed specifically in the next subsection.

3.3 MATRIX EQUATION PROBLEM FORMULATION

Ballistic booster vehicles are sufficiently complex in their physical makeup that a lumped-parameter idealization of the system often has more intuitive appeal than a continuous media model. In a lumped-parameter system the analyst concentrates attention on those aspects of the system which are felt to be dominant (major masses, major structural members), while secondary features are "lumped in" to account for them approximately. Figure 3-2 shows a lumped-parameter model of a loaded elastic line. The deformed shape of the system is
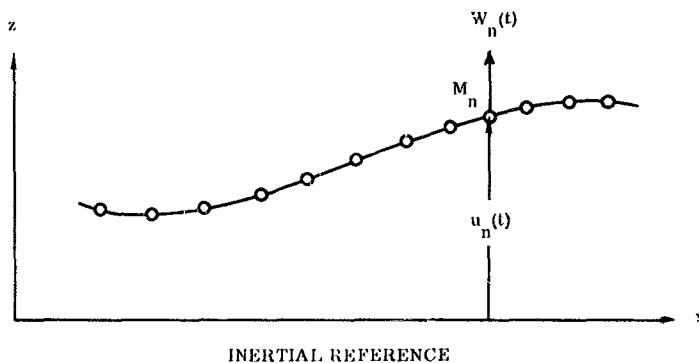
Figure 3-2. Lumped-Parameter Model of a Loaded Elastic Line

given by a finite number of coordinates. Elastic properties are also expressed in lumped fashion as a set of flexibility influence coefficients, C_{mn}, giving the elastic deflection at point m per unit force at point n*. The displacements, $u_n(t)$, are measured relative to an inertial reference. Three equations of motion are written (small displacements assumed):

(Summing forces vertically)

$$\sum_n M_n \ddot{u}_n = \sum_n W_n \qquad (3\text{-}5)$$

(Summing moments about the coordinate origin)

$$\sum_n M_n x_n \ddot{u}_n = \sum_n W_n x_n \qquad (3\text{-}6)$$

(Elastic deflection)

$$u_n - u(o) - x_n \frac{\partial u}{\partial x}(o) = \sum_m C_{nm} \left[W_m - M_m \ddot{u}_m \right] . \qquad (3\text{-}7)$$

Here $u(o)$ and $\frac{\partial u}{\partial x}(o)$ are the deflection and slope of the elastica at the origin of x. In this case the flexibility influence coefficients are to be thought of as giving elastic deflections relative to this reference line in the beam.

It is found convenient in further analytic manipulations to set the origin of x coincident with the system mass center, i.e., $\sum_n M_n x_n = 0$. This arrangement is assumed in the following discussion.

3.3.1 Free Vibrations. With $W_n = 0$, Equation 3-7 may be rewritten, using (3-5) and (3-6), to yield:**

$$u_n = - \sum_m \bar{C}_{nm} M_m \ddot{u}_m \qquad (3\text{-}8)$$

where the $\bar{C}_{nm}$'s are the flexibility influence coefficients for the unrestrained (floating) beam.*** Written in matrix form, for all n mass points in harmonic motion, this becomes:

$$\left| u_n \right| = \omega^2 \left[\bar{C}_{nm} \right] \left\{ M_m \right\} \left| u_m \right| . \qquad (3\text{-}9)$$

Equation (3-9) is in a form suitable for solution for the orthogonal elastic modes (eigenvectors, $\phi^{(i)}$) and their natural frequencies (eigenvalues, ω_i). The rigid-body displacements have been "swept out" through the use of Equations (3-5) and (3-6) in deriving Equation (3-9); hence, only elastic modes ($\omega_i \neq 0$) are obtained from Equation (3-9). These modes are orthogonal with weighted orthogonality (cf. Equation 3-2):

$$\sum_n \phi_n^{(i)} \phi_n^{(j)} M_n \, dx = \begin{cases} 0 & i \neq j \\ \mathcal{M}_i & i = j \end{cases} .$$

It is also true that these modes are orthogonal with any rigid-body displacements (translation and rotation), as may be shown using Equations (3-5) and (3-6) with $W_n = 0$.

3.3.2 Forced Vibrations. To treat the forced vibration case it is found most expeditious to employ the free vibration normal orthogonal modes to describe the total system displacement as:

$$u_n = \sum_i q_i(t) \cdot \phi_n^{(i)} \qquad (3\text{-}10)$$

---

*Deflection and force here are defined in the general sense, i.e., rotations and couples are included. These deflections are all measured relative to an arbitrary reference station in the beam. The effects of shear deformation are conveniently introduced into the problem at this point by accounting for them in the structural calculation of the C_{mn}, (see Appendix A4).

** See Reference 7, pp. 173-180.

*** See also Reference 6, Article 3-7 where this proof is carried out in integral equation form.

Here the q_i's are functions of time called <u>normal coordinates</u>. The $\phi_n^{(i)}$'s are the orthogonal normal modes (spatial functions) and are understood now to include the rigid-body modes of <u>translation</u> of the center of gravity and <u>rotation</u> of the principal centroidal axes. Thus:

$$\phi_n^{(\text{translation})} = 1, \; \omega_T = 0$$

$$\phi_n^{(\text{rotation})} = x_n, \; \omega_R = 0.$$

For intuitive appeal, one often writes $\bar{z}$ and Θ for the normal coordinates of these modes. Note that the rigid-body velocity, $\dot{\bar{z}}$, in this case is the velocity with respect to a fixed coordinate system; i.e., this is <u>not</u> a body-axes coordinate system (cf. Appendix C3).

If Equation 3-8 is substituted into Equations 3-5, 3-6, and 3-7, the equations of motion uncouple to yield the following set:

$$\left.\begin{array}{l} \ddot{\bar{z}} \; \sum_n M_n = \sum_n W_n \\[2mm] \ddot{\Theta} \; \sum_n M_n x_n^2 = \sum_n W_n x_n \\[2mm] \ddot{q}_i + \omega_i^2 q_i = Q_i(t)/\mathcal{M}_i \end{array}\right\} \qquad (3\text{-}11)$$

where

$$\mathcal{M}_i = \sum_n M_n (\phi_n^{(i)})^2$$

$$Q_i = \sum_n W_n \phi_n^{(i)}.$$

Equations 3-11 are the general set for the motions of the normal coordinates under the action of external forces. The only coupling between these orthogonal modes can occur through a dependency of the forces, W_n, upon the motions themselves. The general form of equation may be compared with that of Equation 3-4, derived for the continuous media model: it is identical.

The observations relative to the properties of normal modes, given in this and the last subsections, form the basis for their use in writing the detailed system equation to follow.

3.4 PLANE MOTION OF A FLEXIBLE VEHICLE – GENERAL EQUATIONS

In deriving the equations of motion of the missile airframe and propellant in normal coordinates we will use the mathematical model shown in Figure 3-3. The missile is partitioned into the following elements:

    n   concentrated masses, each free to translate and rotate,

    m   rocket engine masses attached through torsional springs and,

    s   concentrated sloshing masses attached to the elastic axis of the beam by springs.

Moments (pure couples) due to sloshing propellants are also applied at the bottom of each liquid tank. The propellant sloshing masses, attachment springs, attachment locations, and other propellant parameters are dictated by the spring-mass analogy of sloshing propellants (see Appendix A, subsection A3).

The missile is constrained to motion in a single plane with translational and rotational degrees of freedom. For small displacements (bending displacements are always small when compared to the gross dimensions of the missile) the concentrated body masses and engine masses will be assumed to translate laterally and to rotate, but not to translate longitudinally. The sloshing masses are restricted to translation normal to the elastic axis

of the missile. The number of degrees of freedom of such a system is: $2n + m + s$. As discussed in Appendix A4, it is often found satisfactory to omit the rotary inertias (and hence rotary degrees of freedom) from the modal calculations. In this case the number of degrees of freedom reduces to: $n + m + s$.*

In performing a stability analysis of a missile and its flight control system, there are several approaches which may be taken to describe the system's motion:

a. The orthogonal modes of the entire missile structure with propellants may be calculated; this means including the rocket engines and the sloshing propellants in the modal calculations. This approach results in a minimum of coupling between the modes, such coupling only arising through the dependency of the aerodynamic forces and control forces (rocket engine deflections) upon the system's motions. Of these forces the aerodynamic group are small for an unwinged booster.

b. The artificially uncoupled bending and rigid body modes may be calculated by excluding the sloshing portion of the propellants in the modal calculations. The uncoupled sloshing modes of each individual tank will have been calculated previously by means of a hydrodynamic solution, in order that one may know which portion of the propellant is considered to be sloshing. In this case the bending modes will be coupled by means of the flight control system, aerodynamics, and the various sloshing propellant modes.

c. The artificially uncoupled bending, rigid-body, and sloshing modes may first be coupled together by calculating orthogonal modes of the system from the free-vibration equations of motion. These modes will then be reasonable approximations to the orthogonal normal modes of the first approach. They may then be treated as in the first approach by coupling them together with the flight control system and the aerodynamics of the missile.

In the study of bending stability, in the majority of cases the use of artifically uncoupled modes (uncoupled in a prescribed manner) will prove as satisfactory as the use of orthogonal system modes. As will be shown later in Subsections 2 and 3 of Section 4, the rigid-body modes, sloshing modes, and the bending modes (other than the bending mode being investigated) may be omitted in the analysis for the majority of cases. In the cases where these other modes may be omitted, a comparison of the orthogonal system modes with the artifically uncoupled bending modes will show that there is a negligible difference between the bending mode properties (mode, shape, generalized mass, and frequency) and the corresponding orthogonal mode properties.

When the artifically uncoupled bending, sloshing, and rigid-body control frequencies are in the vicinity of one another, all of those modes in that vicinity will most likely have to be included in the stability analysis. Here the use of orthogonal modes, either approximate or exact, will be easier since they will not couple with one another as strongly as the artifically uncoupled modes. This lower coupling is evidenced by the fact that there will be an appreciably larger frequency separation between all of the orthogonal modes concerned. This separation allows one to treat some of those modes, if not all, exclusive of the others.

It follows from the previous discussion that if a complete stability analysis of the missile (with the control system) is to be conducted, i.e., bending, rigid-body, and sloshing stability, the first approach would be easier than the other two. This is true since the calculation of orthogonal modes by means of a detailed digital computer program will not appreciably increase the input data nor the operating time as compared to calculation of artifically uncoupled bending modes.

In order that the stability analysis may be made using artifically uncoupled bending, rigid-body, and sloshing modes, the generalized equation of motion will be written showing force inputs from the sloshing propellants. Also, separate equations of motion will be written for the artifically uncoupled modes of the sloshing propellants. If, however, sloshing propellants are to be included in the missile modal calculations (orthogonal modes) the generalized equation of motion will remain the same: one simply omits the sloshing terms (Y's) and drops the sloshing equations of motion.

The general equations of motion are to be written using the form of Equations 3-11. To accomplish this it is only necessary to display the generalized forces acting on each mode. These forces will be discussed briefly at this point.

---

* Henceforth the number of degrees of freedom and/or number of modes in the various summations shown will be denoted by the symbol r. In theory r could be equal to the number of degrees of freedom, there being that many normal modes; in practice a far smaller number of modes is used.

3.4.1 Inertial Forces. The equations will be written for artificially uncoupled body modes (rigid and elastic) and sloshing modes, and for a set of additional degrees of freedom representing the engine thrust chamber's motions due to action within the positioning servos. The coupling which will arise between these modes will be displayed by applying inertia forces (D'Alembert's reversed effective forces) to each sloshing mass element and to each rocket engine chamber.

3.4.2 Rocket Engine Forces and Moments. Referring to Figure 3-3, the rocket engine may be seen to be gimbaled at the engine's injector head. At the time of writing this technique is the most common one used for thrust-vector control of liquid propellant engines. Other thrust-vector control techniques will very likely be idealized to a model compatible with this one; hence, its generality is probably assured.

NOTE: ALL ELASTIC MODAL
DEFLECTIONS ARE
SHOWN AS FOR A UNIT
NORMAL COORDINATE
DISPLACEMENT $q^{(i)}$ 1

$//$ DENOTES PARALLEL LINES
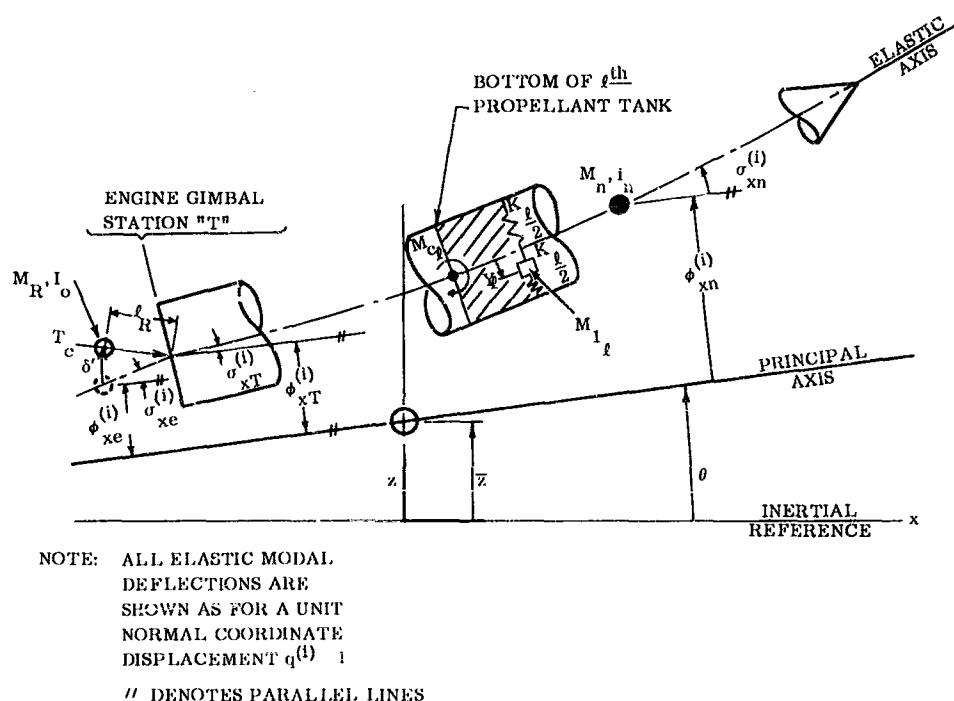
Figure 3-3. Schematic Showing General Relations of the Coordinates Used for Elastic Motion

Since the entire engine is gimbaled instead of just the thrust vector, the gimbaling of the engine will exert inertial forces as well as thrust forces on the missile body. These inertial forces are appreciable, and their lateral components will occasionally equal those of the thrust forces when the engine is gimbaled sinusoidally. For current engines this crossover occurs somewhere between 3-1/2 and 7 cycles per second. An engine using jet-evators or vanes for thrust-vector deflection will exhibit forces similar to those produced by a gimbaled thrust nozzle.

In addition to the propulsive thrust and chamber inertial forces, there are friction forces exerted at the gimbal due to relative movement there. These forces are applied to both the missile and the engine, and are a function of both the modal deflections and the engine perturbation angle.*

---

*The total angle between the center line of the engine chamber and expansion nozzle and the elastic axis of the structure at the gimbal point consists of two parts: a) an angular displacement which is contained within the mode shape itself (due to the elasticity of the engine's torsional spring mounting as employed in the modal calculations) while the servo positioning system is locked, and b) an additional degree of rotational freedom added to represent the motion accompanying action within the positioning servo. The latter motion is referred to throughout as the perturbation angle, δ'_k.

For small angles the lateral propulsive force exerted on the missile at the hinge point of the rocket engine due to a total engine chamber angular deflection $(\delta'_k - \sum_j \sigma^{(j)}_{xe} q_j)$ is:

$$T_k (\delta'_k - \sum_j \sigma^{(j)}_{xe} q_j).$$

However, we choose to omit that portion of this component due to the angle between the principal inertial axis and the elastic axis at the gimbal point; i.e., the only work done on the mode by the propulsive forces is assumed to be that due to the inclination between the thrust vector and the elastic axis at the gimbal:

$$T_k (\delta'_k - \sum_j (\sigma^{(j)}_{xe} - \sigma^{(j)}_{xT}) q_j) .$$

This approximation is made to offset the omission of the work done by longitudinal movement of the thrust vector; it is discussed in detail in Appendix C-4.

The bearing friction moment about the hinge point due to gimbaling of the rocket engine is:

$$\bar{C}_{f_k} \left[\dot{\delta}'_k - \sum_{j=1}^{r} (\sigma^{(j)}_{xe} - \sigma^{(j)}_{xT}) \dot{q}_j \right] .$$

Here $\bar{C}_f$ is the linearized gimbal friction of a specific frequency and amplitude of oscillation of the engine angle, with respect to the elastic axis at the gimbal (see Appendix B4).

3.4.3 Liquid Propellant Sloshing Forces and Moments. There are two popular mechanical analogies which duplicate the frequencies, forces, and moments resulting from the hydrodynamic solution of a rigid circular cylindrical tank, undergoing translation and rotation in a "carried acceleration field."* These analogies are the pendulum and spring-mass analogies, and they are discussed in greater detail in Appendix A3 under the heading Sloshing Basic Data. For our purposes, we choose to use the modified spring-mass analogy, since it may be arranged to place the point of application of the lateral sloshing forces at the center of pressure for the sloshing fluid. This arrangement is made through the addition of a pure couple to represent moments due to the hydrodynamic forces on the bottom of the propellant tank (see Appendix A3).

When the sloshing propellant masses are not incorporated within the elastic beam modal calculation (as is the case if an artificially uncoupled mode approach is taken) explicit terms must be written for the sloshing masses' forces and moments reacting on the tank walls.

The lateral force exerted on the missile due to deflection of the sloshing mass, M_ℓ, is $K_\ell Y_\ell$. This force expression may be used as an alternate to the inertial forces in coupling the sloshing to the body modes. And, the moments exerted on the bottom of the tank due to acceleration and deflection of the sloshing mass, M_ℓ, are:

$$M_{c\ell} \ddot{Y}_\ell + M_{1\ell} \alpha_T Y_\ell .$$

3.4.4 Aerodynamic Forces and Moments. In this analysis only quasi-steady-state aerodynamics are considered, as discussed in Appendix A5. This mathematical model for aerodynamic forces assumes the forces to be directly proportional to, and in phase with the instantaneous local angle of attack at each body station. The linear aerodynamic property is a good approximation, since the angle of attack seldom exceeds six to eight degrees for this class of vehicle during the time of flight when dynamic pressures are significant (mid-portion of the boost phase). No aerodynamic interaction between stations (downwash effect) occurs. This model is essentially the slender body-airship theory of Munk and Jones (Reference 9) which presumes two-dimensional flow in planes transverse to the flight direction. In preference to using the theoretical local lift curve slopes, which are known to be inaccurate (see Appendix A5), experimental or at least empirically corrected values are employed.

---

*A "carried acceleration field" is an acceleration field that is fixed with respect to the maneuvering vehicle. In the case of a booster vehicle the total thrust of the engines is directed along the longitudinal axis and rotates with the vehicle. The lateral acceleration, due to a thrust vector deflection with respect to the longitudinal axis, is accounted for as one of the forcing functions of the sloshing propellants.

The adequacy of this aerodynamic model for slender, non-lifting bodies at modest angles of attack may be assumed a priori for low values of effective frequency of oscillation, since steady-state experimental or empirical lift distribution data is to be employed. In the case of the slender-body oscillatory problem the criterion against which to judge whether or not an oscillatory frequency is "low" is the reduced frequency parameter, $k = \omega l/V$, where l is the body length. In general, this parameter should be less than unity for the slender-body hypothesis to be valid (Reference 9).

For rigid body mode oscillations of ballistic boosters the typical range of this parameter is from 0.1 to 1; hence one concludes that the quasi-steady aerodynamic model should be satisfactory for this mode. For the higher frequency (elastic) modes the situation is neither so simple nor so clear. Parameter k for these higher modes may range from 1.0 to 100, when based upon use of total body length. One can argue that this unit of length is meaningless in this case,* but regardless of selection of a reasonable alternative, the reduced frequency parameter remains too high to justify completely the use of the quasi-steady model for the elastic modes' aerodynamic force effects.

No suitable alternative to the quasi-steady model for high frequency motions of a slender body is known to exist. By inference from the properties of non-steady aerodynamics of lifting surfaces one might conclude that the non-steady effects are those leading to a reduction in force amplitude and to a modest phase lag.** Such effects could be of major importance in the study of sustained oscillations of a system which extracts its energy from the air, e.g., wing flutter. For the servo-elastic problem of the unwinged ballistic booster, however, the aerodynamic forces play a secondary role and the small phase shift is of little importance. Hence, the quasi-steady model is still suitable and will be employed herein.

Another phenomenon further complicates the study of the unsteady aerodynamic forces; viz., <u>transonic buffeting</u>. This phenomenon manifests itself in the form of sizable oscillatory pressures acting on the vehicle during its passage through the transonic speed region. The nature of the mechanism of this buffeting is obscure; it has been observed on fixed and oscillating models of a variety of two- and three-dimensional shapes, over a sizable transonic speed range. The phenomenon is generally attributed to regions of separated flow which appear prominently in the transonic range over blunt bodies. This separation has been observed to result in a hysteresis effect in the aerodynamic coefficients, such that under certain conditions increased amounts of energy may be extracted from the airstream.

Much of the model testing work done in the area of transonic buffeting is reported only in the classified literature (e.g., Reference 12), although some earlier results are more generally disseminated (Reference 13). The phenomenon is highly configuration-dependent and is so little understood that no general treatment of it, either analytic or semi-empirical, is available. Some statistical design approaches have been made; however, the application of stationary, random-process analytic methods to an accelerating vehicle is questionable.

Transonic buffeting is believed to be a problem only on those ballistic booster configurations having reductions in diameter (negative "skirt-angle" effects) which require a flow expansion behind a bulbous forward stage or "hammerhead payload." A configuration with continually increasing stage sizes going aft should experience a minimum of trouble from this source. Actual flight experience to date of ballistic boosters carrying bulbous forward stages or payloads has been meager, and the data obtained is inconclusive as regards the presence and/or significance of the transonic buffeting phenomenon. Flight experience with vehicles of monotonically increasing diameters has confirmed the absence of any serious effects due to buffeting, for such configurations.

The problem of providing a suitable aerodynamic model for the ballistic booster carrying a lifting surface payload and/or fins is a formidable one, for which no simple general solution is available. Here, downwash and wing-body interference effects can be significant. Here, too, the amount of energy which may be extracted from the air (or, equally, the magnitude of lifting forces) is much greater than that associated with the unwinged booster. Fortunately, a larger body of theory and experience is available to be applied against the problem.

For treatment of the lifting surface problem herein the following observations are made: the range of reduced frequencies, $k = \omega b/V$, where b is the semichord of a lifting surface attached to a ballistic booster, is usually low if consideration of modal frequencies is restricted to those of the overall vehicle structure (including its

---

* The law of null forward propagation of effects at supersonic speeds certainly makes it questionable.
** See for instance a plot of Theodorsen's function C (k) on p. 272 of Reference 6.

elastic modes). Thus, "local" modes of the lifting surfaces, with their higher uncoupled natural frequencies, are omitted from consideration. The Mach number range in which the aerodynamic forces for the winged booster are significant is usually from 0.4 to 4.0. Hence, the range of the parameter, kM, is not sufficiently high to justify application of the simple "piston theory" (Reference 11), which applies for kM >> 1. However, since the range of the lifting surface reduced frequency parameter, k = ωb/V, is low, continued use of the quasi-steady aerodynamic model for these lifting surfaces is reasonable. Moreover, it permits a unified description of aerodynamic forces over the entire vehicle.

Thus, in the following discussion quasi-steady aerodynamics are indicated for all portions of the vehicle. The extension of the equations to incorporate a more sophisticated aerodynamic model (when available) is direct but is not given herein because of the specialized nature of any such treatment, dependent as it is upon configuration, Mach range, and experience and personal taste of the analysts.

Following the quasi-steady approach the lift distribution along the vehicle is obtained, as discussed in Appendix A5. By integrating the aerodynamic normal force coefficient per unit length, per unit angle of attack over the length of the individual partitioned segments of the missile, one obtains a normal force coefficient per unit angle of attack for each segment, $(C_{N/\alpha})_{xn}$. Applying these coefficients at the centroid of the partitioned length, one writes the aerodynamic force at the segment's centroid as the product of the normal force coefficient and angle of attack of the centroid of the segment.

The local angle of attack due to the deflection of the r bending and rigid body modes (q_j) is (see Figure 3-4):*

$$\alpha_{xn} = \sum_{j=1}^{r} \left(-\frac{\phi_{xn}^{(j)}}{V} \dot{q}_j + \sigma_{xn}^{(j)} q_j \right) .$$
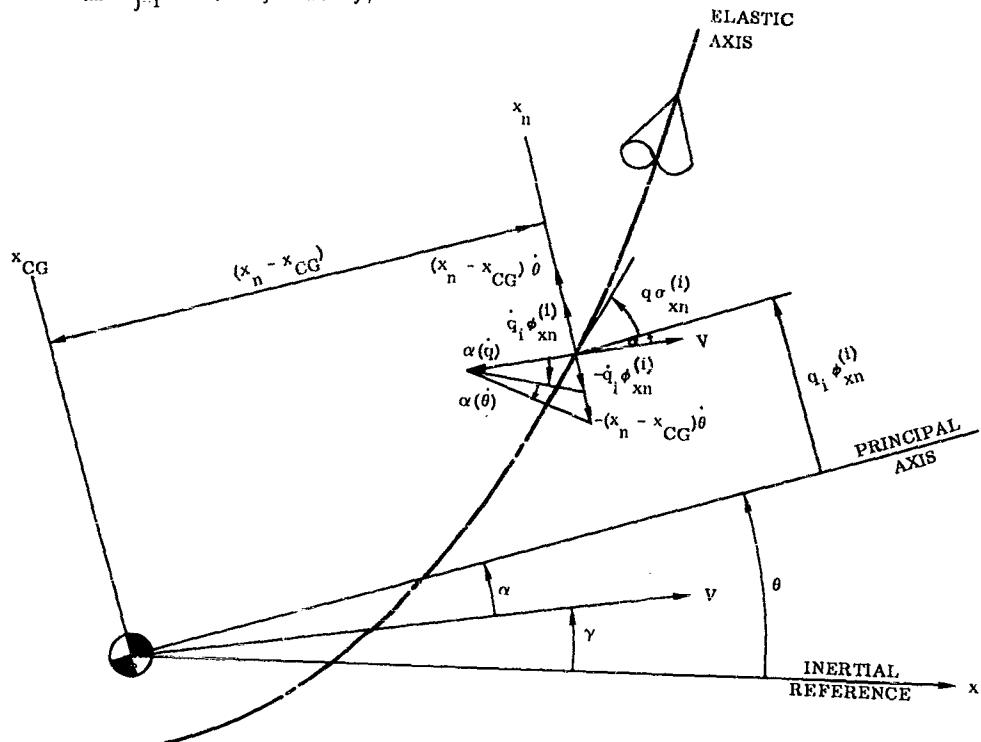
Figure 3-4. Determination of Effective Angle of Attack

*The perturbation angle of the flight path, γ, is taken as zero, i.e., $\theta \doteq \alpha$

This makes the aerodynamic force applied at station X_n equal to:

$$P(C_{N/\alpha})_{xn} \sum_{j=1}^{r} \left(- \frac{\phi_{xn}^{(j)}}{V} \dot{q}_j + \sigma_{xn}^{(j)} q_j \right)$$

where $P = q S_{ref}$.

No aerodynamic couple is applied on any beam segment in this model, since it is assumed that the centroids of area and pressure coincide.

3.4.5 Internal Dissipative (Damping) Forces. Some of the forces already discussed are velocity-dependent (e.g., certain aerodynamic forces and engine-gimbal-bearing friction torques) and will therefore be dissipative in nature. However, there exist other dissipative (damping) effects due to material strain hysteresis, coulomb friction in structural joints, and to viscous propellant action in the tanks.

The nature of all these additional damping effects is obscure and does not lend itself to anything other than an approximate empirical treatment. This treatment represents the gross effect of these scattered dissipative mechanisms as an equivalent viscous damping, added to each mode as appropriate. The damping is thus assumed to produce no coupling between modes. While this mechanization is not entirely realistic, it is justified by the following observations:

a. The actual damping is very low and is found by test to produce little coupling. Thus, nearly pure normal modes of a system may be excited and the system observed to decay almost harmonically. The indication given is that velocity-dependent coupling is very small.

b. If one were to show a velocity-dependent coupling, the coefficient would have to be determined experimentally. Since the direct damping coefficient is itself difficult enough to measure, it is clear that one could hardly expect to improve the accuracy of a study by introduction of still more suspect data.

The structural damping force is a function of the deflection of the generalized coordinate of the mode but in phase with the velocity of the generalized coordinate of that mode. To treat this damping as a viscous damping requires that the mode oscillate in a quasi-harmonic manner. This damping force may then be expressed as a damping factor, ζ_i, where $2\zeta_i \omega_i \dot{q}_i$ is the internal damping force of the ith mode per unit generalized mass.

The fluid propellant damping forces result from the dissipative nature of a viscous fluid undergoing shear. Although there are some approximate methods for calculating damping forces, these forces are most commonly arrived at by experimental testing of the actual tank, in the case of small missiles, and a model tank in the case of large missiles. These forces may be represented as a propellant damping factor, ζ_ℓ, in the expression $2\zeta_\ell \omega_\ell \dot{Y}_\ell$, which is the damping force per unit sloshing mass.

In Appendix C3 it is shown that the rate-of-change-of-mass terms, including jet-damping, are negligible for the class of vehicles considered. Therefore, these terms are assumed to be zero.

3.4.6 Servo Actuation Torques. The engine positioning servo actuation system produces a torque on the engine chamber, denoted here by $T_{L_{servo}}$. Its elaboration in terms of the servo system properties and autopilot command signals is a specialized study for each such system (see Section 4).

3.4.7 Equations of Motion. By defining a few special symbols concerned with the rigid-body degree of freedom, the equations of motion of the vehicle body modes may be written in a general form which will include rigid-body pitching, rigid-body plunging and body bending. Let

$$\sigma_{xn}^{(\theta)} = 1 \text{ and}$$

$$\phi_{xn}^{(\theta)} = x_n - x_{CG}$$

Here $\sigma_{xn}^{(\theta)}$ is the normalized slope of the rigid-body pitching mode at station n along the longitudinal axis of the vehicle; $\phi_{xn}^{(\theta)}$ is the normalized deflection in this mode. Note that $\sigma_{xn}^{(\theta)}$ is dimensionless and $\phi_{xn}^{(\theta)}$ has units of

ft/radian. The pitching mode normal coordinate is q_θ θ and is dimensionless.* The generalized mass for the pitching mode becomes:

$$\mathcal{M}_\theta = \int m(x) \left| \phi^{(\theta)}(x) \right|^2 dx = \int m(x - x_{CG})^2 dx = 1.$$

Also define

$$\sigma_{xn}^{(\bar{z})} = 0$$

$$\phi_{xn}^{(\bar{z})} = 1$$

where $\phi_{xn}^{(\bar{z})}$ is the normalized rigid-body plunging mode deflection at station n.

The generalized mass for this mode is:

$$\mathcal{M}_{\bar{z}} = \int m(x) \left| \phi^{(\bar{z})}(x) \right|^2 dx = \int m dx \equiv M.$$

It will be noted that $\sigma_{xn}^{(\theta)}$ and $\phi_{xn}^{(\bar{z})}$ are constant along the longitudinal axis of the vehicle since they are pure rotation and translation, respectively, of the vehicle's principal axis, behaving as a rigid body.

By use of this choice of symbols the rigid-body mode equations become identical in form with those of the elastic modes. Hence, in this section we will denote their normal coordinates as q_j's, just as for the elastic modes. Two other classes of degrees of freedom are distinct enough in their nature that they will be carried with their own distinctive symbols: the control deflections of the rocket engines will be denoted by δ_k' and the translation of the sloshing masses, by Y_ℓ.

The modes assumed to describe the body shape are orthogonal modes, computed with the rocket engine masses afixed. Inertial coupling between the body modes and the engine then occurs only through the perturbation angle accelerations, $\ddot{\delta}_k'$. To write the equation of motion of δ_k', the rocket engine chamber mode, we begin by summing forces and torques about that engine's center of gravity.

$$\Sigma M_{CG} = I_0 (\ddot{\delta}_k' - \Sigma_j \sigma_{xc}^{(j)} \ddot{q}_j) = T_{L,servo} + V_T \ell_R - T_f$$

$$\Sigma F = M_R (\ell_R \ddot{\delta}_k' + \Sigma_j \phi_{xc}^{(j)} \ddot{q}_j) = -V_T,$$

where V_T is the transverse shear force acting on the engine (and vehicle) at the gimbal point, due to the engine's transverse acceleration; T_f is the gimbal friction torque; and $T_{L,servo}$ is the torque generated by the servo actuation device. If one eliminates V_T from the above, the general equation for the rocket engine is obtained as shown below.

In cases where the sloshing liquid elements have been included in the calculation of the body modes, the slosh displacements are given within the modal description. The slosh modes are then orthogonal to the body modes and the sloshing terms of Equation 3-12 may be omitted; this includes dropping the tank bottom couples $(M_{,\ell} \alpha_T Y_\ell)$ and $(M_{c\ell} \ddot{Y}_\ell)$, which are now accounted for in the modal calculation (see Appendix A4). Equation 3-14 is also not needed in such a case.

---

* From these remarks one sees that the units of the pitching mode coordinate are unique, all other modal coordinates having units of feet. An arbitrary unit of length could be introduced to the pitching coordinate to make it conform, but no basic advantage would thereby accrue.

(i^{th} body mode, rigid or elastic)

$$\mathcal{M}_i \ddot{q}_i + 2\zeta_i \omega_i \mathcal{M}_i \dot{q}_i + \mathcal{M}_i \omega_i^2 q_i = -\sum_{k=1}^{m} \Bigg[(M_{R_k} \ell_{R_k} \phi_{xe_k}^{(i)} - I_{0_k} \sigma_{xe_k}^{(i)}) \ddot{\delta}_k' +$$

$$T_k \Bigg[\delta_k' - \sum_{j=1}^{r} (\sigma_{xe}^{(j)} - \sigma_{xT}^{(j)})_k q_j \Bigg] \phi_{xT}^{(i)} \Bigg] +$$

$$\sum_{k=1}^{m} \bar{C}_{f_k} \Bigg[\dot{\delta}_k' - \sum_{j=1}^{r} (\sigma_{xe}^{(j)} - \sigma_{xT}^{(j)})_k \dot{q}_j \Bigg] (\sigma_{xe}^{(i)} - \sigma_{xT}^{(i)})_k - \qquad (3\text{-}12)$$

$$\sum_{\ell=1}^{s} \Bigg[K_\ell Y_\ell \cdot \phi_{x\ell}^{(i)} + (M_{c\ell} \ddot{Y}_\ell + M_{1\ell} \alpha_T Y_\ell) \sigma_{x\ell_B}^{(i)} \Bigg] +$$

$$P \sum_n (C_{N/\alpha})_{xn} \sum_{j=1}^{r} (\sigma_{xn}^{(j)} q_j - \frac{\phi_{xn}^{(j)}}{V} \dot{q}_j) \phi_{xn}^{(i)}$$

(k^{th} rocket engine)

$$(M_{R_k} \ell_{R_k}^2 + I_{0_k}) \ddot{\delta}_k' = -\sum_{j=1}^{r} (M_{R_k} \ell_{R_k} \phi_{xe_k}^{(j)} - I_{0_k} \sigma_{xe_k}^{(j)}) \ddot{q}_j -$$

$$\bar{C}_f \Big(\dot{\delta}_k' - \sum_{j=1}^{r} (\sigma_{xe_k}^{(j)} - \sigma_{xT_k}^{(j)}) \dot{q}_j \Big) + T_{L_{servo}} \qquad (3\text{-}13)$$

(ℓ^{th} propellant sloshing mode)

$$M_{1\ell} \ddot{Y}_\ell + 2\zeta_\ell \omega_\ell M_{1\ell} \dot{Y}_\ell + K_\ell Y_\ell = M_{1\ell} \sum_{j=1}^{r} \phi_{x\ell}^{(j)} \ddot{q}_j \qquad (3\text{-}14)$$

3.5 THREE-AXIS RIGID VEHICLE EQUATIONS

The rigid-body equations of motion of a booster vehicle which possesses six degrees of freedom are presented herein. The vehicle is considered to be asymmetric, both inertially and aerodynamically. By asymmetry it is meant that the center of gravity and center of pressure do not necessarily coincide with the geometric or control axes of the vehicle. Eulerian (body fixed) axes are used in writing the equations of motion. The axes are placed along the pitch, yaw, and roll geometric or control axes, with the origin referenced at the longitudinal center of gravity of the "reduced vehicle."*

It is assumed that in flight a booster vehicle will have only small angular deviations about the body-fixed coordinates in the yaw and roll directions. The angular displacement about the pitch axis (Y-Y') will be considered to be composed of two parts: the steady state pitch angle, θ_0, and the perturbation pitch angle, θ.

$$\Theta = \theta_0 + \theta$$

$$\Phi = \phi$$

$$\Psi = \psi$$

where ϕ, θ and ψ are the perturbation quantities.

---

*The "reduced vehicle" is that portion of the vehicle which acts as a unitary mass at the rigid-body control frequency. This is usually taken to be the entire vehicle mass minus the mass of the sloshing portion of the liquid propellants, and for this analysis will be defined as such.

(i^{th} body mode, rigid or elastic)

$$\mathcal{M}_i \ddot{q}_i + 2\zeta_i \omega_i \mathcal{M}_i \dot{q}_i + \mathcal{M}_i \omega_i^2 q_i = -\sum_{k=1}^{m} \left[(M_{R_k} \ell_{R_k} \phi_{xe_k}^{(i)} - I_{0_k} \sigma_{xe_k}^{(i)}) \ddot{\delta}'_k \right.$$

$$T_k \left[\delta'_k - \sum_{j=1}^{r} (\sigma_{xe}^{(j)} - \sigma_{xT}^{(j)})_k q_j \right] \phi_{xT}^{(i)} \right] +$$

$$\sum_{k=1}^{m} \bar{C}_{f_k} \left[\dot{\delta}'_k - \sum_{j=1}^{r} (\sigma_{xe}^{(j)} - \sigma_{xT}^{(j)})_k \dot{q}_j \right] (\sigma_{xe}^{(i)} - \sigma_{xT}^{(i)})_k - \qquad (3\text{-}12)$$

$$\sum_{\ell=1}^{s} \left[K_\ell Y_\ell \cdot \phi_{x\ell}^{(i)} + (M_{c\ell} \ddot{Y}_\ell + M_{1\ell} \alpha_T Y_\ell) \sigma_{x\ell_B}^{(i)} \right] +$$

$$P \sum_n (C_{N/\alpha})_{xn} \sum_{j=1}^{r} (\sigma_{xn}^{(j)} q_j - \frac{\phi_{xn}^{(j)}}{V} \dot{q}_j) \phi_{xn}^{(i)}$$

(k^{th} rocket engine)

$$(M_{R_k} \ell_{R_k}^2 + I_{0_k}) \ddot{\delta}'_k = -\sum_{j=1}^{r} (M_{R_k} \ell_{R_k} \phi_{xe_k}^{(j)} - I_{0_k} \sigma_{xe_k}^{(j)}) \ddot{q}_j -$$

$$\bar{C}_f \left(\dot{\delta}'_k - \sum_{j=1}^{r} (\sigma_{xe_k}^{(j)} - \sigma_{xT_k}^{(j)}) \dot{q}_j \right) + T_{L\text{-}servo} \qquad (3\text{-}13)$$

(ℓ^{th} propellant sloshing mode)

$$M_{1\ell} \ddot{Y}_\ell + 2\zeta_\ell \omega_\ell M_{1\ell} \dot{Y}_\ell + K_\ell Y_\ell = M_{1\ell} \sum_{j=1}^{r} \phi_{x\ell}^{(j)} \ddot{q}_j \qquad (3\text{-}14)$$

3.5 THREE-AXIS RIGID VEHICLE EQUATIONS

The rigid-body equations of motion of a booster vehicle which possesses six degrees of freedom are presented herein. The vehicle is considered to be asymmetric, both inertially and aerodynamically. By asymmetry it is meant that the center of gravity and center of pressure do not necessarily coincide with the geometric or control axes of the vehicle. Eulerian (body fixed) axes are used in writing the equations of motion. The axes are placed along the pitch, yaw, and roll geometric or control axes, with the origin referenced at the longitudinal center of gravity of the "reduced vehicle."*

It is assumed that in flight a booster vehicle will have only small angular deviations about the body-fixed coordinates in the yaw and roll directions. The angular displacement about the pitch axis (Y-Y') will be considered to be composed of two parts: the steady state pitch angle, θ_0, and the perturbation pitch angle, θ.

$$\Theta = \theta_0 + \theta$$

$$\Phi = \phi$$

$$\Psi = \psi$$

where ϕ, θ and ψ are the perturbation quantities.

---

*The "reduced vehicle" is that portion of the vehicle which acts as a unitary mass at the rigid-body control frequency. This is usually taken to be the entire vehicle mass minus the mass of the sloshing portion of the liquid propellants, and for this analysis will be defined as such.

The forward velocity along the steady-state pitch geometric axis, U, is assumed to be relatively large. Lateral perturbation velocities, V and W, are written as angles of attack: $\alpha = \dfrac{W}{U}$ and $\beta = \dfrac{V}{U}$. All angles will be written in radian measure.

The Euler angles are defined as those angles through which one axis system must be rotated sequentially to superimpose it upon another having an initial angular displacement from the first. In Figure 3-5 these rotations are made sequentially about the vehicle's pitch, yaw, and roll axes in that order.
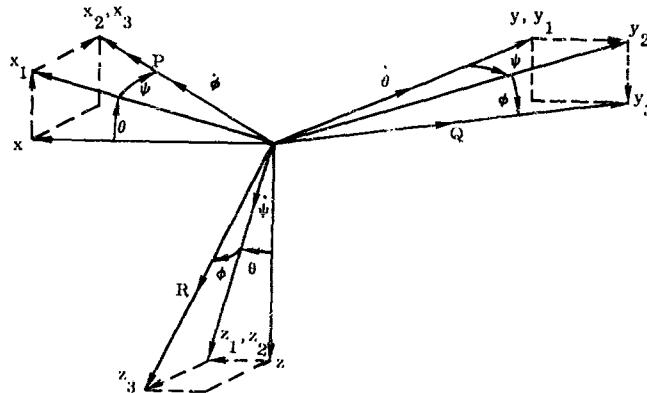
Figure 3-5. Angular Notation Used for a Three-Axis Analysis (θ-ψ-ϕ System)

The following relations can be obtained by direct resolution of the vectors in Figure 3-5:

$$P = \dot{\phi} + \dot{\theta} \sin \psi$$

$$Q = \dot{\theta} \cos \psi \, \cos \phi + \dot{\psi} \sin \phi$$

$$R = \dot{\psi} \cos \phi - \dot{\theta} \cos \psi \, \sin \phi$$

By rearranging these equations the rates of change of the Euler angles may be expressed as functions of the instantaneous angular velocities:

$$\dot{\phi} = P + R \sin \phi \tan \psi - Q \cos \phi \tan \psi$$

$$\dot{\theta} = Q \left(\frac{\cos \phi}{\cos \psi} \right) - R \left(\frac{\sin \phi}{\cos \psi} \right)$$

$$\dot{\psi} = R \cos \phi + Q \sin \phi.$$

These equations are linearized by assuming small perturbations only: ϕ and ψ must be restricted to small angles; P, Q, and R are small also:

$$\dot{\phi} = P$$

$$\dot{\theta} = Q$$

$$\dot{\psi} = R.$$

Figure 3-6 presents the mathematical model and coordinate system used. Figure 3-7 presents a modification for vehicles with aerodynamic surfaces of a typical manned ballistic boost-glide configuration, carrying a lifting surface payload and stabilizing fins on the first stage booster.
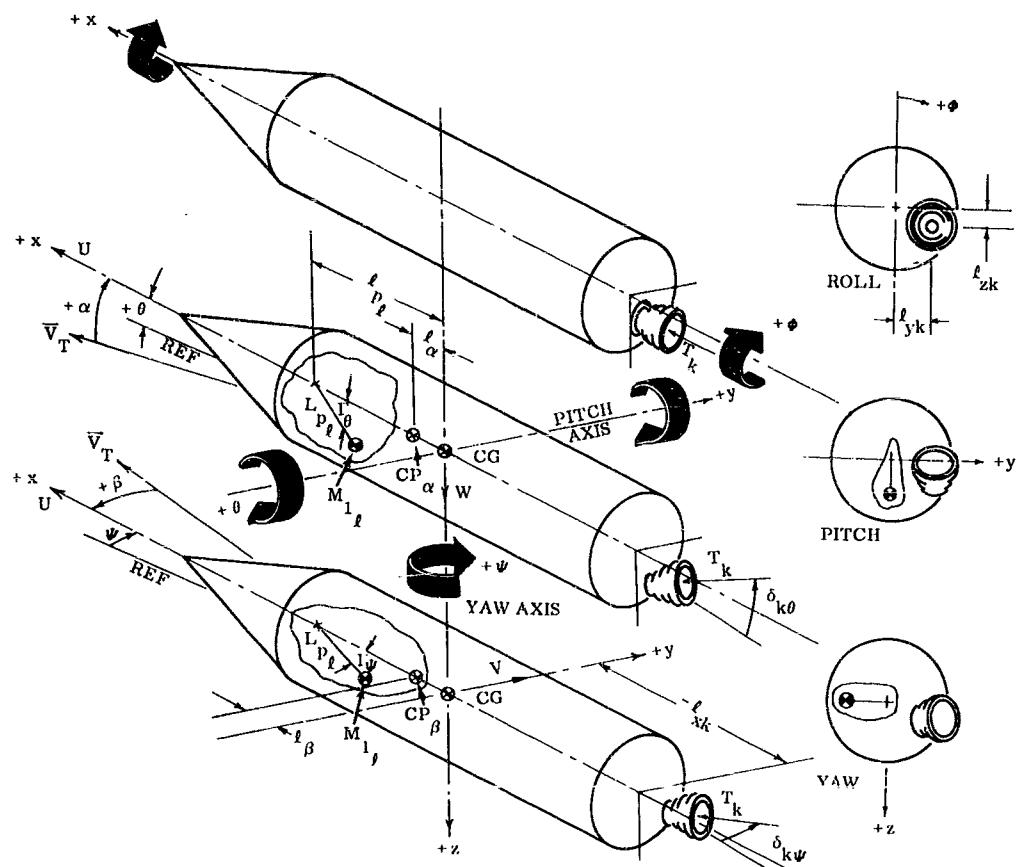
Figure 3-6. Three-Axes Schematic of a Boost Vehicle
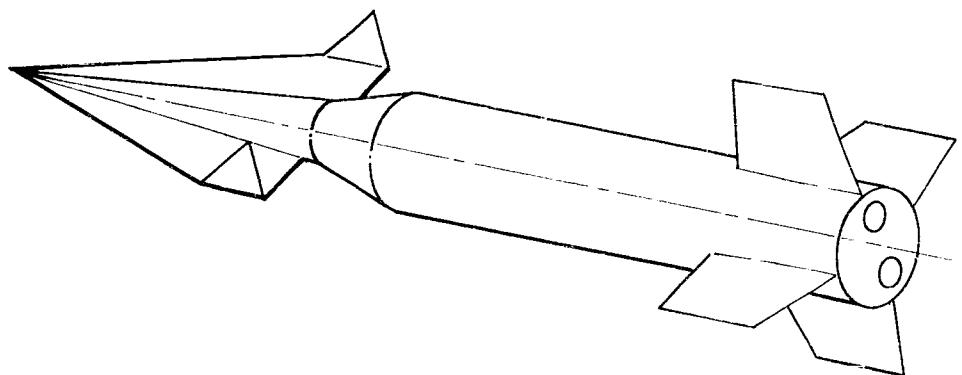
Figure 3-7. Typical Boost-Glide Vehicle Configuration Showing Lifting Surfaces
on the Booster and its Payload

The equations of motion of a rigid vehicle about a body-fixed axis system are derived in numerous references, e.g., Reference 11. The equations will therefore not be derived but only presented. Attention will be directed instead to development of those facets of the equations peculiar to the ballistic booster and which distinguish it (and its analysis) from the lift-sustained vehicle. These items are discussed following the presentation of the general equations themselves.

3.5.1 Three Axis-Equation of Motion:

$$\dot{U} = \frac{\Sigma F_x}{M_T} - Q\alpha U + R\beta U - g \sin \theta_0$$

$$\dot{\alpha} = \frac{\Sigma F_z}{U M_0} - P\beta + Q + \frac{g \cos \theta_0}{U} - \frac{\dot{U}\alpha}{U} - \frac{\Delta Y_{CG}}{U} \dot{P}$$

$$\dot{\beta} = \frac{\Sigma F_y}{U M_0} + P\alpha - R + \frac{g\lambda}{U} - \frac{\dot{U}\beta}{U} + \frac{\Delta Z_{CG}}{U} \dot{P}$$

$$I_{XX} \dot{P} = I_{XY} \dot{Q} + I_{XZ} \dot{R} + \Sigma L$$

$$I_{YY} \dot{Q} = I_{XY} \dot{P} + I_{YZ} \dot{R} + \Sigma M$$

$$I_{ZZ} \dot{R} = I_{XZ} \dot{P} + I_{YZ} \dot{Q} + \Sigma N$$

where

$$\lambda = \phi \cos \theta_0 + \psi \sin \theta_0$$

and

$$\int \dot{P} = P \qquad ; \qquad \int P = \phi$$

$$\int \dot{Q} = Q \qquad ; \qquad \int Q = \theta$$

$$\int \dot{R} = R \qquad ; \qquad \int R = \psi$$

Note that the equations are written for body-fixed coordinates (see Appendix C3).

3.5.2 Forces.
The forces F_x, F_y, and F_z have contributions from the aerodynamic forces (sub a), propulsion forces (sub p), and sloshing forces (sub s).

$$\Sigma F_x = X_p + X_a$$

$$\Sigma F_y = Y_a + Y_p + Y_s$$

$$\Sigma F_z = Z_a + Z_p + Z_s .$$

3.5.2.1 Aerodynamic Forces.
The aerodynamic forces arise from angles of attack in pitch and yaw (α and β), from the roll, pitch and yaw body rates ($P = \dot{\phi}$, $Q = \dot{\theta}$, and $R = \dot{\psi}$) and from aerodynamic control surface deflections. Expressed in terms of aerodynamic coefficients these are as follows:

$$X_a = - qS C_D$$

$$Y_a = - qS C_{N/\beta} \beta + qS C_{y/p} \dot{\phi} - qS C_{y/R} \dot{\psi} + qS C_{y/\delta_\psi} \delta_\psi$$

$$Z_a = - qS C_{N/\alpha} \alpha - qS C_{z/p} \dot{\phi} + qS C_{z/Q} \dot{\theta} + qS C_{z/\delta_\theta} \delta_\theta$$

where δ_ψ and δ_θ are the aerodynamic control surface deflections in yaw and pitch respectively.

3.5.2.2 Propulsion Forces:

$$X_p = \sum_{k=1}^{m} T_k$$

$$Y_p = -\sum_{k=1}^{m} T_k \, \delta_{k_\psi}$$

$$Z_p = \sum_{k=1}^{m} T_k \, \delta_{k_\theta}$$

3.5.2.3 Sloshing Forces:

$$Y_s = \frac{\Sigma F_x}{M_T} \, M_{1\ell} \, (-\Gamma_\psi + \Gamma_\theta \phi)$$

$$Z_s = \frac{\Sigma F_x}{M_T} \, M_{1\ell} \, (\Gamma_\theta + \Gamma_\psi \phi)$$

The $\Gamma_\theta \phi$ and $\Gamma_\psi \phi$ terms are due to the assumption that there is zero shear between the propellant and the missile tank wall. As a consequence, the missile is considered to rotate around the fluid.

3.5.3 Moments.
The moments L, M, and N likewise consist of the moments due to the aerodynamic forces, propulsive forces, and sloshing forces:

$$\Sigma L = L_a + L_p + \Delta Z_{CG} \, \Sigma \, F_Y - \Delta Y_{CG} \, \Sigma \, F_x$$

$$\Sigma M = M_a + M_p + M_s - \Delta Z_{CG} \, \Sigma \, F_x$$

$$\Sigma N = N_a + N_p + N_s + \Delta Y_{CG} \, \Sigma \, F_x \, .$$

3.5.3.1 Aerodynamic Moments.
Aerodynamic moments are proportional to angles of attack in pitch and yaw (including a nonlinear product term), to body axis rates, and to control deflections. They are expressed in coefficient form:

$$L_a = L_{\alpha\beta} \, qS \, \bar{\ell} \, \alpha\beta + qS \, \bar{\ell} \, C_{\ell/\beta} \, \beta - qS \, \bar{\ell} \, C_{\ell/P} \, \dot\phi + qS \, \bar{\ell} \, C_{\ell/R} \, \dot\psi + qS \, \bar{\ell} \, C_{\ell/\delta_\phi} \, \delta_\phi$$

$$M_a = qS \, \bar{\ell} \, C_{m/\alpha} \, \alpha + qS \, \bar{\ell} \, C_{m/P} \, \dot\phi - qS \, \bar{\ell} \, C_{m/Q} \, \dot\theta + qS \, \bar{\ell} \, C_{m/\delta_\theta} \, \delta_\theta$$

$$N_a = - qS \, \bar{\ell} \, C_{n/\beta} \, \beta + qS \, \bar{\ell} \, C_{n/P} \, \dot\phi - qS \, \bar{\ell} \, C_{n/R} \, \dot\psi - qS \, \bar{\ell} \, C_{n/\delta_\psi} \, \delta_\psi$$

where $\bar{\ell}$ is a reference length and δ_ϕ represents a differential deflection of the aerodynamic surfaces to produce a roll-control moment.

3.5.3.2 Propulsive Moments:

$$L_p = \sum_{k=1}^{m} T_k \, \ell_{y_k} \, \delta_{k_\theta} + \sum_{k=1}^{m} T_k \, \ell_{z_k} \, \delta_{k_\psi}$$

$$M_p = \sum_{k=1}^{m} T_k \, \ell_{z_k} - \sum_{k=1}^{m} T_k \, \ell_{x_k} \, \delta_{k_\theta}$$

$$N_p = - \sum_{k=1}^{m} T_k \ell_{y_k} - \sum_{k=1}^{m} T_k \ell_{x_k} \delta_{k_\psi}$$

3.5.3.3 Sloshing Moments:

$$M_s = - Z_s \ell_{p\ell}$$

$$N_s = Y_s \ell_{p\ell}$$

3.5.4 Propellant Sloshing Equations of Motion:

$$\ddot{r}_{\theta\ell} = \frac{F_{\Gamma\theta\ell}}{L_{p\ell}} - \frac{\Sigma F_x}{M_T} \frac{r_{\theta\ell}}{L_{p\ell}}$$

$$\ddot{r}_{\psi\ell} = \frac{F_{\Gamma\psi\ell}}{L_{p\ell}} - \frac{\Sigma F_x}{M_T} \frac{r_{\psi\ell}}{L_{p\ell}}$$

where

$$F_{\Gamma\theta\ell} = - \left[\frac{\Sigma F_z}{M_0} - \dot{Q} (\ell_{p\ell} - L_{p\ell}) + \left\{ \frac{\Sigma F_y}{M_0} + \dot{R} (\ell_{p\ell} - L_{p\ell}) \right\} \phi \right]$$

$$F_{\Gamma\psi\ell} = \left[\frac{\Sigma F_y}{M_0} + \dot{R} (\ell_{p\ell} - L_{p\ell}) - \left\{ \frac{\Sigma F_z}{M_0} - \dot{Q} (\ell_{p\ell} - L_{p\ell}) \right\} \phi \right]$$

3.5.5 Discussion of Three-Axis Coupling Effects for a Ballistic Booster.

Coupling in the three-axis system arises from four sources:

a. inertial coupling, since principal axes are not presumed,

b. coupling due to asymmetric aerodynamic configurational aspects,

c. coupling through the control system (aerodynamic and reaction jet), and

d. propellant sloshing in inertial planes about which the vehicle rolls.

The cross-coupling due to inertial asymmetry is significant when the body axis system does not coincide with the principal axes. This type of coupling is often negligible in analysis of ballistic boosters which are built symmetrically by intent. The principal inertial axes will very nearly coincide with the geometric or control axes, making such coupling very low. Typically, the ratios of products of inertia to moments of inertia for this class of vehicles will be of the order of 0.001 to 0.01.

Aerodynamic symmetry in the booster vehicle is also maintained by intent. Although the symmetry may be only plane symmetry, it is with respect to two planes and is usually enough to eliminate most aerodynamic configuration coupling. Inspection and discussion of the various aerodynamic forces and moments will give an indication of the origin and relative importance of the aerodynamic terms, such that it will be evident that many of these terms may be omitted from the three-axis equations of motion and may likewise justify using a plane-motion study for rigid-body stability.

3.5.6 Aerodynamic Coupling Due to Drag Force Increments.

To minimize aerodynamic loading during flight, ballistic missiles or boosters are purposely flown on zero-lift trajectories, either by pre-programming the desired flight path angle or through direction from some form of guidance system. In addition, an angle-of-attack attitude control loop may be employed which will try to maintain a zero angle of attack (zero lift) when the missile is flying through wind shears and gusts (see Section 2, Subsection 2.2.2). It follows then that the lift distribution on the aerodynamic surfaces is low (nominally zero). Consequently, any vehicle maneuvers or differential control deflections which produce asymmetric lifting surface loadings will result in very little cross coupling

between axes due to drag force increments. For example, a differential aileron deflection to produce roll will result in equal drag increases on the two main surfaces (if they have no lift) and, hence, will not be accompanied by a yaw couple. Likewise, a roll rate ($\dot{\phi} \equiv P$) will result in equal (but opposite) lifts and equal drag increments on the main surfaces due to the induced angle of attack.

It should also be noted that such differential drags as do occur on the main surfaces act at a very small moment arm from the yaw axis, leading again to the conclusion that roll-to-yaw coupling due to drag increments is negligibly small.

3.5.7 <u>Forces and Moments Due to Yaw Angle of Attack or Sideslip.</u> The forces F_1, F_2, F_3, and F_4 of Figure 3-8 are exerted on the vehicle due to a relative wind angle, β. The force F_1 is the total aerodynamic force exerted on the aft fins in the Z-plane. The fins on the booster section of the vehicle would be symmetrically
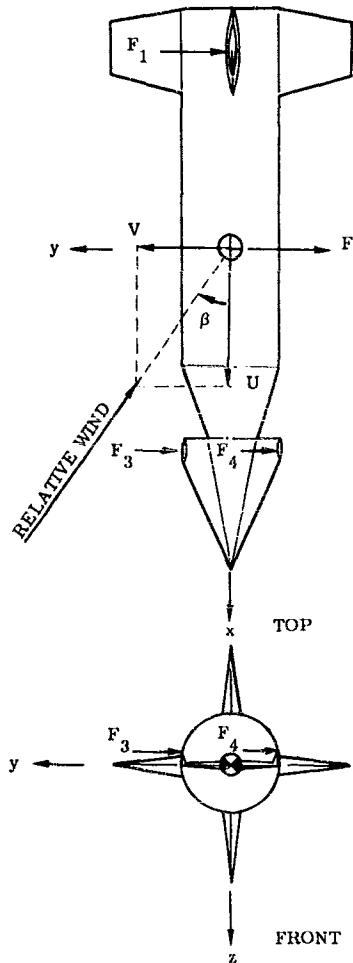
Figure 3-8. Aerodynamic Forces Due to Sideslip on a Ballistic Booster with Lifting Surfaces

placed with respect to the yaw plane such that the force F_1 would intersect the X-axis, and, therefore not contribute a rolling moment. The payload on the forward part of the vehicle will not necessarily be symmetric about the yaw plane, as shown in Figure 3-8. Here the forces F_3 and F_4 impart a rolling moment which is the

$(qS \bar{\ell} C_{\ell/\beta}\beta)$-term of the aerodynamic roll moment L_a. All of the forces (F_1, F_2, F_3 and F_4) are included in the $(qS C_{N/\beta}\beta)$-term of the lateral aerodynamic force Y_a. The roll moment imparted by F_3 and F_4 would be quite small as compared to the other aerodynamic and control rolling moments and is often safely omitted.

3.5.8 <u>Forces and Moments Due to Roll Rate.</u> The forces F_1, F_2, F_3, F_4, F_7, and F_8 of Figure 3-9 produce no net lateral force but are the main contributors of the $(qS \bar{\ell} C_{\ell/p}\dot{\phi})$-term of L_a. The conventional roll-yaw coupling is either zero or negligible, as previously mentioned, since boost vehicles are flown on a zero-lift trajectory or nominal zero angle of attack.
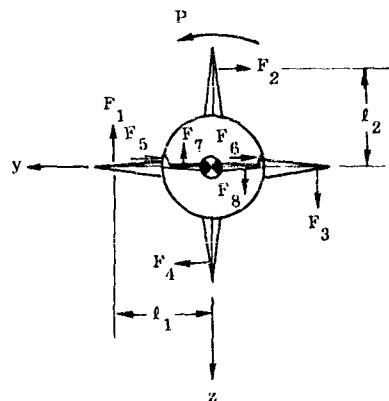
Figure 3-9. Aerodynamic Forces Due to a Rolling Rate
on a Ballistic Booster with Lifting Surfaces

The forces F_5 and F_6 do however, contribute a yawing moment due to rolling velocity, but this moment is again much less than the yaw control moments. It is not likely that there will be asymmetry in both of the lateral planes of the aerodynamic payload and, therefore, as shown in the figure, the forces F_7 and F_8 do not contribute pitching forces or moments.

3.5.9 <u>Forces and Moments Due to Yaw Rate.</u> The forces F_1, F_2, and F_3 of Figure 3-10 produce a yawing moment that opposes the yawing motion. Forces F_2 and F_3 also contribute a small roll moment, L_a.

3.5.10 <u>Forces and Moments Due to Yaw Control Surface Deflection.</u> The control forces F_1 and F_2 of Figure 3-11, due to deflection of the vertical fin control surfaces in the same direction, cause an overall control force in the Y-direction and a yawing moment, since the forces do not pass through the center of gravity of the missile. Since the fins are symmetric there is no roll moment produced.

3.5.11 <u>Forces and Moments Due to Roll Control Surface Deflection.</u> All of the control surfaces may contribute to the roll control of the missile by either deflecting clockwise or counterclockwise. The forces F_1, F_2, F_3 and F_4 in Figure 3-12 produce no net lateral force but only a rolling moment since the fins are symmetrical in each plane. No significant yaw moment is produced, either.

In summary, ballistic or boost vehicles are purposely limited to low turning rates so as to minimize structural loads. They also nominally fly zero lift trajectories. Guidance commands produce much slower maneuvers than do the control commands of manned aircraft and therefore do not appreciably affect the problem. In rigid-body studies of booster vehicles it is therefore common to ignore all of the terms other than the major term in each of the aerodynamic force and moment equations. Thus, for the ballistic booster without lifting surfaces one writes:
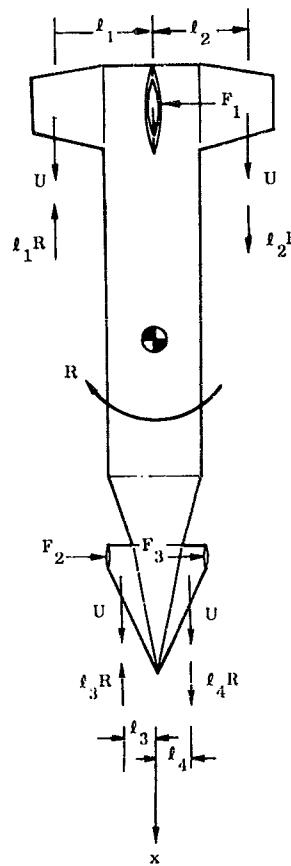
Figure 3-10. Aerodynamic Forces Due to Yaw Rate on a Ballistic Booster
with Lifting Surfaces
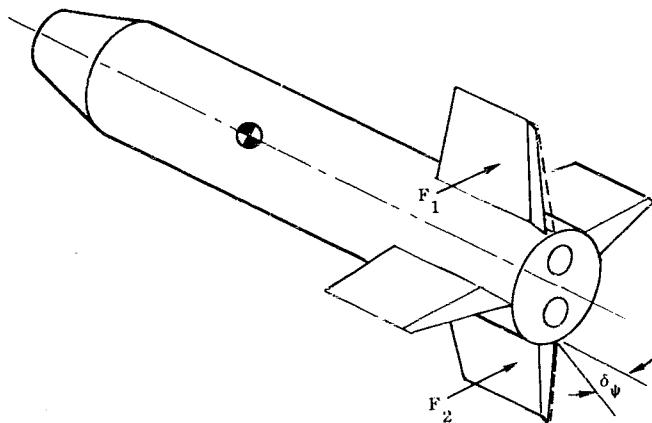
Figure 3-11. Aerodynamic Control Force Deflection, Yaw (Typical)
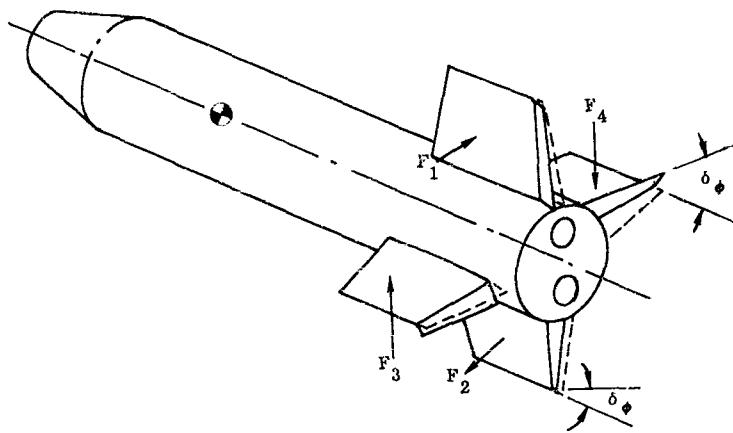
Figure 3-12. Aerodynamic Control Force Deflection, Roll

(Aerodynamic Forces)

$$X_a = - qS \, C_D$$

$$Y_a = -qS \, C_{N/\beta} \, \beta$$

$$Z_a = - qS \, C_{N/\alpha} \, \alpha$$

(Aerodynamic Moments)

$$L_a = L_{\alpha\beta} \, qS \, \bar{\ell} \, \alpha\beta$$

$$M_a = qS \, \bar{\ell} \, C_{m/\alpha} \, \alpha$$

$$N_a = - qS \, \bar{\ell} \, C_{n/\beta} \, \beta$$

For the ballistic booster carrying lifting surfaces the aerodynamic damping coefficients $C_{m/Q}$ and $C_{n/R}$ may be significant enough to warrant inclusion of their terms. If these same surfaces are activated for control, the aerodynamic control forces as reflected in the coefficients C_{Y/δ_ψ}, C_{Z/δ_θ}, C_{ℓ/δ_ϕ}, C_{m/δ_θ}, and C_{n/δ_ψ}, are included also.

SECTION 4

SIMPLIFICATION AND APPROXIMATION OF TRANSFER FUNCTIONS

SYMBOLS USED IN SECTION 4

Symbol	Definition	Units
A	area of hydraulic actuator piston	ft^2
B	bulk modulus of hydraulic fluid	lbs/ft^2
C_{f_k}	gimbal bearing friction coefficient for the kth engine	lb ft sec/rad
$\bar{C}_L$	hydraulic actuator leakage coefficient	$ft^5/lb.\ sec.$
$(C_N/\alpha)_{xn}$	local aerodynamic normal force coefficient per unit angle of attack at station n along the longitudinal axis	1/rad
I	reduced moment of inertia (see Appendix A1-5)	$slug\ ft^2$
I_{0_k}	moment of inertia in pitch or yaw of the kth engine about its own center of gravity	$slug\ ft^2$
I_{R_k}	moment of inertia of the kth engine about its gimbal point	$slug\ ft^2$
k	rocket engine index	N.D.*
K_c	hydraulic actuator (no load) open loop velocity gain	$\dfrac{(rad/sec)\ \delta}{rad\ \delta_c}$
K_c'	hydraulic actuator effective (at load) open loop velocity gain as defined in Equation 4-12	1/sec
K_E	equivalent spring constant for hydraulic actuator system equals $\left(\dfrac{V_T}{4BA^2} + \dfrac{1}{K_m}\right)^{-1}$	lbs/ft
K_{H_k}	hydraulic actuator spring constant for the kth engine $= \dfrac{4BA^2}{V_T}$	lbs/ft
K_ℓ	spring constant of sloshing mass in the ℓth propellant sloshing tank	lbs/ft
K_m	actuator structural spring constant	lbs/ft
ℓ	sloshing propellant index	N.D.
ℓ_a	aerodynamic moment arm	ft
ℓ_c	control thrust level arm about center of gravity	ft
$\ell_{p\ell}$	sloshing pendulum moment arm for ℓ^{th} propellant tank	ft
ℓ_R	rocket engine lever arm measured from the gimbal point at the engine center of gravity	ft
m_i	generalized mass for the ith mode	slugs

---

* Non-dimensional

SYMBOLS USED IN SECTION 4 (Continued)

Symbol	Definition	Units
$M_{c\ell}$	sloshing moment coefficient for the ℓth propellant sloshing tank	lb sec^2
$M_{1\ell}$	first mode sloshing mass in ℓ^{th} propellant (sloshing tank)	slugs
M_R	mass of rocket engine	slugs
$M_{\dot\theta}$	aerodynamic moment due to pitching rate	ft lbs sec
P	aerodynamic force parameter $= q\,S_{ref}$	lbs
P_L	load pressure on hydraulic actuator	lbs/ft^2
q_i	generalized displacement of the ith mode	ft
Q_i	generalized force for the ith elastic bending mode	lbs
R	moment arm of hydraulic actuator	ft
s	Laplace operator ($s = \sigma + j\omega$)	1/sec
T	total rocket engine thrust	lbs
T_c	thrust of control engine (s)	lbs
T_f	thrust of fixed rocket engine (s)	lbs
T_k	thrust of kth rocket engine	lbs
V	vehicle velocity	ft/sec
X_1	actuator deflection due to load pressure acting on the actuator elastic compliance	ft
X_n	X coordinate (longitudinal) of station n	ft
Y_ℓ	lateral displacement of the sloshing mass in the ℓth sloshing propellant tank	ft
α	angle of attack	rad
α_T	vehicle longitudinal acceleration $= \dfrac{T - D}{M}$	ft/sec^2
δ	angle between rocket engine thrust vector and vehicle elastic axis at gimbal point; includes elastic deformation of engine position servo and actuation within the servo itself	rad
δ'	angle between thrust vector and elastic mode at rocket engine's center of gravity, due to actuation within the positioning servo	rad
δ_ϵ	rocket engine error angle (defined in Equation 4-20)	rad
ζ_{cn}	damping ratio for hydraulic actuator	N.D.
ζ_i	damping ratio for the ith mode	N.D.
ζ_i'	generalized damping ratio for the ith mode	N.D.

SYMBOLS USED IN SECTION 4 (Continued)

Symbol	Definition	Units
ζ_i''	damping ratio as defined in Equation 4-13	N.D.
ζ_ℓ	damping ratio of the sloshing mass in the ℓth propellant sloshing tank	N.D.
θ	vehicle pitch angle	rad
μ_α	aerodynamic effectiveness parameter defined in Equation 2-2	$1/sec^2$
μ_δ	engine control effectiveness parameter defined in Equation 2-2	$1/sec^2$
σ	normalized modal slope	rad/ft
τ	time constant	sec
ϕ	normalized modal deflection	ft/ft
ω_c	natural frequency for hydraulic actuator	1/sec
ω_i	natural frequency for i^{th} mode	1/sec
ω_i'	generalized natural frequency for i^{th} mode	1/sec
ω_i''	modal natural frequency defined in Equation 4-13	1/sec
ω_ℓ	natural frequency of sloshing mass in ℓ^{th} propellant sloshing tank	1/sec

Subscripts

A	station A (location of lateral translation sensor)	
c	station c (center of gravity of rocket engine)	
G	station G (gyro or other angular sensor location)	
ℓ_B	station B (bottom of tank) of ℓth propellant sloshing tank	
n	station n	
T	station T (rocket engine gimbal or thrusting point)	
x	coordinate along the longitudinal axis	

4.1 AIMS OF SIMPLIFICATION

In any field of analysis, one of the main concerns of the analyst is to determine to what degree of complexity or completeness he must commit himself in performing the analysis so that the solution obtained is significant and sufficiently accurate to satisfy the purpose for which it was intended. In the field of automatic control, this problem manifests itself in the form of determining the most suitable equations of motion (or transfer functions, if the problem may be linearized) for description of the "forward path", i.e., the plant or process being controlled. Present-day control theory, in combination with modern computer facilities, is probably sufficient to give reasonable assurance that solutions to the control problem may always be obtained, provided the proper mathematical model of the controlled process can be written.

From a practical as well as a philosophical viewpoint, it is desirable to determine and possess the simplest equations of motion or transfer functions that will yield sufficiently accurate results, keeping in mind the purpose of the analysis. As a consequence of having a suitably simplified analysis, good results may be obtained with the most efficient use of time and money. The simpler transfer functions will permit illumination of the most significant features of the problem; they will allow application of powerful analytic tools thereby providing great insight to the nature of the problem; they will obviate the necessity for massive computer simulations within which the heart of the problem is often buried from sight.

In this section a group of simplified approximate transfer functions for the large ballistic booster are given. These transfer functions have a limited range of applicability. The limitations are well defined since each transfer function is tailored to permit investigation of certain specific flexible booster/autopilot control problems by the least elaborate of analytic methods. In every case these simplified transfer functions may be viewed as being extractions from the general system equations of motion given in Section 3. The basis for this extraction is now discussed.

4.2 BASES OF SIMPLIFICATION

Since the primary application of the simplified or approximate transfer functions will be in performing stability analyses of the elastic booster with autopilot control, it is natural that the basis of simplification be established with stability analysis criteria. It is necessary, however, to keep in mind also that these same approximate transfer functions should, if possible, be useful for load analyses and other system studies wherein the time-domain response of the system is most important. For these reasons, it is felt that the suitability of approximate transfer functions can best be judged relative to behavior of the complex roots of the Laplace variable, (s). Effects of approximations on these roots can, in turn, be judged most effectively from the graphic interpretations possible in root-locus plotting methods.

Hence, while many alternate interpretations of the approximations may be made in the frequency realm (Bode plots, Nyquist diagrams), these will rarely be employed here; then only insofar as they lead to a convenient way of cataloging some effects.

Judgments as to the efficacy of a particular approximation are very difficult to arrive at in a truly objective manner - they are almost certain to be colored by the user's own experience. To this degree the approximate transfer functions given in this section represent a distillation of the authors' experience. In addition, however, certain objective measures of these equations' suitability can be applied. These measures will be discussed in each area, along with other approximations made, since they will provide the reader with an appreciation of the range of applicability of the equations as well as with some techniques which may prove useful in evaluating new approximations for the unforeseeably strange vehicle configurations of the future.

Approximations may be placed in one of the following two categories:

a.   The relative size of coefficients of the same order of (s) in a transfer function (secondary effects) is considered.

b.   The importance of terms of different orders of (s) (higher or lower) are studied. These terms usually represent other modes or physical effects associated with certain regions of the frequency spectrum.

In every case the criteria for evaluating these two classes of approximations may be interpreted from their significance in affecting the modes' complex roots and, hence, their stability and time-domain behavior.

4.2.1 Neglect of Secondary Effects. Terms deleted from the equations of motion, as under a. above, have the effect of representing either small changes in the loop gain of the system or small shifts in the position of the open-loop poles or zeros and hence of the phase of the system. Here the importance of such a term is readily weighed relative to the effect it has on the position of the closed loop roots. Very often such a comparison may be made solely on the question of the size of such a term in comparison with the uncertainties in the values of the larger, dominant parameters, i.e., the accuracy with which it is expected other parameters in the system will be known or controlled.

As an example, the angular-velocity-dependent aerodynamic damping term is usually omitted in studying rigid-body pitch axis stability of nonwinged ballistic boosters.* One way in which this term might be evaluated is to observe its role in the rigid-missile transfer function, θ/δ. If incorporated, the transfer function becomes

$$\theta/\delta = \mu_\delta \; \frac{1}{s^2 + M_{\dot\theta}/I \; s - \mu_\alpha} \quad \text{(cf. Equation 2-4 of Section 2, from which the notations are borrowed).} \quad \text{The result-}$$

ing shift in the two real poles (at approximately $\pm \sqrt{\mu_\alpha}$), due to inclusion of the damping term, is negligible as it affects the closed loop root for the class of boosters considered. The situation is depicted graphically by the root locus plot of Figure 4-1.
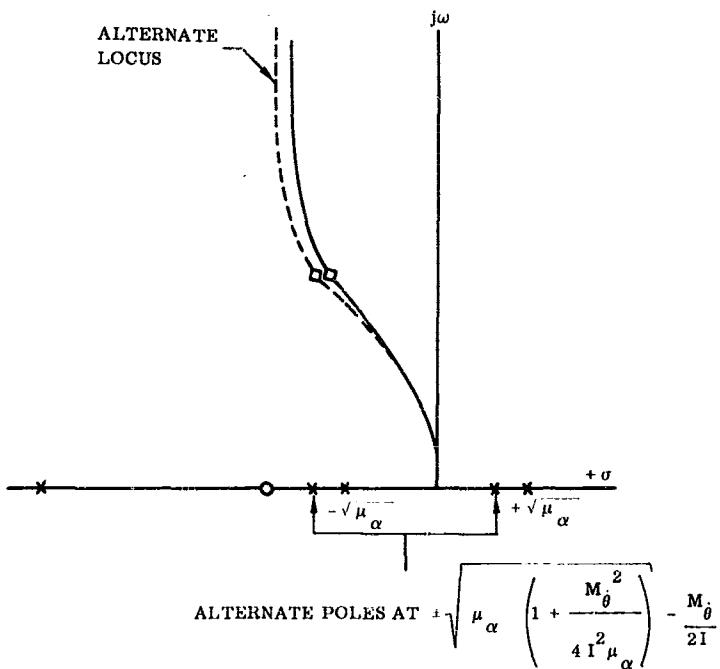
Figure 4-1. Effect of Aerodynamic Damping on Rigid-Body Locus

---

* In Equation 3-12 this term appears as $P \; \underset{n}{\Sigma} \; (C_N/\alpha)_{xn} \; \dfrac{\left[\phi_{xn}^{(2)}\right]^2 \; \dot{q}_2}{V}$ and would be written more commonly

as $\dfrac{P}{V} \; \left(\underset{n}{\Sigma} \; (C_N/\alpha)_{xn} \; x_n^2 \; \right) \dot\theta \; = \; M_{\dot\theta} \; \dot\theta.$

Alternately, one could observe the effect of incorporation of this term on the closed-loop characteristic equation of the system (cf. Equation 2-5). This aerodynamic damping term, if added, would appear in two coefficients of powers of (s) also containing velocity gain constants of the autopilot; in magnitude it would be but a few percent or less of these coefficients. Physically, the aerodynamic damping of unwinged vehicle oscillations is negligible compared to that introduced by velocity-dependent elements of the control system. It is not necessary to incorporate these minor terms of the system equations when the autopilot gain constants, which determine the major effects, are not themselves controlled to within comparable absolute accuracies.

There exists, however, a complementary example to the one just cited, viz., a comparison of the relative contribution of this same velocity-dependent aerodynamic damping to the damping of a body bending elastic mode coupled through the autopilot.* Here, system damping from structural dissipation is extremely low and hence the aerodynamic damping, which yields a damping contribution of comparable magnitude at certain flight times, becomes too important to neglect. This situation may also be analyzed through the relative importance of a small shift in the open-loop pole of the bending mode which this aerodynamic damping term accomplishes. While the effect on closed-loop roots of small shift in the open loop pole for the rigid-body mode may be negligible (as noted earlier), it can be of critical importance for the elastic mode roots. Many of these modes will be gain-stabilized, i.e., their loci will depart from the open loop pole, heading towards the $j\omega$ axis (and the right half of the complex plane). Whether or not the closed loop root is stable depends upon the loop gain (how far the root departs from the pole) and upon the distance the pole is away from the $j\omega$ axis. This, in turn, is dependent upon modal damping. The situation is depicted graphically in Figure 4-2. It should be apparent that a conservative analysis can always be made omitting this aerodynamic damping.
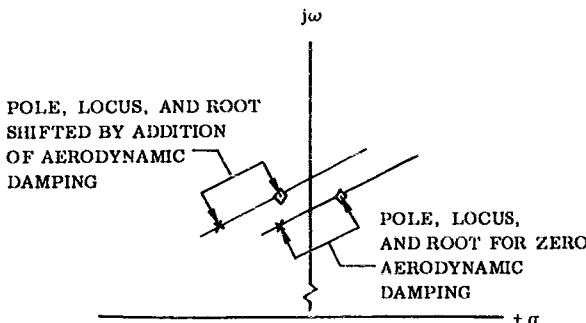
Figure 4-2. Effect of Aerodynamic Damping on Body Bending Mode Roots

From the foregoing one sees that the approximations just discussed have as their bases certain characteristics associated with the vehicle class under study. However, their validity is readily re-evaluated on the same bases for any vehicle of strikingly different characteristics.

4.2.2 **Terms of Different Orders of (s)**. There exist a variety of ways in which terms of different orders of (s) appear in a problem. A few of these are as follows:

a. Added degrees of freedom representing other modes of the controlled vehicle,

b. inertial effects added to a system to account for their presumed importance in a problem, and

c. high frequency characteristics of various system elements.

---

* In Equation 3-12 this term appears as $\dfrac{P}{V} \sum\limits_{n} (C_n/\alpha)_{xn} \left[\phi^{(i)}_{xn} \right]^2 \dot{q}_i.$

Because of the varied nature of these effects, it is more difficult to make generalizations as to their assessment. A useful point of view, however, is alluded to in the above listing, viz., taking the position of evaluating terms as additions to a given system of simplified equations. This of course is the inverse of the problem posed by Equations 3-12, where a very general set of equations is presented from which the desired approximations are to be synthesized. The situation in many ways is analogous to the classical synthesis-analysis cycle of design and, hence, should not appear foreign to the practicing engineer.

If this last viewpoint is adopted, a number of useful indications of treatments of "higher order terms" may be had from the following considerations.

An added degree of freedom may be evaluated, relative to its effects in the root-locus plot. If it is a mode of the system (almost invariably the case), it will appear as a group of pole-zero dipoles and, depending upon the strength of its coupling with the other modes (through the elastic, inertial, or generalized forces), will produce some shifting of the other mode's open loop poles and zeros. Hence, two measures of the effect of an added mode on other modes present themselves: 1) its effect in shifting the "existing" open loop poles and zeros and, 2) the effect of its dipole(s) as seen from the area of the closed loop roots of the former system. Naturally, this added mode must itself be analyzed for its own stability, but this is a separate problem.

As an example of the foregoing one may cite the coupling between rigid-body plunging and pitching modes brought about by aerodynamics. When studying pitch attitude stability (θ/δ), the plunging mode coupling manifests itself as a small dipole at the origin and as minor shifts in the pitch mode poles (cf. Equation 2-2). Its effect on the pitch mode closed loop root is therefore minor (see Figure 4-3).
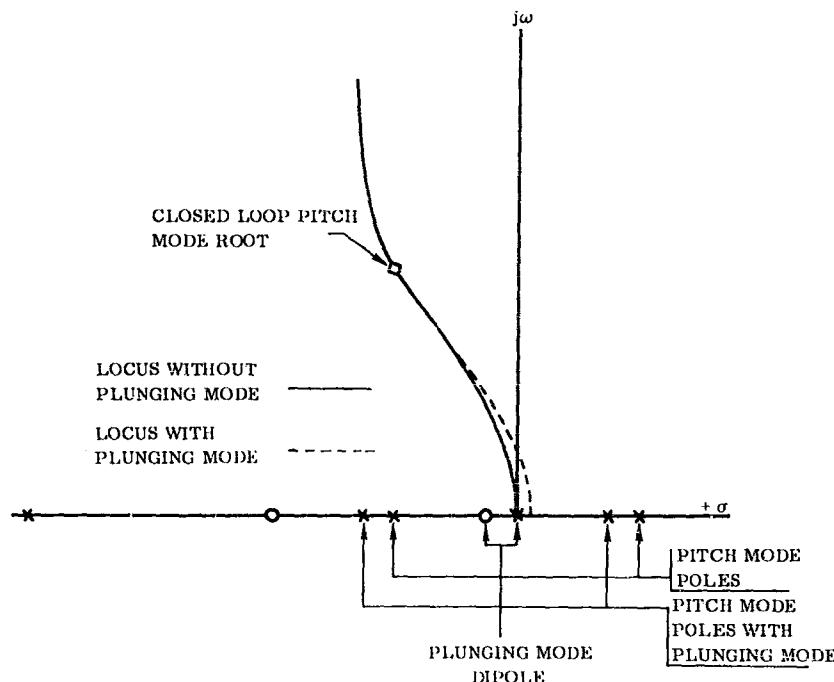
Figure 4-3. Effect of Coupling of Rigid Body Plunging Mode with Rigid Body Pitching Mode

Another example is the effect of a body bending mode on rigid-body pitching stability. Coupling occurs through the autopilot (significant) and through aerodynamics (minor). The added mode produces a conjugate pair of dipoles (cf. Equation 2-11) and appears as shown in Figure 4-4. As may be seen there, the effect on the rigid-body pitching mode phase and gain is negligible.

GAIN CHANGE TO RIGID BODY
MODE DUE TO BENDING IS
THE RATIO:

$$\frac{r_1 r_1'}{r_2 r_2'}$$
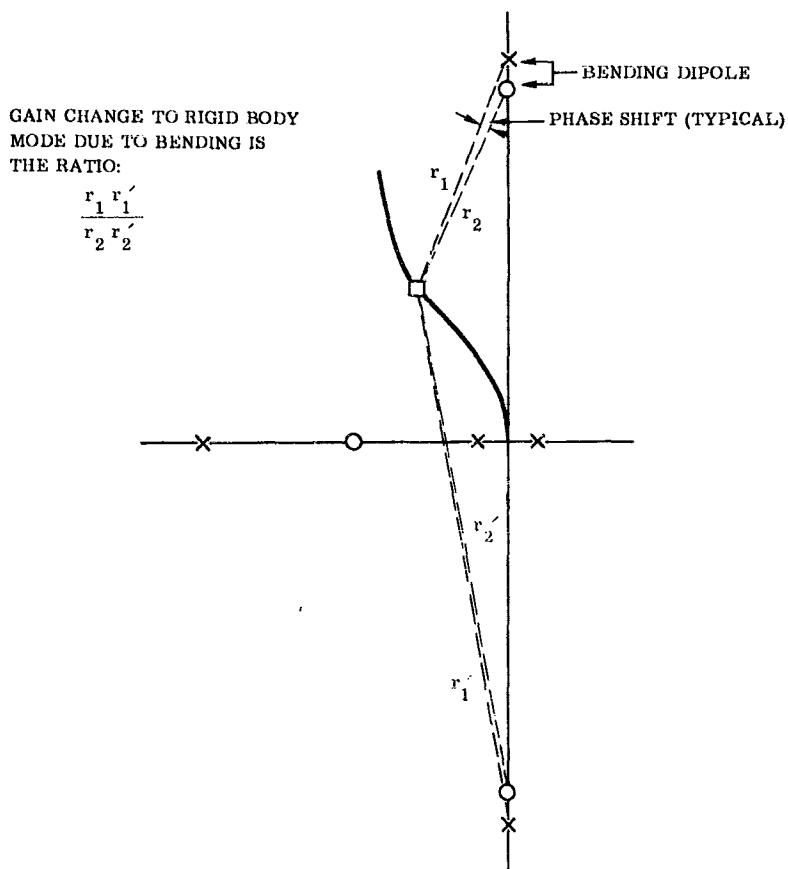
Figure 4-4. Effect of a Bending Mode Dipole on the Rigid Body Mode

Inertial effects are added to the equations because of their presumed importance in a frequency region to be studied. Depending upon where these effects are added in the equations, they may simply modify existing coefficients (e.g., the inclusion of aerodynamic inertial terms would only serve to modify the body inertial coefficients), or they may add new open loop elements (e.g., the "tail-wags-dog zero", TWD, which appears when rocket engine inertias are included in the rocket control force term; cf. Subsection 2.2.8). These new added loop elements will always appear in conjugate pairs. Their effect on phase shift and gain of an "existing mode" is readily evaluated from the root locus plot. Figure 4-5 shows the graphic interpretation of the effect of the TWD zeros on the rigid-body pitching mode's closed loop roots.

As it is obvious that the effect of the TWD zero on the rigid-body mode is minor in this case, so too is it clear that the effect will be of paramount importance for body bending modes in the range of the TWD zero's frequency or above. Thus, for body bending studies this effect becomes a dominant factor, and certain other low frequency effects (e.g., the precise position of the rigid body pitching mode poles) become less significant.

Higher frequency characteristics of elements in the system may be evaluated readily from the poles and zeros introduced by them to the root locus plot. Such effects as roll-off characteristics of the servo positioning system, the sensors (gyros and platform), the amplifiers or any other elements in the control loop appear as real or complex poles and zeros. Their influence on the stability of a mode being analyzed is quickly gaged from their contribution to phase and gain changes in the vicinity of the complex plane where the mode of interest lies.
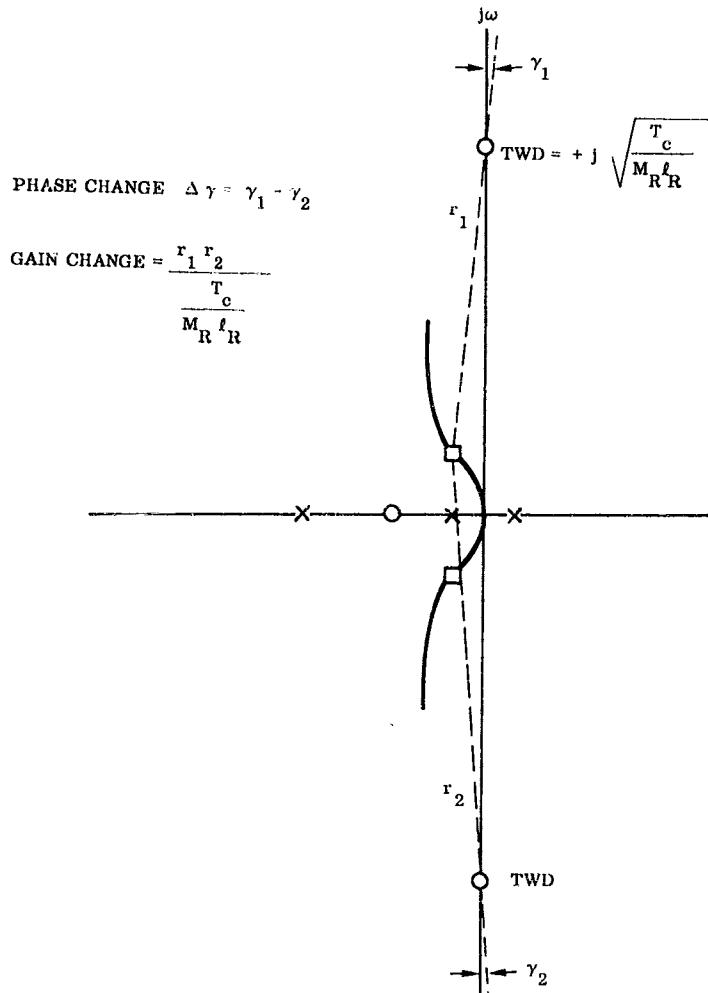
Figure 4-5. Effect of Engine TWD Zeros on Rigid Body Pitching Mode

4.2.3 Effects of Flight Environment and Configuration Changes. From the foregoing discussions it is clear that simplifications and approximations cannot be made categorically without due consideration of the great variations in system characteristics (and hence parameters) which occur over the course of a flight. Thus, an approximation which neglects the effects of propellant sloshing modes on rigid-body control modes at liftoff (a good approximation) may be invalid near burnout of a booster stage, simply because the change in system parameters has greatly increased the coupling between these modes. Hence, any approximations given must be tempered with these considerations.

In the remainder of this section various approximate transfer functions are given which have been found of practical value in the analysis of elastic ballistic boosters. These transfer functions may be looked upon as simplifications of the general equations of Section 3 and elsewhere. Comments as to the nature of the approximations made in arriving at these equations are given, along with expected areas of applicability of each. The transfer functions are also illustrated, where appropriate, by control system block diagrams and by root locus plots.

4.3 SIMPLIFICATION OF THE GENERAL EQUATIONS OF A FLEXIBLE BOOSTER VEHICLE.

The preceding subsection illustrated how several particular effects, when considered as additions to simple transfer functions, could be easily evaluated as to their importance. In this Subsection the general plane motion equations for a flexible booster vehicle (see Section 3) are simplified for use in the stability analysis of closed loop bending autopilot coupling. Thus, the methods of simplification will be based upon the possibility of omitting terms or classes of terms from the equation.* These methods are, in general, based upon considerations discussed earlier in this section.

Prior to simplification and approximation certain facets of the problem must be noted. These considerations have to do with the type of modes that are to be used in the study. The three classes of modes (cf. Section 3) are: 1) normal modes, 2) artificially uncoupled modes, and 3) assumed arbitrary shapes. Of the three classes of modes only the first two are considered in this report. The equations to follow are for modes of the artificially uncoupled type, in that the sloshing propellants are not included in the mode calculation. If these propellants are included in the modes then the equations are modified by omitting all sloshing terms (see Section 3).

In the calculation of system bending modes the flexibility of the rocket engine actuation linkage may be either accounted for in the modal calculations, or the linkage may be represented as a rigid link. In the latter case the flexibility of the linkage is included in the engine servo mechanism, itself. This is the approach followed in deriving the engine servo equations of Appendix B4.2. The flexibilities are incorporated therein as a mounting spring of stiffness, K_m, and a finite hydraulic fluid bulk modulus, B. This model leads to the more complex engine servo equations. When the modal solutions do not include the actuation flexibility of the rocket engines, the modal slope on the missile structure side of the rocket engine gimbal block, σ_{xT}, is equal to the modal slope on the rocket engine side, σ_{xe}. Therefore, the difference expression, $\sigma_{xe}^{(i)} - \sigma_{xT}^{(i)}$, is equal to zero, making all terms containing this difference expression also equal to zero (cf. Equation 3-12). In this case

$$\delta_k \equiv \delta_k' .$$

When, on the other hand, the actuation system flexibility is included in the modal calculations, the servo loop equations are computed with infinite rigidities: $K_m \to \infty$, $B \to \infty$. Some simplification of the servo loop transfer function results. In the following discussion the actuation linkage flexibilities will be assumed accounted for in the calculations:

$$\hat{\delta}_k \qquad \delta_k' - \sum_i^n (\sigma_{xe}^{(i)} - \sigma_{xT}^{(i)}) \, q_i .$$

With this approach one of the normal vehicle body modes will be primarily that associated with the resonance of the engine chamber, elastically mounted from the vehicle. This mode will be referred to as the "engine-body" normal mode, since it is of particular significance.

4.3.1 Simplification of Dependent Variable Coefficients.
The first step in simplifying the equations of motion may be accomplished by an analysis of the various terms comprising the total coefficient of the dependent variable, viz., the elastic normal coordinate, q_i. This simplification amounts to neglect of secondary effects. The modal equation of motion (cf. Equation 3-12) is rewritten here in transformed form.

$$\left[\mathcal{M}_i \, s^2 + \left(2 \zeta_i \, \omega_i \mathcal{M}_i + \sum_{k=1}^m \tilde{C}_{f_k} \left(\sigma_{xe}^{(i)} - \sigma_{xT}^{(i)} \right)_k^2 + \frac{P}{V} \sum_n (C_N/\alpha)_{xn} \, \phi_{xn}^{(i)2} \right) s + \right.$$

$$\left. \left(\omega_i^2 \mathcal{M}_i - \sum_{k=1}^m T_k \, \phi_{xT_k}^{(i)} \left(\sigma_{xe_k}^{(i)} - \sigma_{xT_k}^{(i)} \right) - P \sum_n (C_N/\alpha)_{xn} \, \phi_{xn}^{(i)} \, \sigma_{xn}^{(i)} \right] q_i =$$

* Certain observations will be made throughout this section concerning the evaluation of terms, with regard to the usual range of magnitude of the various terms. These observations are based upon analysis of several (proposed) large space booster configurations as well as experience with present-day space booster and ICBM configurations. However, it must be realized that these observations cannot apply to all possible configurations: but that the dependency upon modal frequencies, displacements, slopes, generalized masses, and generalized forces may alter these observations.

$$= - \sum_{\substack{j=1 \\ (j \neq i)}}^{r-1} \left[\left(\sum_{k=1}^{m} \bar{C}_{f_k} \left(\sigma_{xo_k}^{(i)} - \sigma_{xT_k}^{(i)} \right) \left(\sigma_{xo_k}^{(j)} - \sigma_{xT_k}^{(j)} \right) + \frac{P}{V} \sum_{n} (C_N/\alpha)_{xn} \phi_{xn}^{(i)} \phi_{xn}^{(j)} \right) s - \right.$$

$$\left. \left(\sum_{k=1}^{m} T_k \phi_{xT_k}^{(i)} \left(\sigma_{xo}^{(j)} - \sigma_{xT}^{(j)} \right) + P \sum_{n} \left(C_N/\alpha \right)_{xn} \phi_{xn}^{(i)} \sigma_{xn}^{(j)} \right) \right] q_j -$$

$$\sum_{k=1}^{m} \left[\left(M_{r_k} \ell_{r_k} \phi_{xo_k}^{(i)} - I_{o_k} \sigma_{xo_k}^{(i)} \right) s^2 - \bar{C}_{f_k} \left(\sigma_{xo_k}^{(i)} - \sigma_{xT_k}^{(i)} \right) s + T_k \phi_{xT_k}^{(i)} \right] \dot{\delta}_k' -$$

$$\sum_{\ell=1}^{s} \left[M_{c_\ell} \sigma_{x_{\ell_B}}^{(i)} s^2 + \left(K_\ell \phi_{x_\ell}^{(i)} + M_{1_\ell} \alpha_T \sigma_{x_{\ell_B}}^{(i)} \right) \right] Y_\ell \qquad (4\text{-}1)$$

In dealing with a second order system such as the ith mode, it is helpful to think of the first order term of that variable, $s q_i$, as the modal damping term and the zero-order term, q_i, as the modal frequency term. One can then separate the various contributions to the coefficients into components affecting damping and those affecting frequency.

4.3.1.1 Modal Damping Term, $s q_i$. The total coefficient of the $s q_i$-term is composed of: (1) the structural damping term, $2\zeta_i \omega_i$, (2) the aerodynamic damping term, $\frac{P}{V} \sum_{n} (C_N/\alpha)_{xn} \phi_{xn}^{(i)^2}$, and (3) the damping term

due the engine gimbal friction, $\sum_{k} \bar{C}_{f_k} \left(\sigma_{xo}^{(i)} - \sigma_{xT}^{(i)} \right)_k^2$. This coefficient will hereafter be denoted as, $2\zeta_i' \omega_i'$, the effective modal damping.

$$2\zeta_i' \omega_i' = 2\zeta_i \omega_i + \frac{1}{\mathfrak{m}_i} \sum_{k=1}^{m} \bar{C}_{f_k} \left(\sigma_{xo}^{(i)} - \sigma_{xT}^{(i)} \right)_k^2 + \frac{P}{\mathfrak{m}_i V} \sum_{n} (C_N/\alpha)_{xn} \phi_{xn}^{(i)^2} . \qquad (4\text{-}2)$$

For the various elastic modes the $2\zeta_i \omega_i$ term is limited to a relatively small range, as the damping factors ζ_i are found to be between 0.0025 and 0.02 (see Sections 2 and 6).

The second term, that due to engine gimbal friction, $\sum_{k=1}^{m} \bar{C}_{f_k} \left(\sigma_{xo}^{(i)} - \sigma_{xT}^{(i)} \right)_k^2$, can take on a variety of values. For an engine in the 150,000-pound thrust class normal friction levels for gimbals with sleeve bearings are 500 lb-ft-coulomb friction and 2000 lb-ft/rad/sec viscous friction. Depending upon the value of $\sigma_{xo}^{(i)} - \sigma_{xT}^{(i)}$, this damping term may vary from less than $2\zeta_i \omega_i$ for the lower body bending modes to a much greater value for the higher bending modes. For an engine-body mode this term may be the dominant damping term, reaching eight to ten percent of critical damping. It should also be noted that since the friction coefficient $\bar{C}_{f_k}$ is a linearized value representing both viscous and coulomb friction, the effect of this term will vary with frequency and amplitude of engine motion; i.e., this term will increase in importance as amplitude decreases. This term does not appear in the rigid-body modes nor in modes computed with a rigid-engine position-servo linkage, since $\sigma_{xo} - \sigma_{xT}$ is zero in each case.

In regions of high dynamic pressure the aerodynamic damping term, $\frac{P}{V} \sum_{n} (C_N/\alpha)_{xn} \phi_{xn}^{(i)^2}$, for most classes of unwinged flexible boosters is usually of the same order of magnitude as the structural damping term. As the aerodynamic damping coefficient is directly proportional to P/V, its effect is usually important only during the time of high dynamic pressure and can be ignored during the other flight times. Its omission is conservative. A damping term also exists due to aerodynamic coupling between the modes. This term is small compared to the primary aerodynamic damping term, so is universally omitted.

The effect of the aerodynamic damping on the rigid-body pitching and plunging modes is likewise negligible and may be omitted for most vehicles of the class considered.

Although it is conservative to omit both the gimbal friction and aerodynamic damping terms, it is recommended that all three of the terms comprising $2\zeta_i' \omega_i'$ be retained (except for expediency when simple hand solutions are being used) for more accurate stability analysis and transient responses of the system.

4.3.1.2 Natural Frequency Term q_i. The total coefficient of the q_i term, designated as $\omega_i'^2$, is analogous to the natural frequency of a second order harmonic oscillator:

$$\omega_i'^2 = \omega_i^2 - \frac{1}{\mathcal{M}_i} \sum_{k=1}^{m} T_k \, \phi_{xT_k}^{(i)} \left(\sigma_{xe}^{(i)} - \sigma_{xT}^{(i)} \right)_k - \frac{P}{\mathcal{M}_i} \sum_n (C_N/\alpha)_{xn} \, \phi_{xn}^{(i)} \, \sigma_{xn}^{(i)} . \qquad (4\text{-}3)$$

The class of vehicles considered are: 1) those having relatively constant cross section over their length, 2) those with no major aerodynamic surfaces (wings, fins, etc.), and 3) those controlled by means of a gimbaled thrust-vector located at the base of the missile. For this class of vehicles the aerodynamic forces, due to an elastic modal deflection, q_i, are low relative to the elastic forces. From another point of view, the modal divergence speed (at which $\omega_i \longrightarrow 0$) is very high. The thrust term is likewise very small in its effect on frequency. Thus, when considering the elastic modes of the class of vehicles under study, these two terms are usually much less than the modal frequency term, ω_i^2. Only with the very slender boosters, or with boosters having lifting surfaces will the aerodynamic term become significant. However, this aerodynamic term is important in the rigid-body modes.

4.3.2 Simplification of Forcing Functions. The next, and more difficult, step in simplifying Equation 4-1 is an evaluation of the various forcing functions which represent excitations of a given mode. The excitations appear in several guises:

a. The orthongonal body modes are coupled directly through the action of such nonconservative forces as aero-dynamic, bearing friction, and propulsive.*

b. The artificially uncoupled sloshing modes exhibit inertial coupling with the normal body modes.

c. Regenerative and coupled excitations occur through the autopilot in modes whose motion is detected by an autopilot sensor; these modes may, in turn, be excited directly by control forces.

d. Indirect coupling may occur through the autopilot in two classes:

1) Modes whose motion is detected by certain of the control sensors, but upon which the control forces cannot act directly; e.g., if propellant sloshing were detected by a sensor placed in a tank for that purpose the resultant signal could command control forces, but these forces could not act directly on the propellant modes.

2) Modes whose motion is not detected by the control sensors but upon which modes the control force does act directly, e.g., the rigid-body plunging in an attitude-only control system.

The above types of coupling might be categorized as "open-loop" (a. and b.) and "closed-loop" (c. and d.).

4.3.2.1 Direct Modal Coupling Terms Between Normal Modes (Open Loop Coupling). Direct modal coupling between normal body modes occurs through the nonconservative forces. Figure 4-6 is a block diagram illustrating the couplings between two of the normal body modes. The direct modal coupling appears (for example) as a feedback path around the ith mode of:

$$\frac{\partial Q_j}{\partial q_i} \cdot \frac{\partial q_j}{\partial Q_j} \cdot \frac{\partial Q_i}{\partial q_j} .$$

The general effect of this coupling is to produce a shift in the position of the open-loop poles of the ith mode. Experience dictates that the portion of this shift due to aerodynamics is minor for these normal body modes (as one might expect), since the "aerodynamic gains" in the loop (the $P (C_N/\alpha)_{xn} \, \sigma_{xn}^{(j)}$ and $\frac{P}{V} (C_N/\alpha)_{xn} \, \phi^{(j)}$ terms) are both very low. Consequently, the jth mode forcing function coefficients are usually omitted in writing a simplified i^{th} mode transfer function. The exception could be for the vehicle carrying lifting surfaces near the

---

* The individual mode's regenerative excitations by these nonconservative forces were treated as part of the normal coordinate's coefficients in Subsection 4.3.1.
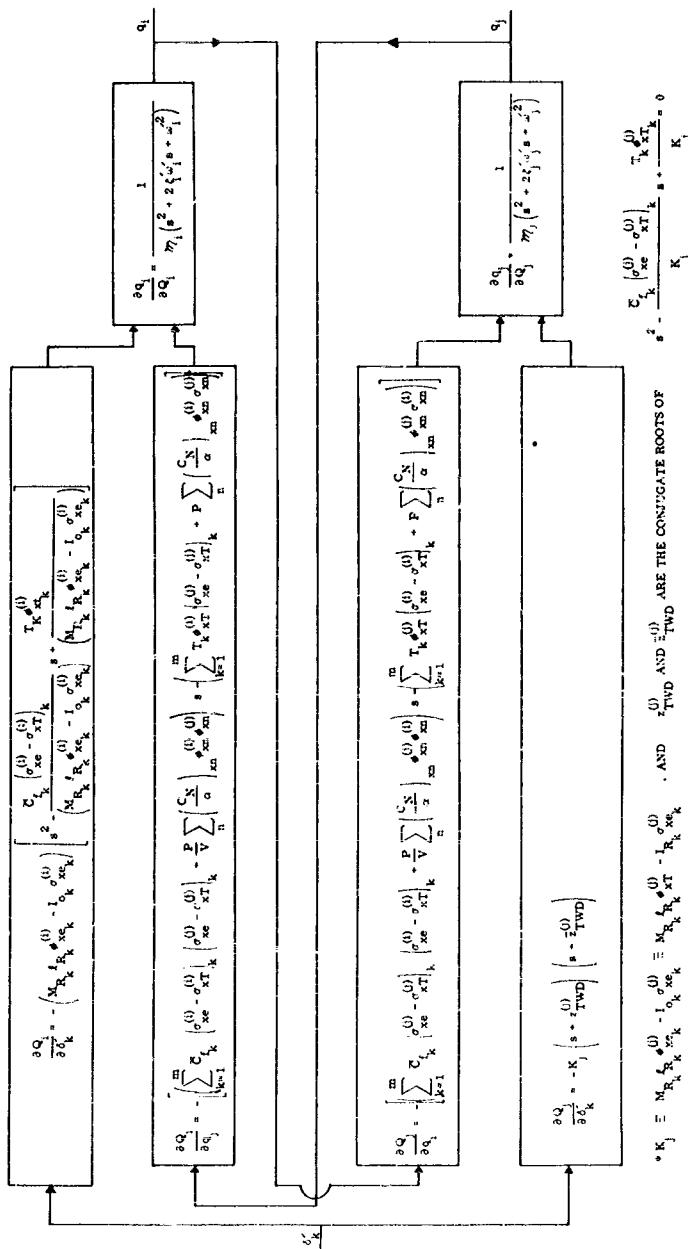
Figure 4-6. Direct Modal Coupling Block Diagram

times of maximum dynamic pressure. This problem then becomes that of the aeroelastician, where, for sufficiently high q, the system roots (open loop poles) can move onto the $j\omega$ axis. Because of its minor role and/or specialized nature (derivation of the mathematical model for the unsteady aerodynamic forces on the lifting surface is certain to be a highly specialized problem), no further treatment of this type of open loop coupling is made herein.

The other open-loop coupling terms are either:

a. Nonexistent (the case where the servo mount elastic compliance is not incorporated into the modal calculations so that, $\sigma_{xe}^{(i)} - \sigma_{xT}^{(i)} \equiv 0$, in which case the coupling will still appear but in a different form (see Subsection 4.3.2.5), or

b. Dependent upon the gain, $\sigma_{xe}^{(i)} - \sigma_{xT}^{(i)}$, through which the thrust vector and bearing friction forces act. For most body modes these terms are low, since their frequency separation from the engine-body mode (present when servo mount compliance is incorporated in the modes) is great enough that this relative motion is not greatly excited.* The obvious exception then may occur in the case of coupled motions between an engine-body mode and a body mode. If these modes are at all close in frequency (a distinct possibility since the engine-body mode frequency is relatively constant throughout flight, see Appendix A4 for an example of almost coincident modal frequencies), then significant coupling can occur. This being an "open-loop" effect, one can expect this coupling to appear for both active (commanded) and passive (noncommanded) engines. The effect manifests itself as a shift in the open-loop poles for the body mode being studied.

The effect is greatest, of course, if the two modes have nearly coincident frequencies and may be either beneficial (stabilizing) or harmful (destabilizing) to the body mode being studied. The effect is discussed further in Section 5 and in Appendix C5.

Occasionally, then, a case may arise where it is desired to test for the adequacy of this simplification. For this purpose the following test may be employed.

First, it is noted that the simplified transfer functions arrived at during the course of this study are intended to be used both for stability analysis and time-domain response. In both of these analyses the behavior of a lightly damped, elastic mode is greatly affected by a small lateral shift in its open-loop poles due to a phase shift. A small change in the gain will not significantly affect the damping (real part) of the closed-loop root as it will only modify the frequency (imaginary part) of the root. This effect is much less serious. Therefore, the test will be conservative if it is assumed that the root locus departs directly toward the $j-\omega$ axis from the open-loop pole. By assuming that the closed-loop root is approximately on the $j-\omega$ axis (a zero real part), the numerical value for the natural frequency may be substituted for the Laplace variable ($\sigma + j\omega$), and the contribution of the auxiliary path or feedback loop may be evaluated.

The transmission around the ith mode representing j^{th} mode coupling is:

$$\left(\frac{\partial q_i}{\partial Q_i}\right)\left(\frac{\partial Q_i}{\partial q_j}\right)\left(\frac{\partial q_j}{\partial Q_j}\right)\left(\frac{\partial Q_j}{\partial q_i}\right)\frac{\left[\partial Q_i/\partial q_j\right]}{\mathcal{M}_i(s^2 + 2\zeta_i\omega_i s + \omega_i'^2)} \times \frac{\left[\partial Q_j/\partial q_i\right]}{\mathcal{M}_j(s^2 + 2\zeta_j\omega_j s + \omega_j'^2)}. \quad (4\text{-}4)$$

Evaluating at $s = j\omega$ we obtain the following expression for the magnitude of the signal in this path:

$$|M| = \left[\left(\sum_{k=1}^{\bar{m}} \bar{C}_{f_k}\left(\sigma_{xe}^{(i)} - \sigma_{xT}^{(i)}\right)_k\left(\sigma_{xe}^{(j)} - \sigma_{xT}^{(j)}\right)_k + \frac{p}{V}\sum_n (C_N/\alpha)_{xn}\phi_{xn}^{(i)}\phi_{xn}^{(j)}\right)^2\omega_i^2 + \right.$$

$$\left.\left(\sum_{k=1}^m T_k \phi_{xT_k}^{(i)}\left(\sigma_{xe}^{(j)} - \sigma_{xT}^{(j)}\right)_k + P\sum_n (C_N/\alpha)_{xn}\phi_{xn}^{(i)}\sigma_{xn}^{(j)}\right)^2\right]^{1/2} \times \quad (4\text{-}5)$$

*The response of the ith mode is nonharmonic in general. However, since these modes are lightly damped they are also highly tuned (selective) and the dominant signal strength is at their resonant frequencies.

$$\frac{\left[\left(\sum_{k=1}^{m} \widetilde{c}_{f_k}\left(\sigma_{x e}^{(j)} - \sigma_{x T}^{(j)}\right)_k \left(\sigma_{x e}^{(i)} - \sigma_{x T}^{(i)}\right)_k + \frac{P}{V}\sum_{n}(C_N/\alpha)_{xn} \phi_{xn}^{(i)} \phi_{xn}^{(j)}\right)^2 \omega_i^2 + \left(\sum_{k=1}^{m} T_k \phi_{x T_k}^{(j)}\left(\sigma_{x e}^{(i)} - \sigma_{x T}^{(i)}\right)_k + P\sum_{n}(C_N/\alpha)_{xn} \phi_{xn}^{(j)} \sigma_{xn}^{(i)}\right)^2\right]^{1/2}}{\mathscr{m}_i \mathscr{m}_j \left(2\zeta_i' \omega_i'^2\right)\left[\left(\omega_j'^2 - \omega_i'^2\right)^2 + \left(2\zeta_j' \omega_j' \omega_i'\right)^2\right]^{1/2}}$$

$$(4-5)$$

If this magnitude does not exceed a numerical value of 0.09, the maximum percentage error in the loop modal damping is less than 10 percent.

As an example, Figure 4-7 shows the $\left(\dfrac{\partial q_i}{\partial \delta'_k}\right)$ transfer function with the jth mode feedback loop around it:
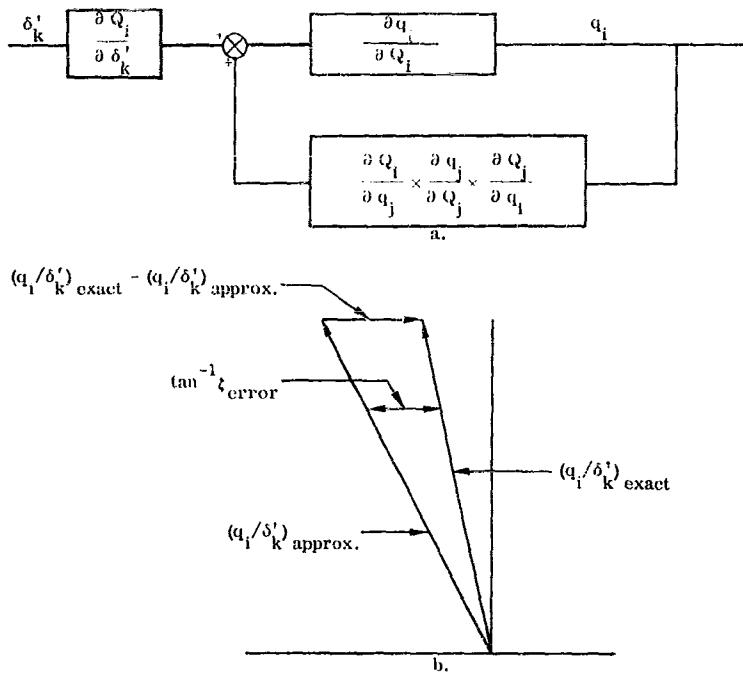
Figure 4-7. Evaluation of Direct Modal Coupling

$$\left(\frac{q_i}{\delta'_k}\right)_{\substack{\text{with } j^{th} \\ \text{mode} \\ \text{coupling}}} \left(\frac{q_i}{\delta'_k}\right)_{\substack{\text{without } j^{th} \\ \text{mode} \\ \text{coupling}}} \times \frac{1}{1 - \dfrac{\partial q_i}{\partial Q_i}\dfrac{\partial Q_i}{\partial q_j}\dfrac{\partial q_j}{\partial Q_j}\dfrac{\partial Q_j}{\partial q_i}}$$

$$(4-6)$$

or, if the percentage error in the approximation is defined as:

$$\frac{\left(\dfrac{q_i}{\delta'_k}\right)_{exact} - \left(\dfrac{q_i}{\delta'_k}\right)_{approx.}}{\left(\dfrac{q_i}{\delta'_k}\right)_{exact}} \quad , \tag{4-6a}$$

one finds this is identically equal to:

$$\frac{\partial q_i}{\partial Q_i} \cdot \frac{\partial Q_i}{\partial q_j} \cdot \frac{\partial q_i}{\partial Q_j} \cdot \frac{\partial Q_j}{\partial q_i} \quad .$$

Hence, the magnitude of this quantity, as computed in Equation 4-5 gives a percentage error measure.

Also, as seen in Figure 4-7, the ratio in Equation 4-6a is an upper-bound approximation to the error in the damping of the open loop pole. (Upper-bound because the error is greatest if the exact and approximate poles have the relationship shown in Figure 4-7). If no phase shift resulted, the ratio would give the gain change (less serious, as observed earlier). By the above means the significance of direct mode coupling may be evaluated.

4.3.2.2 <u>Auxiliary Path For Engine Forcing Function</u>. Referring to Figure 4-6, it is seen that the jth normal mode also affords an auxiliary path by which the control engine motion, δ'_k, can excite the ith normal mode. This path is:

$$\frac{\partial Q_j}{\partial \delta'_k} \cdot \frac{\partial q_j}{\partial Q_j} \cdot \frac{\partial Q_i}{\partial q_j} \quad .$$

As might be expected this is a comparatively weak path, for if the autopilot system is responding to motions of the ith mode (at frequency ω_i), then engine responses, δ'_k, through the auxiliary path are highly filtered by the jth mode. Hence, it is a good approximation to show the ith mode responding to the engine δ'_k only through the primary path, $\partial Q_i / \partial \delta'_k$.

Again, for completeness one may wish to apply a test to determine the relative importance of these paths (secondary to primary).

Thus (refer to Figure 4-6 for notations):

$$\frac{Secondary}{Primary} \quad \frac{\dfrac{\partial Q_j}{\partial \delta'_k} \dfrac{\partial q_j}{\partial Q_j} \dfrac{\partial Q_i}{\partial q_j}}{\dfrac{\partial Q_i}{\partial \delta'_k}} \quad = \quad \frac{K_j (s + z^j_{TWD})(s + \bar{z}^j_{TWD}) \dfrac{\partial Q_i}{\partial q_j}}{K_i (s + z^i_{TWD})(s + \bar{z}^i_{TWD}) \mathcal{M}_j (s^2 + 2\zeta'_j \omega'_j s + \omega'^2_j)}$$

$$\tag{4-7}$$

If this function is evaluated at $s = j\omega_i$, it may be used to gage both the percentage error in the loop gain and phase of the ith mode incurred by omitting this auxiliary path through the jth mode.

4.3.2.3 <u>Direct Modal Coupling Terms Between Artificially Uncoupled Modes (Open Loop Coupling)</u>.

A. <u>Body Modes and Propellant Modes</u>. The artificially uncoupled propellant sloshing modes are forced only by inertial coupling with the vehicle body modes (rigid and elastic). The coupling of these sloshing modes back into the vehicle, in turn, is displayed as a combination of inertial and elastic coupling.* No direct coupling through any other force system exists.

---

* The difference is only a matter of convenience and could be changed by rearranging the equations. No physical meaning should be attached to the terms "elastic and inertial" coupling as they may be shown to be mathematically interchangeable.

This coupling between modes in the "open-loop" equations of motion manifests itself as pairs of dipoles-one conjugate pair for each mode-in the transfer functions. For example, the transfer function for the ith normal body mode with a single sloshing tank coupled into it (other body modes omitted, as per previous discussion) is:

$$\frac{q_i}{\delta'_k} = \frac{1}{\mathscr{m}_i} \frac{\partial Q_i}{\partial \delta'_k} \left[\frac{s^2 + 2\zeta_\ell\, \omega_\ell\, s + \omega_\ell^2}{(s^2 + 2\zeta_i\, \omega_i s + \omega_i^2)(s^2 + 2\zeta_\ell\, \omega_\ell\, s + \omega_\ell^2) + \Delta} \right]$$

where (4-8)

$$\Delta = s^2 \frac{M_{1\ell}}{\mathscr{m}_i} \phi_{x_\ell}^{(i)} \left[\frac{M_c}{M_{1\ell}} \sigma_{x_{\ell_B}}^{(i)} s^2 + \omega_\ell^2\, \phi_{x_\ell}^{(i)} + \alpha_T\, \sigma_{x_{\ell_B}}^{(i)} \right] \,.$$

The denominator factors into two sets of conjugate poles, one near the uncoupled slosh mode poles. Figure 4-8 depicts the situation graphically.
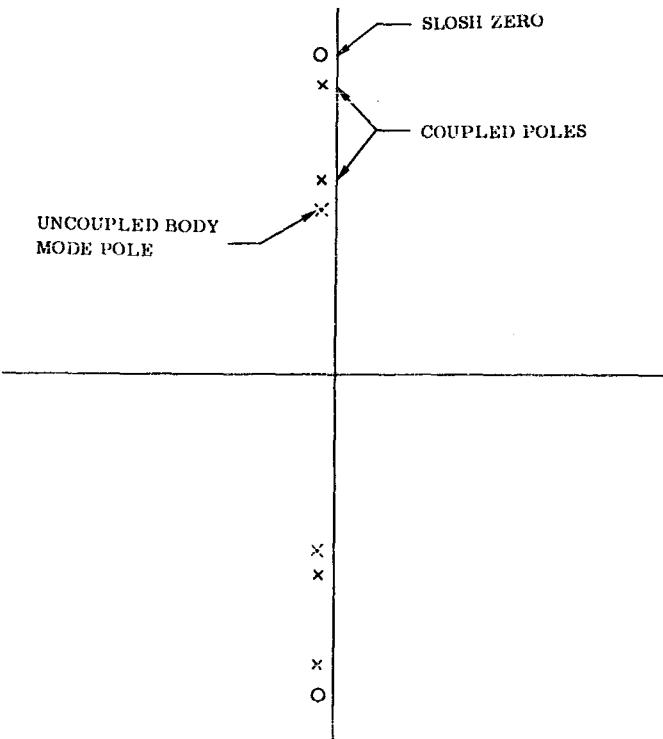
Figure 4-8. Poles and Zeros of q_i/δ'_k with and without a Slosh Mode

This same situation was encountered previously in Section 2 for a simple single tank slosh case. Therein the body mode considered was rigid-body pitching, $\omega_i = 0$, for which mode the poles are at the origin, where they remain even when sloshing coupling is added.

It is not possible to generalize too sweepingly on the efficacy of an approximation which omits a sloshing mode from a body-mode transfer function, or visa versa. However, it is clear on simple grounds that a wide frequency separation between the uncoupled modes would make such an approximation suitable. Also,

the body-mode amplitude at the sloshing mass station, $\phi_{x_\ell}^{(i)}$, is a good index. As seen in Equation 4-3, if this parameter has a zero value then the sloshing dipoles are nulled (pole on zero). Another parameter affecting the "strength" of the sloshing dipole (separation between pole and zero) is the mass ratio, $M_{1_\ell}/\mathcal{M}_i$.

As a general rule for body bending modes whose frequencies are several octaves above the slosh frequencies (a common situation), the sloshing may be omitted in writing simplified transfer functions. For the rigid-body pitching mode this same approximation is only partially satisfactory, since the closed-loop roots for this mode often approach a slosh frequency (see discussion below on closed-loop coupling).

Obviously, if the spring-centered sloshing masses have been included within the calculation of the body normal modes, this entire issue is obviated, there being no separate sloshing modes to couple in "open loop". In this case one passes immediately to the question of closed loop coupling between body modes (Subsection 4.3.2.5).

B. Body Modes and the Rocket Deflection Mode. The rocket engine deflection mode, δ' (or δ), is artificially uncoupled from the body modes and, hence, will exhibit inertial coupling as well as coupling due to the other nonconservative forces (propulsive and bearing friction).

If the positioning servo's elastic compliance has been incorporated into the body mode calculation, then δ' is the symbol for the rocket engine deflection mode, representing that portion of the total rocket motion, δ, due to action within the servo device itself. That portion of δ due to elastic compliance already appears in the orthogonal body modes; it produces an open-loop coupling due to the nonconservative forces and was discussed in Subsection 4.3.2.1. There remains, however, a further compliance within the servo system due to fluid leakage and parasitic pickup of the feedback transducer signal. It produces an open-loop coupling involving inertial forces as well as the nonconservative forces. Discussion of this coupling is given more fully in Subsection 4.3.2.5.

If the positioning servo's elastic compliance has not been incorporated into the body modes, then the complete rocket engine control motion (mode), δ, is artificially uncoupled from the body modes. In this case open loop coupling between δ and the body modes involves inertial, propulsive, and bearing friction forces.

4.3.2.4 Coefficients of the Rocket Engine Forcing Function (δ_k). The major regenerative and coupled feedback paths occur through the control system in a ballistic booster. Because of their importance, a few remarks on the coefficients of the control forces which effect these excitations are appropriate at this point.

In a multi-engine installation all the rocket engines will deflect due to interaction of the inertial load torque, mount elasticity, leakage orifice flow, and the engine servo control valve flow. However, only the engine or engines being commanded by the autopilot are usually considered as gimbaling. This assumption is not a good one when the mode under investigation is an engine mount mode or is in the frequency range of an engine mount resonance of an uncommanded engine. In this case, the deflection δ_k of the uncommanded, "zeroed," engine may become sufficiently large to warrant the inclusion of that engine's forcing function in the overall transfer function. A means of accounting for the motion of the uncommanded engine, δ_k, when advisable, is discussed in Appendix C5.

A. Rocket Engine Inertia ($s^2 \delta_k'$ Term).

$$\left(M_{R_k} \ell_{R_k} \phi_{xc_k}^{(i)} - I_{o_k} \sigma_{xc_k}^{(i)} \right) \left(M_{R} \ell_{R} \phi_{xT_k}^{(i)} - I_{R_k} \sigma_{xc_k}^{(i)} \right)$$

The preceding terms constitute the force and moment necessary to gimbal the rocket engine relative to the ith mode. For most engine gimbal configurations these terms become important for the high frequency modes. The term may sometimes be omitted for rigid-body modes, and may also be omitted for several of the common thrust deflectors such as jetavators, jet vanes, etc. which have low gimbaled mass.

B. $s \delta_k'$ Term. This term is important even though it may be small. This is illustrated by the root locus (Figure 4-9). This force makes the sole contribution to the displacement of the TWD (tail-wags-dog) zero laterally from the imaginary ($j\omega$) axis. The roots of the elastic modes which are in the vicinity of the TWD

zero may exhibit an appreciable phase and gain error if the TWD zero is misplaced. Although this is an important effect, it is quite often omitted from the analysis. This omission is acceptable under some conditions, as this term is amplitude-dependent; i.e., the TWD zero will approach the imaginary axis as the amplitude of oscillation increases. Therefore, if a small limit cycle can be tolerated this term may be omitted.
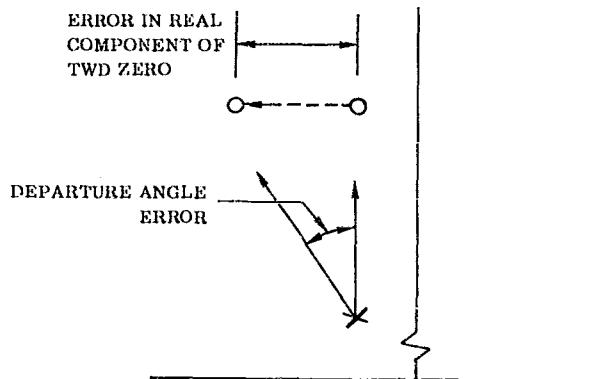
Figure 4-9. Effect of Velocity Dependent Term in TWD Zero

4.3 2.5 Coupled Excitations Through the Autopilot.

A. Coupled Bending Excitations. In this section it is assumed that previous tests have shown the direct open loop coupling between the orthogonal body modes to be small. Also, it will be assumed that suitable uncoupling exists between the body bending modes and sloshing modes such that their coupling may be omitted.*

If these simplifications are made, then Equation 3-12 reduces to:

$$
\mathscr{M}_i \left(s^2 + 2 \zeta_i' \omega_i' s + \omega_i'^2 \right) q_i \quad - \sum_{k=1}^{m} \left[\left(M_{R_k} \ell_{R_k} \phi_{xT_k}^{(i)} - I_{R_k} \sigma_{xe_k}^{(i)} \right) s^2 - \right.
$$

$$
\left. \bar{C}_{f_k} \left(\sigma_{xe}^{(i)} - \sigma_{xT}^{(i)} \right)_k s + T_k \phi_{xT_k}^{(i)} \right] \delta_k .
$$

(4-9)

For purposes of the analysis, it has been assumed here that the actuation linkage flexibility is included in the modal calculations; the following rocket engine equation of motion may be used (see Subsection 4.3.3 for derivations).

$$
\hat{\sigma}' \quad \frac{-K_E \left(\dfrac{\bar{C}_L}{\Lambda^2} - \dfrac{K_C}{K_H} \right) \sum\limits_{j=1}^{r} \left(\sigma_{xe}^{(j)} - \sigma_{xT}^{(j)} \right) q_j + K_c \delta_c}{(s + K_c)} .
$$

(4-10)

The control system for the elastic missile-autopilot system is depicted in Figure 4-10. This figure includes only two modes, q_1 and q_2. Additional modes would only complicate the picture at this time; they are of identical form. Also, only a single control rocket engine is assumed, representative of one or a cluster of similar engines.

---

* Alternately, one might presume that the spring-centered sloshing masses have been included in the elastic body mode calculations. In this case, this paragraph may be looked upon as treating the closed loop coupling between two of the higher frequency body bending modes; the next Subsection considers coupling of one high and one low frequency bending mode.
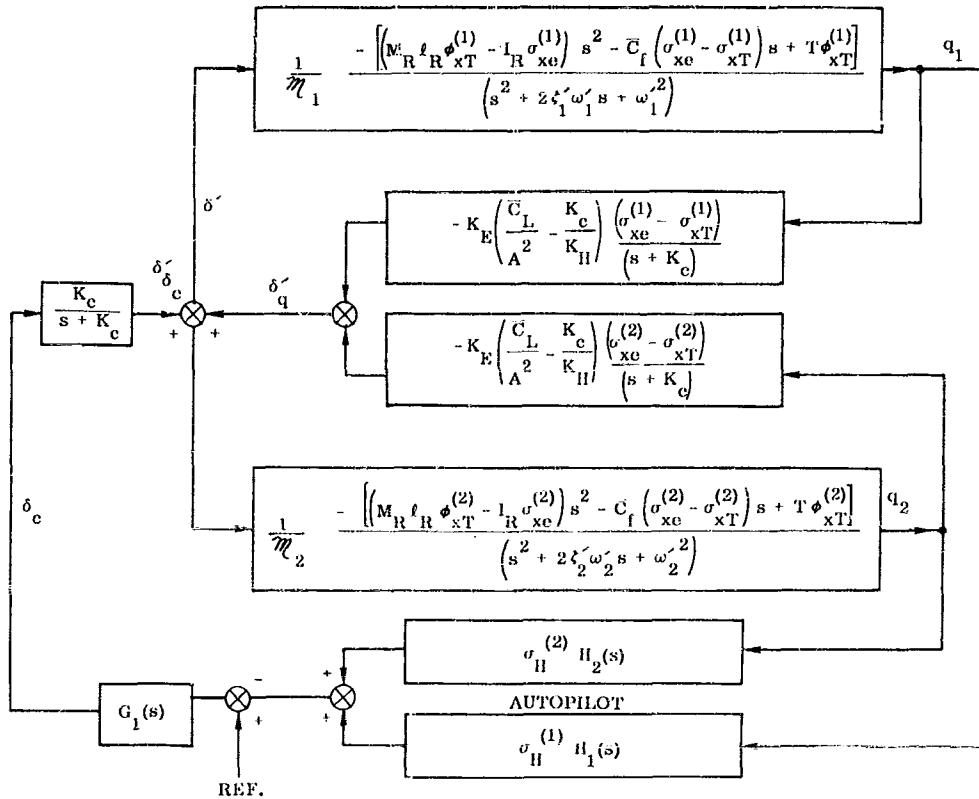
Figure 4-10. Autopilot Modal Coupling Paths

A general autopilot is assumed in which a variety of sensors at different locations will appear to offer different transmittances to the two modes. The forward path compensation, G_1 (s), is assumed common to all sensor paths.

1. **Open-Loop Coupling Due to Servo Compliance.** It will be observed that in Figure 4-10 the system still contains some open-loop coupling terms between the body modes. These terms arise because of additional compliance within the servo actuation system assumed. This "compliance" is contributed by a damping leakage orifice and by signal pickup (by the feedback transducer, see Equation 4-20) of the hydraulic fluid compressibility. This open loop coupling was not included in the earlier open loop coupling discussion for several reasons. First, it is a fundamentally different coupling - that occurring between two nonorthogonal modes, q_j and δ'. As such it contains an inertial force coupling term in its coefficient as well as the nonconservative propulsive and bearing friction forces.* Second, this term depends greatly upon the exact nature of the servo positioning system whether or not there is a leakage orifice; how much of the actuator compliance is sensed by the feedback transducer, i.e., K_E/K_H; and upon the loop gain, K_C. Thus, this really is a coupling through the autopilot.

A servo positioning loop may be stiff enough to minimize these additional feedbacks in some cases. They are, in fact, zero if a fixed linkage is used to position the rocket chamber.

---

* Note that if the servo actuator elastic compliance had not been incorporated into the bending modes, that part of the open-loop coupling between modes due to elastic compliance (see Subsection 4.3.2.1) would appear here instead, since $\sigma_{xe} - \sigma_{xT}$ would be zero. The extra coupling would manifest itself, in that Equation 4-10 could not be used for the engine servo but, instead, one including elastic compliance (Equation 4-23) would be used.

2. **Closed Loop Coupling.** In the following discussion, the above open-loop feedback around an individual mode (due to the additional servo compliance) will be assumed accounted for. The inter-mode coupling due to this effect will be disregarded. The latter simplification is generally well justified, the arguments being a direct parallel with those applied in Subsection 4.3.2.2 for neglecting an "auxiliary path for the engine forcing function". Here, too, the analyst may check for the accuracy of such an approximation, using techniques equivalent to those of Subsection 4.3.2.1.

If these additional feedback loops are to be included in the analysis, they are readily incorporated by substituting Equation 4-10 into Equation 4-9. If this is done, the q_i/δ_c transfer function may be written:

$$\frac{q_i}{\delta_c} = \frac{-\dfrac{K_c}{m_i}\left[\left(M_R \ell_R \phi_{xT}^{(i)} - I_R \sigma_{xe}^{(i)}\right)s^2 - \bar{C}_f\left(\sigma_{xe}^{(i)} - \sigma_{xT}^{(i)}\right)s + T\phi_{xT}^{(i)}\right.}{(s + K_c')_i\,(s^2 + 2\zeta_i'' \omega_i'' s + \omega_i''^2)} \qquad (4\text{-}12)$$

Here the denominator is the factored form which displays the roots of the following cubic:

$$s^3 + \left[K_c + 2\zeta_i' \omega_i' - \frac{K_E}{m_i}\left(\frac{\bar{C}_L}{A^2} - \frac{K_c}{K_H}\right)\left(\sigma_{xe}^{(i)} - \sigma_{xT}^{(i)}\right)\left(M_R \ell_R \phi_{xT}^{(i)} - I_R \sigma_{xe}^{(i)}\right)\right]s^2$$

$$+ \left[K_c\,(2\zeta_i' \omega_i') + \omega_i'^2 + \frac{K_E}{m_i}\left(\frac{\bar{C}_L}{A^2} - \frac{K_c}{K_H}\right)\left(\sigma_{xe}^{(i)} - \sigma_{xT}^{(i)}\right)^2 \bar{C}_f\right]s \qquad (4\text{-}13)$$

$$+ \left[K_c\,\omega_i'^2 - \frac{K_E}{m_i}\left(\frac{\bar{C}_L}{A^2} - \frac{K_c}{K_H}\right)\left(\sigma_{xe}^{(i)} - \sigma_{xT}^{(i)}\right)T_k \phi_{xT}^{(i)}\right] = 0$$

Approximate roots of this cubic are given by:

$$K_c' \approx K_c \qquad (4\text{-}14a)$$

and

$$(s^2 + 2\zeta_i'' \omega_i'' s + \omega_i''^2) \approx$$

$$\left\{s^2 + \left[2\zeta_i' \omega_i' - \frac{K_E}{m_i}\left(\frac{\bar{C}_L}{A^2} - \frac{K_c}{K_H}\right)\left(\sigma_{xe}^{(i)} - \sigma_{xT}^{(i)}\right)\left(M_R \ell_R \phi_{xT}^{(i)} + I_R \sigma_{xe}^{(i)}\right)\right]s + \right.$$

$$\left.\left[\omega_i'^2 + \frac{K_E}{m_i}\bar{C}_f\left(\frac{\bar{C}_L}{A^2} - \frac{K_c}{K_H}\right)\left(\sigma_{xe}^{(i)} - \sigma_{xT}^{(i)}\right)^2\right]\right\} \qquad (4\text{-}14b)$$

With these engine servo feedback loops incorporated as in Equation 4-12 the system may be reduced to that pictured in Figure 4-11. Here the body bending modes are coupled only through the control system.

To evaluate the effect of modal coupling of mode (2) on mode (1) the percentage error in the closed-loop roots is computed as follows:

$$\text{error} = \frac{G_1 \cdot \sigma_H^{(2)} \, H_2 \cdot \dfrac{q_2}{\delta_c}}{1 + G_1 \left[\sigma_H^{(1)} \, H_1 \dfrac{q_1}{\delta_c} + \sigma_H^{(2)} \, H_2 \dfrac{q_2}{\delta_c} \right]} \qquad (4\text{-}15)$$
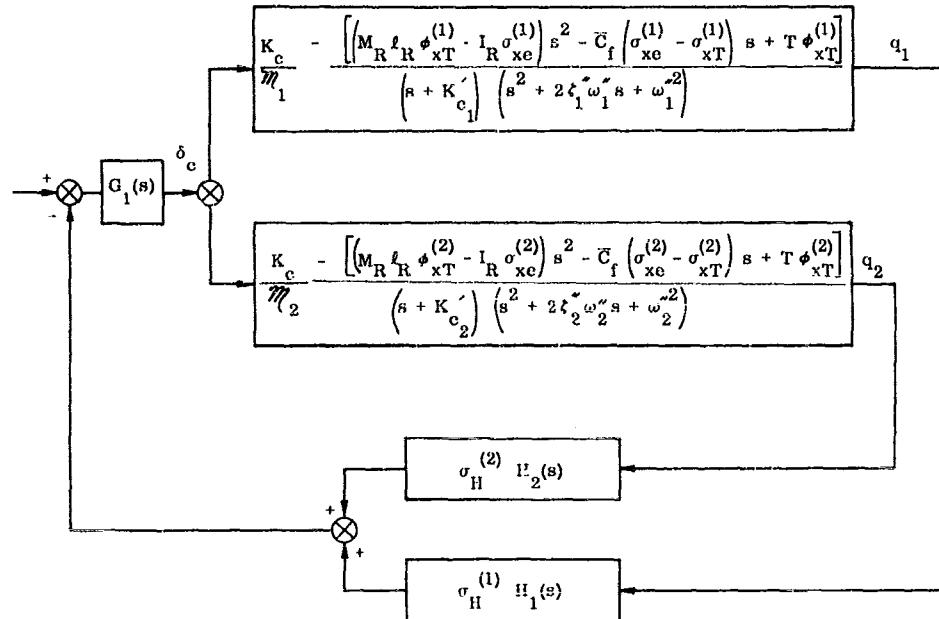
Figure 4-11. Simplified Modal Autopilot Coupling Diagram

As for the open loop roots (Subsection 4.3.2.1), this function can be interpreted to give both the percentage error in: 1) gain, or in 2) the damping of the closed loop root for mode (1), if the coupling of mode (2) is omitted. The evaluation of this function would be carried out for $s = j\omega_1''$, this being a good enough estimate of the location of the mode (1) closed-loop root.

It is difficult to go beyond making generalizations with regard to the closed-loop coupling error equation, 4-15. This difficulty arises because of the specialized nature of the equation, involving as it does the transmittances, $\sigma_H^{(1)} H_1$ and $\sigma_H^{(2)} H_2$, peculiar to a particular vehicle. The following generalizations are offered, however:

First, it is clear that the closed-loop cross-coupling error is gain-dependent. It follows that the error is smaller for modes whose frequencies are beyond the bandwidth of G_1.

Second, the error is directly proportional to the mode (2) transmittance, $\sigma_H^{(2)} H_2 \, q_2/\delta_c$. From this fact it follows that the error is small if pickup of this mode by the sensors is small. It also follows that this error is low if the natural frequency of mode (2) is well below ω_1'', since this will put the "test frequency" well beyond the roll-off point. (From this point it follows easily that rigid body modes will have very little coupling effect on a body bending mode.)

Third, the error is low if the mode (1) response is high relative to mode (2). Thus, if mode (1) is lightly damped, its response at ω_1'' will be very great; if the mode (2) natural frequency is reasonably far removed, or if mode (2) is nearby but is highly damped, its response will be relatively low, leading to low error.

Fourth, if again one of these two modes is an engine-body mode, strong coupling may exist because of very little frequency separation. It is also true that this engine-body mode has greater effective damping than a "regular" body bending mode, because of the gimbal bearing friction. This damping tends to spread the bandwidth of this mode further, propagating its coupling effects.

B. **Coupled Bending-Sloshing Excitations.** Two points of view may be adopted here, each of which is discussed herein briefly in general terms.

1. If the spring-centered sloshing masses have been included with the vehicle elastic and inertial characteristics when the body bending modes were computed, then the sloshing and bending are orthogonal normal modes. These can be coupled only through the flight control system in a manner exactly analogous to that just discussed in Subsection 4.3.2.5.A, above. The same general conclusions apply.

It should be noted, however, that the sloshing mode frequency is usually well removed from the other elastic mode frequencies and, hence, coupling is very low. Moreover, from the point of view of the bending modes, since their frequencies are usually well beyond those of the sloshing modes, it is quite reasonable to neglect the sloshing modes.

2. If the sloshing modes have been treated as artificially uncoupled modes, their open-loop coupling is displayed as shown in Subsection 4.3.2.3. As for closed loop coupling, it is noted that the propellant modes are not acted upon directly by the autopilot control forces; hence, coupling through the flight control system is indirect.

If the flight control system directly senses propellant motions (by means of liquid sensors placed in the tanks for that purpose), then it responds to these signals and reacts upon the body modes; these, in turn, affect the propellant modes. If the flight control system does not sense propellant motions directly (the more common situation), then it sees these motions only as they affect the body modes (which is the case with the conventional sensors). In either case, propellant sloshing modes, if they are to be sustained regeneratively, must have their loops "filtered" by the body modes. It follows then that these propellant modes will only couple significantly with modes in their immediate frequency range or with modes having a large enough pass band to encompass the slosh frequencies. Of the various body modes, the rigid-body pitching is the only one which generally has such a bandwidth.

4.3.3. **Engine Equations.** Subsection 3.4 gives the equation for the angular motion of the kth engine, δ_k', with respect to the elastic axis of the missile in terms of the modal motion, q_j, and actuator load torque, $T_{L_{servo}}$. All parameters are assumed to be for the kth engine:

$$\ddot{\delta}' + \frac{\bar{C}_f}{I_R} \dot{\delta}' = \frac{-1}{I_R} \sum_{j=1}^{r} \left(M_R \ell_R \phi_{xT}^{(j)} - I_R \sigma_{xe}^{(j)} \right) \ddot{q}_j + \frac{\bar{C}_f}{I_R} \sum_{j=1}^{r} \left(\sigma_{xe}^{(j)} - \sigma_{xT}^{(j)} \right) \dot{q}_j + \frac{1}{I_R} T_{L_{servo}}.$$

(4-16)

The servo torque is a function of the servo actuation system used to position the engine or control system. For this discussion, a hydraulic actuator employing a flow control valve and a leakage orifice across the piston will be used. The servo torque for such a system (see Figure 4-12) is:

$$T_{L_{servo}} = -AR\, P_L$$

(4-17)

where the load pressure, P_L, is given by (cf. Subsection B4.2, Equation B-6, B-7, and B-14.

$$\left(\frac{A^2}{K_m} + \frac{V_T}{4B} \right) \dot{P}_L + AR\, \dot{\delta} - \tilde{C}_L\, P_L - K_c\, AR\, \dot{\delta}_\epsilon .$$

(4-18)

where $\dot{\delta}_\epsilon$ is the servo loop actuating error (see below).

$$K_E = \frac{K_H K_m}{K_H + K_m} = \frac{1}{\dfrac{V_T}{4BA^2} + \dfrac{1}{K_m}}$$

II DENOTES PARALLEL LINES.
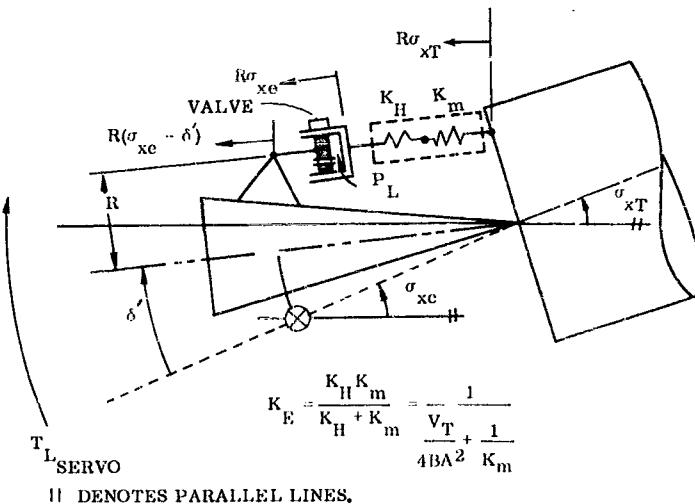
Figure 4-12. Schematic of Position Servo Model Showing Division
of Compliances and Actuation

When the flexibility associated with the actuator linkage and hydraulic fluid compressibility is included in the modal calculations, the left hand side of Equation 4-18 is set equal to zero ($K_E \longrightarrow \infty$):

$$\dot{\delta}' + \frac{\bar{C}_L}{AR} P_L + K_c \delta_\epsilon .\tag{4-19}$$

The engine control system as shown in Figure 4-12 will be used for the following discussion. This control system consists of a hydraulic actuator with no control or leakage orifice but having a spring, K_E. This equivalent spring K_E represents the actuator structural spring, K_m, and hydraulic spring, K_H, in series. The motion of the hydraulic actuator due to flow from the control valve and the leakage orifice is represented by a hydraulic piston in series with the spring, K_E. The hydraulic fluid in the actuator piston is then treated as incompressible. This piston has the leakage orifice for damping and a servo valve for control.

Now the error signal, δ_ϵ, is given by:*

$$\delta_\epsilon = \delta_c - \delta' - \frac{A P_L}{R K_H}$$

$$\tag{4-20}$$

$$\delta_c - \delta' - \frac{K_E}{K_H} \left(\sigma_{xT}^{(i)} - \sigma_{xe}^{(i)} \right) q_i .$$

By combining Equations 4-16, 4-17, 4-19 and 4-20 one obtains the engine transfer function as:

$$\dot{\delta}' = \cfrac{-\sum_{j=1}^{r} \left[\left(M_R \ell_R \phi_{xT}^{(j)} - I_R \sigma_{xe}^{(j)} \right) s^2 - \bar{C}_f \left(\sigma_{xe}^{(j)} - \sigma_{xT}^{(j)} \right) s + \dfrac{K_c A^2 R^2}{\bar{C}_L} \cdot \dfrac{K_E}{K_H} \left(\sigma_{xe}^{(j)} - \sigma_{xT}^{(j)} \right) \right] q_j + \dfrac{K_c A^2 R^2}{\bar{C}_L} \delta_c}{I_R \left\{ s^2 + \left[\dfrac{\bar{C}_f}{I_R} + \dfrac{A^2 R^2}{I_R \bar{C}_L} \right] s + \dfrac{K_c A^2 R^2}{I_R \bar{C}_L} \right\}} \tag{4-21}$$

---

* The feedback transducer sees the total relative motion between piston and cylinder, which includes the effects of hydraulic fluid compliance.

A very satisfactory simplification for hydraulic actuators is made by dropping the K_E/K_H term, representing pickup of the hydraulic compliance by the feedback transducer.

An alternate form of the preceding equation also exists. This may be calculated by letting the load pressure be expressed in terms of the modal deflections only. For a given load pressure (P_L), the hydraulic spring (K_H) and the actuator structural spring (K_m) deflect a total distance, X_1, given by:

$$X_1 = \frac{A\, P_L}{K_E}.$$

This deflection (X_1) may also be expressed as the summation of the differences in the modal slopes on each side of the gimbal block times the radius arm (R) (cf. Figure 4-12):

$$X_1 = R \sum_{j=1}^{r} \left(\sigma_{xe}^{(j)} - \sigma_{xT}^{(j)} \right) q_j .$$

Solving for P_L one obtains:

$$P_L = \frac{K_E\, R}{A} \sum_{j=1}^{r} \left(\sigma_{xe}^{(j)} - \sigma_{xT}^{(j)} \right) q_j .$$

Substituting this in Equation 4-19 and using 4-20, the engine equation becomes:

$$\delta' = \frac{-K_E \left(\dfrac{\bar{C}_L}{A^2} - \dfrac{K_c}{K_H} \right) \sum\limits_{j=1}^{r} \left(\sigma_{xe}^{(j)} - \sigma_{xT}^{(j)} \right) q_j + K_c\, \delta_c}{(s + K_c)} . \tag{4-22}$$

Equation (4-22) will yield correct results if the data used is accurate. One area which must be checked for accuracy is the difference of modal slopes $\left(\sigma_{xe}^{(j)} - \sigma_{xT}^{(j)} \right)$. An inaccuracy here will introduce an error in the δ'/q_j portion of the transfer function; however, this portion is usually small with respect to δ'/δ_c and, therefore, will not appreciably affect the accuracy of the determination of closed-loop roots. In a similar manner, the transfer function for the case where the actuator compliance is not included in the modal calculations may also be obtained. With finite stiffness K_E, the resultant engine transfer function is (see Appendix B4.2):

$$\delta = \delta' = \frac{-\left(M_R \ell_R \phi_{xT}^{(j)} - I_R \sigma_{xe}^{(j)} \right) s^2 \left[s + K_E \left(\dfrac{\bar{C}_L}{A^2} + \dfrac{K_c}{K_m} \right) \right] q_j + K_c\, K_E\, R^2\, \delta_c}{I_R \left\{ s^3 + \left[K_E \left(\dfrac{\bar{C}_L}{A^2} + \dfrac{K_c}{K_m} \right) + \dfrac{\bar{C}_f}{I_R} \right] s^2 + \dfrac{K_E}{I_R} \left[\bar{C}_f \left(\dfrac{\bar{C}_L}{A^2} + \dfrac{K_c}{K_m} \right) + R^2 \right] s + \dfrac{K_c\, K_E\, R^2}{I_R} \right\}} \tag{4-23}$$

It may be noted that the gimbal friction term, $\bar{C}_f/I_R \left(\sigma_{xe}^{(j)} - \sigma_{xT}^{(j)} \right) q_j$, is omitted from the equation. This is done because (by hypothesis) there is no relative motion of the engine with respect to the back end of the missile due to modal deflections, i.e., $\left(\sigma_{xe}^{(j)} - \sigma_{xT}^{(j)} \right) = 0$.

4.3.4 Elastic Booster Coupling Classification Summary. As an aid in achieving perspective from which to review the foregoing subsections, the following tabulation and remarks concerning couplings are given.

a. Open Loop Coupling - Orthogonal Modes

  1) (Coupling Mode q_i to mode q_j)

    Only through nonconservative forces:

      Aerodynamic - minor for nonwinged booster

      Propulsive (Engine Thrust)

      Dissipative (Bearing Friction)

      } Major

b. Open Loop Coupling - Nonorthogonal Modes*

  1) (Coupling Mode q_i to mode δ' or δ)**

    Forces:

    Inertial $(M_R \ell_R \phi_{xT}^{(i)} - I_R \sigma_{xe}^{(i)})$

    Propulsive

    Dissipative

  2) (Coupling Mode q_i to mode y_ℓ)

    Forces:

    Inertial

    Elastic

c. Closed Loop Coupling

  1) (Coupling Mode q_i to q_j)

    Forces:

    Inertial

    Propulsive

      This coupling depends upon transmittance from mode to control system, i.e., the way mode is sensed by the control.

4.4 SUMMARY OF APPROXIMATE FLEXIBLE VEHICLE TRANSFER FUNCTIONS

In this subsection are summarized certain approximate flexible-booster vehicle transfer functions useful for conducting rapid manual calculations of the stability of the various vehicle modes. For such computation it is desirable that the transfer functions be reduced to simple single-mode equations with all elements appearing in factored form (or at least in a form easily factored by hand calculation). These properties have been attained here with, it is believed, a minimum penalty in accuracy for most applications. The transfer functions are grouped according to which dominant vehicle mode is of concern: flexible vehicle transfer functions, rigid vehicle with sloshing propellants and finally rigid vehicle with rigid contents. The assumptions made in obtaining each transfer function, along with an indication of its area of applicability, are given.

---

* This coupling actually effects a coupling between orthogonal body modes as seen in Subsection 4.3.2.5.

** The difference is that coupling with δ' is through the agency of the servo control compliance alone. Coupling with δ is through both servo elastic and control compliances.

4.4.1 <u>Flexible Vehicle Transfer Functions</u>. Given herein are some approximate transfer functions useful for a stability check of one elastic mode coupling with the flight control system.

a. <u>Assumptions</u>:

1) Modal coupling with other body modes (rigid, sloshing, or elastic) through aerodynamics, the control system or conservative forces (for nonorthogonal modes) is neglected.

2) Only one (or a group of identical) gimbaled engines is commanded.

3) Noncommanded engine coupling effects are neglected (see Section 5 and Appendix C5).

4) Aerodynamic effects and engine inertial feedback for the mode considered may be included if desired.

5) It is assumed that the engine-positioning servo compliance is accounted for in the engine servo transfer function itself.* Thus, the vehicle body bending modes to be used are those computed with no servo elastic compliance allowed for in those modes.

The general form of the simplified q_i/δ' transfer function is as follows:

$$\frac{q_i}{\delta'} = \frac{-K_i\,(s + z_{i_{TWD}})\,(s + \bar{z}_{i_{TWD}})}{\mathcal{M}_i\,(s^2 + 2\zeta_i'\,\omega_i'\,s + \omega_i'^2)} \tag{4-24}$$

where:

$$K_i = (M_R\,\ell_R\,\phi_{xT}^{(i)} - I_R\,\sigma_{xe}^{(i)})$$

$$(s + z_{i_{TWD}})\,(s + \bar{z}_{i_{TWD}}) = \left[s^2 + \frac{T_c\,\phi_{xT}^{(i)}}{K_i}\right]$$

and $\delta = \delta'$.

The actuator transfer function is (from Equation B-25, Appendix B4.2, and Equation 4-23):

$$\delta = \delta' \frac{-\dfrac{K_i}{I_R}\,s^2\left[s + K_E\left(\dfrac{\bar{C}_L}{\Lambda^2} + \dfrac{K_c}{K_m}\right)\right]q_i + K_c\,\omega_c^2\,\delta_c}{s^3 + 2\zeta_{cn}\,\omega_{cn}\,s^2 + \omega_{cn}^2\,s + K_c\,\omega_c^2}, \tag{4-25}$$

where

$$\omega_c^2 = \frac{K_E\,R^2}{I_R}$$

$$\omega_{cn}^2 = \omega_c^2 + \frac{\bar{C}_f}{I_R}\,K_E\left(\frac{\bar{C}_L}{\Lambda^2} + \frac{K_c}{K_m}\right)$$

$$2\zeta_{cn}\,\omega_{cn} = \frac{\bar{C}_f}{I_R} + K_E\left(\frac{\bar{C}_L}{\Lambda^2} + \frac{K_c}{K_m}\right).$$

---

* Incorporation of this servo compliance into the body mode calculations yields better results for a <u>detailed</u> stability study in which coupled modes are employed. For a simple, uncoupled, single mode stability check, however, the method given here is adequate. A comparison between the coupled mode approach and that indicated in 5) is given in Section 5.

This third order denominator is readily handled manually, since it always factors into at least one real root. This root is found by trial by dividing out several trial values until a second order function with no remainder is left as the quotient. A value of $s = -K_c$ is always a good first trial.

The autopilot pictured in Figure 4-13 has the following θ_f/q_i transfer function:

$$\frac{\theta_f}{q_i} = \left[\left(\frac{K_R \, \omega_{RG}^2 \, \sigma_{RG}^{(i)}}{s^2 + 2\zeta_{RG} \, \omega_{RG} \, s + \omega_{RG}^2} \right) s + \frac{\sigma_{PG}^{(i)}}{(\tau_{PG} \, s + 1)} \right] \quad (4-26)$$

Here a simple lag represents the attitude reference dynamics; these may be far more complex (cf. Appendix B2.3).

FLEXIBLE MODE FEEDBACK TO ACTUATOR

$$\frac{-\dfrac{K_i}{I_R} s^2 \left[s + K_E \left(\dfrac{\bar{C}_L}{A^2} + \dfrac{K_c}{K_m} \right) \right]}{K_c \, \omega_c^2}$$

AMPLIFIER K_A

AUTOPILOT FILTER & INTE-GRATOR

HYDRAULIC ACTUATOR

$$\frac{K_c \, \omega_c^2}{s^3 + 2\zeta_{cn} \, \omega_{cn} \, s^2 + \omega_{cn}^2 \, s + K_c \, \omega_c^2}$$

FLEXIBLE BODY DYNAMICS

$$\frac{-K_i \left(s + z_{i_{TWD}} \right) \left(s + \bar{z}_{i_{TWD}} \right)}{\mathcal{m}_i \left(s^2 + 2\zeta_i' \omega_i' s + \omega_i'^2 \right)}$$

GYROS

$$K_R \frac{\omega_{RG}^2 \, s}{s^2 + 2\zeta_{RG} \, \omega_{RG} \, s + \omega_{RG}^2}$$

ELASTIC INPUT TO GYROS $\sigma_{xG}^{(i)}$
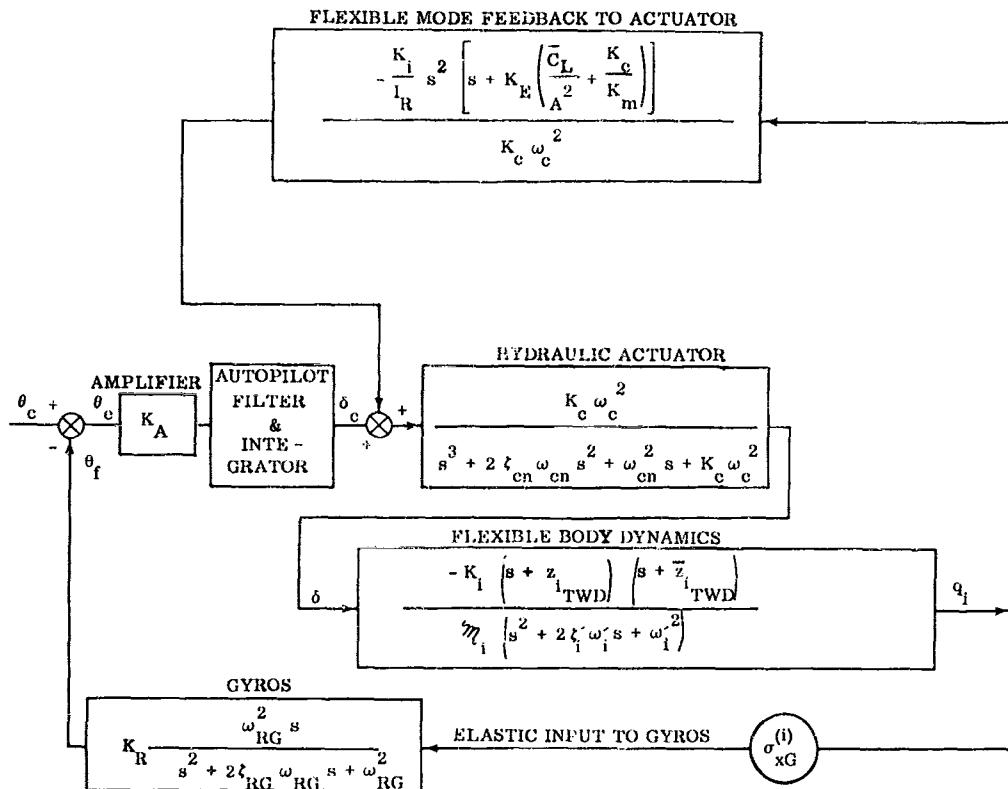
Figure 4-13. Block Diagram of Closed Loop Elastic Mode System (Servo Mount Flexibility Incorporated in Servo Actuator)

In general, for elastic mode coupling studies the contribution of the attitude-position signal is negligible (unless the attitude position sensor is located at a point of great modal flexure, such as the nose, while the rate gyro is located near an antinode) and the above simplifies to:

$$\frac{\theta_f}{q_i} = \frac{K_R \, \omega_{RG}^2 \, \sigma_{RG}^{(i)} \, s}{(s^2 + 2\zeta_{RG} \, \omega_{RG} \, s + \omega_{RG}^2)} \quad (4-27)$$

The feedback path labeled "flexible mode feedback to actuator" in Figure 4-13 may be omitted for stability checks of most modes. The exceptions would be modes at or near engine-servo-mount resonant frequency (approximately $\sqrt{K_E R^2/I_R}$), for which the path becomes significant. If this path is omitted the open loop transfer function may be read directly from Figure 4-13.

The additional feedback path may be eliminated algebraically from the equations by substituting Equation 4-24 into 4-25 to obtain a higher order transfer function. The result is:

$$\frac{\delta}{\delta_c} = \frac{K_c \, \omega_c^2 \, (s^2 + 2\zeta_1' \, \omega_1' \, s + \omega_1'^2)}{(s^3 + 2\zeta_{cn} \, \omega_{cn} \, s^2 + \omega_{cn}^2 \, s + K_c \, \omega_c^2)(s^2 + 2\zeta_1' \, \omega_1' \, s + \omega_1'^2) + \frac{K_1^2}{m_1 \, I_R} (s^3 + 2\zeta_c \, \omega_c \, s^2)\left(s^2 + \frac{T_c}{K_1}\right)} , \tag{4-28}$$

where

$$2\zeta_c \, \omega_c = K_E \left(\frac{\bar{C}_L}{A^2} + \frac{K_c}{K_m}\right) .$$

The flexible mode feedback is displayed here as the added higher-order terms of the denominator. Clearly, if these are dropped the transfer function reverts to a simple third order equation:

$$\frac{\delta}{\delta_c} = \frac{K_c \, \omega_c^2}{s^3 + 2\zeta_{cn} \, \omega_{cn} \, s^2 + \omega_{cn}^2 \, s + K_c \, \omega_c^2} . \tag{4-28a}$$

It is not recommended that Equation 4-28 be used to account for servo-mount compliance in checking body bending modes whose frequency is at or near the uncoupled servo-mount frequency. To use Equation 4-28 one would employ a machine routine to factor the fifth-order denominator. It is felt that better use may be made of this machine time to obtain roots of the coupled body bending and engine-body modes (where the servo-mount compliance is incorporated in the body-mode calculations). Equation 4-28 is given only as an alternate means of rationalizing the omission of the "flexible-mode-feedback-to-the-actuator" path (leading thereby to Equation 4-28a).

Occasionally, it is desired to display the body-bending mode coupled through the autopilot to the rigid-body mode. This presumably would be the case for a very low frequency bending mode. The transfer function giving the attitude perturbations, as seen by the gyro package is:

$$\frac{\theta_G}{\delta} = \frac{(X_{CG} - X_H) \, K_1 \, (1 - A_1)\left(s^2 + \frac{T_c \, \phi_{xT}^{(1)}}{K_1}\right)\left(s^2 + \frac{2\zeta_1 \, \omega_1 \, s}{1 - A_1} + \frac{\omega_1^2}{1 - A_1}\right)}{I \, s^2 \, (s^2 + 2\zeta_1 \, \omega_1 \, s + \omega_1^2)} \tag{4-29}$$

where

$$A_1 = \frac{I \, \sigma_{xG}^{(1)} \, \phi_{xT}^{(1)}}{m_1 \, (X_{CG} - X_H)}$$

$$K_1 = (M_R \, \ell_R \, \phi_{xT}^{(1)} - I_R \, \sigma_{xe}^{(1)})$$

Here aerodynamics have been neglected. This equation is an extraction of Equation 2-15 of Section 2. Figure 4-14 shows a typical control loop.
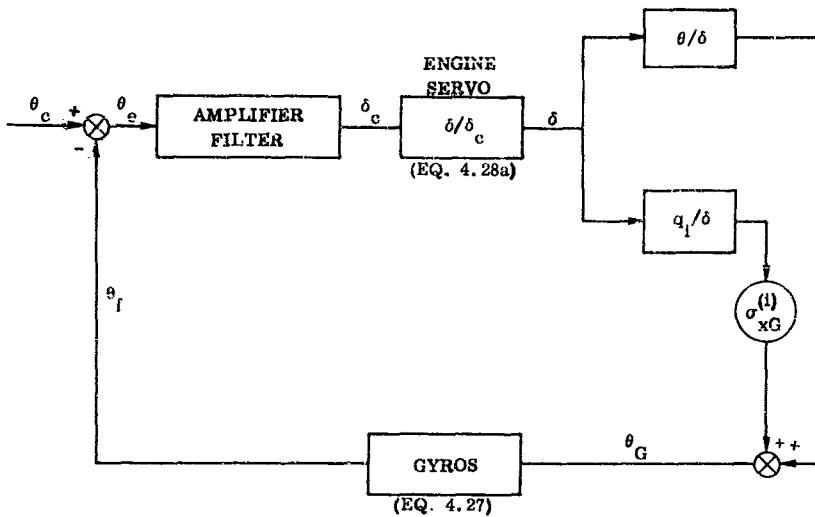
Figure 4-14. Rigid Body Pitching and Body Bending Coupling Control Loop

4.4.2 <u>Rigid Vehicle With Sloshing Propellant Modes.</u> Given herein are some approximate transfer functions useful for sloshing propellant mode stability checks.

a. <u>Assumptions</u>:

1) The sloshing propellants' fundamental modes only are considered (see Appendix A3).

2) The pendulum mechanical analogy is employed. Corresponding interpretations may be made for the spring-centered sloshing mass.

3) Propellant damping is omitted in writing the equations.

4) Aerodynamic effects are omitted (see comment in Subsection 2.2.5).

5) Artificially uncoupled sloshing modes are assumed.

6) Control engine inertial effects are neglected (see Subsection 4.4.4, below).

4.4.2.1 <u>Single Sloshing Tank.</u>

$$\frac{\theta}{\delta} = \frac{\mu_\delta}{s^2} \frac{s^2 + \omega_\ell'^2 + \dfrac{\alpha_T}{L_{p\ell}} \dfrac{M_{p\ell}}{M} \dfrac{\ell_{p\ell}}{\ell_c}}{s^2 + \omega_\ell'^2 + \dfrac{\alpha_T}{L_{p\ell}} \dfrac{M_{p\ell}}{M} \dfrac{\ell_{p\ell}}{\ell_c} \dfrac{(\ell_{p\ell} - L_{p\ell})\ell_c}{r^2}}$$

$$r^2 = \frac{I}{M}, \qquad \omega_\ell'^2 = \omega_\ell^2 \left(1 + \frac{M_{p\ell}}{M}\right) \tag{4-30}$$

$$\alpha_T = \frac{T-D}{M_{TOT}}, \qquad \mu_\delta \quad \frac{T_c \ell_c}{I}$$

99

The remaining parameters are defined in Figure 4-15, and the equation is derived in Section 2 (Equation 2-9).

WHERE
$T = T_c + T_f$
f "FIXED"
c "CONTROL"
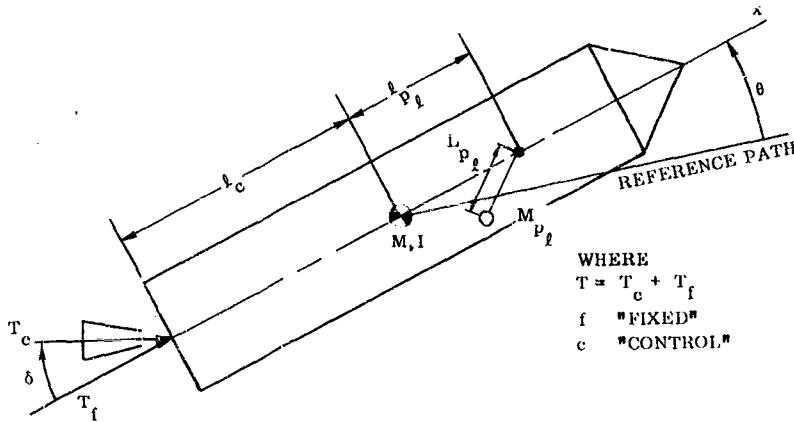
Figure 4-15. Single Tank Propellant Sloshing Model

Equation 4-30 may be used for sloshing stability studies in a control loop such as that of Figure 4-16. For this study a simple δ/δ_c transfer function such as Equation 4-28a or even a first order transfer function (see Appendix B4.2, Equation B-28) may be used. The choice of δ/δ_c function is dependent upon the expected frequency of slosh roots relative to the servo actuator bandwidth.
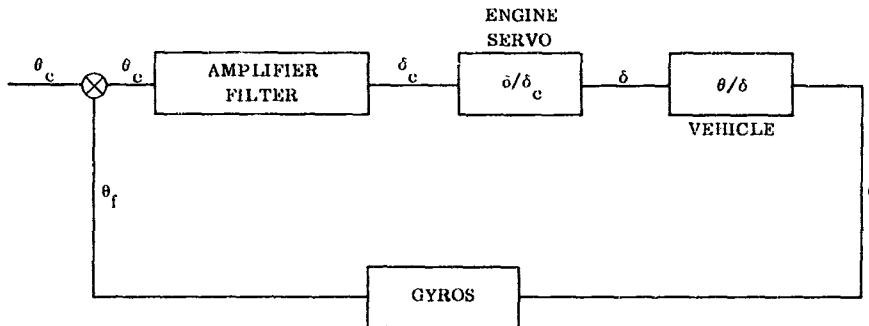
Figure 4-16. Rigid Body and Sloshing Stability Control Loop

4.4.2.2 Multiple Sloshing Tanks. For an n-tank vehicle with aerodynamics omitted, one may write: (see Reference 15)

$$\frac{\theta}{\delta} = \frac{\mu_\delta}{s^2}\left[1 + \frac{1}{M(x_{CG}-x_T)} \sum_{\ell=1}^{n} \frac{M_{p_\ell} \ell_{p_\ell}\left(1 - \frac{(\ell_{p_\ell} - L_{p_\ell})\ell_c}{r^2}\right)\omega_\ell^2}{s^2 + \bar\omega_\ell^2}\right],$$

(4-31)

where

$$\bar\omega_\ell^2 = \omega_\ell^2 \left[1 + \frac{M_{p_\ell}}{M}\left(1 + \frac{\ell_{p_\ell}(\ell_{p_\ell} - L_{p_\ell})}{r^2}\right)\right]$$

4.4.3 Rigid Vehicle With Rigid Contents. The rigid-body (rigid-vehicle) transfer function (θ/δ) will be presented first in its simplest form, based upon several restrictive assumptions. These restrictions will be removed one by one, showing the change to the transfer function. The rigid vehicle that is discussed in this study is assumed to have a reasonable slenderness ratio, and δ is restricted to small angular motions. Figure 4-17 is the mathematical model.
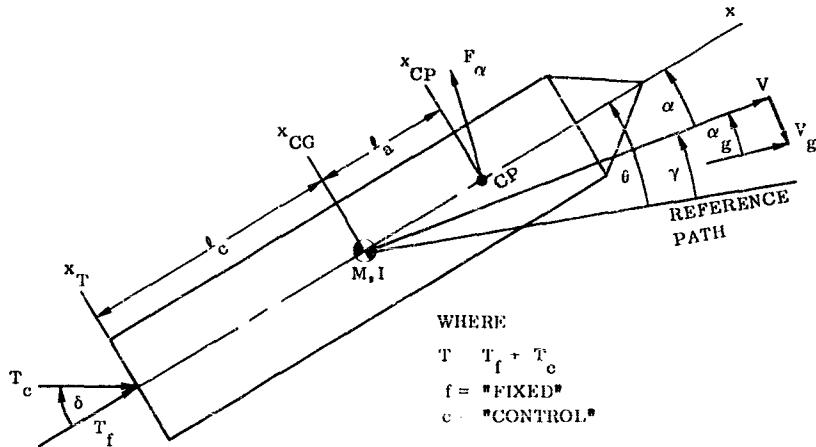
Figure 4-17. Rigid Vehicle Parameters

Assuming zero dynamic pressure (q) and no inertial moment coupling of the rigid-body mode with the engine, the θ/δ transfer function is:

$$\frac{\theta}{\delta} = \frac{\mu_\delta}{s^2} \ , \quad \text{where } \mu_\delta = T_c \ell_c / I \qquad . \tag{4-32}$$

Next, the effect of aerodynamics on pitching is added, but the rigid body plunging mode and engine inertial coupling are omitted. One obtains:

$$\frac{\theta}{\delta} = \frac{\mu_\delta}{s^2 - \mu_\alpha} \ , \quad \text{where } \mu_\alpha = F_\alpha \ell_a / I. \tag{4-33}$$

Equation 4-33 is rationalized differently in Section 2, Subsection 2.2.1.

If the plunging mode is coupled to the pitching mode by the aerodynamic forces, one has:

$$\frac{\theta}{\delta} = \frac{\mu_\delta}{s} \ \frac{s + \dfrac{T + F_\alpha\left(1 + \dfrac{\ell_a}{\ell_c}\right)}{MV}}{s^2 + \dfrac{T + F_\alpha}{MV} s - \mu_\alpha} \tag{4-34}$$

Other useful rigid-body transfer functions of the same "class" as 4-34 are:

$$\frac{\alpha}{\delta} = \mu_\delta \ \frac{1 + \dfrac{T_c}{MV} \ \dfrac{s}{\mu_\delta}}{s^2 + \left(\dfrac{T + F_\alpha}{MV}\right)s - \mu_\alpha} \tag{4-35}$$

$$\frac{\alpha}{\theta} = \frac{s\left[1 + \frac{T_c}{MV}\frac{s}{\mu_\delta}\right]}{\left[s + \frac{T + F_\alpha\left(1 + \frac{\ell_a}{\ell_c}\right)}{MV}\right]} \tag{4-36}$$

$$\frac{\gamma}{\delta} = -\frac{T}{MV}\frac{s^2 - \frac{T\ell_c}{I_\delta}\left[1 + \frac{F_\alpha}{T}\left(1 + \frac{\ell_a}{\ell_c}\right)\right]}{s^2 + \left(\frac{T + F_\alpha}{MV}\right)s - \mu_\alpha} \tag{4-37}$$

From geometry:

$$\theta = \gamma + \alpha \tag{4-38}$$

and

$$\alpha_g = \tan^{-1}\frac{V_g}{V} \approx \frac{V_g}{V} \tag{4-39}$$

For gust response studies one may use:

$$\theta = \left(\frac{\theta}{\delta}\right)\delta + \frac{\mu_\alpha}{s}\frac{s + \frac{T}{MV}}{s^2 + \left(\frac{F_\alpha + T}{MV}\right)s - \mu_\alpha}\alpha_g . \tag{4-40}$$

From Equation 4-36 one may show that $\alpha \approx \theta$ is a good approximation for this class of vehicle. Figure 4-18 is a Bode plot of Equation 4-36 with break frequencies at typical values during flight.
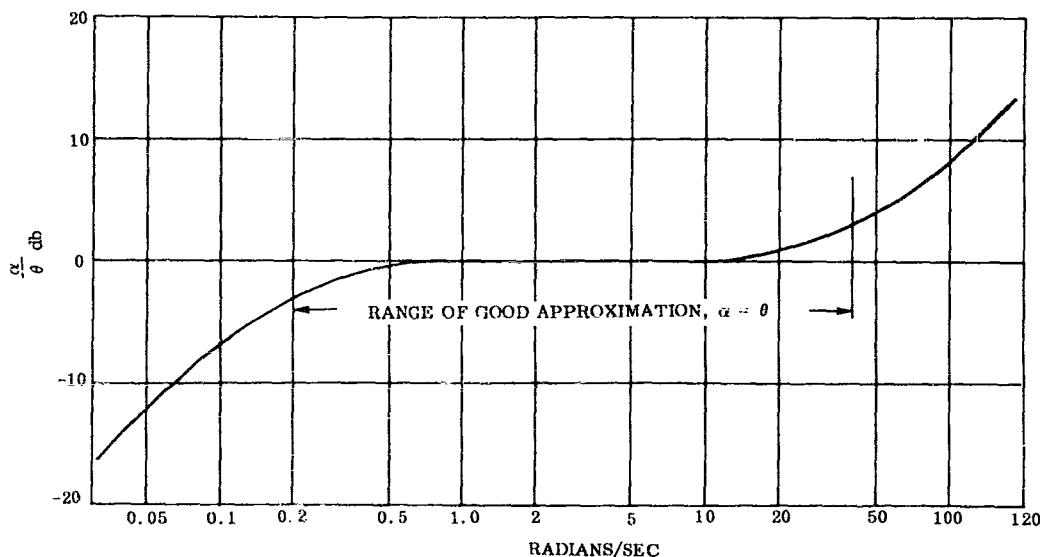
Figure 4-18. Log – Amplitude vs. Frequency Plot of α/θ Transfer Function for a Large Booster in Flight

If one wishes to study the effects of auxiliary feedbacks on loop stability, two other useful transfer functions are available:

$$\alpha_{\text{sensor}} = (1 - \frac{\ell_s \, s}{V}) \; \alpha_{\text{vehicle}} \tag{4-41}$$

where ℓ_s is the distance an angle-of-attack sensor is mounted ahead of the vehicle center of gravity.

$$\ddot{Z}_{\text{sensor}} = (\ell_s - \frac{T_c}{M\mu_\delta}) \left(s^2 + \frac{T_c \; \frac{\frac{\mu_\alpha}{\mu_\delta} + F}{\mu_\delta}}{\ell_s \, M - \frac{T_c}{\mu_\delta}} \alpha \right) \theta \tag{4-42}$$

Here ℓ_s is the distance an accelerometer is located ahead of the vehicle center of gravity.

4.4.4 Concluding Remarks on Engine Inertial Effects. Engine inertial effects arise in two ways: 1) the inertial loads of the gimbaling engine mass react on the body modes and 2) the accelerations of the body modes load the engine-positioning servo.

The first of these effects if displayed by inclusion of the inertial gain, $K_i = M_R \ell_R \phi_{xT}^{(i)} - I_R \sigma_{xe}^{(i)}$, and the tail-wags-dog zeros, z_i TWD and $\bar{z}_i$ TWD (see Subsection 4.3.2.4). This effect is seldom important for rigid body and most sloshing modes for contemporary classes of rocket engines. However, it is likely to be significant for some future gimbaled powerplants of great mass, even for rigid body modes. This effect is best accounted for in approximate modal analyses by returning to the general equations of motion, Section 3, from which simplified equations for a mode or modes are quickly extracted.

The importance of the second inertial effect in moving the engine depends upon two factors: 1) proximity of the signal frequency (modal frequency) to the engine servo mount frequency and 2) softness of the positioning servo (servo loop gain and dead zone size). For the lower frequency modes it is unlikely that frequencies will approach the servo resonant frequencies. However, the effect of servo-loop softness is sometimes significant in determining limit-cycle behavior, particularly when a sizeable servo "dead-zone" is present. This effect is readily incorporated in the rigid body and sloshing mode analyses as follows:

If Equation 4-25 is simplified by letting $\omega_c^2 \rightarrow \infty$ (a good approximation for modes well below the servo resonant frequency) one has:

$$\delta = \frac{-\frac{K_i \, s^2}{R^2} \left(\frac{\bar{C}_L}{A^2} + \frac{K_c}{K_m} \right) q_i + K_c \, \delta_c}{s \left[1 + \frac{\bar{C}_f}{R^2} \left(\frac{\bar{C}_L}{A^2} + \frac{K_c}{K_m} \right) \right] + K_c} \quad .$$

For use with rigid body and artificially uncoupled sloshing modes, $\phi_{xT}^{(\theta)} = -\ell_R$, $\sigma_{xe}^{(\theta)} = 1$ and thus:

$$K_i \, q_i = -(M_R \ell_R \ell_c + I_R) \, \theta.$$

Then one has:

$$\delta = \frac{\left(\dfrac{M_R\, \ell_R\, \ell_c\; +\; I_R}{R^2} \right) \left(\dfrac{\bar{C}_L}{A^2} + \dfrac{K_c}{K_m} \right) s^2\, \theta\; +\; K_c\, \delta_c}{s\left[1 + \dfrac{\bar{C}_f}{R^2} \left(\dfrac{\bar{C}_L}{A^2} + \dfrac{K_c}{K_m} \right) \right]\; +\; K_c} \qquad (4\text{-}43)$$

Equation 4-43 may be used in place of Equation B-26 for an actuator transfer function in rigid-vehicle studies to display the effects of inertial loads on the positioning servo.

SECTION 5

SOME COMPARISONS OF MODAL COUPLING EFFECTS

5.1 GENERAL

In previous chapters detailed system equations of motion have been written from which various simplified transfer functions were derived. By far the greatest simplification is made when the coupling between modes is omitted and the stability of a single mode is analyzed with a minimum of secondary feedback paths. This simplification is employed sweepingly in compiling the approximate transfer functions of Subsection 4.4.

For the lower frequency modes (rigid body and propellant sloshing), experience has shown this simplification to be well justified in general. In cases where it is not (e.g., rigid-body coupling with a low frequency, artificially uncoupled sloshing mode), a single simple transfer function can be obtained for the coupled system. Hence, the transfer functions given for these modes are readily applied with little qualification.

For the higher frequency modes (body bending) the situation is not so simple, in that various coupling effects and/or auxiliary feedback paths can occasionally be very significant. Their omission in applying a simple transfer function for rapid manual analysis will sometimes lead to results which can only be considered crude and barely adequate for a rough check. In this section certain of these effects are discussed and example problems are shown to display the nature of the coupling phenomena.

The major secondary effects in dealing with the higher frequency modes are as follows:

a. open-loop coupling between normal modes due to nonconservative forces (propulsive, dissipative, aerodynamic),

b. open-loop coupling through rocket engine servo compliance (inertial, propulsive and dissipative forces), and

c. closed-loop coupling through the control system.

Open-loop coupling due to aerodynamics is generally negligible. The exception could be for the vehicle carrying lifting surfaces near the times of maximum dynamic pressure (see Subsection 4.3.2.1). Because of its specialized nature no further treatment of this type of open-loop coupling is given herein.

5.2 OPEN LOOP COUPLING COMPARISONS

The first type of open-loop coupling due to the nonconservative forces (propulsive and bearing friction) arises due to the elastic compliances within the engine-positioning servo. These elastic compliances permit a relative angular motion in each body mode between the engine chamber centerline and the elastic axis at the gimbal, $\sigma_{xe}^{(i)} - \sigma_{xT}^{(i)}$. (Note that restriction of the open-loop coupling from these forces to this sole source is actually a consequence of the omission of certain other propulsive force work terms which are very nearly self-cancelling, as explained in Appendix C4.)

A second type of open-loop coupling arises through the internal compliance of the servo actuation system. This coupling involves the nonorthogonal engine deflection mode, δ', and hence, inertial as well as propulsive and dissipative forces are concerned.

These couplings manifest themselves as shifts in the open-loop poles of the body modes being studied. Because of the rather specialized nature of these two types of open loop couplings (due to their great dependence upon characteristics of a given servo installation), no attempt is made in the following discussion to distinguish between them or to generalize on their relative contributions to an open-loop pole shift.

Figure 5-1 shows some root comparisons computed for a large ballistic booster vehicle employing gimbaled nozzle liquid rocket engines. The figure shows a body bending mode's open loop poles, first when it is uncoupled and second when it is coupled with an engine-body mode. Set one shows a body mode at a frequency of 52 radians per second coupling with an engine-body mode whose natural frequency is 46 radians per second. Set two shows a body mode at 67 radians per second coupling with an engine body mode whose natural frequency is 77 radians per second. In set three one sees the much smaller effect of coupling with an engine body mode at 77 radians per second when the body modal frequency is far removed (101 radians per second) from that range. A typical electrohydraulic servo-actuator with leakage orifice damping was assumed for these calculations.
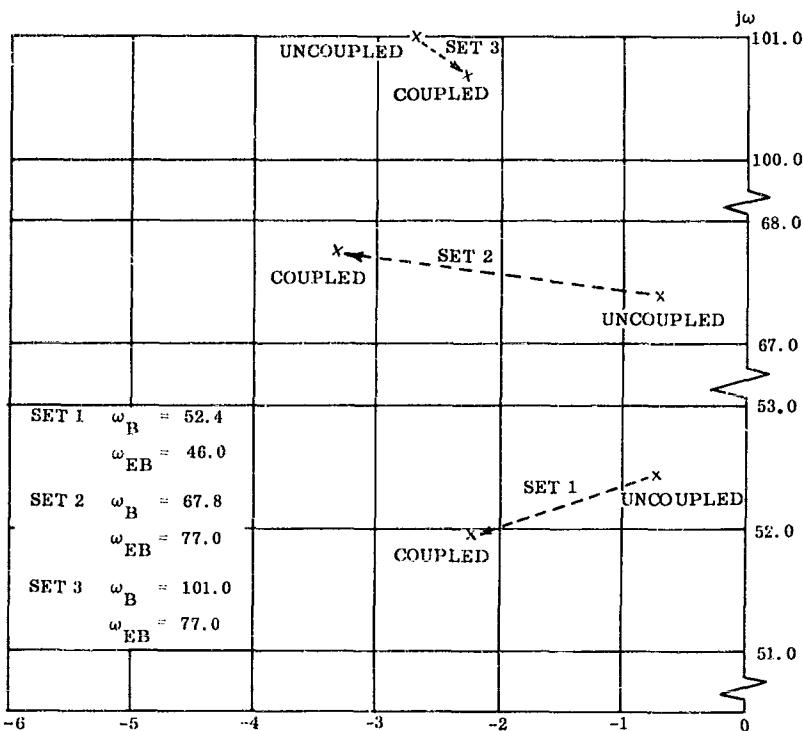
Figure 5-1. Effects of Open Loop Coupling Between a Body Bending Mode Frequency (ω_B)
and an Engine-Body Mode (ω_{EB})

The figure also illustrates the rule-of-thumb, given in Appendix C5, that the open-loop coupling effect from "wagging" an engine is generally stabilizing (i.e., tends to move the open loop poles to the left) for modes whose frequencies are above the engine's TWD frequency. The TWD frequency for Set one was at 32 radians per second, and for Sets two and three it was at 42 radians per second. The higher frequency mode (Set three) shows, however, the reverse trend; thus, the rule-of-thumb does not always apply for very high frequency modes. The reason is that the phase relationship between modal deflection (ϕ) and slope (σ) at the aft end sometimes changes radically for high frequency modes, thereby changing the sense of this coupling correction. Fortunately, this coupling correction is small for these same high frequency modes; hence, the rule-of-thumb as given is still generally useful.

It should be obvious that open-loop coupling alone will have no other effects on closed-loop roots than those accompanying the shift in the open-loop pole. For the body-bending modes the separation between modes is generally such that a relatively small shift in the open-loop pole is reflected as a simple translation of the root locus in the pole's vicinity. This property is illustrated in Figure 5-2, which shows the effect of open-loop coupling of a noncommanded engine upon a closed-loop root locus for a body mode. (Since the coupling is from a noncommanded engine it obviously cannot include any closed loop coupling.)

The open-loop coupling through propulsive and dissipative forces due to servo-elastic compliance also occurs between two body bending modes when neither one is an engine-body mode (provided, of course,

$\sigma_{xe}^{(i)} - \sigma_{xT}^{(i)} \neq 0$; i.e., the servo-elastic compliance was included in the modal calculations). This coupling is

so small, however, that it is hardly practicable to display it graphically. Several of these modes were selected from those of a typical large booster (these being the closest in frequency which could be found), yet the openloop coupling was found to be negligible. The slight extent of this coupling in a typical case may be seen in Figures 5-9 and 5-10, which were drawn to shown closed-loop coupling, also.
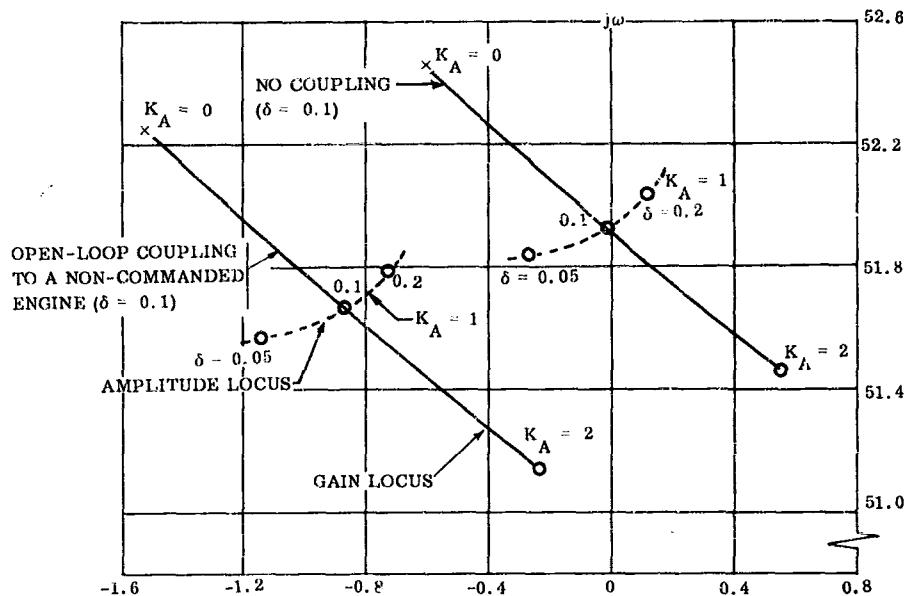
Figure 5-2. Effect of Open Loop Coupling on a Closed-Loop Root Locus

5.3 SOME CLOSED LOOP COUPLING COMPARISONS

As with the open-loop coupling shown above, the strongest high-frequency closed-loop couplings occur between a body-bending and an engine-body mode. Here, however, effects are often more striking than the open-loop coupling effects.

Figure 5-3 shows a comparison of closed-loop roots for a body-bending mode and an engine-body mode, reasonably well separated in frequency. The difference between coupled and uncoupled closed-loop roots is considerable for the engine-body mode. This difference, however, is not so great for the body-bending mode (the more critical one), although it could be important in a more marginal system than the one shown.

Figure 5-4 is another such comparison, this time for a body-bending mode and an engine-body mode quite close in frequency. Here, the coupling effect is proportionately greater, being critical to the system stability.

Since the effect of engine-body mode coupling may be considerable, it is not generally advisable to omit this mode in performing a stability check of a body mode. However, incorporation of this added mode, with its various couplings, greatly increases the labor in a manual computation. Hence, for a simple manual check it is recommended that the various couplings of the engine control mode be accounted for by incorporation of all the engine-servo compliances into the servo-actuator equations (see Appendix B4). In this way the various servo-mode couplings are represented in the resulting third- or fifth-order actuator function (cf. Equation 4-28, 4-28a) with a resulting control loop which can be treated manually (see Subsection 4.4).

While recommending this approach for simplified manual stability checks, the writers must add a word of caution as to the general accuracy of these results. Experience has shown that root calculations of high-frequency modes are subject to large errors from a variety of sources, a clean evaluation (or weighing) of which is difficult to impossible. It is equally difficult to say which method of solution (coupled body modes or one-mode-plus-higher-order actuator) gives the more accurate results. In numerous test problems, however, the preponderance of results indicated that the coupled body mode solution yielded the more conservative results. A sampling of these results is now given.
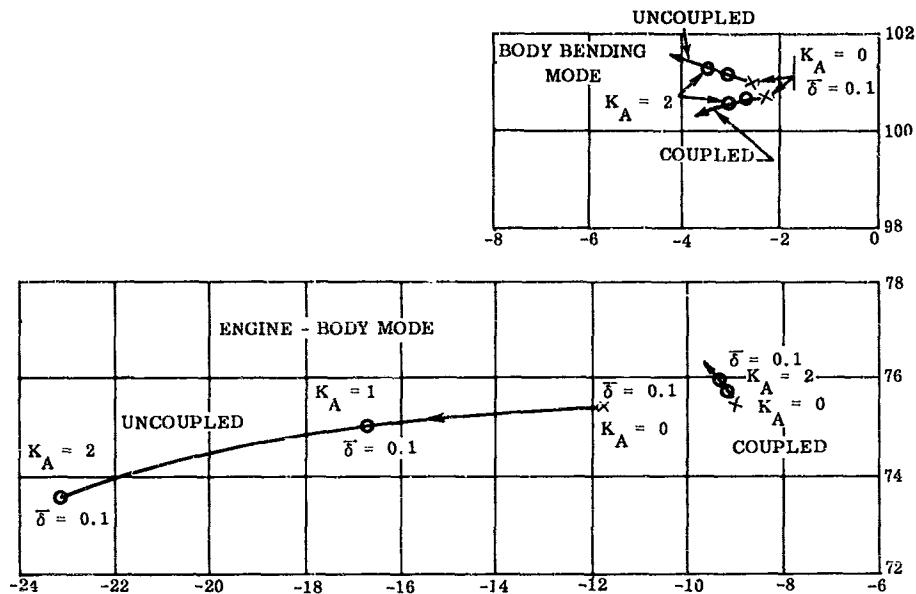
Figure 5-3. A Comparison of Closed Loop Roots for Two Modes (One an Engine-Body Mode)
with and without Coupling Through the Autopilot
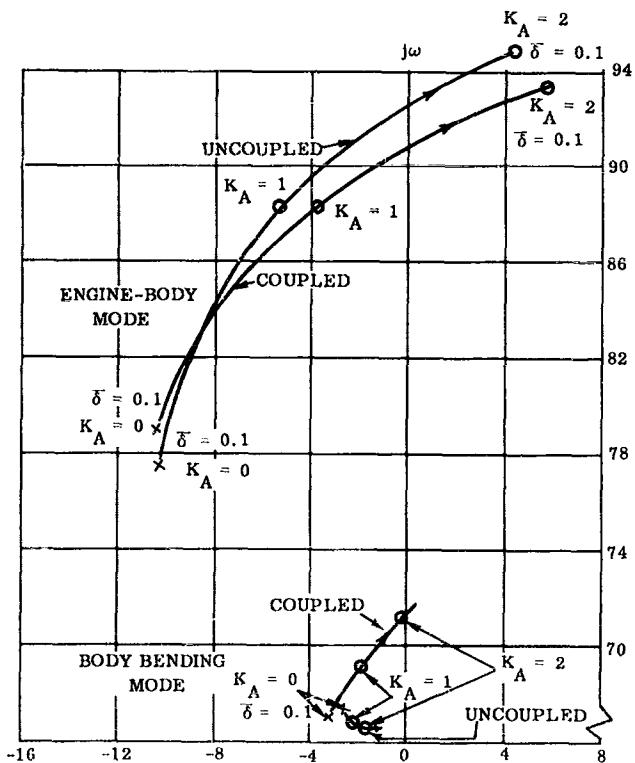
Figure 5-4. Coupled and Uncoupled Body and Engine-Body Modes with Small Frequency Separation

In Figure 5-5 roots are shown for a body mode whose frequency is well above (50 percent) that of the actuator mount resonance (about 73 radians per second). Roots were computed using this mode coupled to an engine-body mode; they also were computed for this mode plus higher-order (third) actuator. As may be seen, the results differ somewhat in gain and phase, the effective gain in the coupled mode system being greater. It is not possible to assert which result is actually the more accurate. The differences which appear are directly the result of elastic modal data differences (ϕ_i^1, σ^1 and $\mathcal{H}_1$), an absolute measure of which was not available in this frequency range.
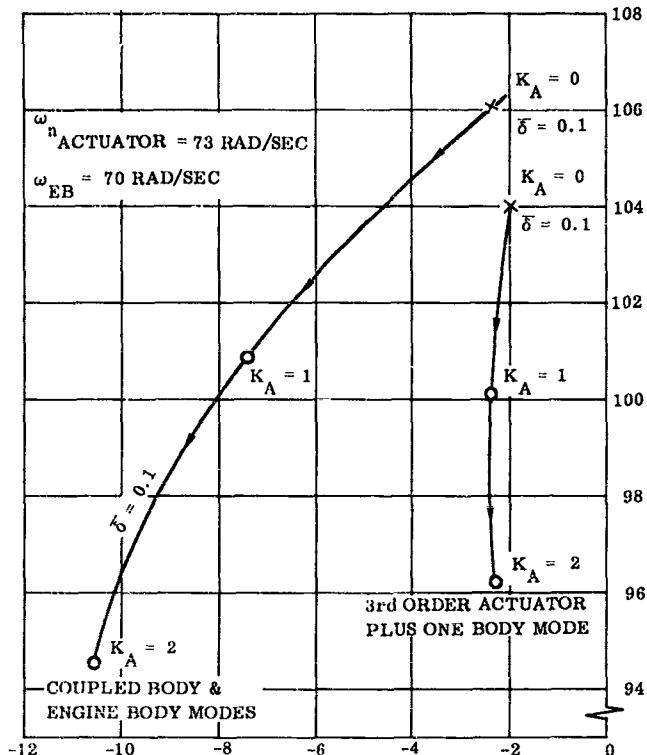
Figure 5-5. Comparison of a Body-Bending Mode's Closed-Loop Roots
by Two Solutions ($\omega_1 \sim 1.5 \, \omega$ actuator)

In Figure 5-6 a similar comparison is given of results for a body mode whose frequency is relatively close to that of the engine servo-actuator resonance. Here, the difference in results is very dramatic. However, this is a case where the higher order actuator should probably not be expected to yield good results; hence, the coupled-mode approach is recommended.*

In Figure 5-7 another body mode, well below (40 percent) the engine servo actuator resonance, is shown, as computed by each method. Here, the results show an apparently poorer agreement than might be expected. However, Figure 5-8 shows the reason. The proximity of this mode to the engine's TWD zero makes its gain very sensitive to movements of this zero.

---

* Note that for this problem the inertial feedback of the mode into the third order actuator (Equation 4-25 or 4-28) was employed to get the best results obtainable.
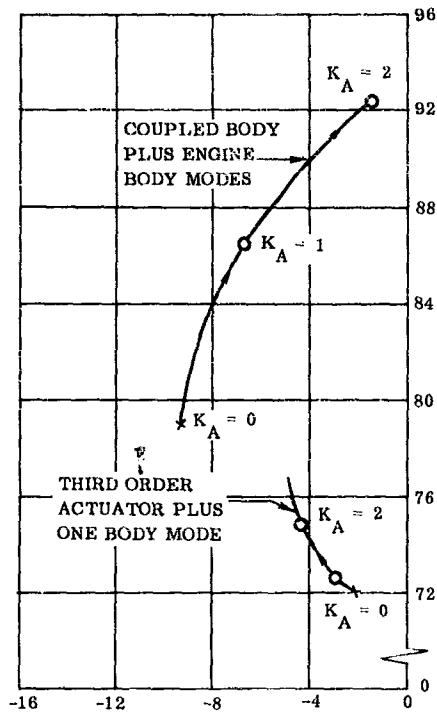
Figure 5-6. Comparison of a Body-Bending Mode's Closed-Loop Roots by Two Solutions $(\omega_i \sim \omega_{actuator})$
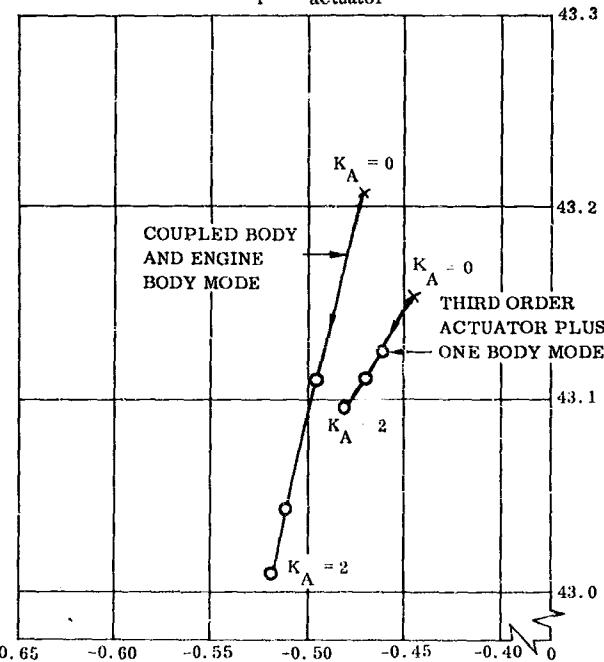
Figure 5-7. Comparison of a Body-Bending Mode's Closed-Loop Roots by Two Solutions $(\omega_i \sim 0.6\,\omega_{actuator})$
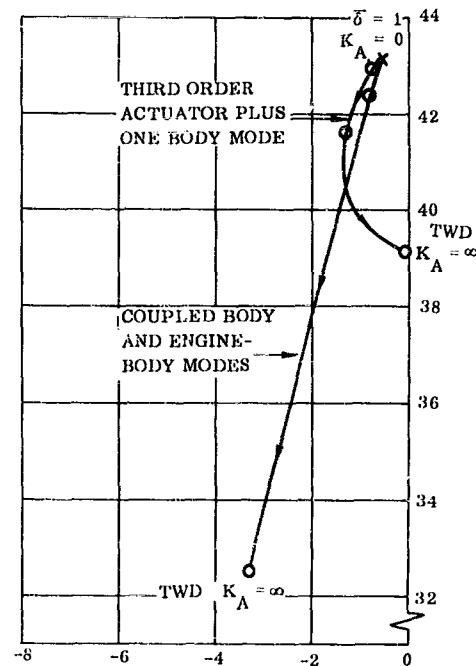
Figure 5-8. Solutions of Figure 5-7 on a Smaller Scale

In that the location of this zero is a function of the modal parameters (ϕ_{xT}, σ_{xT}, and σ_{xe}) and the bearing fric-

tion coefficient (C_f), these variations between the two solutions for the vehicle's modes* will result in different zero positions. Hence, a mode in this immediate vicinity will display a strong response to these changes. Fortunately, however, this same proximity to the TWD zero means that this mode is highly attenuated (note the very close proximity of the closed-loop root to the open-loop pole in Figure 5-7). Hence, the trouble here is more academic than actual.

Finally, we compare closed-loop roots for coupled versus uncoupled body-bending modes. These are displayed in Figures 5-9, 5-10, 5-11, and 5-12 for two vehicle body modes selected because of their relative frequency proximity. As may be seen, the effects of coupling between body-bending modes (engine-body modes excluded) are negligible.

---

* Remember that the coupled-body and engine-body solution uses modes in which the servo-elastic compliance was incorporated; the other solution uses modes computed for zero elastic compliance.
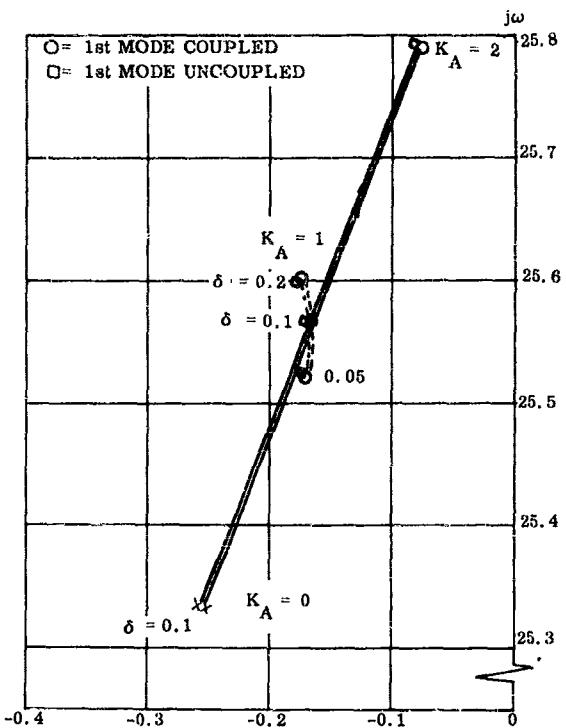
Figure 5-9. First Body-Bending Mode Closed Loop Roots, Coupled and Uncoupled
to Second Body-Bending Mode (At Lift-Off)
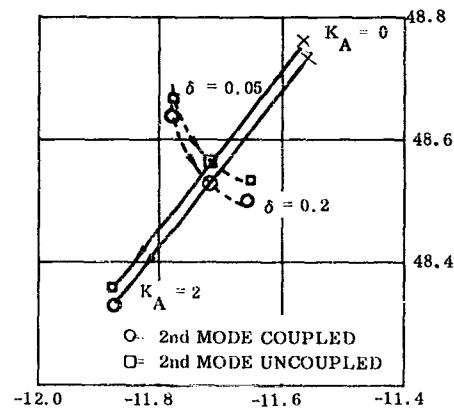
Figure 5-10. Second Body-Bending Mode Closed-Loop Roots, Coupled and Uncoupled
to First Body-Bending Mode (At Lift-Off)

114
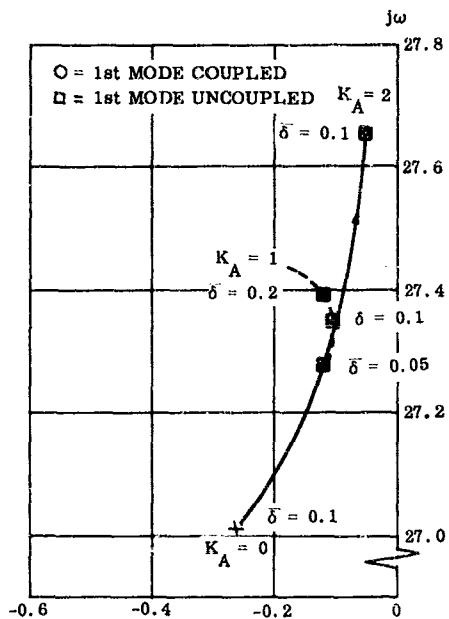
Figure 5-11. First Body-Bending Mode Closed-Loop Roots, Coupled and Uncoupled to the Second Body-Bending Mode (t $=$ 0.6T$_{staging}$)
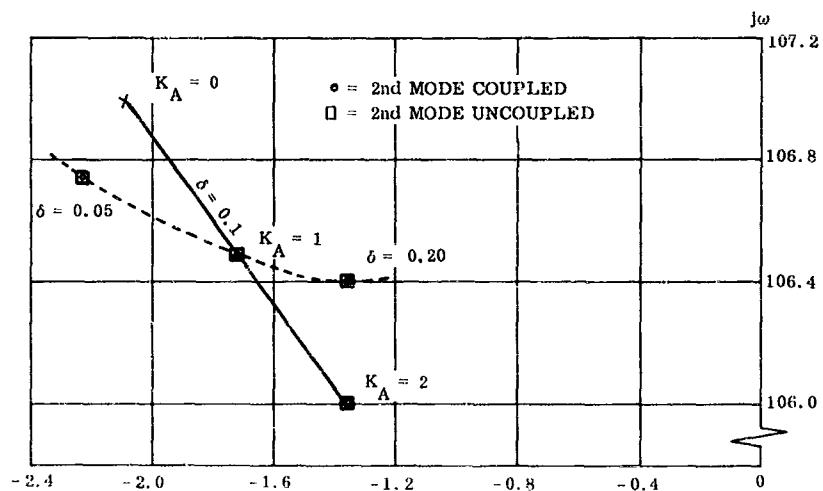
Figure 5-12. Second Body-Bending Mode Closed Loop Roots, Coupled and Uncoupled to the First Body-Bending Mode (t $=$ 0.6T$_{staging}$)

SECTION 6

COMPARISON OF ANALYTIC MODELS WITH TEST DATA

SYMBOLS USED IN SECTION 6

Symbol	Definition	Units
M_E	experimental normalized mass	slugs
M_A	analytic normalized mass	slugs
s	Laplace operator $(s = \sigma + j\omega)$	1/sec
Δx	servo feedback transducer deflection	ft
δ	rocket engine gimbal angle	rad
δ_c	rocket engine gimbal angle commanded	rad
δ_F	rocket engine gimbal angle feedback	rad
ϕ^{1-5}	normalized deflection for the 1-5 mode	ft/ft
ω_1	natural frequency of 1st mode	1/sec
ω_a	normalized natural frequency	1/sec
ω_A	analytic natural frequency	1/sec
ω_E	experimental natural frequency	1/sec
ω_o	undamped natural frequency	1/sec
ω	natural frequency of engine oscillation	1/sec

6.1 GENERAL

Regardless of the complexity, detail, and correctness of the analytic model chosen for the theoretical studies of a flexible booster, it remains an analytic model. Its similarity to the actual hardware components cannot be inferred simply because of the correctness of the mathematics used, but will depend upon the assumptions made and the accuracy with which the basic characteristics of the components and structure are known. Also, the validity of the autopilot and control system analyses will be directly related to how closely the model resembles the real quantities. Tests, and the subsequent use of test data, are the means by which analytical data and methods of approximation and simplification can be improved upon.

This section is divided into two subsections. The first subsection will contain discussions of particular testing done on autopilot components and missile airframes and of ground testing which complements the analytical studies. The second subsection will be limited to a qualitative discussion of information gained during flight tests. Most of the data presented is qualitative only; it is felt that the accuracies of the synthesis-analysis methods can be discussed adequately without the necessity of referring to quantitative data which is of value only in discussing a specific vehicle.

Two aspects of testing will be intermingled throughout the two sections; the first is a general discussion of the benefits of a test program and the second is a discussion of particular tests performed on control-system and bending-mode calculations on Atlas and Atlas space booster configurations. This discussion will be limited to possible benefits rather than the actual mechanics of testing and data reduction. The second topic is presented to back up the methods presented for the calculation of engine servo characteristics in Appendix B and modal properties in Appendix A.

6.2 GROUND TESTING

Ground testing will refer to all testing that is done under conditions that are not design flight conditions. Ground testing is of value, as it provides the earliest opportunity to check on the validity of certain simplifications and approximations used in the preliminary analysis; this testing may be carried out on components, subsystems, complete systems, and even a complete vehicle assembly.

Subsystem testing will be used to define two major areas of uncertainty concerning the preliminary analyses performed; one is the nature of various higher order effects and nonlinearities which were not included in the original analysis; the second is the check on specifications such as gain, phase, frequency, etc. of components and systems which were called out in the design studies. The system parameters may be sufficiently influenced by nonlinear behavior and by second order effects to alter the effective gains, thus altering the system stability margins. The testing then examines certain of the characteristics related to the simplifications and approximation discussed in Appendix B (Subsystem Transfer Functions). Effects which are discarded in applying certain simplifications may come back to haunt the analyst at this stage.

System testing, or testing of a major vehicle assembly, is usually accomplished to evaluate problems concerning the gross behavior of the vehicle. With respect to flight control problem areas, these tests concern overall vehicle modes and control system compatibility with other systems. Operation is observed using airborne power supplies (electric, hydraulic, etc.) under conditions of temperature, vibration, acoustic impingement and loads which most nearly duplicate actual flight environment.

Most system testing of a flexible booster is accomplished under conditions not completely compatible with those existing during flight. Certain constraints are placed upon the flexible booster by its support. This condition makes the accurate evaluation of extra degrees of freedom not included in the analytical model very difficult. Under such conditions it may be necessary to calculate the basic missile properties (elastic modes, propellant sloshing forces, and control system transfer functions) twice: first in order to analyze the in-flight conditions so that the autopilot and control system characteristics and gains may be determined and second, to determine the modes and control system transfer functions under captive conditions. These latter results may be compared directly with data taken on the test stands. A typical schematic comparison of two sets of modes obtained is illustrated in Figures 6-1, 6-2.

Figure 6-1 illustrates the general mode shapes for a vehicle in flight. These modes correspond to the classical "free-free" modes for a beam. In Figure 6-2 the modes with a test restraint are illustrated. These modes correspond to simple beam cantilever modes for the constraint shown. The frequency separation of the two modes is quite appreciable, with the second cantilever mode having about the same frequency as the first "free-free" mode.

FIRST MODE   SECOND MODE
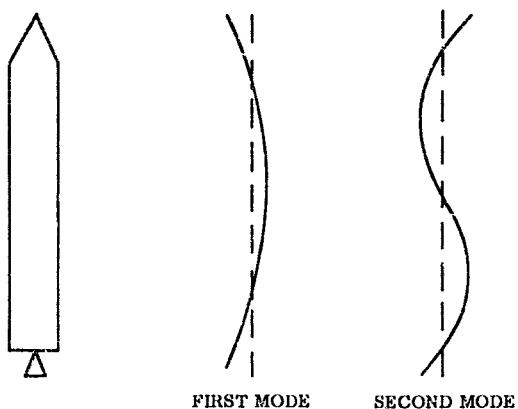
Figure 6-1. In-Flight Bending Modes

FIRST MODE   SECOND MODE
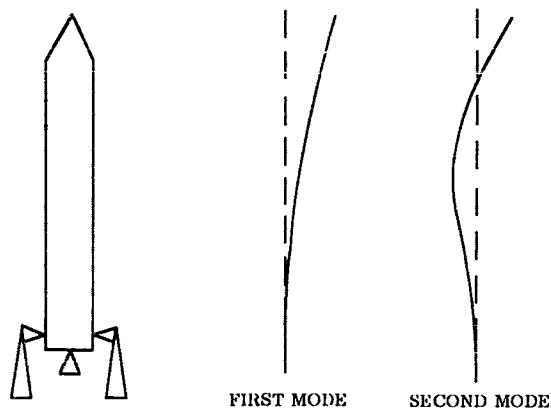
Figure 6-2. Bending Mode for Booster Restrained in Launcher

This double calculation of elastic properties may be necessary to verify the adequacy of the analytic model used. To insure direct comparison, the same booster and control system mass inertial and elastic data must be used in both cases. This then provides a check of the flexible booster model when subjected to test restraints which can be extrapolated to the in-flight simulation.

In addition to obtaining a check on major vehicle modes, the system testing also permits evaluation of such additional effects as:

a.   Evaluation of signal-noise pickup due to local mounting resonances and mechanical transmission of engine noise through the structure. Some of this signal noise may arise through cross-axis pickup in the sensor, such as pickup of accelerations about the output axis of a rate gyro.

b.   Evaluation of other effects associated with the firing of the rocket engines such as gimbal bearing friction measurements and engine alignment shifts due to strain deformation of the structure (from thrust, pressure, temperature).

Some of the subsystem and system tests of most direct concern with the evaluation of approximate transfer functions are discussed now in more detail.

6.2.1 <u>Control Element Positioning Servo.</u> The forces produced on the flexible booster by the control element and its positioning servos constitute the major generalized forces over which direct control can be maintained. These are in contrast to aerodynamic forces which are altered by disturbances (gusts and shears), over which no direct control is exercised, and the propellant sloshing forces, which are affected only slightly by the autopilot. A method of linearization has been presented in Appendix B4.2 for the class of electro-hydraulic control systems now in general use on large flexible boosters. This method makes use of describing functions to linearize the elements in the control system. Checking of the accuracy of this system's transfer functions is a prime objective of ground testing.

The analysis of the results of ground testing is complicated by the additional degrees of freedom which are inherent to the test setup. These include vehicle structural resonances which will be present in flight plus additional structural resonances due to test constraints. These resonances will quite often couple, making it difficult to separate the two and evaluate their individual effects. In addition, in both test and flight evaluation the instruments which are available may give an indirect measurement of the desired data.

As an illustration of the preceding let us examine the schematic of a rocket engine control servo (Figure 6-3).
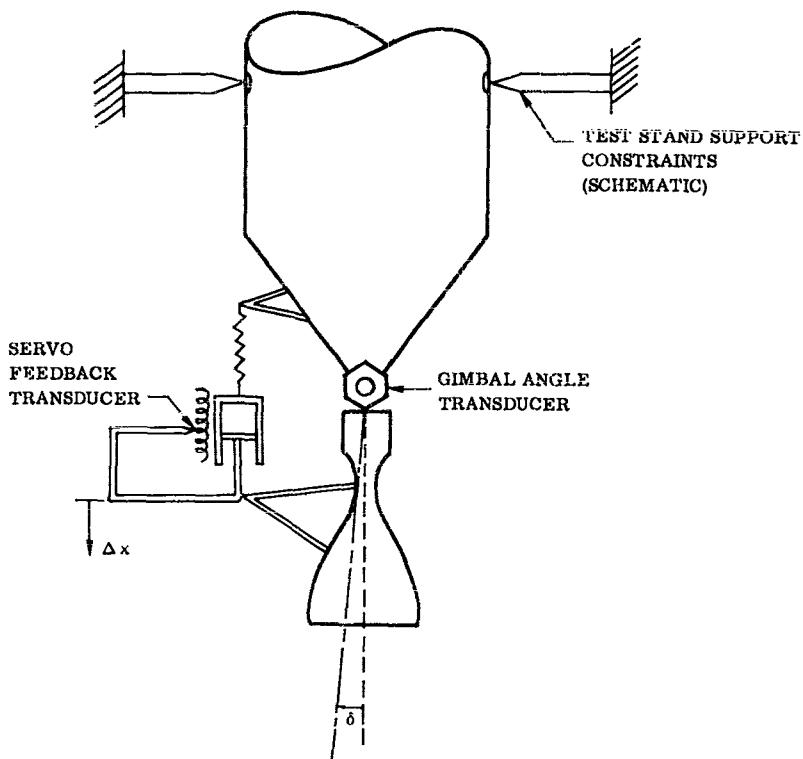
Figure 6-3. Schematic of Electro-Hydraulic Engine Position Servo

In Figure 6-3 the desired measurement is the inertial angle, δ, since the control forces produced are a direct function of this angle. This angle is not, however, exactly equal to the output of the gimbal angle transducer. The output will contain the effects of rotation of gimbal block, engine mount elasticity, booster elasticity, and rigid motion of the booster due to the test stand response. In addition, the gimbal, which may contain two degrees of rotational freedom, is a difficult place to install an accurate transducer. In effect, the output of the gimbal angle transducer is sufficiently accurate only at frequencies below the main support structure's resonant frequency.

The output of the servo feedback transducer is altogether different. It is rigidly mounted to the actuator and its output will be ΔX, as indicated in Figure 6-3. As the servo feedback transducer is an integral part of the control system, it will usually be a more precise unit than the gimbal angle transducer which is used only for test monitoring. The relationship between this transducer's output (Δx) and the thrust chamber swing (δ) is also affected by structural compliance: in this case, the actuator attachment rigging flexibility. Thus, the feedback transducer is not an accurate measure of the engine angle, δ, unless the compliance is accounted for.

Figure 6-4 shows a comparison between Δx and δ test data. This configuration had a massive thrust structure on which the gimbal block was mounted; hence, the measured δ data was not affected by resonances at the gimbal within the frequency band shown. As may be seen, however, the actuator mount stiffness resonance had pronounced effects upon the Δx data.
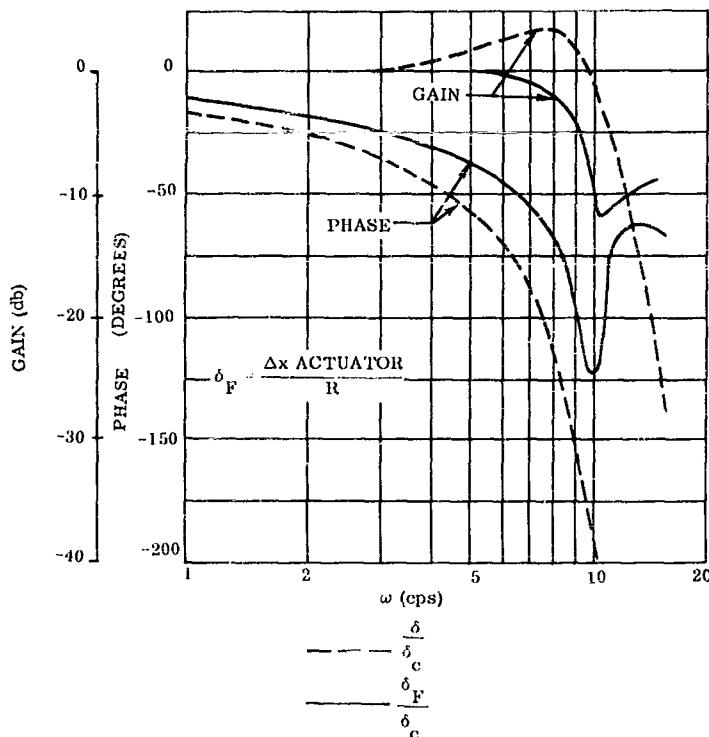
Figure 6-4. Test Data Comparison of Δx and δ vs. δ_c

To get a useful verification of the δ/δ_c transfer function, comparisons between test data and the mathematical model must be made for both $\Delta x/\delta_c$ and δ/δ_c, with the $\Delta x/\delta_c$ test data generally being the more reliable. The two responses shown in Figure 6-5 indicate the agreement that can be expected between a detailed nonlinear analog simulation and test data.

After the accuracy of the nonlinear mathematical model has been verified, the analyst may seek a simpler linear model which will match the system's behavior adequately and yet will facilitate more stability analysis. A plot of the linearized simulation of the third order actuator of Appendix B4.2 is compared with an analog simulation's amplitudes in Figure 6-6.

The preceding discussions indicate the adequacy of both the analog and the linearized simulation in representing the control element and servo system for analysis of a flexible booster and control system. They also indicate how analytical tools can be used to verify data relationships obtained on test stands.

STATIC TEST (HOT FIRING)

——— THEORETICAL FREQUENCY RESPONSE
(ANALOG COMPUTER)
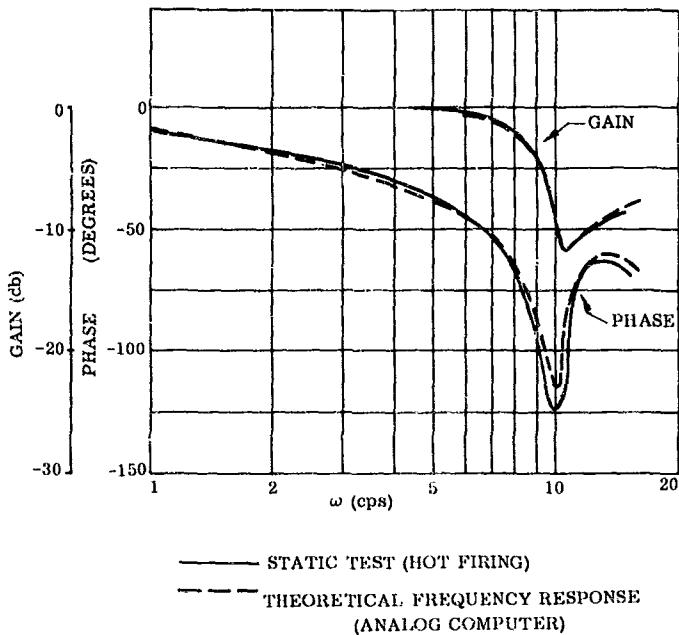
Figure 6-5. Comparison of Analog Versus Static Test (Hot Firing);
Vehicle Restrained by Launcher

6.2.2 Bending Mode Tests.

6.2.2.1 Mode Frequency and Deflection. Studies of an autopilot and control system, in connection with the flexible booster bending dynamics, have shown the importance of accurate mode shape, frequency, and damping data. If structural properties are not sufficiently defined, unstable booster conditions may result, or, (more rarely) an unnecessarily complex autopilot design may result. Much previous work on both missile and airplanes has been directed toward ground testing for determination of in-flight bending mode shapes and frequencies. The results, in general, have not been too promising, resulting in appreciable differences between calculated and observed bending modes for some configurations. The agreement, in general, worsens on the higher modes. This lack of agreement is normally attributed to the influence of constraints on the elastic motion of the missile.

To attempt to verify the adequacy of the methods used to calculate mode shapes, a series of tests were performed on a full size Atlas tank. Two particular Atlas configurations were chosen as test specimens, since there existed a large amount of theoretical calculations with which the test data could be compared. The missile used in these tests was as close to a flight configuration as reasonable, except that the engines were removed; therefore, the elastic modes were calculated with the engine masses removed.

The nature of this type of testing led to the consideration of a soft suspension having an absolute minimum of damping. The suspension system used for these tests consisted of a set of thin vertical columns placed under the engine gimbal blocks and a separate stabilizer to hold the missile erect. This method was considered best suited to simulate actual flight conditions accurately. A schematic representation of this suspension system is given in Figures 6-7 and 6-8. The suspension system provided relatively great lateral and rotational flexibility in one plane, and the support structure also prevented rotation in the other plane. The system was designed to operate with stresses well below the proportional limit. The use of bearings was avoided to eliminate parasitic damping due to friction (Reference 8).

This test setup uses the acceleration of gravity to represent the engine thrust forces. The upright position of the missile aligns these forces in the same direction as the thrust forces would be during flight. The limitation of acceleration forces to one g was not expected to have an appreciable effect on the motion of the bending modes. Since the Atlas is a fairly rigid missile, longitudinal forces can be largely ignored in the computation of lateral
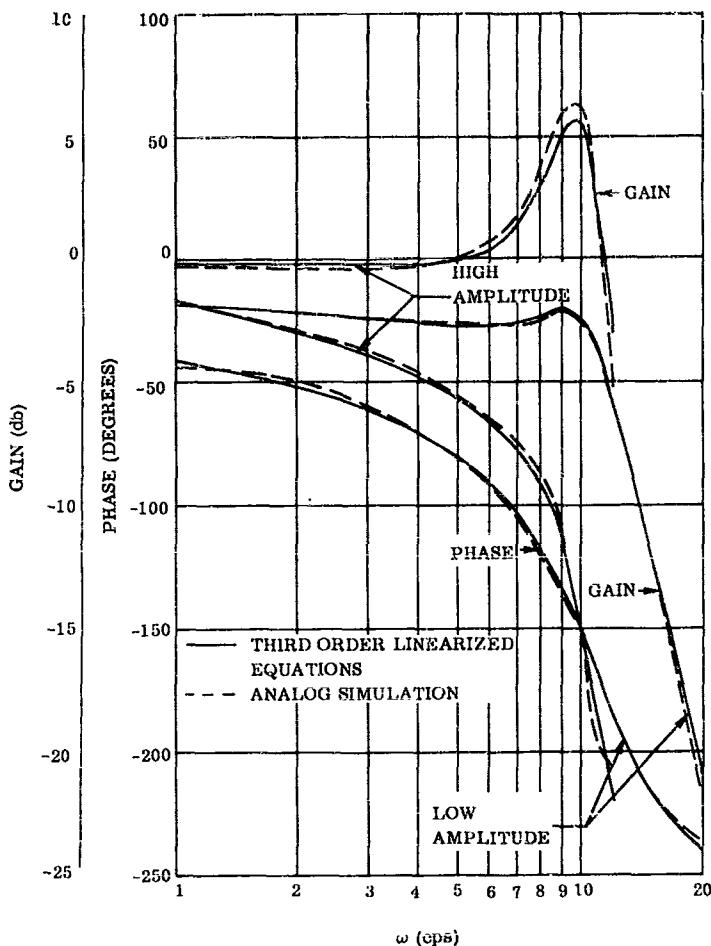
Figure 6-6. Comparison of Analog Simulation Versus Third Order Linearized Equations

bending modes. Vibration tests were performed at various propellant tanking levels, and the tanks were instrumented to obtain mode shapes and damping factors. During testing missile fuel and oxidizer were both represented by water. The amounts of water used were varied to correspond to different instants of flight. Thus the mode data was checked for various times during flight.

Two configurations were evaluated; one was an ICBM configuration, the other was a space booster configuration where the payload was a smaller diameter upper stage. For the tests this upper stage was represented by a dummy stage, as shown in Figure 6-8.

The missile was disturbed for testing by a hydraulic shaker attached to the engine gimbal blocks. The other end of the shaker was attached to a large reaction mass. Since the damping of a normal mode was to be obtained by a free decay, provisions were made to disconnect the shaker from the missile on command.

The missile motion was instrumented by accelerometers only. Thus the slopes of the missile sections were not measured directly but had to be inferred from plotted displacement data. The accelerometers used were of a variety which could be attached directly to the missile skin without cutting or stiffening the skin. In addition, several position transducers were placed between the missile and a service tower.
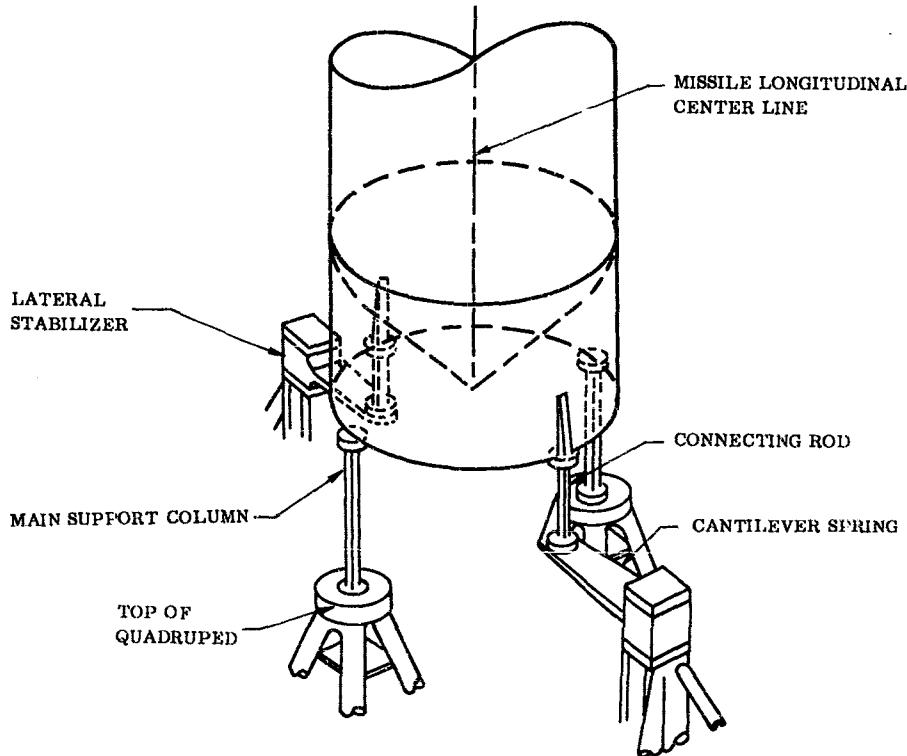
Figure 6-7. Booster Phase Suspension System

Test data will be presented for a typical time of flight. The variation of frequency with flight time is given in Figure 6-9. This figure shows the increase in the modal frequencies as the missile becomes lighter during flight, through expenditure of propellants.

A frequency response of the full condition is given in Figure 6-10. This figure is a plot of nose acceleration for a constant force input. The effect of the first five natural bending modes can be clearly seen.

The theoretical and test results for the first five bending modes are shown in Figures 6-11, 6-12, 6-13, 6-14 and 6-15.

The results (Figures 6-11 through 6-15) illustrate that the shapes of the experimental and analytic modes do not always agree. The frequencies are predicted most accurately, with the mode shape itself being less accurate. A significant "figure of merit" is the gain with which the engine forces excite bending modes; it is inversely proportional to the generalized mass. For the preceding modes the ratios of analytic to experimental generalized masses are as follows:

Mode	Gain Constant
1	0.96
2	1.39
3	0.36
4	1.25
5	2.03

127
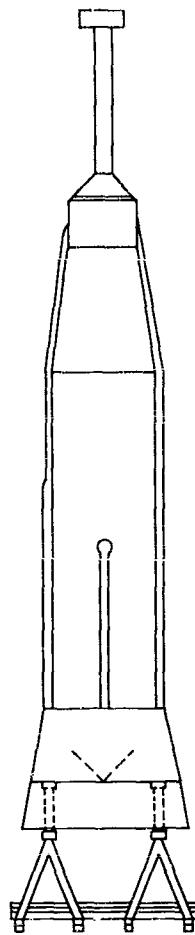
Figure 6-8. Missile Support System Showing Missile with Dummy Upper Stage Attached
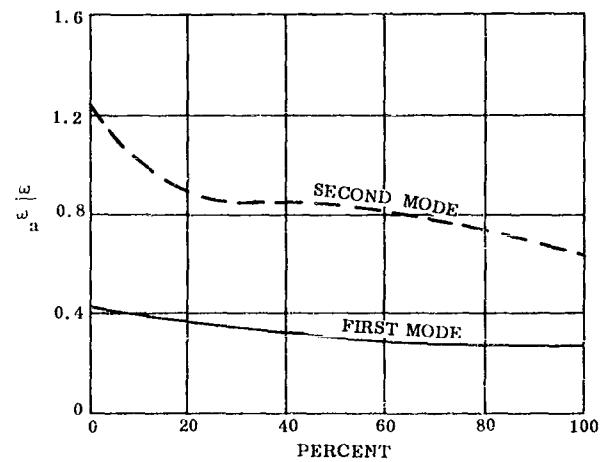
Figure 6-9. Frequency Versus Nominal Percent of Tank Volumes Filled with Liquid
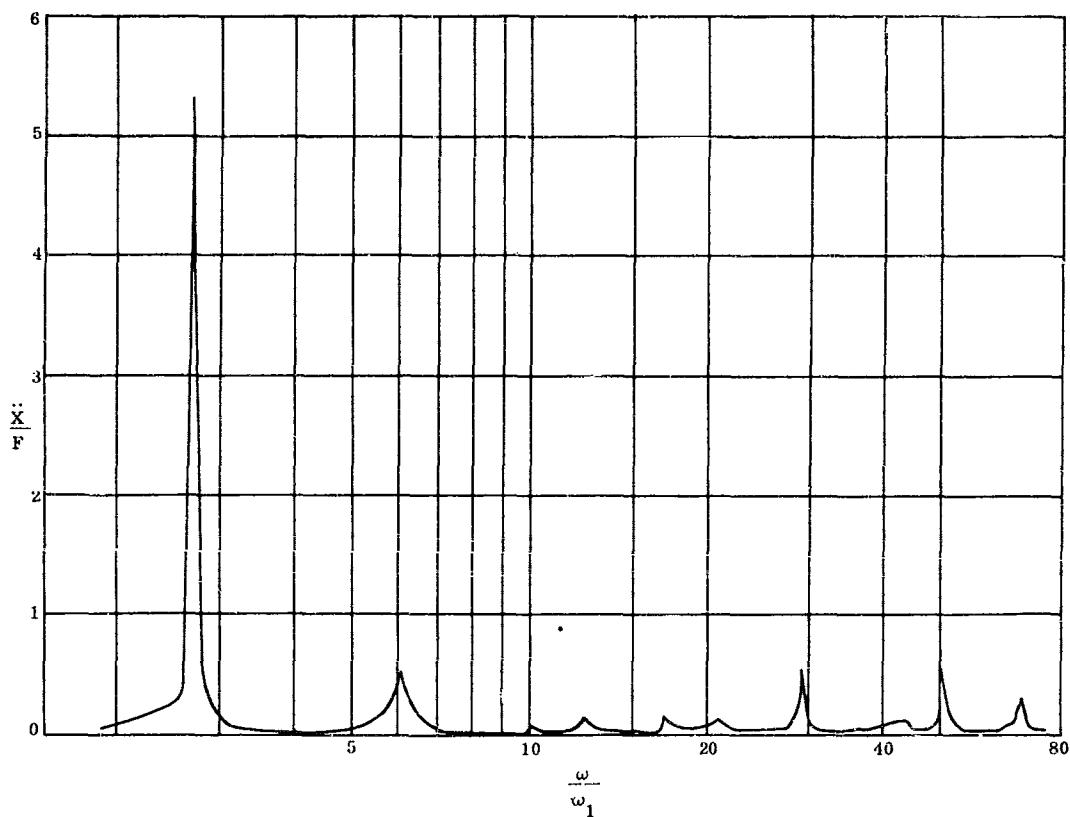
Figure 6-10. Frequency Response Curve
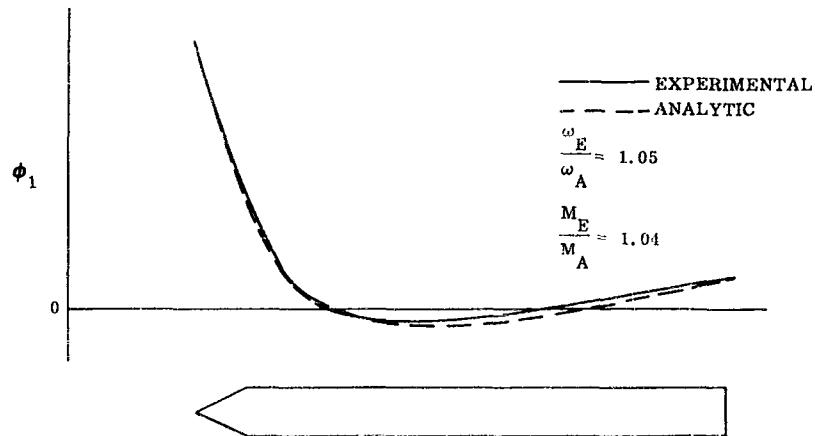
Figure 6-11. First Mode Comparison of Experimental vs. Analytic Modes
for a Space Booster Configuration

EXPERIMENTAL —————————
ANALYTIC   — — — — —

$\dfrac{\omega_E}{\omega_A} = 0.885$

$\dfrac{M_E}{M_A} = 0.718$

ϕ_2

0
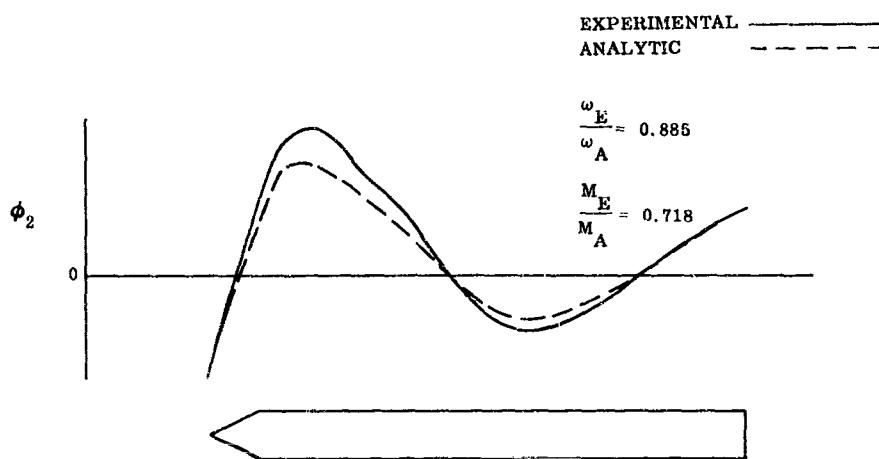
Figure 6-12. Second Mode Comparison of Experimental vs. Analytic Modes for a Space Booster Configuration

0

ϕ_3

$\dfrac{\omega_E}{\omega_A} = 1.06$

$\dfrac{M_E}{M_A} = 2.77$

————— EXPERIMENTAL
— — — ANALYTIC
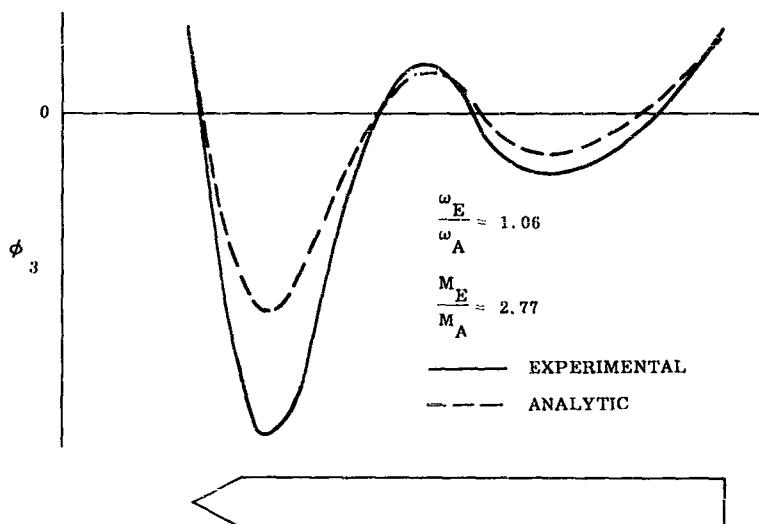
Figure 6-13. Third Mode Comparison of Experimental vs. Analytic Modes for a Space Booster Configuration
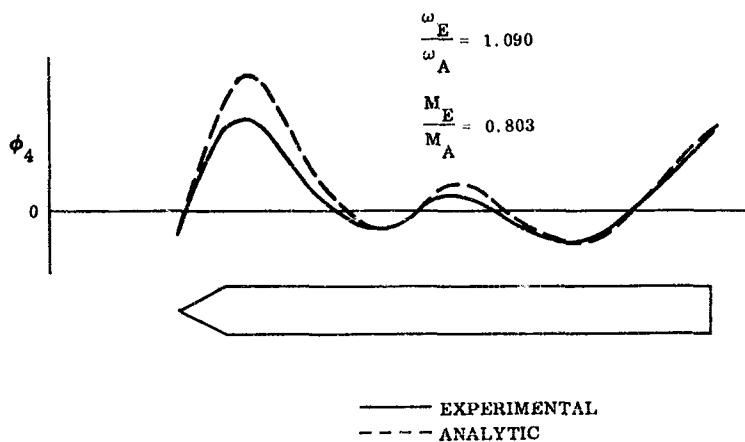
Figure 6-14. Fourth Mode Comparison of Experimental vs. Analytic Modes
for a Space Booster Configuration
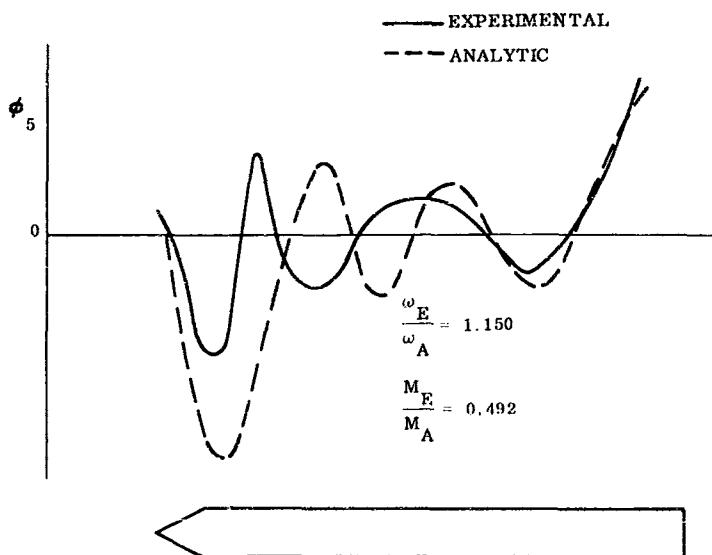
Figure 6-15. Fifth Mode Comparison of Experimental vs. Analytic Modes
for a Space Booster Configuration

The modes illustrated are representative of the accuracy that would normally be obtained from the calculation of modes by the methods outlined in Appendix A3. As can be observed, the agreement in the frequencies is best, with the mode shape and its attendant gain becoming less accurate for the higher modes.

In addition to determination of mode shapes and frequencies, bending mode testing such as this can be used to provide vibration environment information on components attached to the skin of the missile. Such information is useful, as the local motion of the skin may be altered by large masses (autopilot components, antennas, batteries, etc.) attached to it. The motion of these masses attached to the skin can best be determined through testing. These motions may be useful in formulating the vibration specifications which the components must be designed to withstand. The relationship between the mass motion and the mode motion can be obtained very accurately at this time.

6.2.2.2 Mode Damping. Theoretical studies of control system stability as well as other studies involving dynamic response of missiles require accurate knowledge of damping factors. These damping forces can be considered to be the overall effect of innumerable small frictional forces that tend to resist deformation of the missile. These small forces include all the different kinds of friction (coulomb, viscous, mechanical hysteresis, etc.) that occur in and between the various parts of the missile. The importance of each of these frictional forces in a given mode depends upon the relative amount of deformation in or between the various parts, which, in turn, is a function of the mode shape. If follows, then, that different modes may have different damping factors. Also, if a mode shape is altered by a change in mass or by an external constraint, the corresponding damping factor may be changed.

In the tests two configurations were analyzed - one a regular Atlas configuration and the other a space booster configuration with a long slender payload (Figure 6-8). This payload was simulated by a weighted beam. The tests of the space booster configuration indicated a damping factor that was quite low when compared to those of the conventional Atlas. It was felt, then, that the use of the "clean" beam for a composite structure had the effect of lowering the damping for the composite vehicle below what would be expected if the actual payload were installed. The data from the Atlas corresponded closely with that expected from previous studies. The results of the damping studies on the two configurations are presented in Figures 6-16 and 6-17. In some cases damping was observed to vary with amplitude, increasing with increasing amplitude. In Figure 6-16, for the second mode, two values are shown. The damping appeared to be double-valued - higher at high amplitudes and lower at low amplitudes, with a sharp transition between the two points. The results of the Atlas configuration are shown in Figure 6-17.
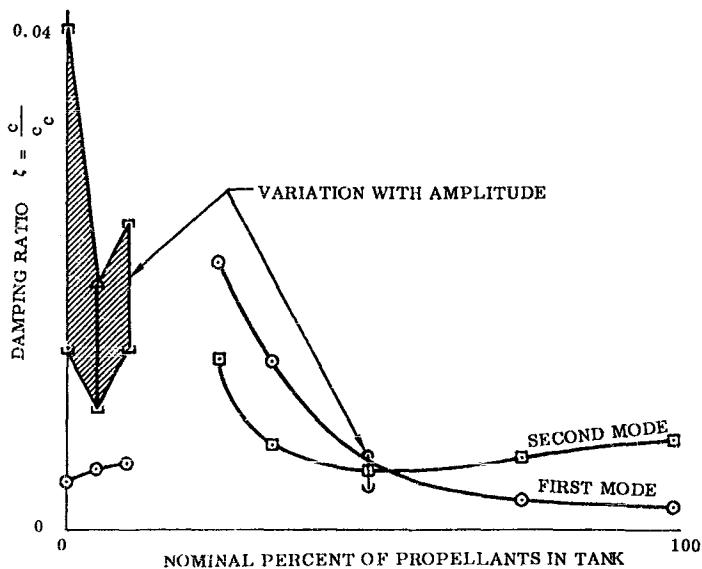
Figure 6-16. Mode Damping vs. Nominal Percent of Tank Volumes Filled
with Liquid, Space Booster Configuration
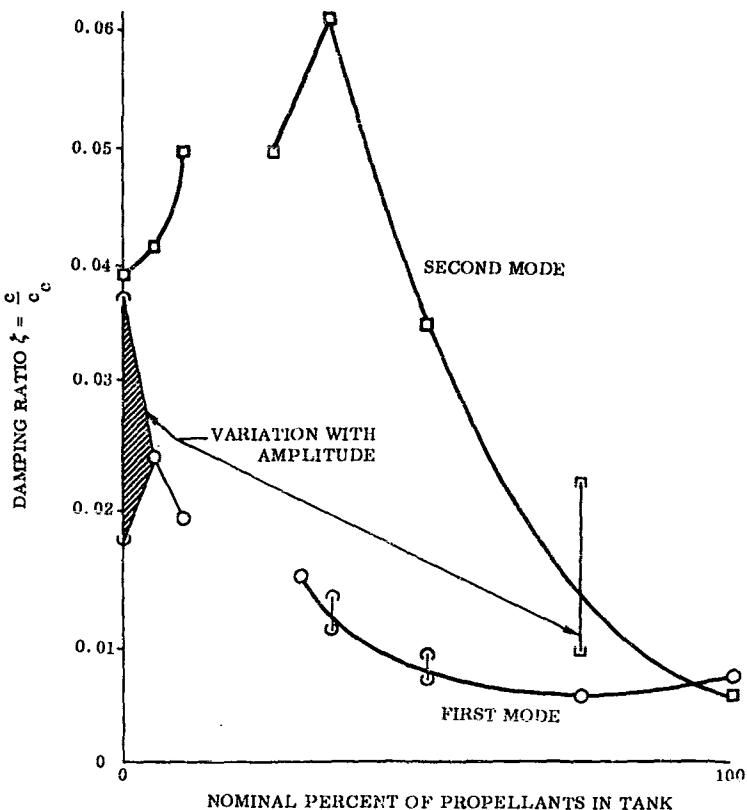
Figure 6-17. Mode Damping vs. Nominal Percent of Tank Volumes Filled
with Liquid, Atlas ICBM

In general the damping tends to increase as one goes on to the higher modes, but specific exceptions were found; an occasional higher mode occurs with low damping.

6.3 FLIGHT TESTS

Flight testing constitutes the final "proof-of-the-pudding", so to speak. On some of the small missiles it has been possible to do a large amount of propulsion, structural, aerodynamic, and control system testing as flight testing. With the larger, more expensive boosters it is prohibitive to attempt extensive design testing as flight testing. Therefore, except for specific blunders leading to dramatic instabilities, little quantitative information relative to stability margins will be obtained through flight testing. Some information can be obtained on a chance basis, and through careful evaluation of this data a great deal can be learned from this information.

The data that can be acquired is limited by the instrumentation available and by the fact that the various modes on which one wishes information may not be excited. The stable modes (propellant sloshing and elastic) will have to be excited by launch transients, random system transients, or "built-in" transients; otherwise they will not be observed during the flight. Those that are observed give data which can be used to check frequency and damping ratio of the predicted modes. The frequency can be used as a check on the modal data, and the damping ratio can be compared with that predicted from the root studies as an autopilot and control system check.

Propellant sloshing modes are usually excited at various instants during flight. These motions give excellent chances to observe the frequencies of oscillation under accelerations in excess of that of gravity. The agreement

in frequency with that predicted in Appendix A has been excellent. The test data on propellant sloshing is presented with the methods for calculation of the analogy in Appendix A.

Bending mode frequencies, as seen from flight transients, are those of the closed-loop roots and as such differ very slightly from the predicted modal frequencies. The difference is usually less than the error in computing the open-loop modal frequencies, themselves. Hence, these in-flight frequencies are usually compared directly with computed normal mode frequencies; the agreement is generally very satisfactory.

Damping ratios of in-flight oscillations, as compared with predicted values from root studies, have minor value except to point out gross errors in the analysis (such as the wrong sign of the real part of a root!). The difficulty can be illustrated by observing an actual locus presented in Figure 6-18. This figure shows the uncertainties in the location of the operating point. From a glance at this locus it is apparent that even extreme motions of the angle of departure and gain would be hard to spot merely by observing the damping in the closed-loop mode's root.
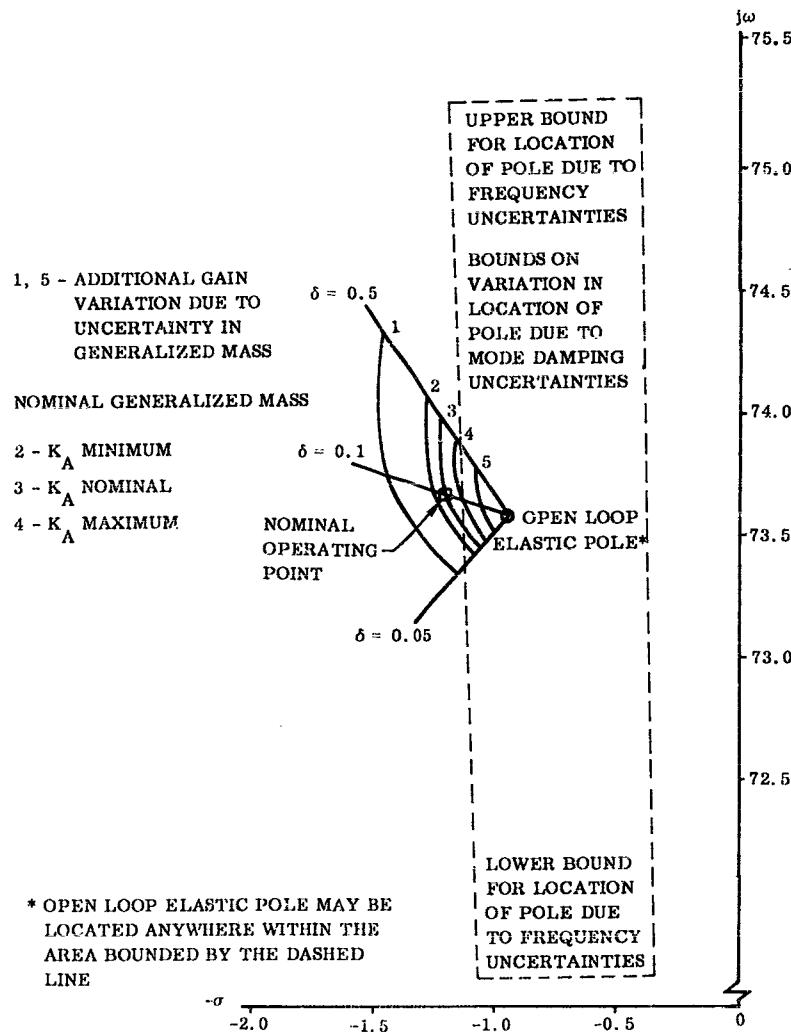
Figure 6-18. Variations Possible in Location of Closed Loop Operating Gain

Flight tests sometimes reveal major omissions in the analysis when these omissions result in a system which, although predicted to be stable, becomes unstable. Although extensive analysis had been performed prior to the first Atlas flights, a 17-cps limit cycle oscillation (third body bending mode) appeared which was of considerable magnitude. An evaluation of the simulations used for preflight analysis indicated several deficiencies in the assumptions used. These deficiencies were primarily connected with the method used to simulate the rocket engine hydraulic servo forces, moments, and deflections. By using a more complete analysis, made possible by a large amount of laboratory and captive missile testing, it was possible to simulate more correctly the conditions occurring in flight. The revised simulation indicated that the third mode could be stabilized by the addition of a lag filter in the control loop. The results from flight test were gratifying in that stable operation was achieved.

Later in the Atlas flight test program a modified configuration exhibited a high-frequency limit cycle oscillation (4th and 5th body bending mode). The methods of analysis were rechecked without result, so it was determined that the mode shapes employed must be in error. Up to this time the vehicle elastic modes had been calculated with the rocket engines removed. The engine forces and moments were then added as generalized forces onto the mode. The inaccuracies resulting from this method can be explained best by observing the schematic missile and mode of Figure 6-19. The aft end of the missile with the engines removed has little mass; hence, the aft
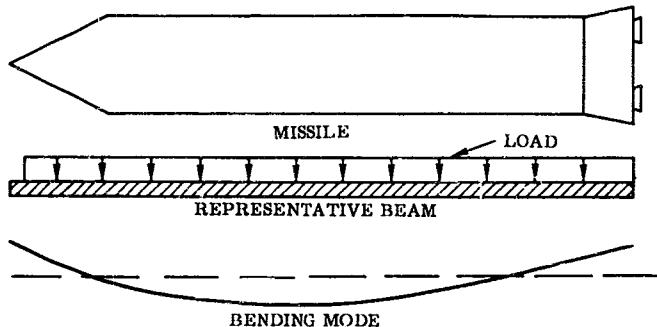
Figure 6-19. Schematic Bending Mode with Engine Masses Excluded
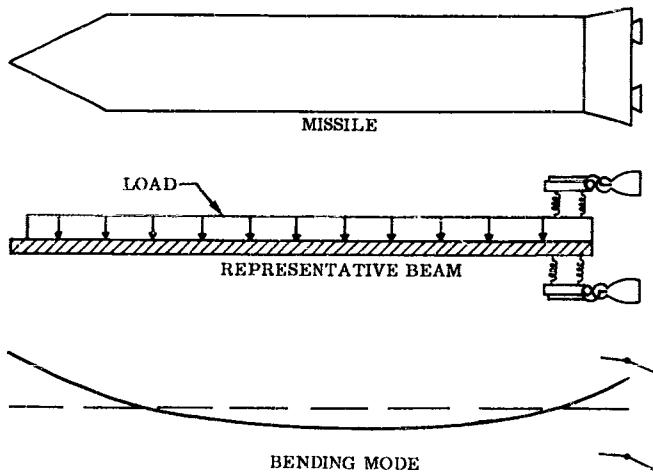
Figure 6-20. Schematic Bending Mode with Engine Masses Included

portion of the modes is relatively straight (no shear or couples at the free end). Therefore, if forces and moments representing the engines are to be added at this point, a large number of modes must be used to represent the actual missile deflection by means of body bending modes. As the analysis is usually carried on with few modes only, errors can result. These errors are not usually significant at frequencies below the aft structure engine mount natural frequency. However, at frequencies near or above this natural frequency the effect can be quite significant, even causing a 180-degree phase reversal in the inertial coupling between engine chamber and mode. This reversal can be seen by the schematic representation of Figure 6-20. Figure 6-20 shows more curvature at the aft end and also illustrates that the engine and mount may be out of phase with the bending mode shape at this point. This phenomenon can effectively reverse the angle of departure of the locus of roots from the pole representing the elastic motion.

The methods of simulation using modes calculated with the engines included furnish good agreement between theoretical and flight test data, to the degree that flight instabilities in these higher modes have been analyzed satisfactorily. The major caution is that for the frequencies of the higher modes the representation of the properties becomes more involved and the accuracies more dubious. Thus, attempts to phase-stabilize the higher modes may meet with failure due to improper agreement of analytic models with the actual booster.

SECTION 7

CONCLUSIONS

7.1 GENERAL

Utilizing the material presented in this report the following concluding remarks can be made:

a.   The basic equations and transfer functions that may be used for first approximation (quick-look) analyses are presented in Section 4. Typical applications are shown in Section 2. The simplified transfer functions of Section 4 are valid for preliminary evaluation of most classes of ballistic booster vehicles.*

b.   The more complete set of system equations of motion, as may be used for comprehensive analyses, are given in Section 3.

c.   The equations of Section 3 are subjected to various simplifying assumptions in Section 4.

These simplifications fall into two general categories, viz., those which simplify coefficients of an equation without changing its order and those which reduce the order of the equations.

Those simplifications which fall into the first group cause no great problem, as they can always be checked and re-incorporated for any configuration about which doubt exists. Those simplifications which reduce the order of the equation are more troublesome to justify.

The majority of difficulties arise when the engine servo elastic mode must be considered coupled to the vehicle normal elastic modes. A qualitative discussion of these couplings is presented in Section 4, Sub-sections 4.3.2, 4.3.4, and 4.3.5.

The open loop coupling due to aerodynamics is generally negligible in the class of vehicles considered.

d.   The results obtained utilizing the simplifications of Section 4 are compared with results from the solution of more complete equations in Section 5. The effects of two general classes of coupling are displayed: 1) open-loop coupling between modes due to non-conservative forces coupling through rocket engine servo compliance and 2) closed-loop couplings through the control system. Quantitative results are presented for specific cases (typical ICBM configuration).

The simplifications involving elimination of secondary feedback terms have little effect for the low frequency modes (rigid-body and propellant sloshing). However, for the higher modes the various coupling effects and/or auxiliary feedback paths can occasionally be very significant. Results also indicate that the simplified approach using a single elastic mode equation with the third order actuator of Equation 4-23 can be used for modes whose frequencies are well removed from that of the actuator servo resonant frequency. For frequencies close to those of the actuator, an engine-body mode must be coupled to the body bending mode being analyzed.

e.   The accuracy of the results is dependent upon the adequacy of the basic data used. Some comparisons of calculated data versus test results are given in Section 6.

f.   Information on methods used to compute basic data for the calculation of the transfer functions is presented in Appendix A.

g.   A discussion of some types of subsystem transfer functions, sensors, servos, and force producers necessary to complete the booster vehicle-autopilot and control system analyses are presented in Appendix B.

---

*Some extreme future configuration may not be adequately represented. Such cases, however, will receive special treatment by the analysts, using the same principles.

SECTION 8

BIBLIOGRAPHY

1. Ferner, R. O. and Schmitt, A. F., "Navigation Guidance and Control Problems for Aerospace Vehicles," Chapter 15 of Computer and Controls Technology, The McGraw-Hill Book Company, 1961.

2. Lukens, D. R., "Methods of Analysis of a Control System for a Large Flexible Missile," Institute of Aeronautical Sciences National Specialists Meeting on Guidance of Aerospace Vehicles, 1960.

3. Truxal, John G., Control System Synthesis, The McGraw-Hill Book Company, 1955.

4. Sissenwine, N., "Windspeed Profile, Windshear and Gusts for Design of Guidance Systems for Vertically Rising Air Vehicles," AFCRC-TN-54-22, November 1954.

5. Court, A., "Vertical Correlations of Wind Components," AFCRC-TN-57-292, March 1957.

6. Bisplinghoff, R. et al., Aeroelasticity, The Addison-Wesley Publishing Company, 1955.

7. Scanlan, R. H. and Rosenbaum, R., Introduction to the Study of Aircraft Vibration and Flutter, The Macmillan Company, 1951.

8. LeVeck, F. W. Jr. and Leondis, A. F., "Parameter Study of Atlas Bending Modes," (Unclassified Title), Convair (Astronautics) Division General Dynamics Corporation, Report AE60-0230, 15 September 1960. (Confidential)

9. Adams, Mac C. and Sears, W. R., "Slender Body Theory - Review and Extension," Journal of Aeronautical Sciences, 1953, pp. 85-98.

10. Ashley, K. and Zartarian, G., "Piston Theory - A New Aerodynamic Tool for the Aeroelastician," Journal of Aeronautical Sciences, December 1956.

11. "Fundamentals of Design of Piloted Aircraft Flight-Control Systems", Vol. II, "Dynamics of the Aircraft," Bureau of Aeronautics Report AE-61-4.

12. Everhart, P. E. and Lindsey, W. F., "Observations on the Flows Past Blunt Bodies at Transonic Speeds," (U) NASA TM X-169, Washington, 1960. (Confidential)

13. Daley, B. N. and Humphreys, M. D., "Effects of Compressibility on the Flow Past Thick Airfoil Sections," NACA TN 1657, Washington, July 1948.

14. Hobbs, N. P., et al., "Development of Interim Wind, Wind Shear, and Gust Criteria for Vertically-Rising Vehicles," (U) WADC Technical Report 59-504, July 1959. (Secret)

15. Greensite, A. L., "Analysis of Liquid Propellant Mode Stability of a Multitank Ballistic Booster Vehicle," Journal of Aerospace Sciences, (to be published 1961).

APPENDIX A

DEVELOPMENT OF BASIC DATA

A1 INTRODUCTION

In order to determine the numerical value of an approximate transfer function that can be used to analyze the stability of any given configuration, it is necessary to evaluate the equations' coefficients. To compute these system equation coefficients, in turn, requires that certain data relative to the vehicle's flight path and body parameters be available. This data, referred to as "basic data", is an accumulation of: 1) trajectory data, 2) aerodynamic data, 3) propellant load data (if required), 4) elastic (modal) data, and 5) mass, center-of-gravity, and other inertial data, all compiled at many discrete time instants during the vehicle's powered flight. Other values may then be interpolated from these points, giving the data at any instant of the vehicle's powered flight.

Some general remarks on the methods used for obtaining these basic data are given first in the four classifications: trajectory, aerodynamic, propellant, and mass, center of gravity, and inertial data. Subsequently, more detailed discussions are given of the derivation of certain of these data, a knowledge of whose origins is important to any appreciation of the degree of approximation involved in autopilot studies. Also given is a detailed discussion of elastic (modal) calculation methods.

A1.1 **Trajectory Data.** Some of the trajectory parameters required for an analysis of the autopilot stability and control problem are thrust (both fixed and gimbaled), weight, acceleration along the vehicle's flight path, and its time integrals, velocity, and altitude. All are required as functions of powered flight time. From this information, additional data such as dynamic pressure and Mach number may be computed.

As a first approximation, a trajectory computed for a point-mass (two degrees of freedom) launched in a standard atmosphere from a nonrotating spherical earth, will yield usable parameters. A drag term for this computation will have to be approximated for the vehicle under study.

A more advanced trajectory can be computed using an elongated body representing the vehicle, with three degrees of freedom. This trajectory will include the effects of aerodynamic lift (hence, a more accurate drag term) and a balancing component of the thrust vector, which is required to overcome the moment produced by the aerodynamic forces.

These nominal trajectory characteristics serve to fix quite closely the basic flight parameters of the vehicle. Subsequent refinements to these trajectory studies, including flight control and guidance effects, off-nominal performance and other assorted dispersions, will seldom result in significant changes to these basic flight parameters.

A1.2 **Aerodynamic Data.** Any vehicle that travels through the atmosphere is subjected to aerodynamic forces and moments which will affect the vehicle's performance and stability. In order to insure that the vehicle is capable of withstanding the environmental conditions imposed upon it during the regime of flight and to evaluate the effect of these conditions on its performance, the vehicle's aerodynamic characteristics must be known. The location and magnitude of the resultant aerodynamic forces normal to the vehicle's longitudinal axis are required to determine the degree of control forces required to balance out these forces and moments. The distributions of lateral force coefficients along the length of the vehicle at the angle of attack are required for the analysis of the aero-elastic deflections of the vehicle structure and for calculation of body bending moments under critical flight conditions.

The aerodynamic force acting on the vehicle is determined from theoretical considerations or wind tunnel tests on the vehicle model, or it is extrapolated from existing data on similar configurations. The force acting on the vehicle is resolved into orthogonal components along the body axes. This data is usually presented in the form of normal force coefficients and centers of pressure as functions of Mach number and angle of attack.

The force coefficient can be separated into two parts: the potential and viscous components. The potential force is that force which would be experienced by the body if it were inclined in an inviscid fluid. This component increases linearly with angle of attack. In a real fluid, this is the only force of measurable magnitude for the first few degrees of angle of attack. Upon further increase of angle of attack, however, viscous effects cause the cross-flow to begin to separate from the lee side of the body. The separation induces a pressure field which causes the force curve to depart from linearity. This departure is defined as the viscous component of the force and is dependent upon the state of the boundary layer; it is larger for laminar than for turbulent flow.

A more complete discussion of the aerodynamic data, along with approximate calculatory techniques, appears in Section A-5.

A1.3 Propellant Data (Liquid). For those vehicles which use liquid-fueled engines the mass of the liquid, of necessity, constitutes a large portion of the total mass. This large mass, oscillating in a tank, may have adverse effects on the vehicle control system, especially if the frequency of oscillation of the liquid is near that of the control system.

In early liquid-fueled vehicles (e.g., German V-2, American Redstone, WAC Corporal, etc.) propellant sloshing was found not to be a problem, and no explicit means of slosh compensation was employed. With the advent of larger vehicles having "cleaner" internal construction, the sloshing phenomena became increasingly important. Methods for determining the forces and moments due to propellant oscillation in "clean" tanks and the effects of internal oscillation suppressing devices (baffles) are discussed in Section A-3. This section presents the forces and moments due to the oscillating liquid and presents methods of handling this phenomena by the use of equivalent mechanical analogies.

A1.4 Propellant Data (Solid). For those vehicles which use solid-propellant engines, Appendix C2 shows that the propellant grain may be treated as a unitary mass and that it does not contribute any appreciable stiffness to the missile structure. Therefore, all that is usually considered is the mass distribution along the axis of the missile.

A1.5 Mass, Center of Gravity, and Inertial Data. The mass, center of gravity, and inertial data, hereafter referred to as inertial data in this section, are obviously required for a complete analysis of any control system. For rigid-body control analysis, where the sloshing is treated as a separate, artificially uncoupled degree of freedom, the inertial data used is that for a "reduced" vehicle. The "reduced" vehicle is the entire vehicle mass minus that mass of liquid propellant considered to be sloshing. Therefore, at any time instant, the inertial data will consist of the sum of the inertial data of the structural vehicle plus its residuals (liquids trapped in small lines and tanks) and the inertial data for that portion of the liquid propellants that are assumed to be rigid (see Appendix A3).

The method for combining these inertial data is given in Section A2, and the inertial data for the "rigid" liquid propellant can be found from an equivalent mechanical analogy as presented in Section A3.

A2 MASS AND RELATED INERTIAL DATA

A2.1 Calculation of Center of Gravity and Moment of Inertia. The property of a body by which it offers resistance to any change in its motion is defined as inertia, and its quantitative measure is called mass.

The mass-center or center of mass is defined as that point of a physical body where the mass could be concentrated so that the moment of the concentrated mass* about any axis or plane would be equal to the moment of the distributed mass of the body about the same axis or plane. If the words area, volume, or line were substituted for the word mass, and the reference to a physical body were deleted, the above definition would be that for the centroid of an area, volume, or line. Therefore, with respect to homogenous physical bodies, the terms centroid and mass-center may be regarded as synonymous.

The total force acting on a body undergoing rectilinear accelerated motion is defined as the resultant of the parallel forces acting on each particle in the body. The magnitude of the resultant of such parallel forces is equal to the algebraic sum of the forces on each particle, and the position of the resultant is such that the moment of the resultant force about any axis or plane is equal to the sum of the moments of the component forces. This position defines the line of action of the resultant force in the given acceleration direction. The resultant force is defined as the body's weight, and its position locates the center of gravity. Thus, the magnitude is:

$$W = \Sigma\ W_i.$$

---

* A mass moment is defined as the product of the quantity of mass by its distance to a reference.

and its line of action is located by:

$$X = \frac{\Sigma W_i x_i}{\Sigma W_i}$$

$$Y = \frac{\Sigma W_i y_i}{\Sigma W_i}$$

$$Z = \frac{\Sigma W_i z_i}{\Sigma W_i} \quad ,$$

where the symbology used is depicted in Figure A-1.
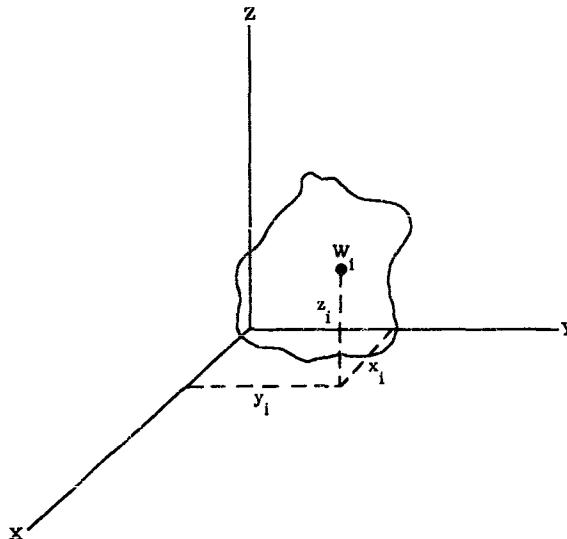
Figure A-1. Coordinate System and Mathematical Model

If we assume a uniform acceleration field, then the weight of each mass particle is proportional to its mass and the center of gravity of a body coincides with the mass-center. For a rigid body the terms are identical regardless of its position or orientation in the acceleration field. The difference between the two terms is that in finding the center of gravity the moment of a force system is involved, and in finding the mass-center the moment of a mass system is involved. In practice, the earth's acceleration field at a weighing station is uniform enough so that the above distinctions are not evident.

Common experience teaches that if a body is free to rotate about an axis, the farther from the axis the material (or mass-center) is placed, regardless of direction (sign sense), the greater is the moment of force required to produce a given angular acceleration of the body; that is, the greater the moment of inertia of the body becomes. Therefore, the moment of inertia or second moment of the mass of a system of particles may be defined, for a

continuous body, as the integral: $I = \int_M r^2 \, dm$; that is, as the summation of the products of the mass of each

particle by the square of its distance from a line or axis.

If the moment of inertia of a body thus found is about an axis passing through the mass-center (centroid) of the body, the moment of inertia of the body may be found about any other parallel axis, by the use of the transfer formula:

$$I_L = I_{Lg} + Md^2,$$

where I_{Lg} = the moment of inertia about the centroidal axis (Lg)

I_L = the moment of inertia about a parallel axis (L)

M = the mass of the body, and

d = the perpendicular distance between axes Lg and L.

During the derivation of the equations of motion for a body, terms containing functions of the form:

$$\int xydm, \quad \int zxdm, \quad \text{and} \quad \int yzdm$$

appear. These terms are defined as the products of inertia and represent the coupling effect of the inertia (mass) about two axes. The transfer formula for products of inertia is similar to that for moments of inertia. That is:

$$I_{L'M'} = I_{LgMg} + Mde,$$

where I_{LgMg} = the product of inertia about the Lg and Mg axes passing through the centroid,

M = the mass of the body, and

$d \ \& \ e$ = the perpendicular distances between the L' and Lg axes and the M' and Mg axes respectively.

In the preceding discussion it was assumed that the moments and products of inertia for each component were known about the component's own centroid. For the vehicles under study it is necessary to determine the inertial data for the entire vehicle by the summation of the inertial data of each component about its own center of gravity and the transfer of this data to the center of gravity of the vehicle.

The weight and center of gravity of each component may be calculated or found quite readily by simple mechanical means, such as scales and weighing fixtures. The moments and products of inertia of each component pose a different problem. An approximate method (which is quite accurate) has been determined to find the moments and products of inertia for the vehicle components. Each component has a characteristic shape (or sum of shapes): spherical, conical, cylindrical, hemisphere-cylindrical, hemisphere-conical, etc. Knowing the weight and dimensions of the component (coupled with the characteristic shape), the moment and product of inertia may be computed, for a constant density, using standard moment- and product-of-inertia equations found in any handbook. This reduces the total inertial data problem to one of transferring the data for each component to the combined center of gravity. In simplified form, the center-of-gravity equations and transfer equations become:

$$W = \Sigma W_i$$

$$x_{CG} = \frac{\Sigma W_i x_i}{\Sigma W_i}$$

$$y_{CG} = \frac{\Sigma W_i y_i}{\Sigma W_i}$$

$$z_{CG} = \frac{\Sigma W_i z_i}{\Sigma W_i}$$

$$I_{XX_{CG}} = \Sigma \left\{ I_{XX_i} + \left[(y_{CG} - y_i)^2 + (z_{CG} - z_i)^2 \right] M_i \right\}$$

$$I_{YY_{CG}} = \Sigma \left\{ I_{YY_i} + \left[(x_{CG} - x_i)^2 + (z_{CG} - z_i)^2 \right] M_i \right\}$$

$$I_{ZZ_{CG}} = \Sigma \left\{ I_{ZZ_i} + \left[(x_{CG} - x_i)^2 + (y_{CG} - y_i)^2 \right] M_i \right\}$$

$$I_{XY_{CG}} = \Sigma \left\{ I_{XY_i} + (x_{CG} - x_i)(y_{CG} - y_i) M_i \right\}$$

$$I_{XZ_{CG}} = \Sigma \left\{ I_{XZ_i} + (x_{CG} - x_i)(z_{CG} - z_i) M_i \right\}$$

$$I_{YZ_{CG}} = \Sigma \left\{ I_{YZ_i} + (y_{CG} - y_i)(z_{CG} - z_i) M_i \right\} ,$$

where the symbology used is depicted in Figure A-2.

* I_i ARE THE MOMENTS AND PRODUCTS OF INERTIA OF THE $i^{\underline{th}}$ PARTICLE ABOUT ITS OWN CENTER OF GRAVITY.
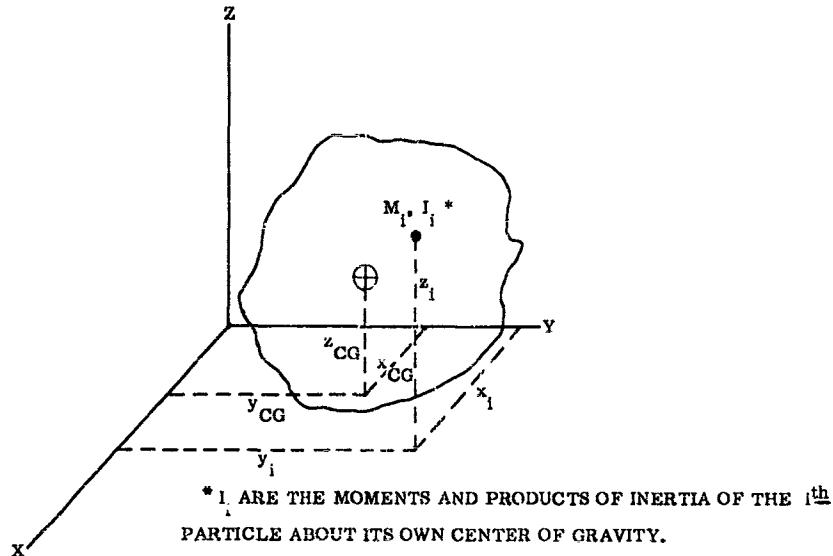
Figure A-2. Coordinate System and Mathematical Model

Since the trajectory, aerodynamic, and sloshing data are presented in relation to the longitudinal axis (axis of symmetry), it is convenient to reference the inertial data to a point on the longitudinal (x) axis. The moment and product of inertia equations then become:

$$I_{XX_T} = \Sigma \left\{ I_{XX_i} + \left[(0 - y_i)^2 + (0 - z_i)^2 \right] M_i \right\}$$

$$I_{YY_T} = \Sigma \left\{ I_{YY_i} + \left[(x_{CG} - x_i)^2 + (0 - z_i)^2 \right] M_i \right\}$$

$$I_{ZZ_T} = \Sigma \left\{ I_{ZZ_i} + \left[(x_{CG} - x_i)^2 + (0 - y_i)^2 \right] M_i \right\}$$

$$I_{XY_T} = \Sigma \left\{ I_{XY_i} + (x_{CG} - x_i)(0 - y_i) M_i \right\}$$

$$I_{XZ_T} = \Sigma \left\{ I_{XZ_i} + (x_{CG} - x_i)(0 - z_i) M_i \right\}$$

$$I_{YZ_T} = \Sigma \left\{ I_{YZ_i} + (0 - y_i)(0 - z_i) M_i \right\}$$

where

$$T = (x_{CG}, \ 0, \ 0).$$

An equivalent method well adapted for hand computions is the use of a table with the following headings:

Component Identification; M, x, y, z, Mx, My, Mz, Mx^2, My^2, Mz^2, Mxy, Mxz, Myz, I_{XX}, I_{YY}, I_{ZZ}, I_{XY}, I_{XZ}, & I_{YZ}.

The mass, center of gravity, moments of inertia, and products of inertia about the center of gravity are computed successively across the tabular format as:

$$x_{CG} = \frac{\Sigma M_i x_i}{\Sigma M_i}$$

$$y_{CG} = \frac{\Sigma M_i y_i}{\Sigma M_i}$$

$$z_{CG} = \frac{\Sigma M_i z_i}{\Sigma M_i}$$

$$I_{XX_{CG}} = \Sigma My_i^2 + \Sigma Mz_i^2 - (\Sigma M_i)(y_{CG}^2 + z_{CG}^2) + \Sigma I_{XX_i}$$

$$I_{YY_{CG}} = \Sigma Mx_i^2 + \Sigma Mz_i^2 - (\Sigma M_i)(x_{CG}^2 + z_{CG}^2) + \Sigma I_{YY_i}$$

$$I_{ZZ_{CG}} = \Sigma My_i^2 + \Sigma Mx_i^2 - (\Sigma M_i)(x_{CG}^2 + y_{CG}^2) + \Sigma I_{ZZ_i}$$

$$I_{XY_{CG}} = \Sigma Mxy_i - (\Sigma M_i)(x_{CG} \, y_{CG}) + \Sigma I_{XY_i}$$

$$I_{XZ_{CG}} = \Sigma Mxz_i - (\Sigma M_i)(x_{CG} \, z_{CG}) + \Sigma I_{XZ_i}$$

$$I_{YZ_{CG}} = \Sigma Myz_i - (\Sigma M_i)(y_{CG} \, z_{CG}) + \Sigma I_{YZ_i},$$

where

M = the mass of each component,

x, y, z = defines the position of the mass-center of each component in the missile coordinate system,

I_{XX}, I_{YY}, I_{ZZ} = moments of inertia of each component about an axis system passing through its own mass-center,

I_{XY}, I_{XZ}, I_{YZ} = products of inertia of each component about an axis system passing through its own mass-center.

The equivalence of the above equations with the preceding equations is readily made.

A2.2 Approximation of Moment of Inertia. It is often sufficiently accurate to ignore the moment of inertia and product of inertia of a component about axes passing through its own centroid when using the moment of inertia transfer formula. This is shown in the following example. A homogeneous right circular cylinder of height, h, and diameter, d, is oriented on the vehicle with its major axis parallel to the longitudinal axis of the missile. We can find the effectiveness of the component's own moment of inertia as its height-to-diameter ratio varies and as the transfer distance varies.
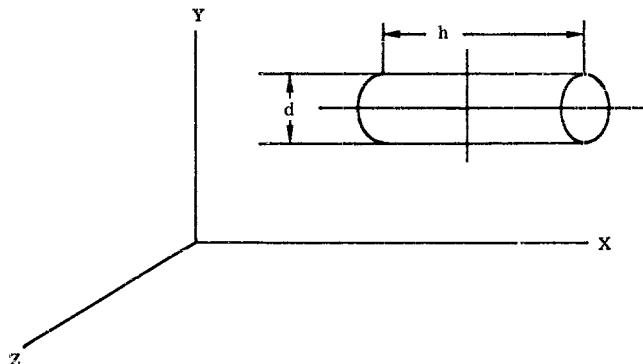
Figure A-3. Approximation of Moment of Inertia

In this example let $A = \dfrac{I_{YY_C}}{I_{YY_C} + M\,x^2}$. For a homogeneous right circular cylinder the moment of inertia about its centroidal axes, in pitch and yaw is:

$$I_{YY_C} = \frac{1}{12}\,Md^2\,(\frac{3}{4} + c^2)$$

where $c = \dfrac{h}{d}$.

Therefore:

$$A = \frac{\dfrac{1}{12}\,Md^2\,(\dfrac{3}{4}+c^2)}{\dfrac{1}{12}\,Md^2\,(\dfrac{3}{4}+c^2) + Md^2 k^2} \quad = \frac{1+1.33\,c^2}{1+1.33\,c^2+16\,k^2}$$

where $k = \dfrac{x}{d}$.

Plotting A versus k for various values of c, (Figure A-4), we find that for values of c = h/d of less than three, the moment of inertia in pitch and yaw of the component about its centroid may be ignored for transfer distances (x) greater than 4 d, and an accuracy of 95 percent may be retained.

A similar study in the roll plane (Figure A-5) shows that the roll moment of inertia of a component may be ignored for transfer distances where x is greater than 1.5 d, and an accuracy of 95 percent may be retained.

In general, for vehicles whose length-over-diameter ratios are greater than eight, the pitch and yaw moment of inertia of the components about their centroids may be ignored 90 percent of the time and the roll moments of inertia of the components may be ignored 40 percent of the time.

A-9
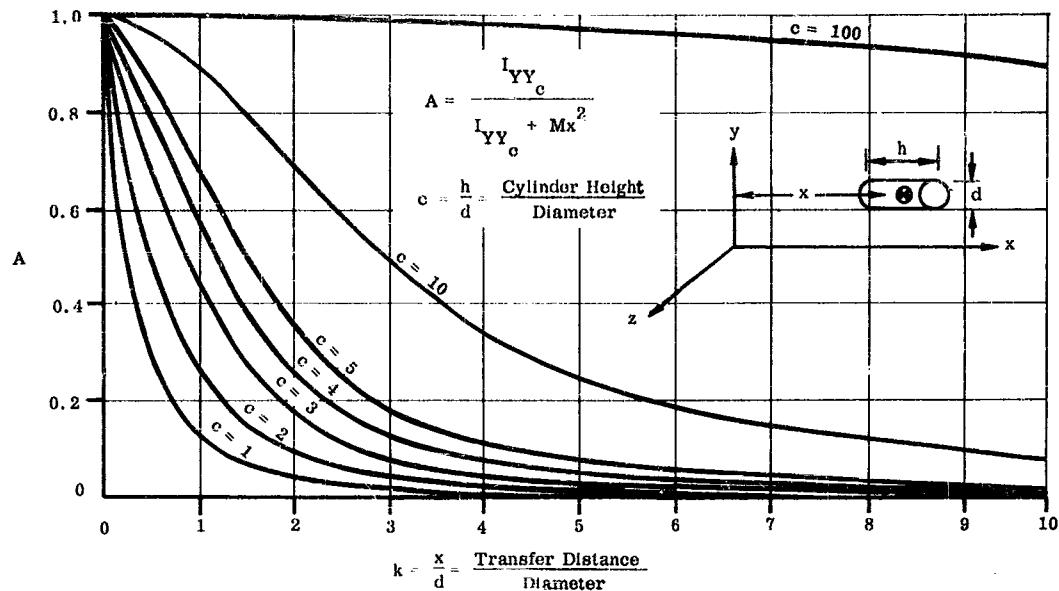
Figure A-4. Effective Pitch and Yaw Moment of Inertia Versus Length-Over-Diameter Ratio for a Homogeneous Cylinder
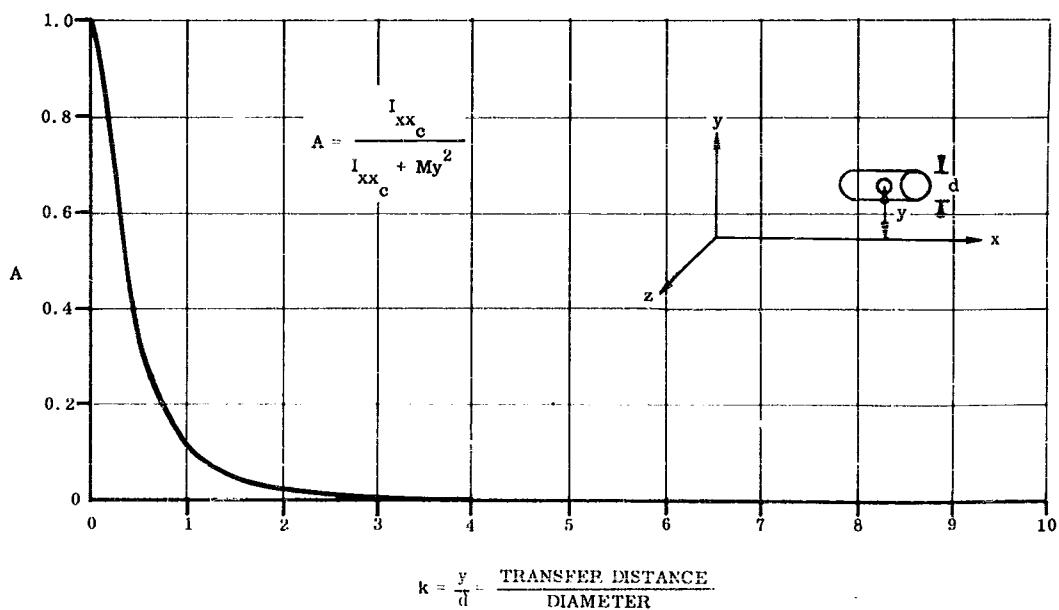
Figure A-5. Effective Roll Moment of Inertia Versus Length-Over-Diameter Ratio for a Homogeneous Cylinder

APPENDIX A3

PROPELLANT SLOSHING DATA

SYMBOLS USED IN APPENDIX A3

Symbol	Definition	Units
a	tank radius	ft
A_1		
B_1		
$\bar{B}_1$		
C_1	dimensionless parameters defined in Tables A-1 through A-6.	
C_1'		
D_1		
D_1'		
d	tank diameter	ft
d_r	diameter ratio for model laws as used in Equation A-12	N.D.*
F	force in X direction	lbs
h	depth of fluid	ft
$h_1, \bar{h}_1, h_1'$	height of sloshing element attach-point above tank bottom in the various mechanical analogies	ft
h_o	height of rigid mass above tank bottom	ft
K	constant used in Equation A-10	N.D.
K'	constant used in Equation A-11	N.D.
K_n	tank parameter $= \xi_n h/a$	N.D.
$\mathcal{M}$	moment on tank	lb ft
$\mathcal{M}_B$	applied moment about tank bottom	lb ft
M	total fluid mass	slugs
M_o	fixed or rigid mass	slugs
M_T	total mass of fluid which a full ellipsoidal tank can hold	slugs
M_1	sloshing or spring mass	slugs
n	ordered number of fluid mode	N.D.

---

* Non-dimensional

SYMBOLS USED IN APPENDIX A3 (Continued)

Symbols	Definition	Units
P	fluid pressure on a baffle in equivalent feet of head	ft
s	Laplace variable	sec^{-1}
x, y, z	tank coordinates (see Figure A-6)	ft
Y	spring mass displacement in x direction	ft
Y_F	analogous fluid "displacement" defined in Equation A-5	ft
α_T	longitudinal acceleration	ft/sec^2
α_r	acceleration field ratio (ground to flight) for model laws as used in Equation A-12	N.D.
Γ_F	analogous fluid "angle" defined in Equation A-1	rad
Γ_p	angle of pendulum with tank axis	rad
Δh	depth of a baffle below liquid free surface	ft
ζ	total damping ratio	N.D.
ζ_b	bottom scrubbing damping ratio	N.D.
ζ_d	ring baffle damping ratio	N.D.
ζ_I	inherent damping ratio	N.D.
ζ_s	side wall wiping damping ratio	N.D.
ζ_t	free surface damping ratio	N.D.
η_1	wave height for first sloshing mode $\approx 0.84a\,\Gamma_p$	ft
μ	viscosity	$lb\ sec/ft^2$
μ_r	viscosity ratio for model laws as used in Equation A-12	N.D.
ν	kinematic viscosity	ft^2/sec
ξ_n	n^{th} root of $J'_1(0)$	N.D.
ρ	liquid density	$slugs/ft^3$
ρ_r	liquid density ratio for model laws as used in Equation A-12	N.D.
τ_r	time constant ratio	N.D.
ω_n	n^{th} fluid mode frequency $=\dfrac{\alpha_T}{h}K_n \tanh K_n$	sec^{-1}

A3.1 Introduction. The motions of a liquid in an open vessel have been the subject of study for many years. During the past several decades significant progress has been made in this field beyond the classic investigations made by Sir Horace Lamb (circa 1879), with interest centered in the forced motion of aircraft fuels.

Numerous methods have been used to describe and solve for the propellant modes, frequencies, and pressure distributions. In general, all investigators have sought solutions to the equation of wave motion of a perfect fluid satisfying the boundary conditions of prescribed motions of the vessel's walls. These solutions then may be further defined to yield the relationships between forces and moments on the vessel's (tank's) walls and the tank's motion. These relationships are given in the following sections for rigid and flexible wall vessels. For the rigid wall vessels two mechanical analogies are presented; either one can be used with rigid vehicle studies. One mechanical analogy is presented for use with flexible vehicle studies.

A3.2 Rigid Wall Vessels. Some of the original work on the sloshing phenomena in rigid tanks was done by E. W. Graham (A-1) and J. Lorell (A-2).* An extension is made from Lamb's work on free oscillations for the case of a rectangular tank, and a mechanical pendulum analogy is derived. The fundamental frequencies and forces involved in liquid free oscillation are given for several tank shapes in addition to the rectangular case.

Schmitt (A-3) has determined the hydrodynamic forces and moments about the base of a circular cylindrical tank undergoing translation along its longitudinal axis and rotation about one of the perpendicular axes, produced by the oscillation of an incompressible, irrotational liquid in the tank. These are given by:

$$F = -s^2 x \sum_n M(1 - A_n) - s^2\theta \sum_n Mh\left(\frac{1}{2} + \frac{a^2}{4h^2} - B_n\right) + \sum_n MA_n \alpha_T \Gamma_{F_n}$$

$$\mathcal{M} = -s^2 x \sum_n Mh\left(\frac{1}{2} + \frac{a^2}{4h^2} - B_n\right) - s^2\theta \sum_n Mh^2\left(\frac{1}{3} + D_n - B_n\right) + \sum_n MhB_n \alpha_T \Gamma_{F_n} \qquad (A-1)$$

$$(s^2 + \omega_n^2)\Gamma_{F_n} = -\frac{\omega_n^2}{\alpha_T}\left[s^2 x + s^2\theta h\left(1 - \frac{\Omega_n^2}{\omega_n^2}\right)\right]$$

where,

$$\Omega_n^2 = \frac{2\alpha_T}{h}\frac{\cosh K_n - 1}{\cosh K_n}$$

and the remaining parameters are defined in Table A-1.

For ease of handling, a mechanical analogy in the form of a pendulum or spring-mass solution is sought. Such an analogy not only gives the engineer insight to the problem, but lends itself to a description of the liquid motion which is readily adapted for digital or analog computer simulations. The forces and moments produced by an analogous pendulum and rigid mass system, as shown in Figure A-6 for the first three modes, are equivalent in form to those of the hydrodynamic equations. These may be written as:

$$F = -s^2 x M_o - s^2\theta h_o M_o + \sum_n M_n \alpha_T \Gamma_{p_n}$$

$$\mathcal{M} = -s^2 x M_o h_o - s^2\theta(M_o h_o^2 + I_o) + \sum_n M_n h_n \alpha_T \Gamma_{p_n} \qquad (A-2)$$

$$(s^2 + \omega_n^2)\Gamma_{p_n} = -\frac{1}{L_{p_n}}\left[s^2 x + s^2\theta(h_n - L_{p_n})\right]$$

---

* Numbers in parenthesis refer to references at the end of Appendix A.

Thus, through a term by term comparison* between Equations A-1 and A-2, the analogous parameters are obtained. They are presented in Table A-1 for the first mode only; the reasons for this will be shown later.
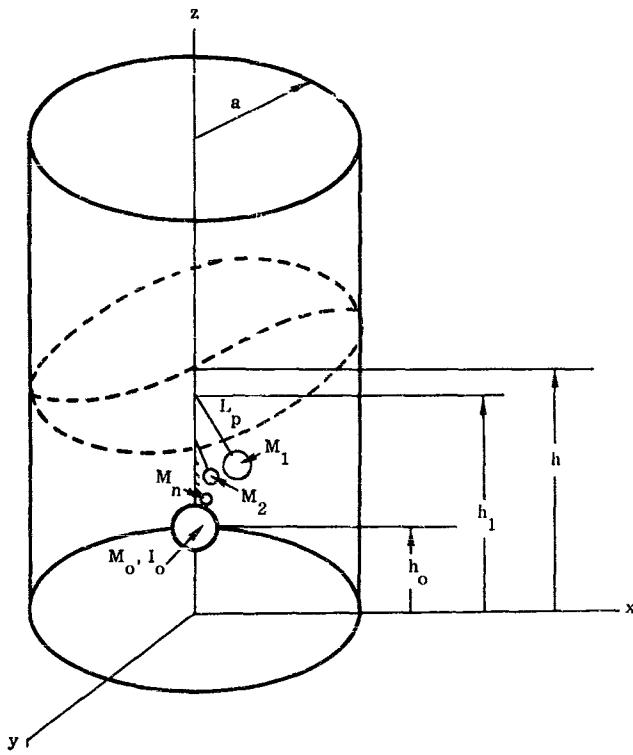
Figure A-6. Tank Model and Coordinates for Pendulum Analogy

---

* In making such a comparison the identity $\dfrac{B_n}{A_n} \equiv 1 - \dfrac{\Omega_n^2}{\omega_n^2} + \dfrac{L_{pn}}{h}$ is useful.

Table A-1. First Mode Sloshing Parameters for Pendulum Analogy (n = 1)
Circular Cylindrical Flat-Bottom Tank

MECHANICAL	HYDRODYNAMIC
$M_o + M_1$	M
M_o	$M(1 - A_1)$
M_1	MA_1
h_o	$h \dfrac{\left(\dfrac{1}{2} + \dfrac{a^2}{4h^2} - B_1\right)}{(1 - A_1)}$
$M_o h_o^2 + l_o$	$Mh^2\left(\dfrac{1}{3} + D_1 - B_1\right)$
h_1	$h\dfrac{B_1}{A_1}$
L_p	$h\dfrac{\coth K_1}{K_1}$
ω_1^2	$\dfrac{\alpha_T}{h} K_1 \tanh K_1$

Where

$$A_1 = \frac{2}{K_1} \frac{\tanh K_1}{(\xi_1^2 - 1)}$$

$$D_1 = \frac{4}{K_1^3} \frac{2 \sinh K_1 - K_1}{(\xi_1^2 - 1) \cosh K_1}$$

$$B_1 = \frac{2}{K_1^2} \frac{2 + K_1 \sinh K_1 - \cosh K_1}{(\xi_1^2 - 1) \cosh K_1}$$

$$\xi_1 = 1.84$$

$$C_1 = \frac{4}{K_1^2} \frac{\cosh K_1 - 1}{(\xi_1^2 - 1) \cosh K_1}$$

$$K_1 = \xi_1 \frac{h}{a}$$

This mechanical analogy exactly duplicates the forces and moments determined from the hydrodynamic solution and accurately reproduces the fluid oscillations, insofar as the assumptions made for the hydrodynamic solution are accurate, viz., an incompressible, irrotational fluid with only small disturbances being admitted.

Usually, only the fundamental mode of oscillation is considered, since the sloshing masses for the succeedingly higher modes have less and less influence. This property can be seen from examination of the force equation in the following form:

$$F = - s^2 x M + \sum_n M \frac{A_n s^4 x}{(s^2 + \omega_n^2)}$$

$$= - s^2 x M + \sum_n M \frac{2 \tanh (\xi_n \frac{h}{a}) s^4 x}{(\xi_n^2 - 1)(\xi_n \frac{h}{a}) \omega_n^2 (1 + \frac{s^2}{\omega_n^2})},$$

(A-3)

A-17

If now the damping-limited peaking for the higher modes is no greater than with the fundamental,* then the forces at resonance for these modes ($s^2 = -\omega^2 = -\omega_n^2$) are proportional to:

$$F_n \propto \frac{(\tanh \frac{\xi_n \, h}{a})^2}{(\xi_n^2 - 1)} \; .$$

One can see that for higher modes (ξ_n = 1.84, 5.335, 8.535, 11.705 ... ξ_{n-1} + π) the hyperbolic tangent in the numerator approaches unity and therefore, the force will vary as $1/(\xi_n^2 - 1)$.

Another argument in support of disregarding the higher modes rests upon the fact that test experience indicates a great deal of turbulent mixing accompanies high frequency tank oscillations. This can be illustrated by observing the motion for steady state and the first two propellant modes sketched in Figure A-7. The increased fluid mixing makes it difficult to display the higher modes except under careful "laboratory" conditions. It also indicates that dissipation (damping) effects for the higher modes are greater, further reducing their significance in control analysis.
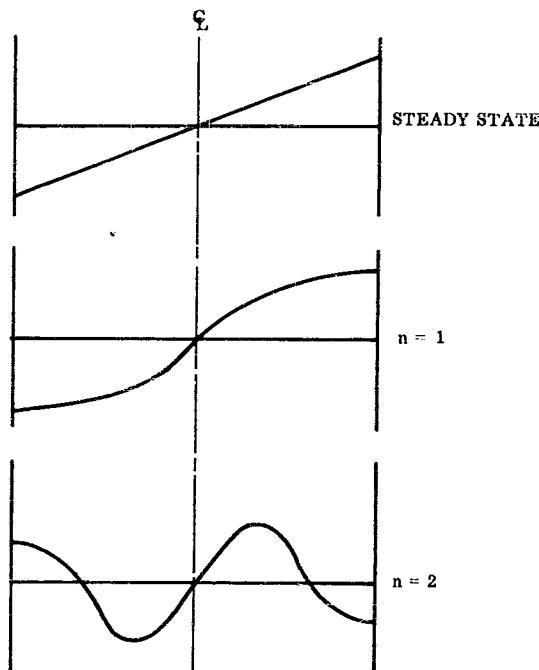
Figure A-7. Sketches of the First Few Mode Shapes (Cylindrical Tank)

Of great practical significance is the fact that the maximum amplitudes and, hence, velocities of the fundamental mode occur adjacent to the tank walls.

Curves representing the parameters in nondimensional form versus the aspect ratio, h/a, are given in Figures A-8 and A-9. Values of the constants given in Table A-1 versus the ratio, h/a, are given in Tables A-2, A-3, and A-4 for the first three sloshing modes.

---

*Experiments bear out this assumption, there being greater turbulent mixing for the higher modes.
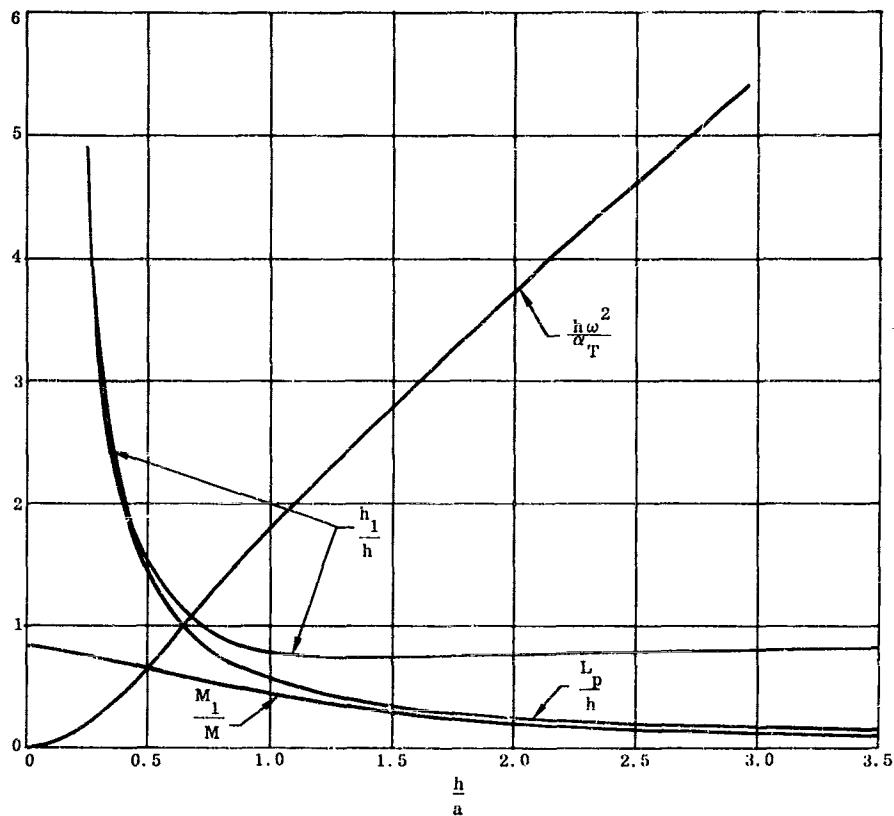
Figure A-8. Nondimensional Sloshing Parameters for Pendulum Analogy
for a Circular, Cylindrical Flat-Bottom Tank (n = 1) (a)
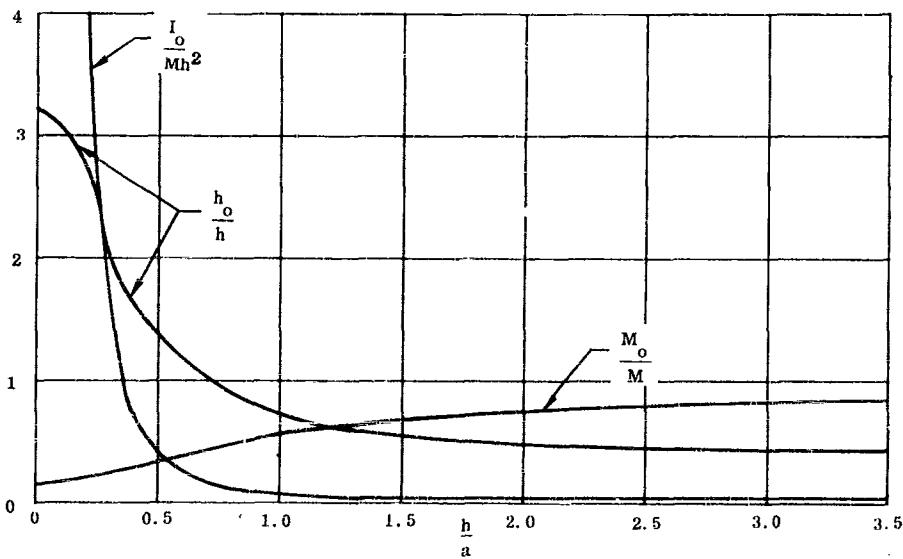
Figure A-9. Nondimensional Sloshing Parameters for Pendulum Analogy
for a Circular, Cylindrical Flat-Bottom Tank (n = 1) (b)

Table A-2. Nondimensional Constants Used in Mechanical Analogies* (First Mode) (n = 1)

h/a	sinh K_1	cosh K_1	tanh K_1	A_1	B_1	C_1	D_1	$\bar{B}_1$
				$\times 10^{+1}$		$\times 10^{+1}$		$\times 10^{+1}$
0.00	0.00000	1.0000	0.0000		∞	10.000	∞	
0.02	0.03681	1.0007	0.0368	8.3799	619.06	8.379	1237.8	4.1905
0.10	0.18504	1.0170	0.1820	8.2903	24.77	8.267	49.2	4.1568
0.20	0.37636	1.0685	0.3522	8.0246	6.20	7.935	12.1	4.0570
0.30	0.58046	1.1563	0.5020	7.6245	2.80	7.437	5.2	3.9062
				$\times 10^{+1}$		$\times 10^{+1}$		$\times 10^{+1}$
0.50	1.0554	1.4539	0.7259	6.6148	1.0335	6.1846	1.7636	3.5225
0.60	1.3423	1.6739	0.8019	6.0898	0.7430	5.5383	1.1767	3.3206
0.70	1.6748	1.9507	0.8586	5.5887	0.5716	4.9258	0.8294	3.1258
0.80	2.0642	2.2937	0.8999	5.1256	0.4630	4.3646	0.6088	2.9433
1.00	3.0689	3.2277	0.9508	4.3321	0.3390	3.4181	0.3584	2.6231
				$\times 10^{+1}$	$\times 10^{+1}$	$\times 10^{+1}$	$\times 10^{+2}$	$\times 10^{+1}$
1.20	4.494	4.604	0.9761	3.7063	2.7337	2.6922	22.938	2.3602
1.40	6.534	6.610	0.9885	3.2171	2.3359	2.1445	15.570	2.1448
1.60	9.470	9.522	0.9945	2.8320	2.0678	1.7314	11.038	1.9662
1.80	13.702	13.738	0.9974	2.5246	1.8716	1.4173	8.093	1.8159
2.00	19.811	19.836	0.9987	2.2753	1.7186	1.1757	6.096	1.6874
				$\times 10^{+1}$	$\times 10^{+2}$	$\times 10^{+2}$	$\times 10^{+2}$	$\times 10^{+1}$
2.25	31.39	31.41	0.9995	2.0240	15.660	9.4713	4.4121	1.5504
2.50	49.74	49.75	0.9998	1.8222	14.419	7.7648	3.2852	1.4339
3.00	124.82	124.82	0.9999	1.5187	12.480	5.4587	1.9496	1.2458
3.50	313.20	313.20	0.9999	1.3018	11.009	4.030	1.2426	1.1003
4.00	785.92	785.92	0.9999	1.1391	9.847	3.0914	0.83716	0.9945
				$\times 10^{+1}$	$\times 10^{+2}$	$\times 10^{+2}$	$\times 10^{+3}$	$\times 10^{+2}$
4.50	1972.1	1972.1	0.9999	1.0125	8.9036	2.4444	5.8951	8.9029
5.00	4949.0	4949.0	1.0000	0.9113	8.1225	1.3806	4.3025	8.1223
6.00	31159.0	31159.0	1.0000	0.7594	6.9061	1.3756	2.4918	6.9060

*Circularly Cylindrical Flat-Bottom Tank

Table A-3. Nondimensional Constants Used in Mechanical Analogies*(Second Mode) (n = 2)

h/a	sinh K₂	cosh K₂	tanh K₂	A₂	B₂	C₂	D₂	B̄₁
				$\times10^{+2}$	$\times10^{+2}$	$\times10^{+2}$	$\times10^{+1}$	$\times10^{+2}$
0.00	0.00000	1.0000	0.00000		∞	1.0000	∞	
0.02	0.10690	1.0057	0.10630	7.2552	639.6900	7.2483	12.7700	3.6311
0.10	0.55917	1.1457	0.48805	6.6623	25.7410	6.5087	4.8964	3.4080
0.20	1.28130	1.6253	0.78833	5.3807	6.8552	4.9223	1.1033	2.9195
0.30	2.37680	2.5786	0.92174	4.1942	3.5562	3.4810	0.4344	2.4537
				$\times10^{+2}$	$\times10^{+2}$	$\times10^{+3}$	$\times10^{+3}$	$\times10^{+2}$
0.50	7.1672	7.2367	0.99041	2.7040	1.9633	17.6410	12.3720	1.8219
0.60	12.2580	12.2990	0.99669	2.2676	1.6724	13.0590	7.6965	1.6146
0.70	20.9220	20.9450	0.99886	1.9479	1.4756	9.9452	5.0882	1.4506
0.80	35.6860	35.6960	0.99961	1.7057	1.3282	7.7720	3.5215	1.3171
1.00	103.7300	103.7400	0.99995	1.3650	1.1141	5.0681	1.8690	1.1116
				$\times10^{+3}$	$\times10^{+3}$	$\times10^{+3}$	$\times10^{+4}$	$\times10^{+3}$
1.20	301.52	301.52	0.99999	0.1137	9.6105	3.5420	10.9840	9.6046
1.40	876.43	876.43	0.99999	9.7506	8.4481	2.6080	6.9616	8.4466
1.60	2547.50	2547.50	0.99999	8.5318	7.5331	1.9982	4.6759	7.5327
1.80	7404.60	7404.60	1.00000	7.5638	6.7943	1.5792	3.2874	6.7942
2.00	21522.00	21522.00	1.00000	6.8254	6.1858	1.2793	2.3975	6.1858
	$\times10^{-6}$	$\times10^{-6}$		$\times10^{+3}$	$\times10^{+3}$	$\times10^{+4}$	$\times10^{-5}$	$\times10^{+3}$
2.25	0.0816	0.0816	1.0000	6.0670	5.5616	10.1060	16.8410	5.5616
2.50	0.3100	0.3100	1.0000	5.4603	5.0509	8.1879	12.2730	5.0509
3.00	4.4653	4.4653	1.0000	4.5503	4.2660	5.6861	7.1054	4.2660
3.50	64.3180	64.3180	1.0000	3.9002	3.6914	4.1775	4.4745	3.6914
4.00	926.4300	926.4300	1.0000	3.4127	3.2528	3.1984	2.9976	3.2528
	$\times10^{-11}$	$\times10^{-11}$		$\times10^{+3}$	$\times10^{+3}$	$\times10^{+4}$	$\times10^{-5}$	$\times10^{+3}$
4.50	0.1334	0.1334	1.0000	3.0335	2.9072	2.5271	2.10530	2.9072
5.00	1.9221	1.9221	1.0000	2.7302	2.6278	2.0470	1.53480	2.6278
6.00	398.7800	398.7800	1.0000	2.2751	2.2041	1.4215	.88817	2.2041

* Circularly Cylindrical Flat-Bottom Tank

A-21

Table A-4. Nondimensional Constants Used in Mechanical Analogies* (Third Mode) (n = 3)

h/a	sinh K_3	cosh K_3	tanh K_3	A_3	B_3	C_3	D_3	$\bar{B}_3$
				$\times 10^{+2}$	$\times 10^{+2}$	$\times 10^{+2}$	$\times 10^{+2}$	$\times 10^{+3}$
0.00	0.0000	1.0000	0.00000		∞		∞	
0.02	0.1715	1.0146	0.16906	2.7570	95.5410	2.7503	190.1500	13.818
0.10	0.9609	1.3869	0.69289	2.2599	3.9492	2.1320	6.8984	11.939
0.20	2.6655	2.8469	0.93628	1.5268	1.2426	1.2395	1.4248	9.0708
0.30	6.4325	6.5098	0.98813	1.0743	0.7601	0.7187	0.5250	7.1490
				$\times 10^{+3}$	$\times 10^{+3}$	$\times 10^{+3}$	$\times 10^{+3}$	$\times 10^{+3}$
0.50	35.664	35.678	0.99961	6.5205	5.0776	2.9714	1.3465	5.0348
0.60	83.748	83.754	0.99993	5.4355	4.3994	2.0976	0.8037	4.3867
0.70	196.630	196.640	0.99999	4.6593	3.8873	1.5518	0.5142	3.8834
0.80	461.670	461.670	1.00000	4.0769	3.4824	1.1916	0.3472	3.4811
1.00	2544.900	2544.900	1.00000	3.2615	2.8797	0.7640	0.1788	2.8796
	$\times 10^{-5}$	$\times 10^{-5}$		$\times 10^{+3}$	$\times 10^{+3}$	$\times 10^{+4}$	$\times 10^{+4}$	$\times 10^{+3}$
1.20	0.1403	0.1403	1.00000	2.7179	2.4526	5.3071	1.0360	2.4526
1.40	0.7733	0.7733	1.00000	2.3297	2.1347	3.8993	0.6526	2.1347
1.60	4.2628	4.2628	1.00000	2.0385	1.8892	2.9854	0.4372	1.8892
1.80	23.4980	23.498	1.00000	1.8120	1.6940	2.3589	0.3071	1.6940
2.00	129.530	129.53	1.00000	1.6308	1.5352	1.9107	0.2239	1.5352
	$\times 10^{-8}$	$\times 10^{-8}$		$\times 10^{+3}$	$\times 10^{+3}$	$\times 10^{+4}$	$\times 10^{+5}$	$\times 10^{+4}$
2.25	1.0941	1.0941	1.0000	1.4496	1.3741	1.5097	1.5723	13.741
2.50	9.2412	9.2412	1.0000	1.3046	1.2435	1.2228	1.1462	12.435
3.00	659.30	659.30	1.0000	1.0872	1.0447	0.8492	0.6633	10.447
3.50	47036.	47036.	1.0000	0.9319	0.9007	0.6239	0.4177	9.007
4.00	...	...	1.0000	0.8154	0.7915	0.4777	0.2798	7.915
				$\times 10^{+4}$	$\times 10^{+4}$	$\times 10^{+5}$	$\times 10^{+6}$	$\times 10^{+4}$
4.50	...	...	1.0000	7.2479	7.0592	3.7742	1.9653	7.0592
5.00	...	...	1.0000	6.5231	6.3702	3.0571	1.4327	6.3702
6.00	∞	∞	1.0000	5.4359	5.3297	2.1130	0.8291	5.3297

* Circularly Cylindrical Flat-Bottom Tank

The forces and moments produced by an analogous spring-mass and rigid-mass system, as shown in Figure A-10, are also equivalent in form to those of the hydrodynamic equations. They may be written as:

$$F = -s^2 x M_o - s^2 \theta h_o M_o + \sum_n k_n Y_n$$

$$\mathcal{M} = -s^2 x h_o M_o - s^2 \theta (M_o h_o^2 + I_o) + \sum_n k_n \bar{h}_n Y_n + \sum_n M_n \alpha_T Y_n \qquad (A-4)$$

$$(s^2 + \omega_n^2) Y_n = - \left[s^2 x + s^2 \theta \bar{h}_n \right]$$

Again, in a term-by-term comparison between Equations (A-1) and (A-4), the analogous parameters are obtained. They are presented in nondimensional form in Table A-5, and curves representing these parameters versus the ratio, h/a, are given in Figures A-11 and A-12. In order for a mechanical analogy (pendulum or spring-mass system) to reproduce the moments from the hydrodynamic solution at low fluid levels (h < 2a), the mechanical elements must be placed above the fluid free surface. This peculiar effect does not affect accuracy in rigid body studies; it does, however, introduce errors when making flexible missile studies.
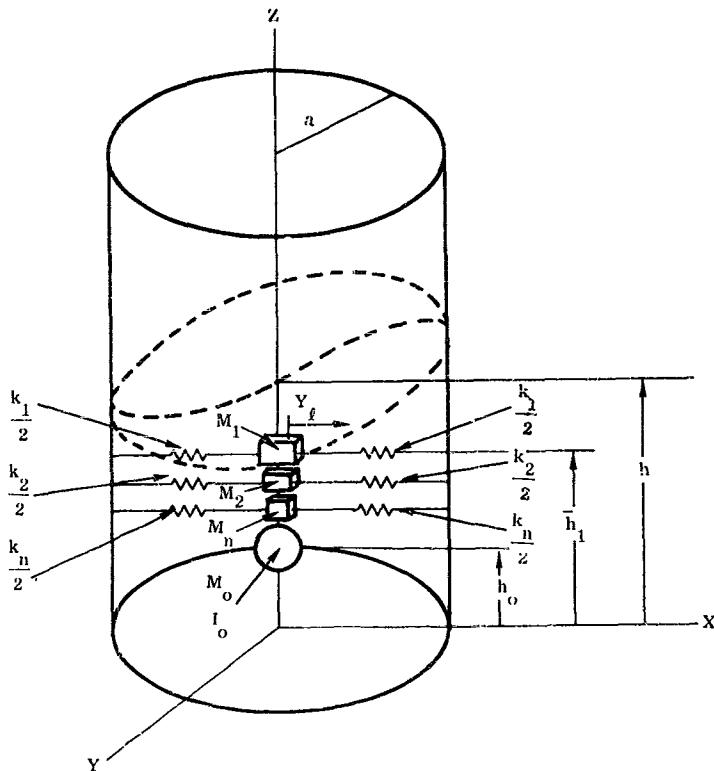
Figure A-10. Tank Model and Coordinates for Spring Mass Analogy
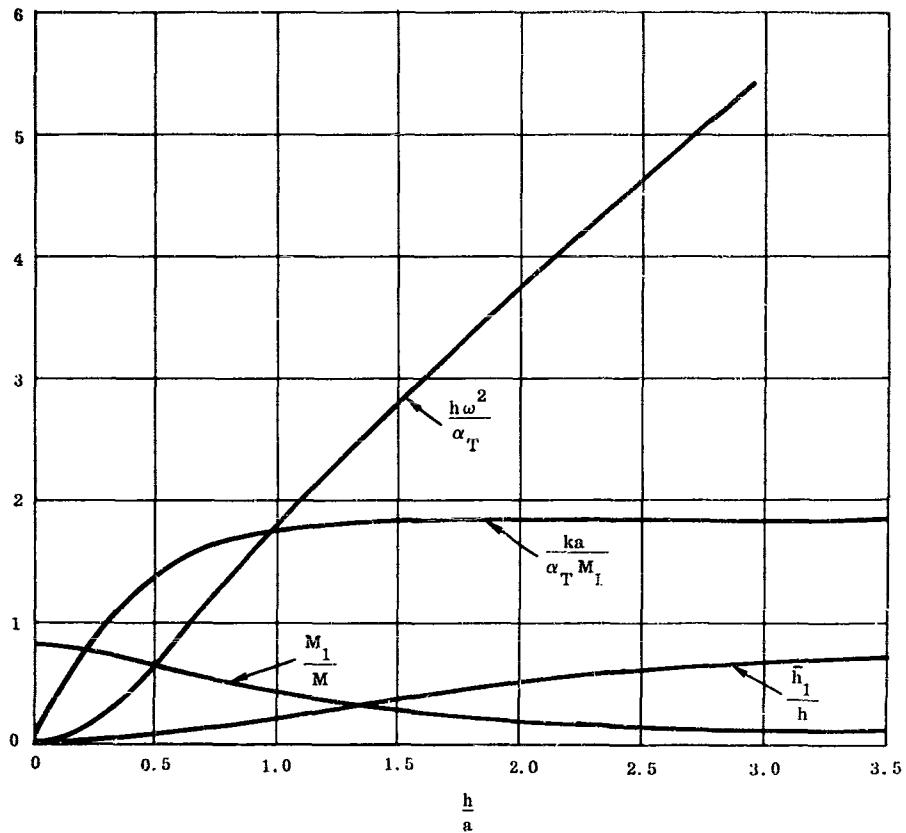
Figure A-11. Nondimensional Sloshing Parameters for Spring Mass Analogy for a Circular, Cylindrical Flat-Bottom Tank (n = 1) (a)

Table A-5. First Mode Sloshing Parameters for Spring Mass Analogy
Circularly Cylindrical Flat-Bottom Tank

MECHANICAL	HYDRODYNAMIC
$M_o + M_1$	M
M_1	MA_1
M_o	$M(1 - A_1)$
$\bar{h}_1$	$h\left(\dfrac{B_1}{A_1} - \dfrac{\coth K_1}{K_1}\right)$
h_o	$h\dfrac{\left(\dfrac{1}{2} + \dfrac{a^2}{4h^2} - B_1\right)}{(1 - A_1)}$
$M_o h_o^2 + I_o$	$Mh^2(\dfrac{1}{3} + D_1 - B_1)$
k	$\omega_1^2 M_1$
ω_1^2	$\dfrac{\alpha_T \xi_1}{a} \tanh K_1$

where the constants are given in Table A-1.

A3.3 Flexible Wall Vessels. For flexible missile studies it is desired that the forces and moments derived from the mechanical analogy act at points on the missile, corresponding to those of the forces and moments as derived from a hydrodynamic solution.

Certain exact solutions to the flexible-wall problem exist in the literature (A-4), (A-5), (A-6). However, their application in general control system studies is by no means direct. Hence, it appears desirable to be able to employ the relatively simple rigid-walled tank solution to the flexible-walled tank problem. Actually, such an application is very easy and direct; and, intuitively, it appears to be reasonably sound for deep tank liquid levels. However, at low liquid levels the mechanical elements appear above the liquid surface when using the rigid tank pendulum (or spring-mass) analogies as above. Therefore, a third analogy is now presented (A-7). This analogy is similar to the above spring-mass analogy except that a pure couple is applied at the tank bottom. This moment is justifiable because the pressure distribution along the bottom in the hydrodynamic solution produces a couple only. The effect of introducing this moment is to lower the spring-mass and rigid mass elements so that they act at wetted tank wall stations for all liquid levels. In order to determine the forces and moments for such a mechanical analogy, the forces and moments obtained from the rigid tank hydrodynamic solution are re-written here in a slightly different form. The moment terms are grouped according to whether they arise from side wall pressures or from pressures on the tank bottom, the latter producing a pure couple.

$$F = -s^2 \, x \, M - s^2 \, \theta \, Mh \, \left(\frac{1}{2}\right) - s^2 \, \sum_n \, MA_n \, Y_{F_n}$$

$$\mathcal{M} = \mathcal{M}_w + \mathcal{M}_B$$
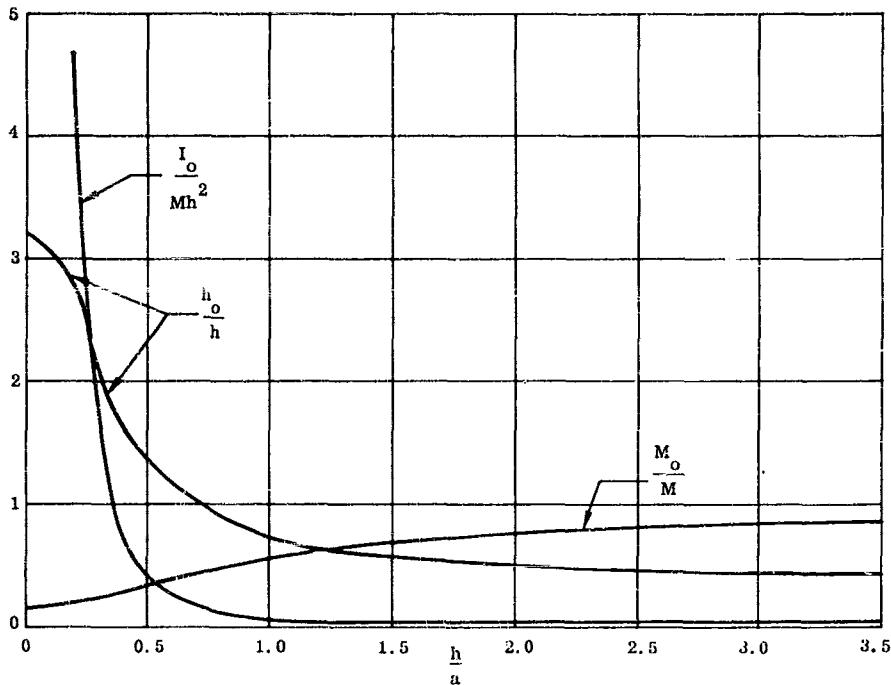
Figure A-12. Nondimensional Sloshing Parameters for Spring Mass Analogy
for a Circular, Cylindrical Flat-Bottom Tank (n = 1) (b)

where

$\mathcal{M}_w$ = moment from side wall

$$= -s^2 x\, Mh\left(\frac{1}{2}\right) - s^2\theta \sum_n Mh^2\left(\frac{1}{3} + C'_n + D'_n - \bar{B}_n \frac{\bar{\Omega}_n^2}{\omega_n^2}\right) - s^2 \sum_n Mh\, \bar{B}_n\, Y_{F_n}$$

$\mathcal{M}_B$ = moment from tank bottom (pure couple)

$$= -s^2 x\, Mh\left(\frac{a^2}{4h^2}\right) - s^2\theta \sum_n Mh^2\left(D'_n + \frac{C'_n}{2}\frac{\bar{\Omega}_n^2}{\omega_n^2}\right) + s^2 \sum_n Mh\, \frac{C'_n}{2}\, Y_{F_n}$$ (A-5)

$$(s^2 + \omega_n^2)\, Y_{F_n} = -\left[s^2 x + s^2\theta\, h\,\left(1 - \frac{\bar{\Omega}_n^2}{\omega_n^2}\right)\right]$$

The mechanical analogy is identical in arrangement with that of Figure A-10, but with the addition of a pure couple term, $\mathcal{M}_B$. The forces and moments for the mechanical analogy are written as:*

---

* Prime values have been used for the positioning of mechanical elements to distinguish them from the rigid wall tank analogy.

$$F = -s^2 x (M_o + \sum_n M_n) - s^2 \theta (M_o h'_o + \sum_n M_n h'_n) - s^2 \sum_n Y_n M_n$$

$$\mathscr{M} = -s^2 x (M_o h'_o + \sum_n M_n h'_n) - s^2 \theta (M_o h'^2_0 + I'_o + \sum_n M_n h'^2_n) - s^2 \sum_n Y_n M_n h'_n + \mathscr{M}_B \qquad (A-6)$$

$$(s^2 + \omega_n^2) Y_n = - \left[s^2 x + s^2 \theta h'_n \right]$$

The rotational acceleration term in the hydrodynamic solutions $\mathscr{M}_B$ either may be ignored, since it is very small, or it may be combined with the rotational acceleration term for the moment from the tank wall. If this latter course is chosen, the analogous mechanical system's first mass moment of inertia becomes the same as that used in the spring mass analogy of Section A3.2 (but does not affect the positioning of the mechanical elements). The analogous moment applied to the tank bottom, rearranged, becomes for the first mode:

$$\mathscr{M}_B = M \frac{h^2}{4a} \omega_1^2 Y + Mh \frac{C'_1}{2} s^2 Y$$

$$= M_1 \alpha_T Y + M_c s^2 Y ,$$

where

$$M_c = Mh \frac{C'_1}{2} \quad \text{and} \quad M_1 \alpha_T = M \frac{h^2}{4a} \omega_i^2 .$$

This is the result employed in the main body of the report for the flexible vehicle equations.

Again, through a term-by-term comparison between Equations A-5 and A-6, the analogous parameters are obtained. They are presented in Table A-6, for the first mode only. Curves representing these nondimensionalized parameters versus h/a are given in Figures A-13 and A-14.

Plots of the nondimensionalized force and moment as functions of h/a, derived from the spring-mass analogy in a flexible-walled, circular, cylindrical tank bending in a parabolic mode shape, are given in Figures A-15 and A-16. The dotted curves represent the forces and moments of the liquid in a circular, cylindrical tank due to an exact solution for this problem, according to Bauer (A-4), while the solid curves represent the forces and moments derived from the mechanical spring-mass analogy. As can be seen, the mechanical spring-mass analogy closely approximates the exact forces and moments on the tank.

A3.4 Noncylindrical Tanks. Up to this point we have considered only cylindrical tanks with flat bottoms and circular cross sectional areas. For this type of tank, we have presented parameters for two mechanical analogies that can be used to reproduce the forces and moments due to liquid oscillations in rigid-wall tanks. We have also discussed the applicability of the analogy to flexible-wall tanks. The question now arises as to how to reproduce the forces and moments produced by liquid oscillations in tanks of other shapes.

Considering noncylindrical missile tanks with circular transverse cross sectional areas, the leading shapes are oblate spheroids, with the sphere as a special case. Also included in this category are those cases of low liquid levels in tanks with nonflat bottoms. These include conical, spheroidal, inverted spheroidal and other shapes.

A solution to the hydrodynamic equations of motion is found, and the parameters for an equivalent pendulum analogy are determined, by A. H. Hausrath (A-8) for oblate spheroids. He determines a series solution consisting of Legendre polynomials, by means of the Rayleigh-Ritz approach. Free vibration and lateral translational vibration only are treated. Curves of these parameters for tanks of various eccentricity are presented in Figures A-17, -18 and -19.

Table A-6. First Mode Sloshing Parameters For Spring Mass Plus a Couple Analogy
Circularly Cylindrical Flat-Bottom Tank

MECHANICAL	HYDRODYNAMIC
$M_o + M_1$	M
M_1	MA_1
M_o	$M(1 - A_1)$
h_o'	$h\left(\dfrac{1/2 - \bar{B}_1}{1 - A_1}\right)$
h_1'	$h\,\dfrac{\bar{B}_1}{A_1}$
$M_o h_o'^2 + M_1 h_1'^2 + I_o'$	$Mh^2\left(\dfrac{1}{3} + C_1' + D_1' - \bar{B}_1\,\dfrac{C_1}{A_1}\right)*$

* Use has been made of the identity $\dfrac{\bar{\Omega}_1^2}{\omega_1^2} = \dfrac{C_1}{A_1}$ in making these comparisons.

where A_1, C_1, D_1 are defined in Table A-1, and

$$\bar{B}_1 = \frac{2}{K_1^2} \cdot \frac{1 + K_1 \sinh K_1 - \cosh K_1}{(\xi_1^2 - 1)\cosh K_1}$$

$$C_1' = \frac{4}{K_1^2 (\xi_1^2 - 1)\cosh K_1}$$

$$D_1' = \frac{4 \sinh K_1}{K_1^3 (\xi_1^2 - 1)\cosh K_1}$$

Bottom Couple:

First form (rotational acceleration terms included)

$$\mathcal{M}_B = - s^2\, xMh\left(\frac{a^2}{4h^2}\right) - s^2\, \theta\, Mh^2\left(D_1' + \frac{C_1' C_1}{2 A_1}\right) + s^2\, Mh\,\frac{C_1'}{2}\, Y$$

Second form (for which I_c from Figure A-12 and Table A-5 is used)

$$\mathcal{M}_B = M_1 \alpha_T Y + M_c s^2 Y; \quad M_c = Mh\, C_1'/2$$
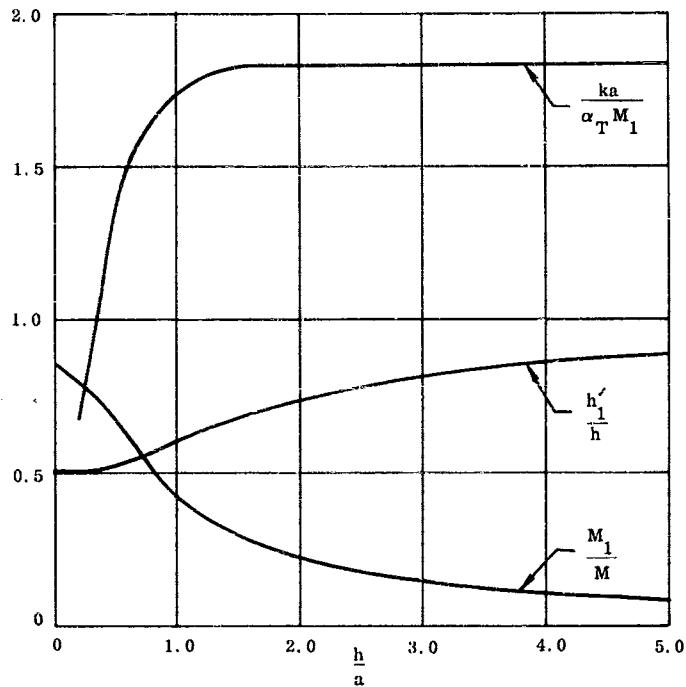
Figure A-13. Spring Mass Analogy for Flexible Wall Tanks (a)
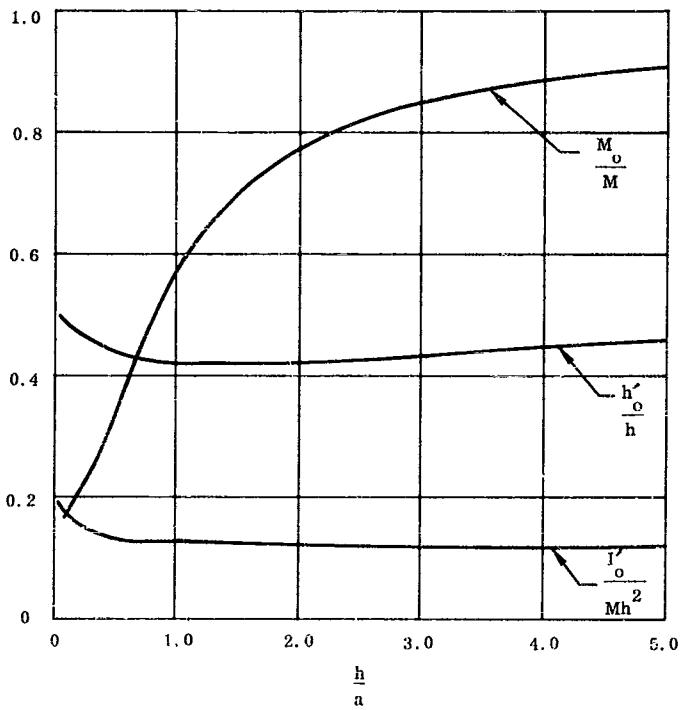
Figure A-14. Spring Mass Analogy for Flexible Wall Tanks (b)

NONDIMENSIONAL FORCE DERIVED FROM SPRING-MASS MECHANICAL ANALOGY.

NONDIMENSIONAL FORCE DERIVED FROM EXACT SOLUTION ACCORDING TO BAUER (A-4).
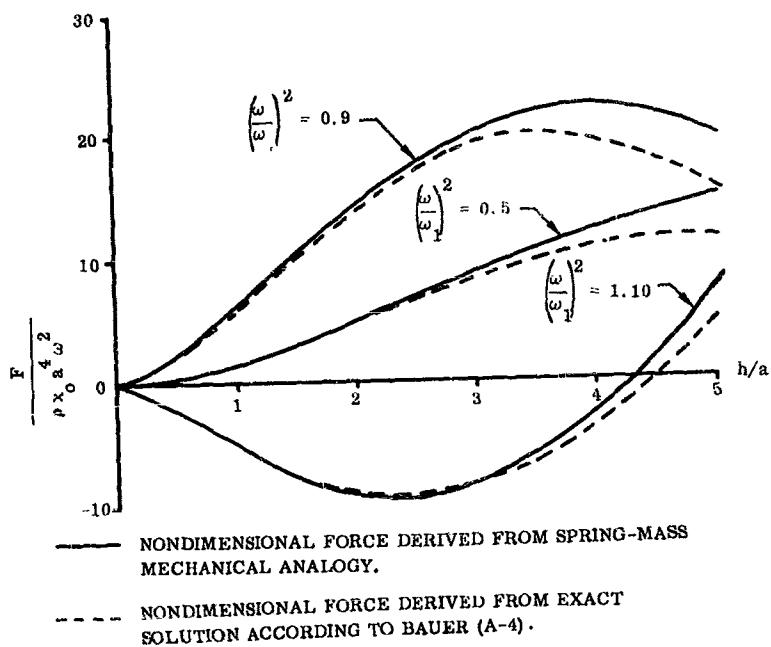
Figure A-15. Comparison of Exact and Approximate Hydrodynamic Force on Tank Walls Due to Bending

NONDIMENSIONAL MOMENT DERIVED FROM SPRING-MASS MECHANICAL ANALOGY.

NONDIMENSIONAL MOMENT DERIVED FROM EXACT SOLUTION ACCORDING TO BAUER (A-4).
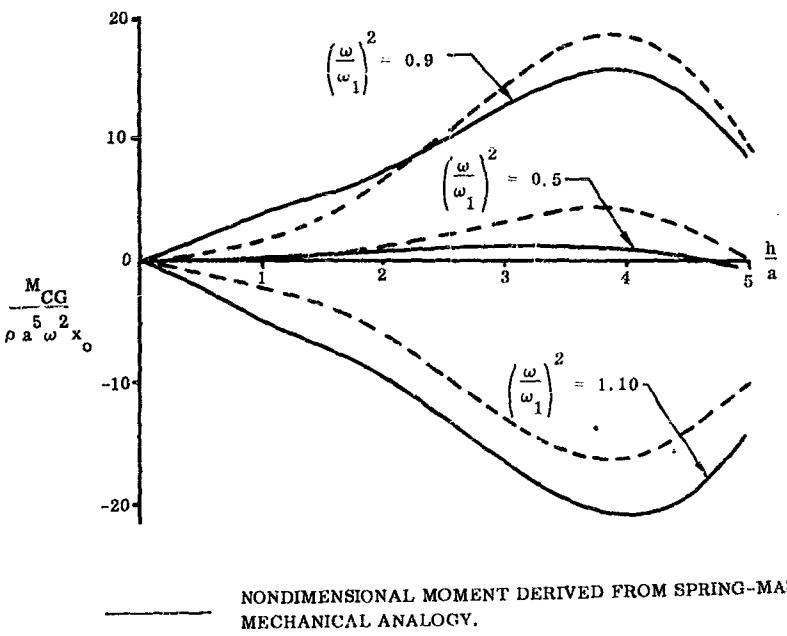
Figure A-16. Comparison of Exact and Approximate Hydrodynamic Moment on Tank Wall Due to Bending

$$e = \sqrt{\dfrac{a^2 - b^2}{a}}$$

e = 0.141
a = SEMI-MAJOR AXIS
b = SEMI-MINOR AXIS
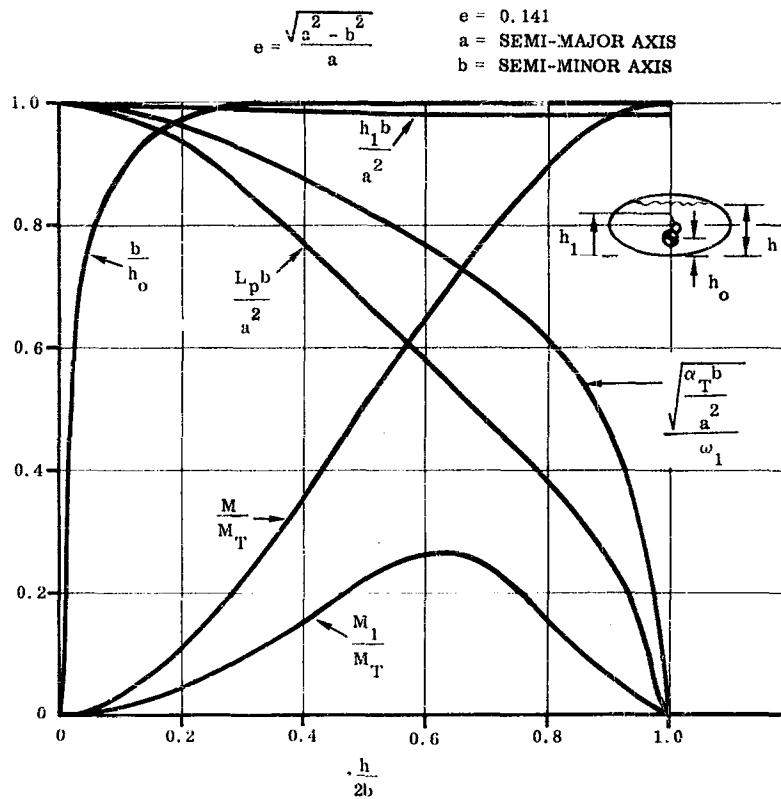
Figure A-17. Sloshing Parameters for the Pendulum Analogy in an Elliptical
Tank (e = 0.141), First Mode (n = 1)

An integral-equation approach has been used by Budiansky (A-9) to determine the natural modes and frequencies of small-amplitude sloshing of liquids in partially filled circular canals and spherical tanks. The circular canal is analyzed for arbitrary depths of liquid, while the sphere is solved only for the nearly full and half-full cases. The results for the sphere, together with the known behavior for the nearly-empty case, are used in conjunction with the trends established for the circular canal as a basis for estimating frequencies for arbitrary depths of liquid in the spherical canal. The frequencies thus determined agree with those determined by Hausrath for the spherical tank. Budiansky discusses the dynamic analysis of the container-fluid system by means of the mode-superposition approach, and modal parameters required in such analyses are presented.

For the case of a conical tank, J. W. Green (A-10) and J. Harper (A-11) both present solutions to a tank of circular transverse cross section. Harper solves the hydrodynamic equations of motion for a liquid in a cone with a 45-degree semi-vertex angle. He derives an equivalent pendulum analogy that duplicates the hydrodynamic forces and moments. The parameters for such an analogy are presented in Table A-7.

Trembath (A-12) presents a mathematical model for the response to liquid oscillations in tanks of arbitrary shape. An incompressible, irrotational fluid is assumed, and only linear effects are considered. Rotation about the longitudinal axis is not permitted. The response is given in the form of integral equations for forces, moments, and wave heights. The equations must be evaluated numerically for specific tank shapes.

$$e = \frac{\sqrt{a^2 - b^2}}{a}$$

e = 0.66

a = SEMI-MAJOR AXIS

b = SEMI-MINOR AXIS
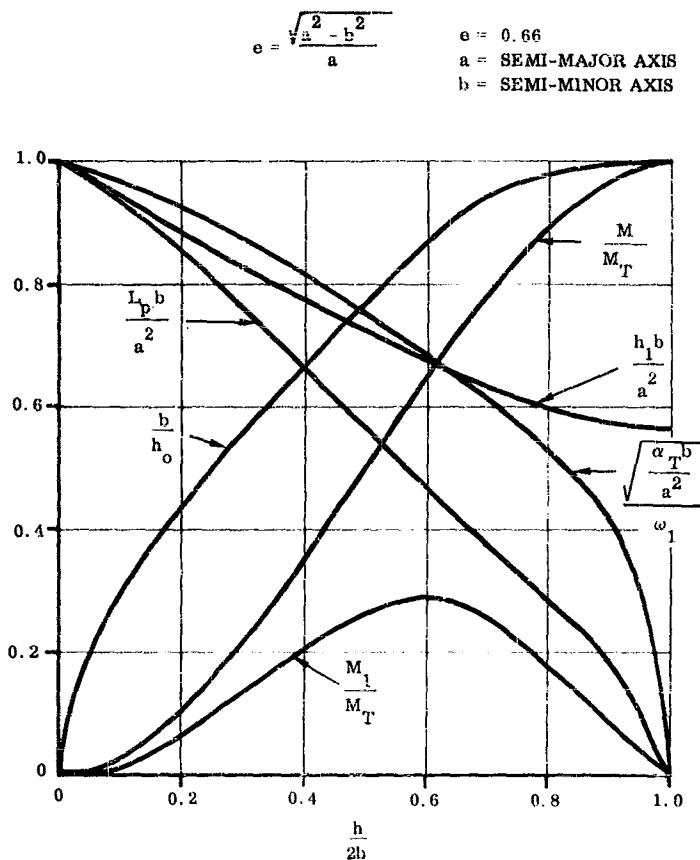
Figure A-18. Sloshing Parameters for the Pendulum Analogy in an Elliptical Tank (e = 0.66), First Mode (n = 1)

Table A-7. First Mode Sloshing Parameters For a 45-Degree Half Angle Cone (See Figure A-20 for Geometry)

MECHANICAL	HYDRODYNAMIC
$M_o + M_1$	M
M_o	0.25 M
M_1	0.75 M
h_o	1.2 h
h_1	1.6 h
ω^2	$\dfrac{\alpha_T}{h}$
Lp	h
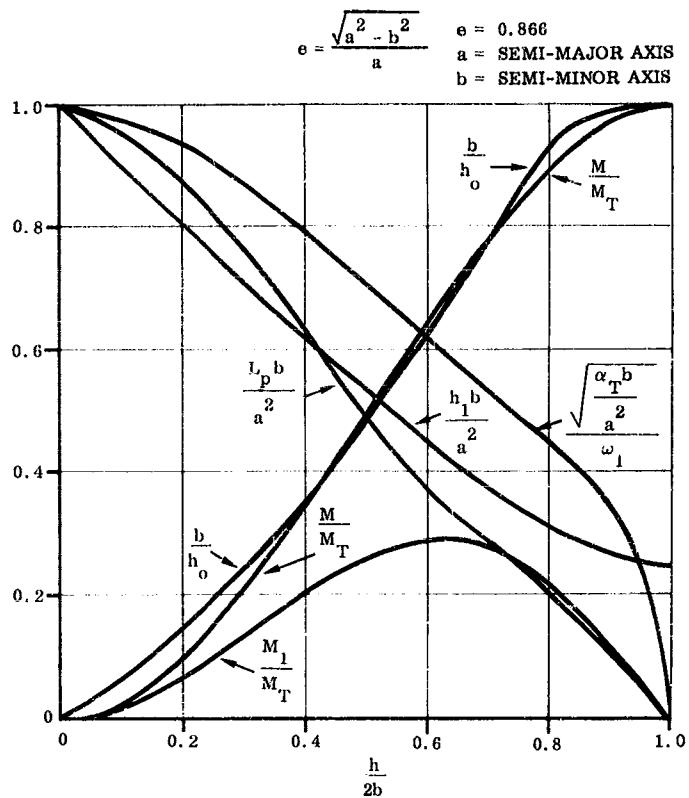
Figure A-19. Sloshing Parameters for the Pendulum Analogy in an Elliptical
Tank (e = 0.866), First Mode (n = 1)
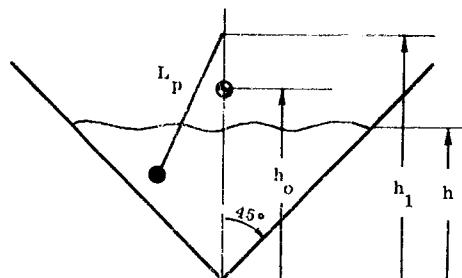
Figure A-20. Geometry, First Mode Sloshing Parameters for a
45-Degree, Half-Angle Cone

A3.5 Approximate Solutions for Vessels that are Bodies of Revolution. The case often arises where the exact solution for the hydrodynamic equations of motion does not exist or is not readily available. If a solution does exist, it may not be in a form that is readily adapted for computation. Therefore, it is desirable to have some method of computing the approximate parameters for a mechanical analogy directly from a given tank shape.

A method for approximating the parameters for a mechanical analogy that reproduces the forces and moments due to liquid oscillations is available in the "equivalent-cylindrical-tank-with-an-equivalent-bottom" analogy. The "sloshing" parameters for spring-mass or pendulum analogies may be found as a function of liquid depth from an "equivalent flat bottom cylinder". This mathematically equivalent tank (shown in Figure A-21 for a spheroid) is a cylinder generated at incremental liquid depths of the original tank by conserving the free surface area and volume of the two tanks (original and equivalent). The "sloshing" parameters are then generated for the equivalent cylindrical tank, at various liquid levels, from one of the rigid-wall tank mechanical analogies presented. (The special rigid-wall, spring-mass analogy, as modified for flexible-wall problems, should not be used, however). Tanks of other shapes are handled in a like manner.

THE FREE SURFACE AREA (RADIUS) AND THE VOLUME OF LIQUID IN THE "EQUIVALENT" CYLINDER ARE THE SAME AS THOSE IN THE SPHEROID.

THE APPARENT LOCATION OF THE MECHANICAL ELEMENTS IS WITHIN THE BOUNDARIES OF THE SPHEROID EXCEPT THE RIGID MASS FOR VALUES OF THE EQUIVALENT TANK'S h/a GREATER THAN 2.
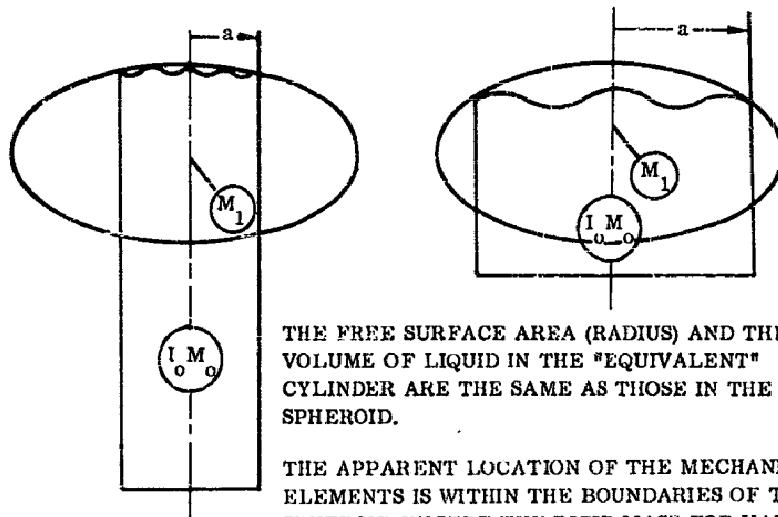
Figure A-21. Equivalent Cylindrical Analogy for an Oblate Spheroid

A3.6 Rotation Produced by Translation (Swirl). For stability analysis it has been customary to ignore the non-linear terms in the Navier-Stokes equation, on the supposition that the motions to be studied were infinitesimally small. It has also been assumed that the viscous terms could be dropped inasmuch as the viscous effects for slightly viscous liquids are confined to a narrow region in the vicinity of the fluid boundary. It was observed during the course of experiments designed to check the linear non-viscous theory that when the forcing frequency was in the neighborhood of the natural frequency, the liquid departed from a planar motion, and a rotational wave was observed to wash around the boundaries. R. R. Berlot (A-13) concluded, after a study of this phenomenon, that any slight departure of the center of gravity of the fluid from the plane containing the axis of the tank (a cylinder in his studies) and the driving vector will, by the action of centrifugal force, be amplified until an equilibrium is reached between the action of centrifugal force and that of gravity. The center of gravity of the liquid will move in an orbit about the axis of the tank, and the angular momentum will be carried by a vortex. Berlot also discusses the results of digital and analog computer studies made to determine the response of a conical pendulum to a driving force. These studies revealed the presence of boundaries between the regions where the oscillations of the pendulum are confined to the plane of the external driving force and the regions where rotary motion results from the planar driving force. These boundaries appear at or near the point where the driving frequency is the same as the natural frequency of oscillation.

This effect may be reproduced quite accurately, using the mechanical analogies already presented. For small amplitudes the motion of a conical pendulum may be duplicated by superposition of the response of two simple pendulums or spring-mass systems mounted perpendicularly to each other. The slosh planes of these two pendulums are usually considered fixed in inertial space, unable to rotate with the tank about its longitudinal axis.

This model is restricted to tanks of revolution whose center lines coincide with the vehicle's longitudinal axis. Of course, if section baffles or similar pieces of construction are present in the tank or if clustered tanks are used, rotation of the liquid about the vehicle's longitudinal axis is impaired.

A3.7 Empirical Verifications and Other Data. It is often quite reasonable and accurate to determine the forces and moments produced by liquid oscillations in a contained vessel by tests with the actual tank or a scale model. H. W. Abramson and G. Ransleben (A-14) present a method for determining the parameters for a scale model tank that can be used to study the liquid oscillations in a prototype tank. The method presented uses dimensional analysis to determine the ratio of the model physical parameters to those of the prototype.

As can be expected, the ratios of the liquid depth, excitation amplitude, and diameters are all equal. If viscosity is neglected, the ratio of the diameters divided by the ratio of the longitudinal accelerations equals the ratio of the time constant squared. The reciprocal of the time-constant ratio equals the frequency ratio.

In any test designed to determine the response of a liquid in a tank to external forces, care must be taken to minimize coupling effects between the sloshing liquid and the tank support structure. Various methods have been devised that show an acceptable solution to this problem (A-15, A-16 and A-17).

A3.7.1 Verification of Analytical Studies. Tests have been conducted to determine and verify the forces, moments, and frequencies of oscillation of a liquid in a contained vessel. Some of the notable tests have been conducted by J. L. McCarty and D. G. Stephens (A-18, -19) under the auspices of the National Aeronautics and Space Administration. In these tests excellent agreement is shown between the experimental data and the results of available theory. Useful plots of a nondimensional frequency parameter versus aspect ratio are given for the first three modes of slosh in spheres, horizontal circular cylinders (transverse and longitudinal modes), upright circular cylinders, and toroidal tanks in three different orientations. No data is given to compare the forces and moments.

For a spheroid the results in general show that, above the half-full condition, the natural frequencies of the first two modes of a liquid in a spheroid of semi-major axis, a, are approximately equal to those in a sphere of radius, a. However, at lower depths the frequency is reduced appreciably. For the first mode, when the tank is near empty, the frequency approaches the frequency of a simple pendulum of length equal to the radius of curvature of the tank wall.

A3.7.2 Inherent Damping. K. M. Case and W. C. Parkinson (A-20) conducted an investigation of the damping of surface waves in right circular cylinders with smooth walls. The question of interest was the dependence of the damping on cylinder height and radius, and the viscosity of the contained fluid. Their results indicate that the inherent damping is the sum of the free surface damping, side wall wiping damping, and the bottom scrubbing damping. These damping terms are given by:

(Free-surface damping)

$$\zeta_t = \frac{4 \pi \nu \xi_n^2}{\omega^2 a}$$

(A-7)

(Side-wall wiping damping)

$$\zeta_s = \sqrt{\frac{\nu}{2\omega}} \frac{\pi}{a} \left\{ \frac{\left[1 + \frac{n^2}{\xi_n^2} \right]}{\left[1 - \frac{n^2}{\xi_n^2} \right]} - \frac{2 \xi_n h}{a \sinh 2 \xi_n \frac{h}{a}} \right\}$$

(A-8)

(Bottom-scrubbing damping)

$$\zeta_b = \sqrt{\frac{\nu}{2\omega}} \frac{\pi}{a} \frac{2 \xi_n}{\sinh 2 \xi_n \frac{h}{a}}$$

(A-9)

A-35

From their studies, two remarks are in order:

a. The damping is rather independent of the shape of the cylinder cross section. Thus, the difference between the result for a circular cylinder and for a square cylinder of the same cross-sectional area is less than 20 percent.

b. The free-surface damping is small compared to the wall-wiping damping - particularly for large cylinders.

A3.7.3 Mechanical Baffle Damping. Several approaches exist which could preclude excessive in-flight sloshing of liquids in smooth-walled tanks of missiles. The control system designer could resort to complex filtering methods or to the use of additional feedback loops using sensors that detect propellant motion. The objective would be to adjust the control system phase in the neighborhood of the sloshing frequency (see Section 2). However, such an approach is not practicable because: 1) the reliability of such complex filtering or auxiliary sensing would be questionable, 2) the vehicle and tank properties change radically over the course of the flight; thus a complicated programming system would be required to provide an effective control system at all flight instants.

The solution employed in practice to stabilize vehicles having a divergent mode of oscillation is to install baffles. Installation of suitable mechanical baffles can introduce the desired amount of damping, but only if a certain limit-cycle oscillation amplitude can be tolerated. That this limit-cycle amplitude is necessary is seen from the fact that baffle damping is amplitude-dependent (see following discussion). Hence, to obtain damping sufficient to prevent excessive slosh buildup, some slosh amplitude must be accepted. The other chief disadvantage of mechanical baffles is the weight penalty involved. It can be shown, however, that the weight of fixed-ring baffles is by no means excessive.

The amount of internal (passive) damping of liquid oscillations provided by fixed-ring baffles has been approximated as a function of the sloshing amplitude for given baffles in a given tank by J. W. Miles (A-21). His formula is:

$$ \zeta_b \;=\; K \; \left(\frac{A_{baffle}}{A_{tank}} \right)^{3/2} \; e^{-4.6 \frac{\Delta h}{a}} \; \left(\frac{\eta_1}{a} \right)^{1/2} \tag{A-10} $$

The areas indicated are plan areas of the tank cross section and annular ring. Another formula presented by J. W. Miles, based upon an alternate set of assumptions, is:

$$ \zeta_b \;=\; K' \; \left(\frac{A_{baffle}}{A_{tank}} \right) \; e^{-5.52 \frac{\Delta h}{a}} \; \left(\frac{\eta_1}{a} \right) \tag{A-11} $$

Each of the above equations has been supported to some degree by test data (after proper empirical choice of the constant, K, or K'). The constant, K in Equation A-10 as given by E. D. Geissler (A-22), has a value between 2.25 and 4.5. J. W. Miles suggests a value of three. H. F. Baer (A-23) predicts that the constant K' has a value of six - a value which agrees very closely with experimental findings at Convair-Astronautics, at least for relatively small baffle areas and damping values.

While the damping of fixed-ring baffles can be estimated by Miles' formulae, a more exact procedure, especially for baffles other than flat annular rings, is the investigation of sloshing motions in model tests. For these tests model laws require, according to H. W. Abramson (A-14), that the following relationship between diameter, acceleration field, viscosity and density ratios be fulfilled:

$$ d_r \;=\; \alpha_r^{-1/3} \; \left(\frac{\mu_r}{\rho_r} \right)^{2/3} $$

This relationship is valid if surface tension is neglected. Acceleration on the ground, being lower than that experienced in flight, requires larger models. Use of heavy liquids, however, permits simulation of high accelerations with reasonably small models.

The pressure in equivalent feet of liquid head applied to the fixed-ring baffle, according to J. W. Miles is found to be

$$P = 5.5 \left(\frac{A_{baffle}}{A_{tank}} \right)^{1/2} e^{-2.76 \frac{\Delta h}{a}} \left(\frac{\eta_1}{a} \right)^{1/2} \eta_1 \cos \phi \qquad (A-12)$$

or, for alternate assumptions, when A_{baffle} / A_{tank} is greater than 0.14:

$$P = 1.9 \; e^{-3.68 \frac{\Delta h}{a}} \left(\frac{\eta_1^2}{a} \right) \cos \phi \qquad (A-13)$$

where ϕ is an angular coordinate around the tank axis measured from the plane of slosh motion.

A knowledge of this force is required for the design of the baffles and support structure.

APPENDIX A4

ELASTIC PROPERTIES OF VEHICLES

SYMBOLS USED IN APPENDIX A4

Symbol	Definition	Units
$C^{\alpha\alpha}(x,\xi)$	Influence function; angular rotation at station x due to a unit moment at station ξ	1/ft lb
$C^{\alpha\delta}(x,\xi)$	Influence function; angular rotation at station x due to a unit lateral force at station ξ	1/lb
$C^{\delta\alpha}(x,\xi)$	Influence function; lateral deflection at station x due to a unit moment at station ξ	ft/ft lb
$C^{\delta\delta}(x,\xi)$	Influence function; lateral deflection at station x due to a unit lateral force at station ξ	ft/lb
$m(x)$	distributed mass per unit length	slugs/ft
$p(x,t)$	distributed external lateral force per unit length	lb/ft
$r(x,t)$	distributed external moment per unit length	ft lb/ft
$u(x,t)$	displacement function	ft
$\mu(x)$	distributed rotary inertia per unit length	lb sec²
η_i	mode shape (eigenfunction) for i^{th} mode	N.D.

Matrix Symbology

$C^{\alpha\alpha}_{(n,n)}$	$=\left[C^{\alpha\alpha}_{ij}\right]$ where $C^{\alpha\alpha}_{ij}$ is an influence coefficient which represents the angular rotation at the ith mass station due to a unit moment applied at the jth mass station	1/ft lb
$C^{\alpha\delta}_{(n,n)}$	$=\left[C^{\alpha\delta}_{ij}\right]$ where $C^{\alpha\delta}_{ij}$ is an influence coefficient which represents the angular rotation at the ith mass station due to a unit lateral force applied at the jth mass station	1/lb
$C^{\delta\alpha}_{(n,n)}$	$=\left[C^{\delta\alpha}_{ij}\right]$ where $C^{\delta\alpha}_{ij}$ is an influence coefficient which represents the lateral deflection at the ith mass station due to a unit moment applied at the jth mass station	ft/ft lb
$C^{\delta\delta}_{(n,n)}$	$=\left[C^{\delta\delta}_{ij}\right]$ where $C^{\delta\delta}_{ij}$ is an influence coefficient which represents the lateral deflection at the ith mass station due to a unit lateral force applied at the jth mass station	ft/lb
$Dm_{(n,n)}$	$=\left[m_1, m_2,\ldots, _i\ldots, _n\right]$; diagonal matrix of n discrete masses	slugs
$D\mu_{(n,n)}$	$=\left[\mu_1, \mu_2,\ldots,\mu_i,\ldots,\mu_n\right]$; diagonal matrix of n discrete rotary inertias	slug ft²
$P_{(n,1)}$	$=\left\{p_1, p_2,\ldots,p_i\ldots,p_n\right\}$; column vector representing external lateral forces at n discrete stations	lb

SYMBOLS USED IN APPENDIX A4 (Continued)

Symbol	Definition	Units
$R_{(n,1)}$	$= \lfloor r_1, r_2, \ldots, r_i, \ldots, r_n \rfloor$; column vector representing external moments at n discrete stations	ft lb
$u_{(n,1)}$	$= \lfloor u_1, u_2, \ldots, u_i, \ldots, u_n \rfloor$; column vector representing displacements at n discrete stations	ft
$x_{(n,1)}$	$= \lfloor x_1, x_2, \ldots, x_i, \ldots, x_n \rfloor$; column vector defining locations of discrete mass stations	ft
$1_{(n,1)}$	$= \lfloor 1, 1, 1, \ldots, 1, \ldots, 1 \rfloor$; unit vector	N.D.

Special Notations

'   "prime" denotes differentiation with respect to x

.   "dot" denotes differentiation with respect to t

*   "asterisk" denotes the transpose of a matrix

°   denotes any null matrix. The order is dependent on the particular sense in which it is used, i.e., the order must be consistent with its usage.

A4.1 General. It was shown in paragraph 3.3 of Section 3 that the normal bending modes (and their associated frequencies) for the unrestrained vehicle are obtained by solving the set of homogenous algebraic equations:

$$\left| u_i \right| = \omega^2 \left[\tilde{C}_{ij} \right] \left\{ M_j \right\} \left| u_j \right| \tag{A-14}$$

Here the matrix, $\tilde{C}_{ij}$, is the matrix of flexibility influence coefficients for the free-free (floating) beam; deflections are measured relative to the centroidal principal axis. It may be shown that this matrix derives directly from the symmetric flexibility influence coefficient matrix, C_{ij}, where deflections are measured relative to an arbitrary line within the structure. In general this matrix includes coefficients relating both translation and rotation to linear forces and couples.

In Section 3 it was noted that the differential equations of forced vibraion for a continuous system are replaced by their matrix counterparts (see Equations 3-7 and 3-9) which represent a lumped parameter system. Some judgment must be exercised when choosing the number and locations for these discrete mass stations. It has been found that the required number of mass stations should be approximately ten times the number corresponding to the highest elastic bending mode to be calculated. For example, if three elastic bending modes are to be calculated, then approximately thirty mass stations are required to represent adequately the bending dynamics of the third mode. This criteria has been established empirically by calculating mode shape, frequency, and generalized mass corresponding to the first three elastic bending modes for typical vehicle configurations in which the numbers of mass stations used were successively increased from eighteen to forty. As expected, the accuracy increased as additional stations were utilized. However, it was observed that no further significant increase in accuracy was achieved by using more than thirty mass stations.

A4.2 Tabulation of Basic Data and the Mathematical Model. The basic data required for the calculation of the natural bending modes consists of: 1) the distributed vehicle inertial properties, i.e., running mass and rotary inertial distribution and 2) the bending and shear stiffness distribution. Note that only rigid masses are to be included in this distribution, that is, only those masses which can be considered to act as an integral part of the unrestrained beam during its vibrations. It cannot be overemphasized that items such as pumps, equipment pods, etc. which are actually mounted elastically to the main structure may significantly alter the bending characteristics of the higher frequency modes. Whether or not such masses are to be treated as integral to the beam or as separate, elastically attached masses, depends upon 1) whether or not the frequencies of the body modes to be computed are less than or greater than the mount frequencies of the discrete masses, and 2) whether or not these masses are great enough to affect the result. (In this connection see also Subsection A4.6, below.)

Figures A-22 and A-23 below illustrate a typical set of curves presenting bending stiffness, EI, and mass distribution, m(x), as a function of vehicle station number. Similarly, curves presenting transverse shear stiffness, KG, and rotary inertia, $\mu(x)$, as functions of vehicle station number are required. From these data a table such as Table A-8, can be constructed. The significance of the subscripts, r, and, i, will be clarified in the following section. However, the following notes are presented at this point.

a. n and s are independent, with $n \leq s + 1$

b. For each x_i there exists an x_r which is numerically identical.

c. There is a one-to-one correspondence between x_i, m_i, and μ_i.

d. There is one-to-one correspondence between x_r, EI_r, and KG_r.

The matrix of structural influence coefficients, C, can be calculated from the data presented in the first four columns of Table A-8. The matrix C is called a flexibility matrix, and the paragraph which follows presents a method for its calculation by a process of triple matrix multiplication.
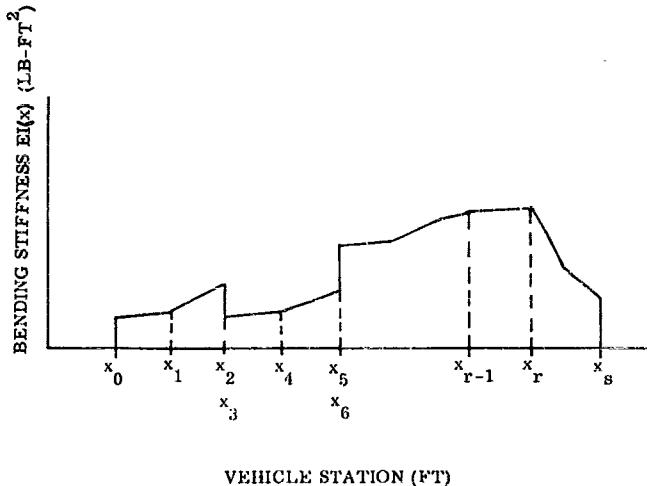
Figure A-22. Typical Vehicle Bending Stiffness
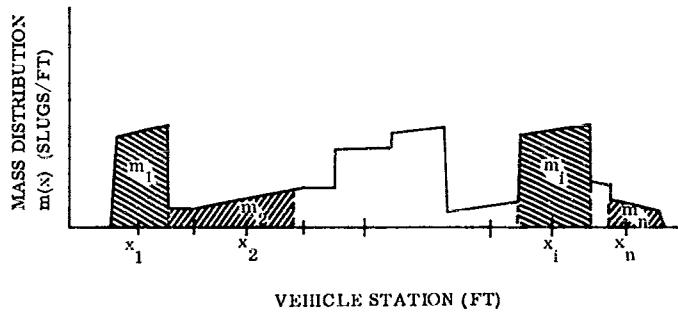
Figure A-23. Typical Vehicle Mass Distribution

A4.3 Flexibility Matrix for a Cantilever Beam: Statically Determinate Case. A cantilever beam subjected to concentrated forces and moments at discrete stations along its elastic axis is shown in its deformed state of equilibrium in Figures A-24 and A-25. The beam is considered to consist of "s" elements which are cascaded end to end. The bending stiffness, EI, and shear stiffness, KG, may in general vary in an arbitrary manner throughout the length of the beam. However, for practical purposes it is usually sufficient to assume a linear variation between the boundaries of any one element.

The internal elastic restoring forces acting on the rth element (bending moments and shears) are shown in Figure A-26.

It is assumed that the rth element is chosen so that no external forces are introduced throughout its length; that is, the external forces act at the points x_{r-1} and x_r. We define a load vector for each of the "s" elements by:

$$S_r = \begin{bmatrix} V_{r-1} \\ M_{r-1} \end{bmatrix},$$
(A-15)

NOTE: Within Subsection A4.3 a different notation is employed for applied torque, t, and for transverse elastic deflections, y, than is used elsewhere in Appendix A4. It appears only in this specialized, selfcontained section and hence should cause no confusion.

Table A-8. Elastic and Inertial Properties

x_r	x_i	EI_r	KG_r	m_i	μ_i
FT.	FT.	LB.-FT.^{2}	LB.	SLUGS	LB.-SEC.^{2}
x_o	x_1	EI_o	KG_o	m_1	μ_1
x_1	-	EI_1	KG_1	-	-
x_2	x_2	EI_2	KG_2	m_2	μ_2
.	.	.	.	.	.
.	.	.	.	.	.
.	.	.	.	.	.
x_r	x_i	EI_r	KG_r	m_i	μ_i
.	.	.	.	.	.
.	.	.	.	.	.
.	.	.	.	.	.
x_s	x_n	EI_s	KG_s	m_n	μ_n

Figure A-24. Cantilever Beam Subjected to Concentrated Forces and Moments
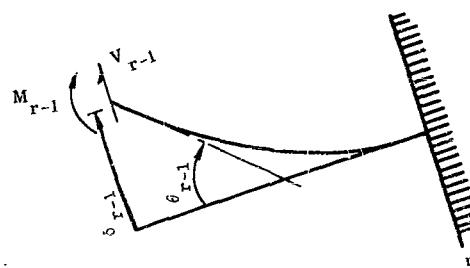
Figure A-25. Displacement Forces
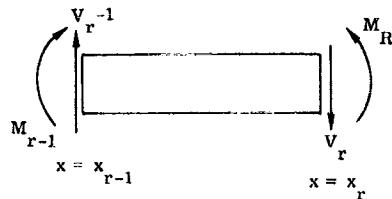
Figure A-26. Internal Elastic Restoring Forces

where V_{r-1} and M_{r-1} are the internal elastic bending moment and shear externally applied to the boundaries of the rth element acting on the r-1 end of the rth element. We now define an externally applied load vector for the entire beam as:

$$F = \left[p_1, p_2, \cdots, p_n, t_1, t_2, \cdots, t_n \right] \quad . \tag{A-16}$$

Now, since the internal elastic restoring forces are linear combinations of the externally applied forces, we write:

$$S_r = b_r F , \tag{A-17}$$

where b_r is a load transformation matrix. The matrix b_r takes the form:

$$b_r = \left[b_{r_1}^p, \cdots, b_{r_n}^p, b_{r_1}^t, \cdots, b_{r_n}^t \right] \quad . \tag{A-18}$$

The matrix b_r is of the order 2 x 2n and has been partitioned into 2n vectors of order 2. The elements of the vectors $b_{r_i}^p$ and $b_{r_i}^t$ represent the internal beam shear and bending moment acting on the r-1 end of the rth element due to a unit force and unit couple respectively applied externally at the ith station.

We next define a displacement vector, v_r, for the rth element. This vector defines the deflection and rotation of r-1 end of the rth element relative to the r end when this element is subjected to the forces, S_r. These displacements are, in turn, a linear combination of the forces producing them, specifically V_{r-1} and M_{r-1}. We express this fact as:

$$v_r = f_r S_r, \tag{A-19}$$

where

$$v_r = \begin{bmatrix} \delta_{r-1} \\ \theta_{r-1} \end{bmatrix} \quad .$$

The displacements δ_{r-1} and θ_{r-1} are illustrated in Figure A-25. The matrix f_r is a flexibility matrix for an elemental cantilever beam. As shown above, f_r is of order 2 x 2 and is defined below. We have:

$$f_r = \begin{bmatrix} f_r^{\delta\delta} & f_r^{\delta\alpha} \\ f_r^{\alpha\delta} & f_r^{\alpha\alpha} \end{bmatrix}, \tag{A-20}$$

where

$$f_r^{\delta\delta} = \frac{\ell_r^3}{3EI_{r-1}} \left(1 + \frac{3}{4} K_1 \right) + \frac{\ell_r}{KG_{r-1}} \left(1 + \frac{1}{2} K_2 \right)$$

$$f_r^{\delta\alpha} = \frac{\ell_r^2}{2EI_{r-1}} \; (1 + \frac{2}{3} \; K_1)$$

$$f_r^{\alpha\delta} = f_r^{\delta\alpha} = \frac{\ell_r^2}{2EI_{r-1}} \; (1 + \frac{2}{3} \; K_1)$$

$$f_r^{\alpha\alpha} = \frac{\ell_r}{EI_{r-1}} \; (1 + \frac{1}{2} \; K_1) \quad,$$

wherein,

$$K_1 = \frac{EI_{r-1}}{EI_r} - 1$$

$$K_2 = \frac{KG_{r-1}}{KG_r} - 1 \text{ and,}$$

$$\ell_r = x_r - x_{r-1} \quad.$$

The total lateral displacement (due to pure bending plus shearing deformations) at the ith station due to all external forces acting on the beam can now be determined from the principle of virtual work. Thus,

$$1 \cdot y_i = \sum_{r=1}^{s} b_{r_i}^{*p} \; v_r$$

$$= \sum_{r=1}^{s} b_{r_i}^{*p} \; f_r \; b_r \; F \tag{A-21}$$

Similarly, we get

$$1 \cdot \alpha_i = \sum_{r=1}^{s} b_{r_i}^{*t} \; f_r \; b_r \; F \tag{A-22}$$

Collecting all of the 2n displacements implied by Equations (A-21) and (A-22), we define a displacement vector U.

$$U = \begin{bmatrix} y \\ \alpha \end{bmatrix} = \sum_{r=1}^{s} b_r^{*} \; f_r \; b_r F \tag{A-23}$$

From the definition of a flexibility matrix, C, we observe from Equation (A-23)

$$C = \sum_{r=1}^{s} b_r^{*} \; f_r \; b_r \tag{A-24}$$

is the complete flexibility matrix for a cantilever beam. Actually, this result is general and is valid for any linear elastic structure, statically determinate or indeterminate. The latter case is necessarily more complicated since the b_r matrices are statically indeterminate. However, Equation (A-24) remains valid. The flexibility matrix, C, given above by Equation (A-24), is the same matrix introduced previously as C_{ij}. This matrix is required for the calculation of the elastic bending modes. The b_r matrices for a statically determinate cantilever beam are dependent only on the stations chosen for the x_r's and x_i's. Some simple rules are presented below for this case.

It is convenient first to partition b_r as:

$$b_r = \begin{bmatrix} \overset{V_p}{b_r} & \overset{V_t}{b_r} \\ \overset{M_p}{b_r} & \overset{M_t}{b_r} \end{bmatrix}$$

The partitions of b_r, i.e., $b_r{}^{V_p}$, $b_r{}^{V_t}$, $b_r{}^{M_p}$, and $b_r{}^{M_t}$ are calculated as follows:

a. Elements of $b_r{}^{V_p}$:

   1) calculate $x_i - x_{r-1}$; $i = 1, 2, \cdots, n$

   2) if $x_i - x_{r-1} \leq 0$, $b_{r_i}{}^{V_p} = 0$

   3) if $x_i - x_{r-1} > 0$, $b_{r_i}{}^{V_p} = -1$

b. Elements of $b_r{}^{V_t}$:

   1) all elements are zero; i.e., $b_{r_i}{}^{V_t} = 0$

c. Elements of $b_{r_i}{}^{M_p}$:

   1) calculate $x_i - x_{r-1}$; $i = 1, 2, \cdots, n$

   2) if $x_i - x_{r-1} \leq 0$, $b_{r_i}{}^{M_p} = 0$

   3) if $x_i - x_{r-1} > 0$, $b_{r_i}{}^{M_p} = x_i - x_{r-1}$

d. •Elements of $b_{r_i}{}^{M_t}$:

   1) calculate $x_i - x_{r-1}$; $i = 1, 2, \cdots, n$

   2) if $x_i - x_{r-1} \leq 0$, $b_{r_i}{}^{M_t} = 0$

   3) if $x_i - x_{r-1} > 0$, $b_{r_i}{}^{M_t} = 1$

A4.4 Elastic Bending Mode Calculations. The elastic bending modes are determined by obtaining the solutions to the set of homogenous algebraic equations given previously by Equation A-14. This equation is rewritten here with a slightly abbreviated and modified notation

$$\lambda u = \bar{C} \, D_1 u, \tag{A-25}$$

where $\lambda = 1/\omega^2$ and the inertial matrix is given a new symbol to signify the incorporation of rotary inertias of the various mass points. It is readily shown that the matrix $\bar{C}$ is related to C such that Equation A-25 may be written (see nomenclature for this section) as

$$\left[I - A \; (A^* \; D_I \; A)^{-1} \; A^* \; D_I \right] \; CD_I \; u \; = \; \lambda \; u,$$

(A-26)

where

$$\underset{(2n,\ 2n)}{I} = \begin{bmatrix} 1 & & & & \\ & 1 & & & \\ & & 1 & & \\ & & & \ddots & \\ & & & & 1 \end{bmatrix}$$

$$\underset{(2n,\ 2n)}{A} = \begin{bmatrix} 1 & x \\ & \\ 0 & 1 \end{bmatrix}$$

$$\underset{(2n,\ 2n)}{D_I} = \begin{bmatrix} D_m & 0 \\ & \\ 0 & D_\mu \end{bmatrix}$$

and

$$\underset{(2n,\ 2n)}{C} = \begin{bmatrix} C^{\delta\delta} & C^{\delta\alpha} \\ & \\ C^{\alpha\delta} & C^{\alpha\alpha} \end{bmatrix}$$

Having constructed the flexibility matrix, C, as outlined in the previous section, the matrix of coefficients in Equation A-26 is constructed by straight-forward matrix operations.

A matrix iteration method (Ref. A-34 and A-35) for calculating the dominant eigenvalue and its associated eigenvector is recommended, due to its simplicity and because it appears to yield results as accurately and rapidly as any of the various methods currently employed. Having determined the dominant eigenvalue, and its corresponding eigenvector, η_3, of the matrix $[I - A (A^* D_I A)^{-1} A^* D_I] \; C \; D_I$, we now wish to determine λ_4 and η_4. The subscript "3", which normally refers to "third mode", is used to emphasize the fact that the first two modes are the rigid-body modes of zero frequency. They are not obtained from Equation A-26, having been "swept out" earlier, see Section 3. One extremely simple technique for determing λ_4 and η_4 is to proceed as follows. We construct a new matrix by calculating:

$$\frac{-\lambda_3}{\mathscr{M}_3} \; \eta_3 \; \eta_3^* \; D_I \quad , \text{ where } \mathscr{M}_3 \text{ is the mode's generalized mass.} \tag{A-27}$$

The new matrix defined by Equation A-27 is now added to the original matrix, $[I - A \; (A^* \; D_I \; A)^{-1} \; A^* \; D_I \;] \; C \; D_I$. The "power method" will now yield λ_4 and η_4 when applied to $[I - A \; (A^* \; D_I \; A)^{-1} \; A^* \; D_I \;] \; C \; D_I -\frac{\lambda_3}{\mathscr{M}_3} \; \eta_3 \; \eta_3^* \; D_I$. This procedure is then repeated for calculating λ_5, η_5, etc.

A4.5 Evaluation of Modal Calculation Techniques. The purpose of this Subsection is to exhibit the effect of transverse shear stiffness and rotary inertia on the calculation of the natural bending modes of a free-free (floating) beam. The pertinent data used and the curves of results obtained are presented. Also, percent error calculations for frequency, generalized mass, and maximum deviations from the base curve (the most comprehensive calculation made) are presented. A discussion of the results and the conclusions reached are also involved.

Deflection, slope, and bending moment curves were calculated and plotted for the first four natural modes of vibration for one large booster configuration, using the following combinations of transverse shear stiffness, KG, and rotary moments of inertia, D_μ:

a.   Case 1 $D_\mu = 0$; KG = KG

b.   Case 2 $D_\mu = D_\mu$; KG = KG ("Base" Case)

c.   Case 3 $D_\mu = D_\mu$; KG = ∞

d.   Case 4 $D_\mu = 0$; KG = ∞

The basic parameters, frequency, and generalized mass for the four cases caluclated are shown in Table A-9. The errors, maximum percentage difference based on mode computed with KG = KG and $D_\mu = D_\mu$, are presented in Tables A-10 through A-15. Table A-10 gives the errors in frequency, Table A-11 gives the error in generalized mass, and Tables A-12, -13, -14, -15 give the maximum deviations in the deflections, slopes and moments for the first four modes versus those values at the maximum point on the curve.

The mode deflections, slopes, and bending moments for the four cases considered are plotted in Figures A-26 thru A-38.

Table A-9. Bending Mode Characteristics for Four Methods of Computation

METHOD	MODE NO.	ω (RAD/SEC)	f (CPS)	$\mathcal{M}$ (SLUGS)
CASE 1 ($D_\mu = 0$; KG = KG)	1	34.32	5.465	3,834
	2	83.60	13.31	1,719
	3	120.25	19.15	1,067
	4	188.2	29.97	23,673
CASE 2 ($D_\mu = D_\mu$; KG = KG)	1	34.20	5.446	3,870
	2	82.38	13.12	1,710
	3	117.3	18.68	1,334
	4	187.7	29.89	33,337
CASE 3 ($D_\mu = D_\mu$; KG = ∞)	1	36.96	5.885	3,419
	2	107.16	17.06	1,216
	3	183.7	29.25	2,798
	4	416.0	66.24	15,967
CASE 4 ($D_\mu = 0$; KG = ∞)	1	37.15	5.916	3,410
	2	111.39	17.74	1,209
	3	194.1	30.91	1,809
	4	472.9	75.30	141,906

Table A-10. Frequency Errors (Base: Case 2)

MODE NO.	CASE NO.	FREQ. (RAD/SEC)	PERCENT ERROR
1	1	34.32	0.351
	2	34.20	0.00
	3	36.96	8 07
	4	37.15	8.63
2	1	83.60	1.48
	2	82.38	0.00
	3	107.16	30.10
	4	111.39	35.30
3	1	120.25	2.51
	2	117.30	0.00
	3	183.70	56.50
	4	194.10	65.50
4	1	188.2	0.268
	2	187.7	0.00
	3	416.0	122.00
	4	472.9	152.00

Table A-11. Generalized Mass Errors (Base: Case 2)

MODE NO.	CASE NO.	MASS (SLUGS)	PERCENT ERROR
1	1	3834	-0.93
	2	3870	0.00
	3	3419	-11.78
	4	3410	-11.90
2	1	1719	0.526
	2	1710	0.00
	3	1216	-28.90
	4	1209	-29.30
3	1	1067	-20.00
	2	1334	0.00
	3	2798	109.80
	4	1809	35.60
4	1	23,673	-29.00
	2	33,337	0.00
	3	15,967	-52.10
	4	141,906	326.00

Table A-12. Percent Error Calculations and Maximum Deviations,
First Mode (Base: Case 2)

Deflection Curve

Percent Error Based on Maximum Deflection Shown by the Base Curve
$$\left(\begin{array}{l} \rho = 4.45 \\ \text{Station} = 430 \text{ in.} \end{array} \right)$$

As Defined:

$$\text{Percent Error} = \frac{\text{Max. Deviation From Base}}{\text{Max. Point on Base (4.45)}} \times 100$$

Case No.	Max. Deviation	Percent Error
1	0.2	4.5
2	Base	Base
3	0.3	6.74
4	0.25	5.62

Slope Curve

$$\text{Percent Error} = \frac{\text{Max. Deviation From Base}}{\text{Max. Point on Base} \left(\begin{array}{l} \sigma = 14.9 \\ \text{Station} = 465 \text{ in.} \end{array} \right)} \times 100$$

Case No.	Max. Deviation	Percent Error
1	0.2	1.34
2	Base	Base
3	3	20.1
4	1.4	9.4

Moment Curve

$$\text{Percent Error} = \frac{\text{Max. Deviation From Base}}{\text{Max. Point on Base} \left(\begin{array}{l} M = 240 \frac{\text{in-lbs}}{\text{ft}} \\ \text{Station} = 825 \text{ in.} \end{array} \right)} \times 100$$

Case No.	Max. Deviation	Percent Error
1	2.5	1.04
2	Base	Base
3	22.5	9.38
4	27.5	11.45

Table A-13. Percent Error Calculations and Maximum Deviations,
Second Mode (Base: Case 2)

Deflection Curve

Percent Error Based on Maximum Deflection Shown by the Base Curve
$\left(\begin{array}{l} \beta = 1.6 \\ \text{Station} = 1310 \text{ in.} \end{array}\right)$

As Defined:

$$\text{Percent Error} = \frac{\text{Max. Deviation From Base}}{\text{Max. Point on Base (1.6)}} \times 100$$

Case No.	Max. Deviation	Percent Error
1	.033	2.08
2	Base	Base
3	.233	14.56
4	.200	12.50

Slope Curve

$$\text{Percent Error} = \frac{\text{Max. Deviation From Base}}{\text{Max. Point on Base} \left(\begin{array}{l} \sigma = 9.4 \text{ Deg/ft.} \\ \text{Station} = 815 \text{ in.} \end{array}\right)} \times 100$$

Case No.	Max. Deviation	Percent Error
1	0.4	4.26
2	Base	Base
3	4.4	46.8
4	4.8	51.1

Moment Curve

$$\text{Percent Error} = \frac{\text{Max. Deviation From Base}}{\text{Max. Point on Base} \left(\begin{array}{l} M = 345 \text{ in lbs/ft} \\ \text{Station} = 1065 \text{ in.} \end{array}\right)} \times 100$$

Case No.	Max. Deviation	Percent Error
1	30	8.7
2	Base	Base
3	240	69.6
4	175	50.7

Table A-14.   Percent Error Calculations and Maximum Deviations,
Third Mode (Base: Case 2)

Deflection Curve

Percent Error Based on Maximum Deflection Shown by the Base Curve
$$\left(\begin{array}{l} \phi = 1.77 \\ \text{Station} = 1325 \end{array} \right)$$

As Defined:

$$\text{Percent Error} = \frac{\text{Max. Deviation From Base}}{\text{Max. Point on Base } (1.77)} \times 100$$

Case No.	Max. Deviation	Percent Error
1	0.2	11.3
2	Base	Base
3	1.6	90.5
4	1.05	59.4

Slope Curve

$$\text{Percent Error} = \frac{\text{Max. Deviation From Base}}{\text{Max. Point on Base } (\sigma = 11; \text{ Station} = 1200 \text{ in.})} \times 100$$

Case No.	Max. Deviation	Percent Error
1	1	9.1
2	Base	Base
3	33	300.0
4	25	227.0

Moment Curve

$$\text{Percent Error} = \frac{\text{Max. Deviation From Base}}{\text{Max. Point on Base } (M = 575; \text{ Station} = 1080 \text{ in.})} \times 100$$

Case No.	Max. Deviation	Percent Error
1	75	13.05
2	Base	Base
3	1225	213.0
4	925	161.0

Table A-15. Percent Error Calculations and Maximum Deviations,
Fourth Mode (Base: Case 2)

Deflection Curve

Percent Error Based on Maximum Deflection Shown by the Base Curve
$$\left(\begin{array}{l} \phi = 4.5 \\ \text{Station} = 700 \text{ in.} \end{array} \right)$$

As Defined:

$$\text{Percent Error} = \frac{\text{Max. Deviation From Base} \quad \times 100}{\text{Max. Point on Base (4.5)}}$$

Case No.	Max. Deviation	Percent Error
1	0.1	2.22
2	Base	Base
3	19.5	434.3
4	43.0	955.0

Slope Curve

$$\text{Percent Error} = \frac{\text{Max. Deviation From Base} \quad \times 100}{\text{Max. Point on Base} \left(\begin{array}{l} \sigma = 80 \text{ Deg/Ft} \\ \text{Station} = 750 \text{ in.} \end{array} \right)}$$

Case No.	Max. Deviation	Percent Error
1	80	100.0
2	Base	Base
3	340	425.0
4	820	1,025.0

Moment Curve

$$\text{Percent Error} = \frac{\text{Max. Deviation From Base} \quad \times 100}{\text{Max. Point on Base} \left(\begin{array}{l} M = 2300 \times 10^6 \dfrac{\text{in.-lbs}}{\text{ft.}} \\ \text{Station} = 755 \text{ in.} \end{array} \right)}$$

Case No.	Max. Deviation	Percent Error
1	400×10^6	17.4
2	Base	Base
3	$10,000 \times 10^6$	435.0
4	$27,896 \times 10^6$	1,213.0

It appears from the curves and from the error calculations that, assuming the base curve (Case 2) to be accurate, the base curve can be closely approximated by a calculation with transverse shear stiffness, KG, included and rotary inertia, $D\mu$, omitted. The test results (cf. Section 6) indicate that large deviations occur in all cases for the higher modes. If only the deflection, ϕ, is required, then the 1st and 2nd mode can be calculated with reasonable accuracy, with transverse shear stiffness, KG, and rotary inertia, $D\mu$ omitted. One result shown by the percent error calculations and curves was that the results in the case where neither KG or $D\mu$ were included were usually more accurate than when only $D\mu$ was included. In the first three modes all the curves seem to show the same general trends, i.e., the same sign appears on ϕ, σ, and M for each case tested, although the amplitudes will vary. In the fourth mode it can be seen that the various properties (deflections, slopes, and bending moments) exhibit critical errors; the sign as well as the amplitude is in error. The significance of this type of error can be appreciated by referring to the control system studies outlined in Sections 2 and 4.

It should be noted how the percent error calculations for maximum deviation are made. The deficiencies inherent in these calculations must be kept in mind when they are to be used.
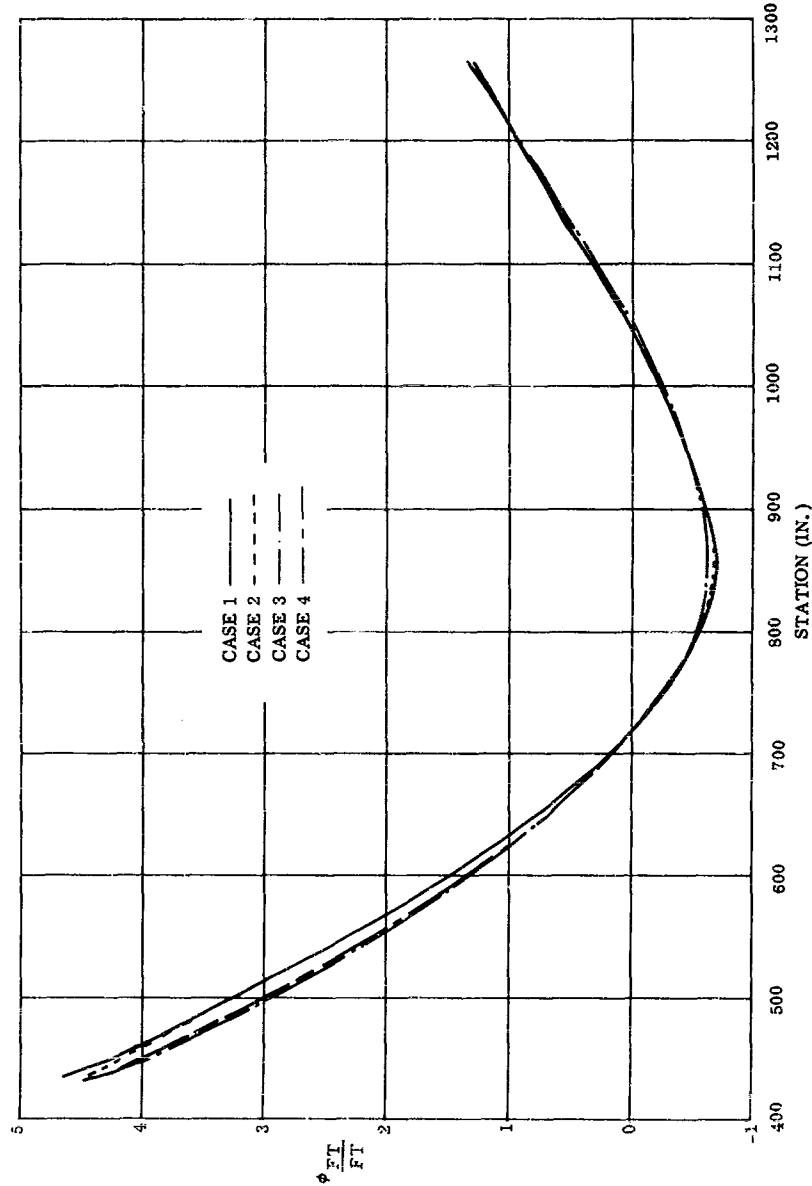
Figure A-27. First Mode Deflections for Four Methods of Computation
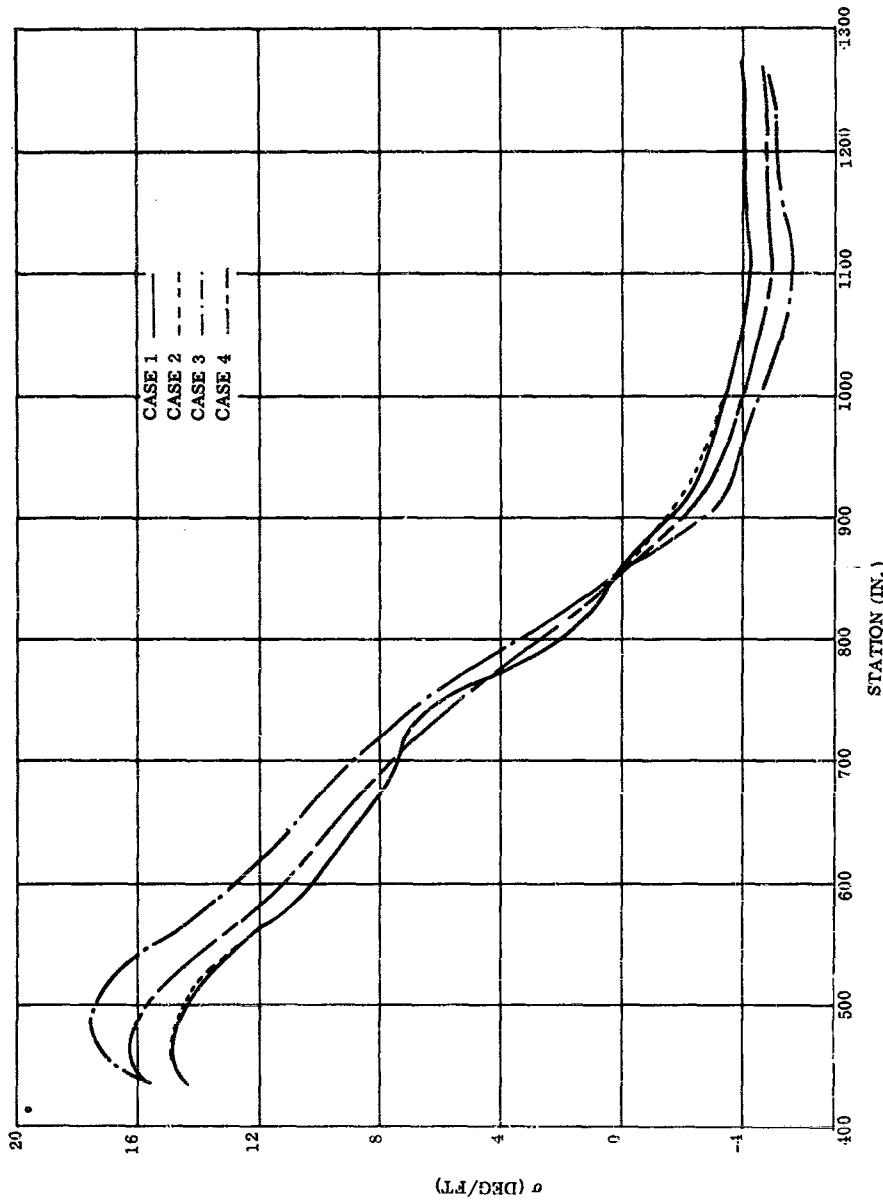
Figure A-28. First Mode Slope for Four Methods of Computation
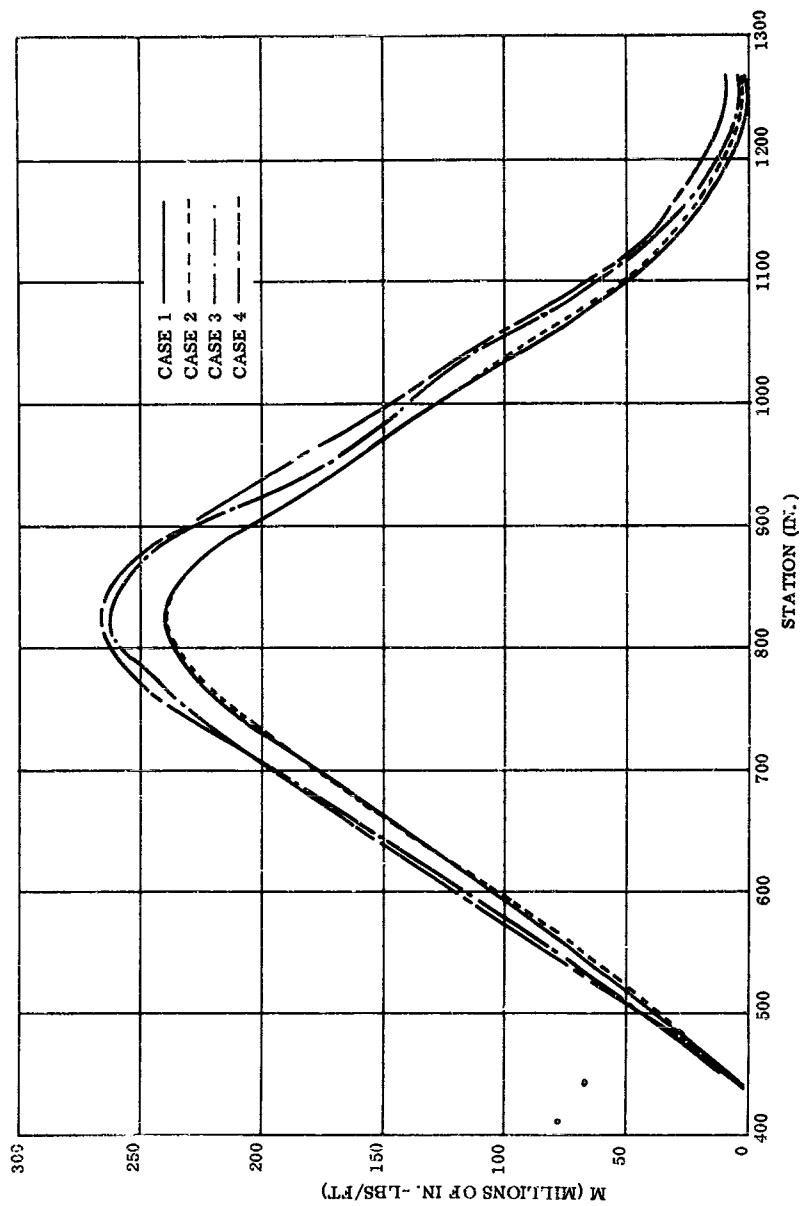
Figure A-29. First Mode Bending Moments for Four Methods of Computation
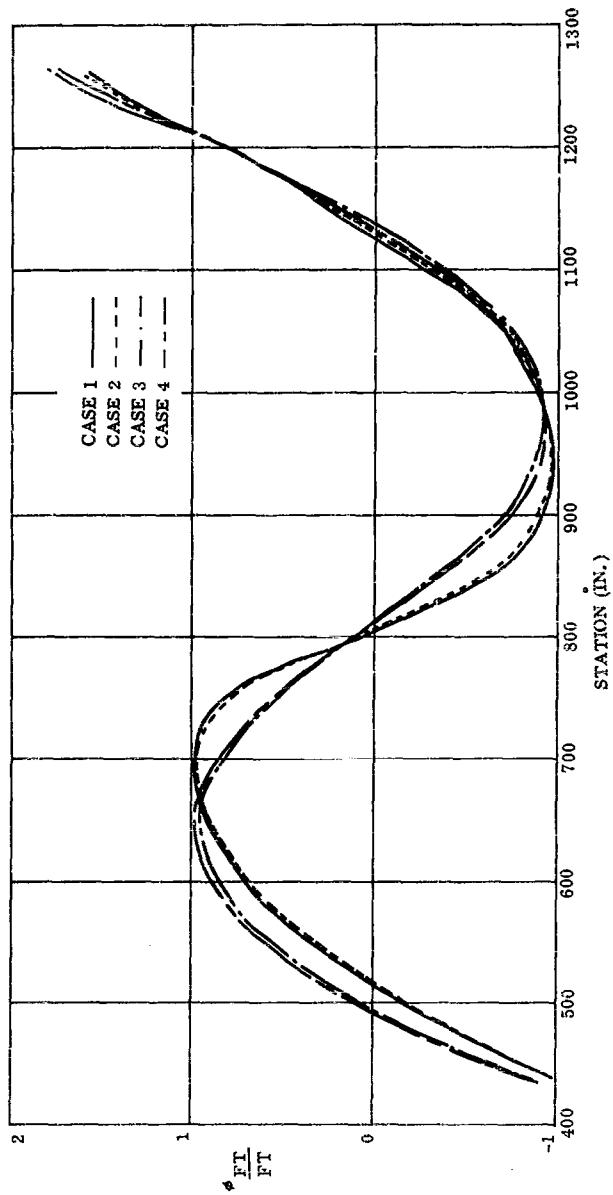
Figure A-30. Second Mode Deflections for Four Methods of Computation
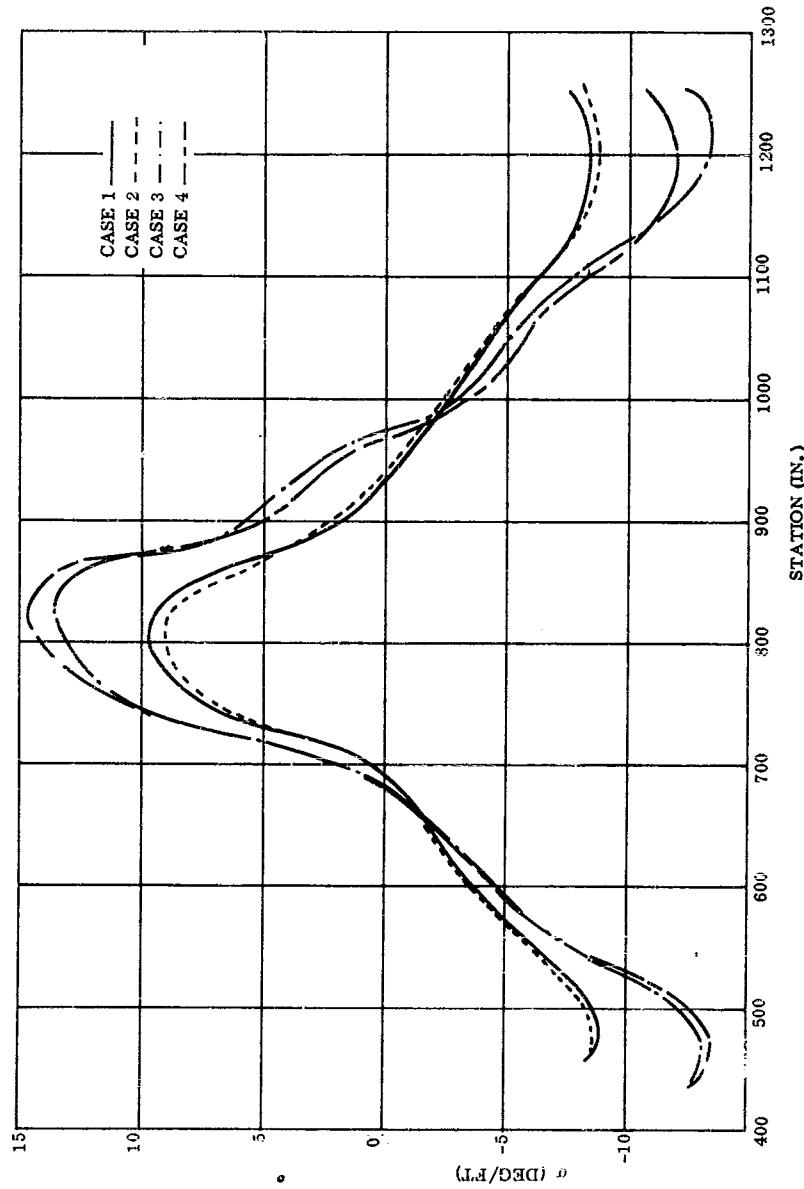
Figure A-31. Second Mode Slope for Four Methods of Computation
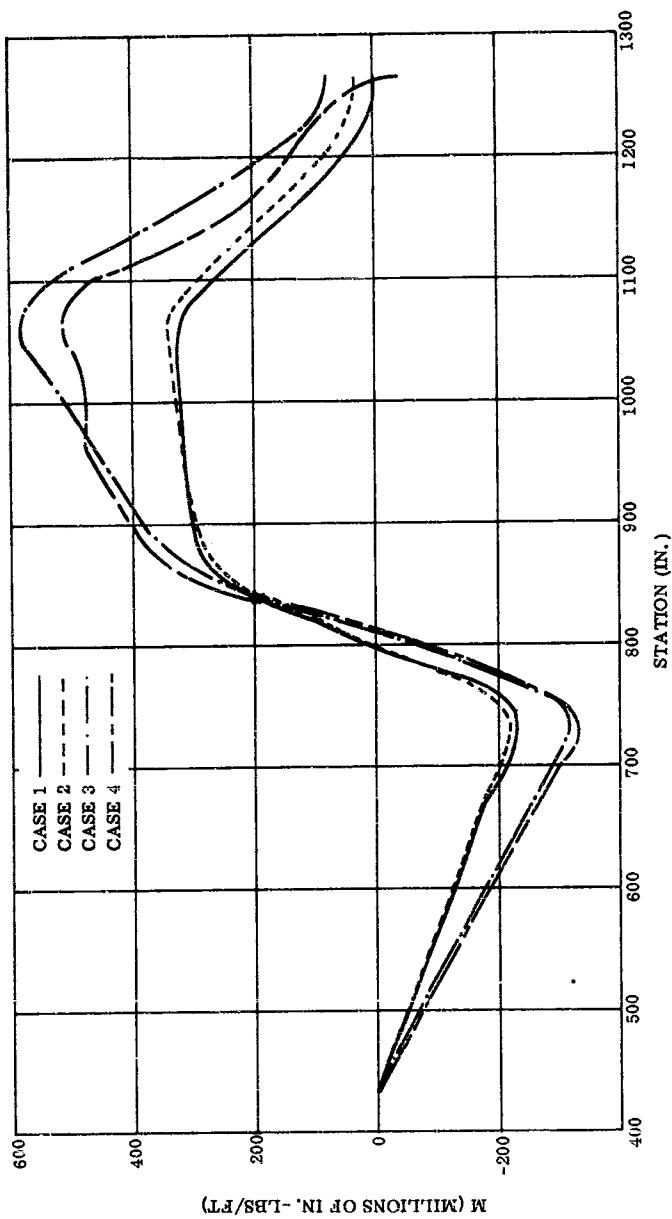
Figure A-32. Second Mode Bending Moments for Four Methods of Computation
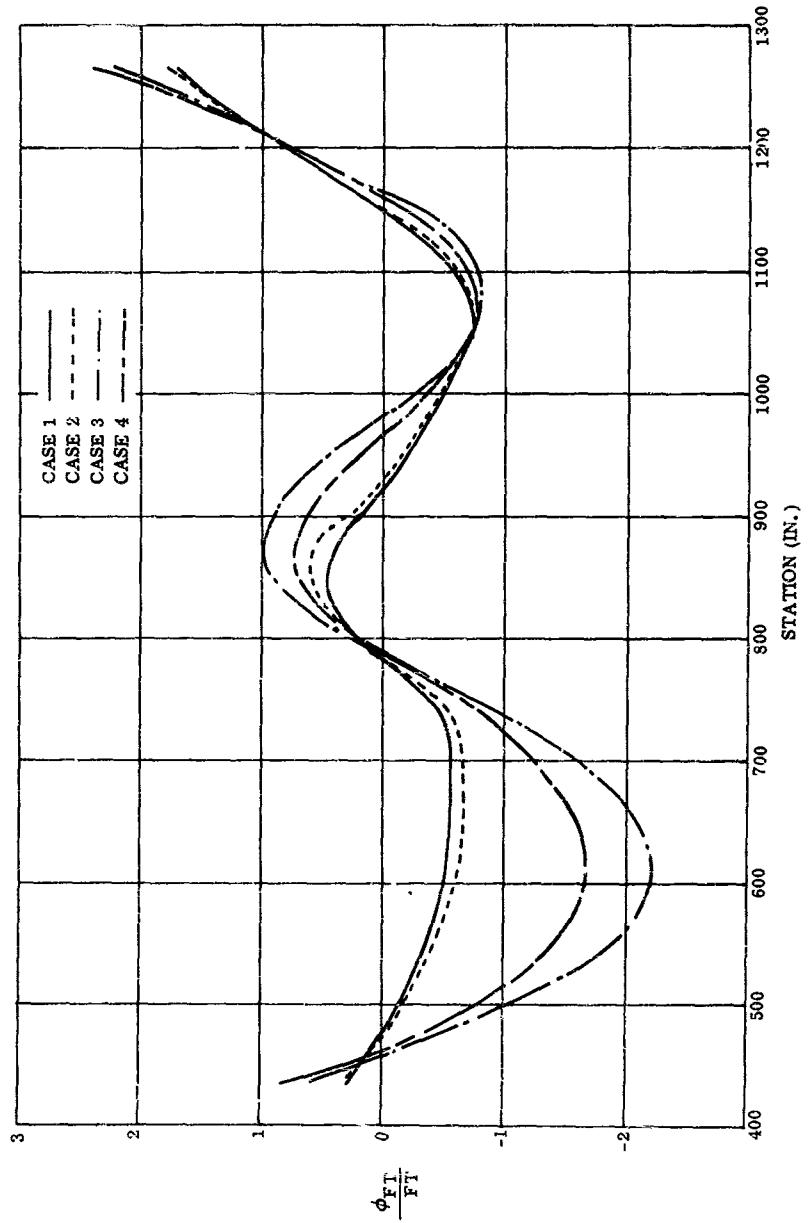
Figure A-33. Third Mode Deflections for Four Methods of Computation
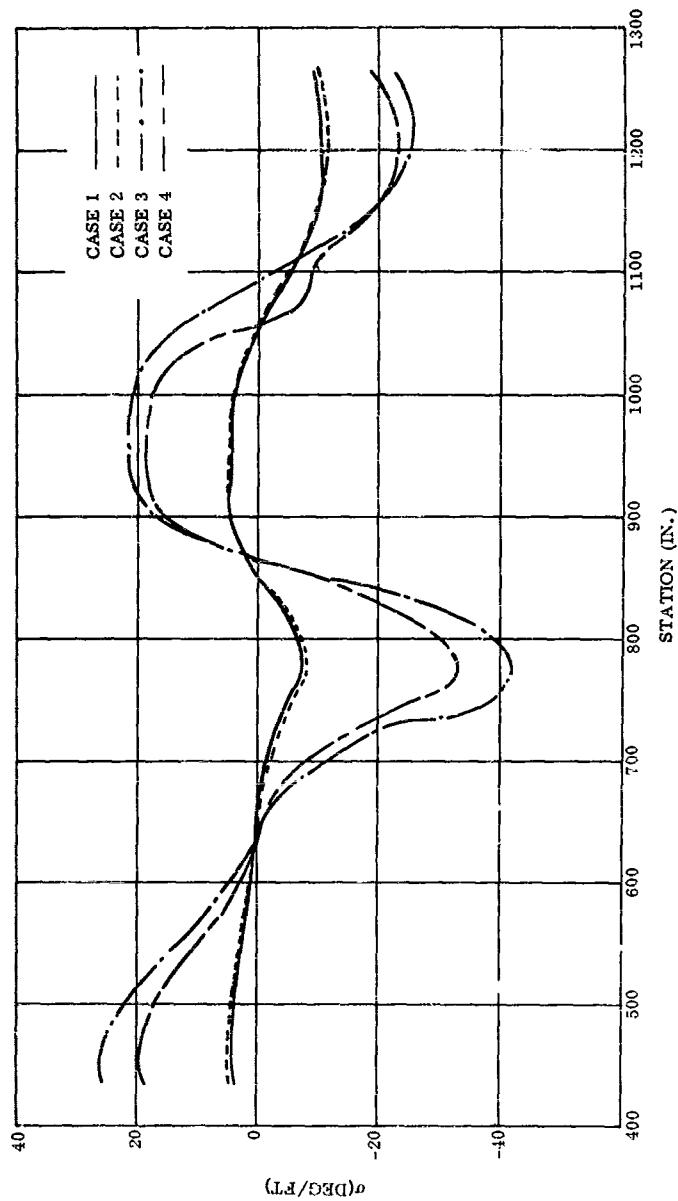
Figure A-34. Third Mode Slope for Four Methods of Computation
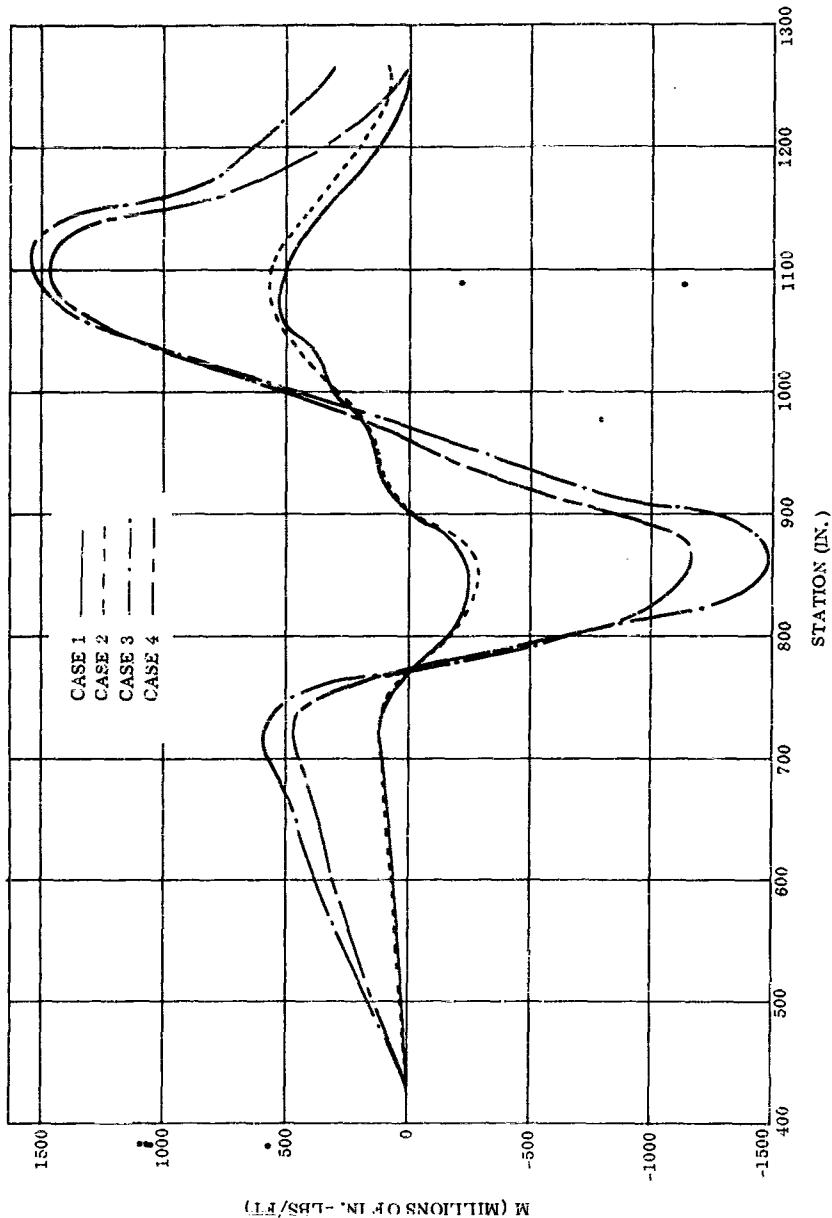
Figure A-35. Third Mode Bending Moments for Four Methods of Computation

STATION (IN.)
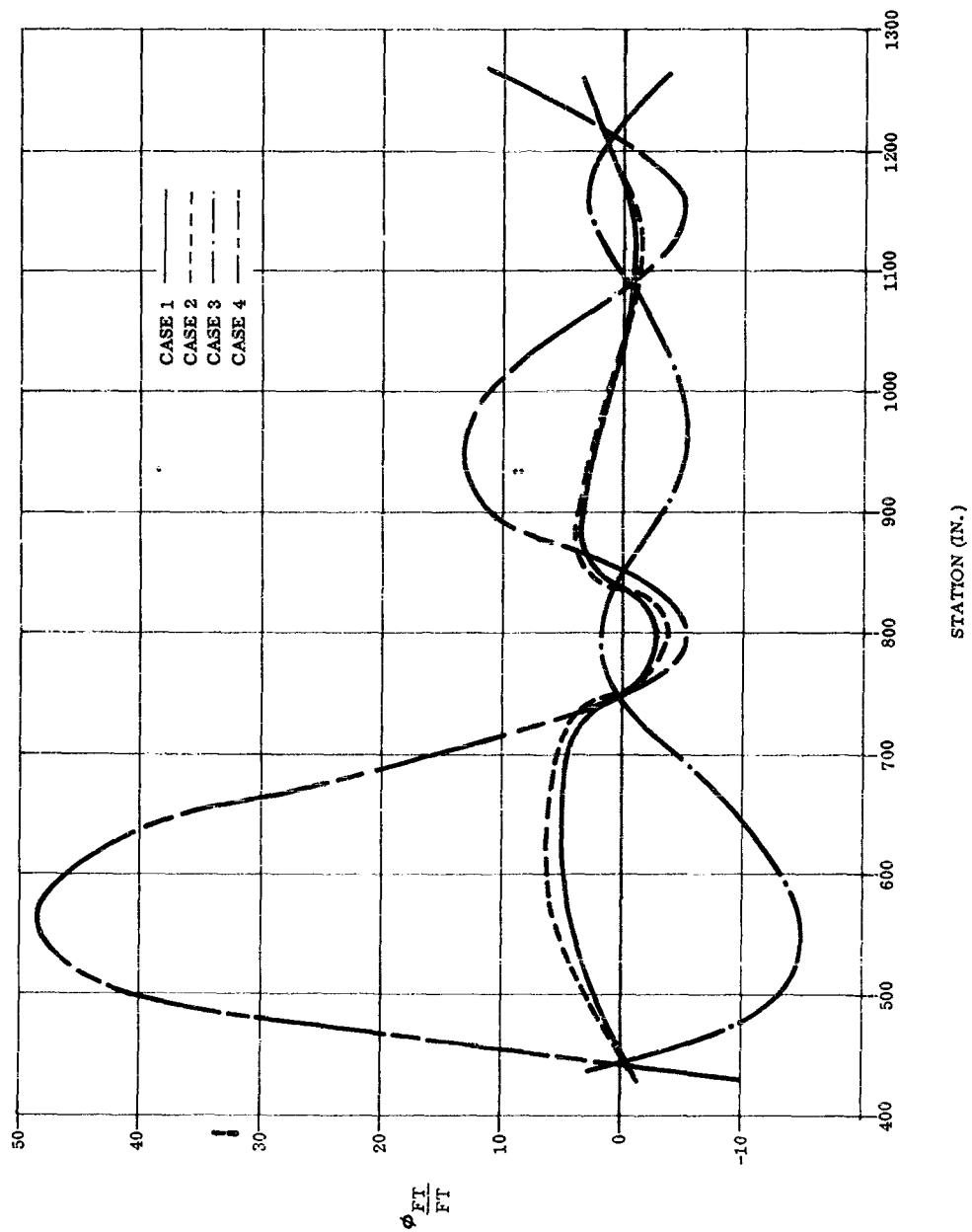
Figure A-36. Fourth Mode Deflections for Four Methods of Computation
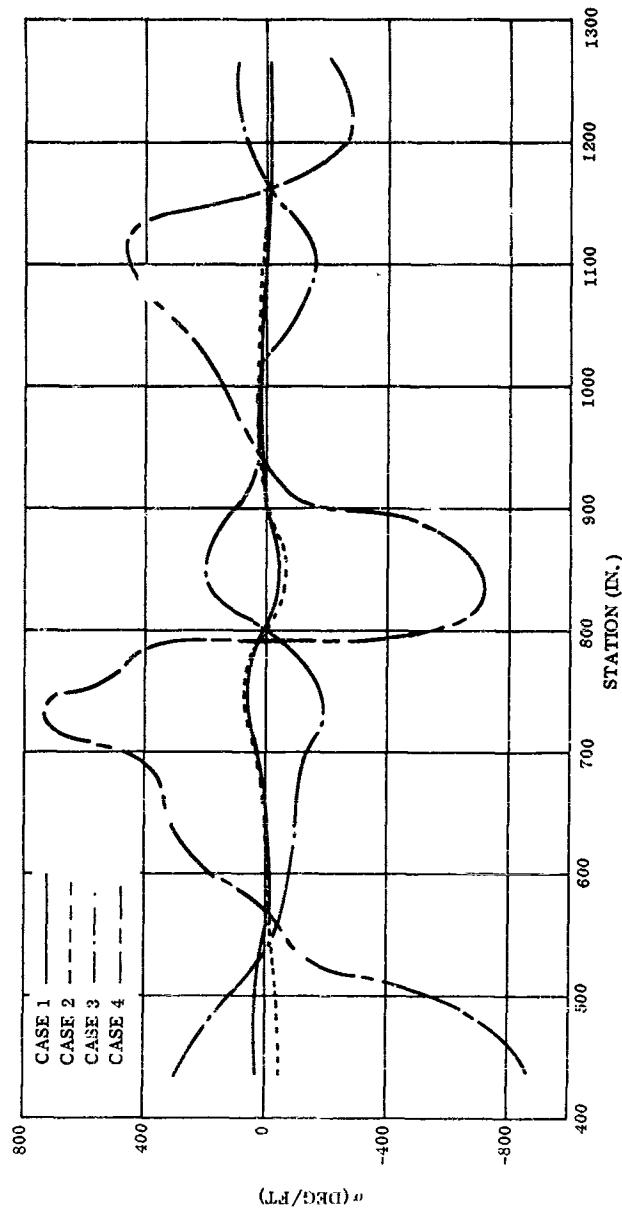
Figure A-37. Fourth Mode Slope for Four Methods of Computation
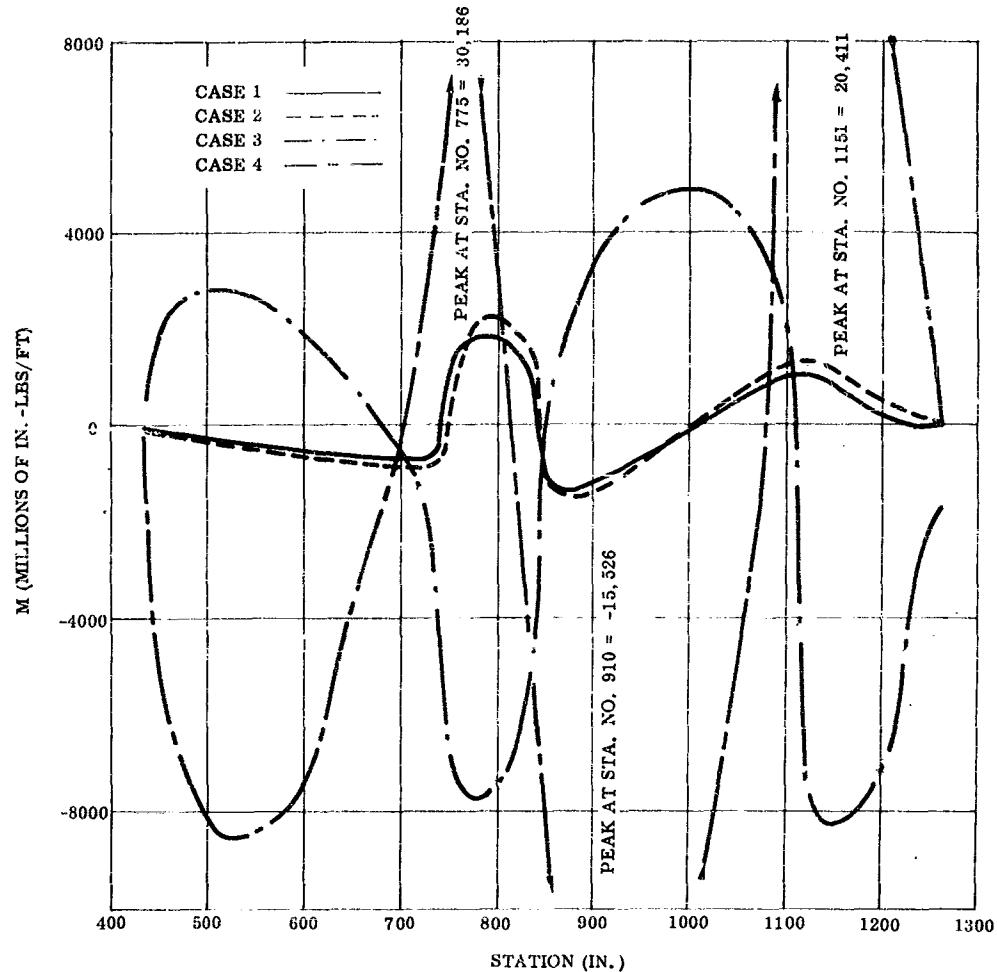
Figure A-38.   Fourth Mode Bending Moments for Four Methods of Computation

A4.5.1 Conclusions.   The curves and tables show that:

a.   Adequate results may be obtained by the elimination of $D\mu$ in the calculation of natural modes of vibration for the free-free beam.

b.   Transverse shear flexibility is very important in typical space booster configurations and should be included in mode calculations.   It is found to be more important in the 2nd, 3rd and 4th modes than in the 1st mode. It is also more important for slope and bending moment than for deflection calculations.

c.   Since $D\mu$ is of such minor importance in the calculation of the modes, doubling the number of mass stations and discarding the $D\mu$ would result in a matrix of the same order and would probably give much better re- sults for the higher modes.

A4.6 Concluding Remarks.   As was mentioned previously, the elastic bending modes, as calculated by the methods presented in this section, reflect only the characteristics of simple beam bending vibration.   It is often

convenient, if indeed not necessary, to include the effects of additional degrees of freedom in the modal calculations. The previous formulae must then be supplemented by additional equations and their associated cross-coupling terms.

In particular, consider the problem of including the effect of propellant sloshing in the elastic bending mode calculations. As shown in Appendix A-3, the effect of a sloshing liquid can be duplicated by a spring-centered-mass mechanical analogy. Furthermore, it was seen that this analogy requires the introduction of a couple at the base of the propellant tank. The magnitude of the couple acting on the base of the tank is a linear combination of both the displacement and acceleration of the spring-centered-mass. Thus, in addition to the lateral force due to the deformation of the spring (this force is applied at the attach point of the spring-centered mass), the action of the couple on the base of the tank must be included. This action may be incorporated by modifying the influence coefficient matrix and inertia matrix in a direct manner.

Another degree of freedom may be added by incorporating the rocket-engine positioning servo's flexibility into the vehicle elastic model. For the hydraulic positioning servo featured throughout this volume, the servo compliance appears in the actuator linkage and mount flexibility (K_m in Figure 4-12 of Section 4) and in the hydraulic fluid compressibility (K_H of the same figure). Whether or not these compliances are incorporated in the modal calculation makes little difference for modal frequencies below the engine servo resonant frequency. Near, at, or above this frequency, however, significant differences may appear in certain of the modal data. Table A-16 compares some critical data for modes at one time of flight, computed with and without servo compliance. The vehicle configuration was one in which the rocket engine chambers were large, "overhanging" inertial masses.

Table A-16. Comparison of Body Bending Mode Data with and without Servo Compliance

MODE	f_i (CPS)	m_i (SLUGS)	$\phi_{xT}^{(i)}$ (FT/FT)	$\sigma_{xT}^{(i)}$ (RAD/FT)	$\sigma_{xe}^{(i)}$ (RAD/FT)
1	3.82	218	0.266	0.0172	0.0172
1'	3.82	220	0.265	0.0184	0.0229
2	5.88	203	0.185	0.0177	0.0177
2'	6.87	202	0.180	0.0217	0.0357
3	11.6	907	0.568	0.0555	0.0555
3'	11.02	1230	0.370	0.051	0.43
3'a	12.98	2280	0.733	0.037	-0.84

Notes:

1. Unprimed modes are those having zero servo mount compliance

2. Artificially Uncoupled servo mount frequency is 11.6 cps. Modes 3' and 3'a are the orthogonal body and rocket engine modes on either side of the common artificially uncoupled frequency of 11.6 cps.

As may be seen in Table A-16, the third body bending mode at 11.6 cycles per second is very strongly affected when the servo mount compliance, resonating the massive rocket chambers at this same frequency, is added. The effect on the lower modes is smaller however. It would, in fact, be minor in an overall closed loop stability analysis, since the servo compliance would be accounted for in the servo actuator equations if it were omitted from the mode. For the third mode, however, simple incorporation of the mount compliance into the actuator equation may lead to significant errors, since certain of the body bending modal data is strongly affected by the changes in basic shape of the body modes (see modes 3 & 3' in Table A-16).

It should be pointed out that the last column of Table A-16 should not be considered as a prime measure of "error", due to omission of servo mount compliance. It is included primarily to show, by change in sign, when a mode has passed the servo mount frequency.

APPENDIX A5

METHODS OF ESTIMATING AERODYNAMIC NORMAL LOAD
DISTRIBUTIONS ON TYPICAL FLEXIBLE BOOSTER CONFIGURATIONS

SYMBOLS USED IN APPENDIX A5

Symbols	Definition	Units
C_N	normal force coefficient, $N/(qS_{ref})$	N.D.*
$\dfrac{d(C_N/\alpha)}{d(x/d)}$	local normal force coefficient, per degree per diameter	1/deg.
d	body diameter	ft
ℓ	body length	ft
ℓ_n	length of conical section (nose)	ft
M	Mach number	N.D.
N	normal force	lbs
q	dynamic pressure	lbs/ft^2
S	body cross-section area	ft^2
α	angle of attack	degrees
β	$\sqrt{M^2 - 1}$	N.D.
θ	$\tan^{-1}$ slope of body surface	degrees
x	axial distance as defined in Figure A-39	ft

Subscripts

ref	reference
v	vertex of nose

_____

*Non-dimensional

A5.1 Introduction. In this appendix the analytical methods and experimental data available for estimating the aerodynamic normal load distributions on typical booster vehicles are discussed. It is intended that the information presented will enable the reader without extensive aerodynamic background to estimate (with the aid of the references listed at the end of Appendix A) the approximate magnitudes and distributions of aerodynamic normal loadings required for a preliminary evaluation of their importance as a parameter affecting flexible-booster-autopilot transfer functions.

The aerodynamic normal forces imposed on a booster vehicle during its launch trajectory will affect the dynamic response of the vehicle to the control-system commands throughout a wide range of flight conditions, from the time of lift-off until the vehicle stages or emerges from the effective atmosphere. The magnitude of these forces will depend on the angle of attack, the Mach number, the dynamic pressure, and the aerodynamic characteristics of the vehicle. The angle of attack will vary with time as a result of the pitch-over program and the effects of slowly varying or transient wind conditions; however, the flow in most cases can be considered as quasi-steady, since the missile forward velocity is usually large in comparison with its pitching velocity. If elastic modes of vibration of the vehicle are excited by the interaction of aerodynamic forces with the control system, the angle of attack will vary locally along its length, and the distributions of aerodynamic normal loads will not correspond exactly to those of a rigid body.

In determining the aerodynamic force distributions on a flexible vehicle, the assumption is initially made that it is a rigid body, inclined at a fixed angle of attack. The effects of elastic bending are then taken into account during the dynamic analysis by assuming that the forces at a particular location along the missile axis vary with the local angle of attack in the same manner as for a rigid body.

For purposes of analysis the aerodynamic forces acting normal to a body inclined at an angle of attack can be separated into potential and viscous flow components. The potential flow component corresponds to the forces induced in an ideal frictionless fluid, and the viscous component of the forces resulting from boundary layer separation of the actual fluid from the lee side of the body. The potential component is assumed to vary linearly with the angle of attack, whereas the viscous component increases nonlinearly but does not become appreciable in magnitude until the angle of attack exceeds several degrees. For the type of vehicle being considered here, the angle of attack range is usually less than that required for the viscous forces to become important; therefore, only the potential flow component of normal force will be considered.

Since the aerodynamic normal force on a booster vehicle may be of importance throughout the launching trajectory, several flight regimes must be considered when estimating these forces. From the standpoint of the nature of the flow over the body, these regimes can be separated into the subsonic, transonic, and supersonic Mach number ranges. For the purpose of illustrating the application of methods available for the estimation of aerodynamic normal loadings on a typical booster vehicle, specific Mach numbers within each of these regimes have been selected. Normal load distributions are presented for a specific non-finned booster configuration which may be considered as quite representative in its over-all shape of vehicles of the type considered in the autopilot transfer function study. The configuration chosen for analysis is sketched in Figure A-39 and consists of a cone-cylinder with a nose semi-vertex angle of 15 degrees and an afterbody fineness ratio of eight.
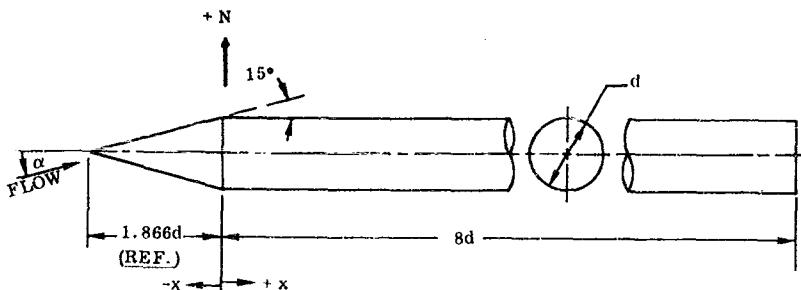

Figure A-39. Sketch of Example Booster Configuration

The discussion will be restricted primarily to a consideration of configurations with pointed or moderately blunted simple nose shapes and cylindrical afterbodies. Effects of external protuberances will not be considered, since these are usually relatively small in size and would thus contribute only a small increment to the normal loading. Although consideration of finned vehicles is beyond the scope of this appendix, it may be noted that Reference A-36 provides a comprehensive treatment of methods of accounting for fin effects for subsonic, transonic, and supersonic Mach numbers.

The local aerodynamic normal loading on a body can be expressed in non-dimensional form as $\dfrac{d(C_N/\alpha)}{d(x/d)}$. The loading in pounds per unit length is then determined by multiplying by $q\alpha \dfrac{S_{ref}}{d}$, where α is the local angle of attack and may include the effect of elastic bending of the body. The distributions presented herein for the example body are in this non-dimensional form. It is apparent from the above that for a given vehicle and Mach number the loads are proportional to the trajectory parameter, αq.

A5.2 Subsonic Flow Regime. Although the dynamic pressure does not typically become large during the subsonic initial phase of booster vehicle flight, the pitch-over program is usually initiated during this phase, with a relatively large resultant angle of attack and a condition of appreciable αq. The effects of winds may also be important in inducing angle of attack during this phase of flight. Aerodynamic loadings may therefore be significant in their effect on control system requirements.

Consideration of the subsonic aerodynamic characteristics of booster vehicles will here be restricted to the range of speeds for which the local flow over the body is everywhere subsonic ($M < 1$). For typical configurations this range, in terms of free stream Mach number, is approximately 0 to 0.7; within this range the flow can be treated as incompressible and independent of Mach number insofar as effects on normal load distributions are concerned.

Slender body potential theory (A-37) provides the only theoretical method available for predicting distributions of normal force on a pointed body of revolution in subsonic flow. This theory is applicable only to slender bodies with no discontinuities in profile slope or curvature. The theory states that the normal force distribution is proportional to the local variation in body cross-section area, i.e.,

$$\frac{d(C_N/\alpha)}{d(x/d)} = \frac{.0349}{S_{ref}} \frac{dS}{d(x/d)}$$

It may be noted that slender-body theory is not restricted to subsonic flow; for sufficiently slender pointed bodies it is also applicable to transonic and supersonic Mach numbers.

The published experimental data pertaining to the subsonic lift characteristics of bodies of the type considered here are very limited. Reference A-38 presents total normal force and pitching moment data for ogive-cylinders with various nose fineness ratios. Reference A-39 presents similar data for a cylindrical body with a conical and various two-section nose shapes, all with fineness ratios of approximately two. These data indicate that slender body theory predicts the total lift on bodies with nose fineness ratios as low as two with reasonably good accuracy. However, the distributions, as is to be expected, are not predicted correctly for bodies with sharp corners at the juncture of the nose and afterbody. Experimental data presented in Reference A-40 for the normal force slopes of cones with semi-vertex angles ranging from 15 to 55 degrees serve to indicate the limitations of slender-body theory when applied to not-so-slender bodies without slope discontinuities. The data show that the theory overestimates the lift on the 15-degree cone by about 30 percent.

Figure A-40 shows the distribution of normal loading on the example body, as determined from unpublished experimental pressure data. Also shown for comparison is the distribution predicted by slender body theory. The total normal force agrees well with the theory; however, the theory overestimates the lift on the nose and does not predict the carry-over of lift onto the afterbody shown by the experimental data. For ogive-cylinder (or other bodies without sharp corners), however, the theoretical distributions of normal force can be expected to agree more closely with experimental data.

A5.3 Transonic Flow Regime. Aerodynamic normal loading in the transonic phase of flight may be particularly significant in a study of transfer functions of flexible boosters, even though any practical booster would probably remain in the transonic speed range for a relatively short time. The transonic flow regime is characterized by unsteady flow conditions and rapidly changing normal force distributions. Appreciable angles of attack may be

Induced by the high velocity steady winds and gusts which can occur in the altitude range at which transonic flow may be expected for boosters of the type under consideration.
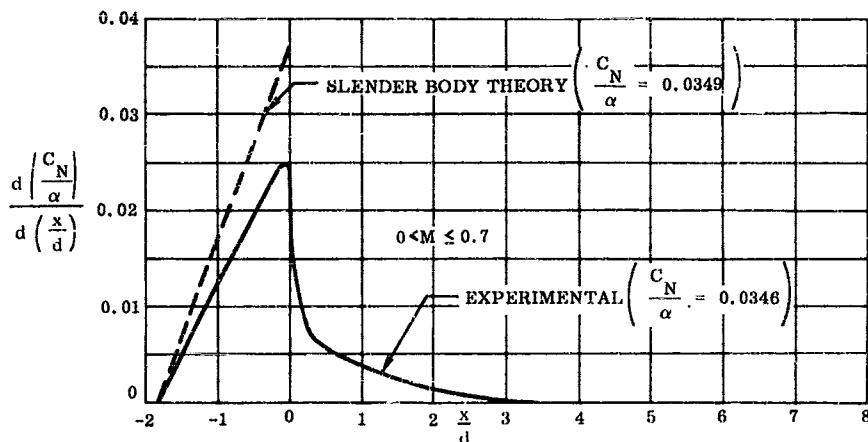

Figure A-40. Distribution of Normal Force Coefficient, Incompressible Flow Regime

The transonic flow regime is defined specifically as the Mach number range during which mixed flow occurs over the body, i.e., there are regions of local supersonic flow and regions of local subsonic flow.

The inability to predict the physical limits of the different flow zones and the complexity of the flow have thus far prevented the formulation of a practical theoretical method for predicting the lift on three-dimensional bodies. Hence, transonic normal force coefficients for such bodies must be obtained exclusively from experimental and empirical data.

A limited amount of transonic wind-tunnel test data pertaining to booster-like bodies at an angle of attack has been published. Most of these available test data give only the average, or "steady-state", forces or pressures. Some of the latest test results do include measurements of the magnitude and frequency of the fluctuating pressures (for the primary purpose of estimating the effect of this unsteady flow on the normal force imposed on the body), but the treatment of unsteady normal force phenomena is beyond the intended scope of this appendix.

Experimental force test data from References A-40, -41, -42 and unpublished pressure test data from two sources have been used to estimate the distribution of steady-state normal force coefficient on the illustrative 15-degree cone-cylinder at three transonic Mach numbers, viz., 0.90, 1.00 and 1.10 (see Figure A-41).

There are four distinct sub-regimes of transonic flow about cone-cylinders (Reference A-43), which are, in order of increasing free-stream Mach number:

a. Subsonic free-stream (flow on cone completely subsonic, zone of locally supersonic flow on the cylinder beginning at the shoulder),

b. Supersonic free-stream with detached shock wave (flow on cone completely subsonic, flow on cylinder completely supersonic),

c. Supersonic free-stream with attached "curved" shock wave (subsonic flow on cone surface, supersonic flow over entire cylinder)

d. Supersonic free-stream with attached conical shock wave (subsonic flow on cone surface, supersonic flow on entire cylinder).

In all of the above sub-regimes flow at the shoulder (cone-cylinder juncture) is sonic.

The division between the transonic and supersonic flow regimes is the Mach number (which is slightly higher than at condition d) when the flow on the cone first becomes supersonic.
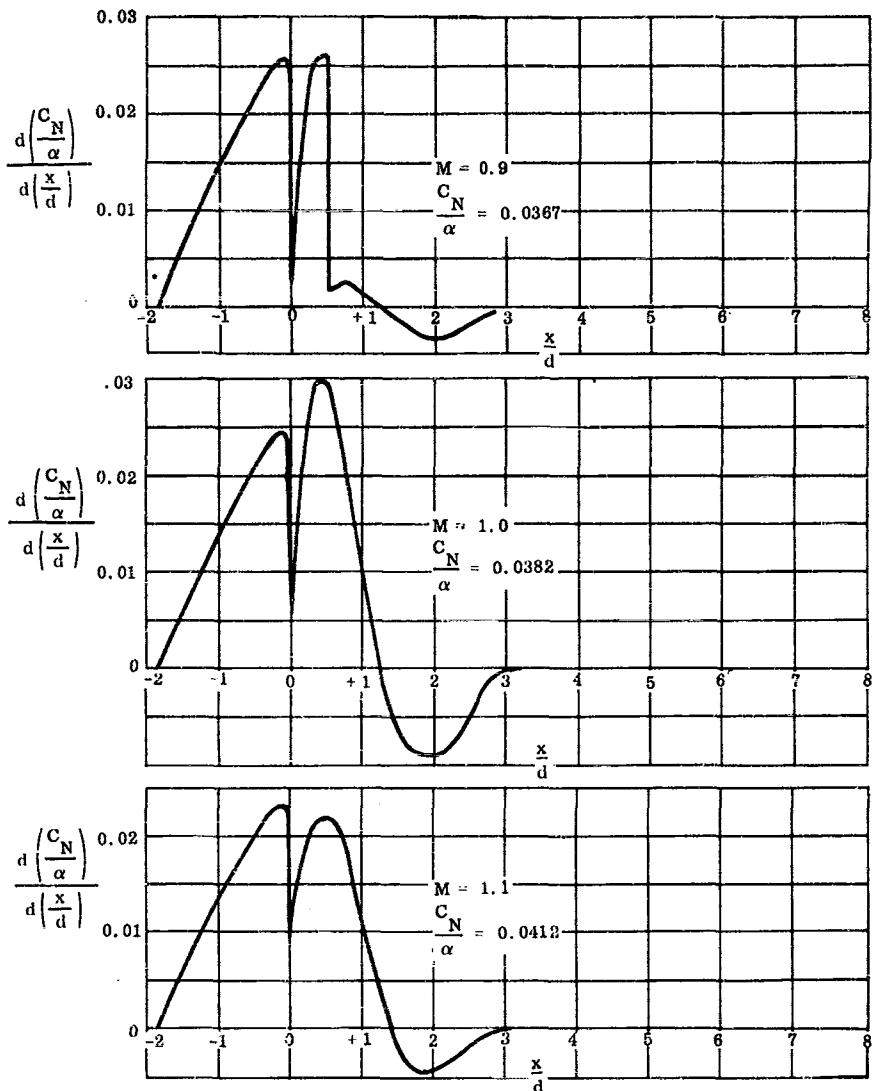
Figure A-41. Distribution of Normal Force Coefficient, Transonic Flow Regime

Experimental data indicate that the magnitude of the normal force coefficient on a slender cone is relatively constant throughout the entire transonic regime. Generally, the distribution of normal force coefficient on the cone is similar to the incompressible case except at the shoulder, where the local coefficient is always zero because sonic flow exists around the entire circumference.

Distribution of normal force coefficient on the cylinder undergoes two distinct phases in the transonic regime, depending on whether the free stream is subsonic or supersonic. At subsonic free-stream Mach number (sub-regime a above) there is a normal shock wave on the cylinder; flow is subsonic on the cone, sonic at the shoulder, supersonic on the portion of the cylinder between the shoulder and the normal shock wave, and subsonic aft of the normal shock wave. At the location of the normal shock wave the magnitude of the local normal force coefficient undergoes an abrupt change. The direction of change of local normal force coefficient between the upstream and downstream sides of the shock wave is always opposite in sign to the upstream value. At sonic and supersonic free-stream Mach numbers (sub-regimes b, c and d above) there is no shock wave on the cylinder and, therefore, no discontinuity in the distribution of normal force on the cylinder.

In general, there is zero or near-zero lift on the aft end of a long cylindrical afterbody in the transonic flow regime. Although negative lift on certain portions of the afterbody is common at transonic (and low supersonic) speeds, the net contribution of normal force on the entire cylinder is always positive.

There is a lack of published experimental data on the magnitude and distribution of lift on bodies other than cone-cylinders. However, certain characteristics can be deduced from cone-cylinder knowledge. Distribution of transonic normal force coefficients on configurations other than cone-cylinders could not be expected to go through the same phases as described above. For example, a cylinder capped by a gently curved nose shape such as an ogive probably would not have the normal shock wave and the discontinuous normal force distribution associated with transonic flow about cone-cylinders at subsonic free-stream Mach numbers. Transonically, the total normal force coefficient on a booster configuration with a reasonably proportioned ogive nose is undoubtedly in the same order of magnitude as that of typical cone-cylinders.

A5.4 Supersonic Flow Regime. The aerodynamic normal loading on a booster vehicle is typically most severe in the low supersonic Mach number range. The dynamic pressure usually reaches its maximum value in this range and occurs within the range of altitudes where winds and gusts are at maximum intensity. The trajectory parameter αq and, therefore, the normal loads will be maximum under such conditions. Aerodynamic loads may also be of importance during the staging condition, which usually occurs in the high supersonic Mach number range.

The supersonic flow regime is defined here as the range of free-stream Mach numbers above one for which the shock wave is attached to the nose of the body (or its pointed extension, in the case of blunted noses) and the local Mach number of the flow over the nose is greater than one. Of the theoretical methods available for estimating the lift of a pointed body of revolution in supersonic flow, the method of characteristics, which is based on the exact flow equations, provides the most accurate results. This method, however, is laborious to apply and requires each case to be worked out on a numerical basis. Reference A-44 outlines the application of the method for inclined bodies. Solutions for the flow over cones at small angles of attack have been obtained by Kopal in Reference A-45 from the exact theory of Stone (A-46). Results of Kopal's work are also available in numerous references, e.g., (A-47).

Several useful approximate theories for the lift of bodies of revolution at supersonic Mach numbers have been developed. Each of these theories has a limited range of applicability, in terms of Mach number, body fineness ratio, and the similarity parameters $\beta \tan \theta_v$, $\beta d/\ell_n$ or $\beta d/\ell$ for which reasonably good agreement with experimental data has been demonstrated.

The application of slender-body potential theory is limited to extremely slender bodies at low supersonic speeds, for which the value of the similarity parameter, $\beta \tan \theta_v$, is much less than one. Van Dyke's first order and hybrid potential theories (A-48) represent a significant improvement over slender-body theory, and are applicable at low and moderate supersonic speeds, for which the free stream Mach angle is greater than the body semi-vertex angle, $\beta \tan \theta_v < 1$. Reference A-49 contains curves of normal force slopes based on first order theory, for cone- and ogive-cylinders and normal force distributions on cone-cylinder afterbodies for a range of configurations and Mach numbers. A comparison is made with a large number of experimental values at normal force slopes; and it indicates a moderately good over-all correlation between the theory and experiment.

At high supersonic Mach numbers, the expansion of the flow over a body of revolution can be treated as locally two-dimensional. The generalized shock-expansion theory of Eggers et al., (A-50), based on this assumption, gives accurate results when the similarity parameter, $\beta d/\ell$, is greater than one. A refinement of this approach, which permits its application to lower Mach numbers by accounting for the three-dimensional flow effects, is the second-order shock-expansion method of Syvertson and Dennis. This theory (A-51 and -52) is shown to agree quite well with experimental data for the normal force slopes and centers-of-pressure of cone- and ogive-cylinders, for Mach numbers between 3 and 6.28, as well as for corresponding values of the similarity parameter, $\beta d/\ell_n$, between 0.4 and 2.0. The theory is shown to be considerably superior to Van Dyke's first order theory in this range. Exact solutions of the general second-order shock-expansion method for normal force and pitching moment slopes of cone-cylinders, and approximate solutions for ogive-cylinders in closed form are presented in the appendices of Reference A-51 and -52. With the aid of the equations and curves presented, the aerodynamic characteristics of such bodies can be evaluated with little effort.

The comparisons (in the last references) of the second-order shock-expansion theory with experimental data do not reveal the limits of the range of applicability of the method. The upper limit, on the basis of calculations made by the authors of the theory, will be exceeded if $\beta \tan \theta_v$ is appreciably more than 2.5. In the range near

2.5 the theory merges with the generalized shock-expansion method. On the basis of a limited comparison of the theory with experimental data for cone-cylinders in the Mach number range from about 1.5 to 2.5, it appears that the method is not applicable below about Mach 2. The theory does not predict the negative-lift regions which have been experimentally observed to occur on the afterbodies of cone-cylinders at low supersonic Mach numbers.

At very high Mach numbers, for which flow conditions approach hypersonic, Newtonian impact theory is applicable. The application of this theory to the determination of the flow over inclined bodies of revolution has been developed by Grimminger and Young (A-53).

A considerable body of experimental data exists for the normal force characteristics of pointed bodies of revolution in supersonic flow. Only some of the more systematic experimental investigations will be mentioned here. Reference A-41 gives data for pointed and blunted cones tested for a wide range at Mach numbers, including the transonic range. In Reference A-54 data for cone cylinders, including the effects of blunting the noses, are presented for M = 1.5 to 4.04. Data for the noses alone are given in Reference A-52. As mentioned previously, References A-51 and -52 give data for a series of cone- and ogive-cylinders tested between M = 3 and 6.28. The effects on normal force of adding base flares consisting of conical frustums of various angles to the cone-cylinders with pointed noses of Reference A-54 have been experimentally determined and are presented for the same range of Mach numbers in References A-55 through A-58. A data correlation and analysis of the normal force characteristics of the flares is presented in Reference A-59. It may be noted that all of the foregoing experimental investigations measured only the overall force and moment characteristics of the bodies tested. However, in these tests various afterbody lengths were included; thus, distributions of normal force on the afterbody can be determined from the data.

The supersonic/hypersonic similarity rule provides a means of correlating experimental data for the aerodynamic characteristics of affinely related bodies of revolution. The supersonic/hypersonic similarity rule states that for bodies of revolution with identical thickness distribution the curve of $\frac{\beta d(C_N/\alpha)}{d(x/d)}$ vs. $\frac{x}{\beta d}$ is the same for each value of parameter $\beta d/\ell_n$ throughout the entire supersonic and hypersonic Mach number range. By use of this rule experimental data obtained for a particular class of bodies, for which the similarity parameters are systematically varied, can be correlated to provide estimates, within engineering accuracy, of the aerodynamic characteristics of such bodies for a wide range of configurations and Mach numbers. Such a correlation, based on the experimental data of Reference A-60 and -61 has been made for the normal force, pitching moment, and normal force distributions of cone-cylinders, and is presented in References A-62. The correlation curves are applicable to configurations with nose fineness ratios ≥ 2 for Mach numbers above 1.5.

Figure A-42 presents estimated distribution of aerodynamic normal force on the example body at Mach numbers of 2 and 6. These Mach numbers were chosen as being representative of typical maximum load and staging conditions, respectively. The afterbody distribution at Mach 2 was determined from the correlation charts of Reference A-62. The distribution at Mach 6 was determined by the second-order shock-expansion method, using the equations and curves in the appendix of Reference A-52. The distributions on the conical nose are related to the total normal force, $(C_N/\alpha)_n$, on the nose, as given in References A-47, -52, or -62 by the equation:

$$\frac{d(C_N/\alpha)}{d(x/d)} = 8 \left(\frac{C_N}{\alpha}\right)_n \left(\frac{\ell_n + x}{d}\right) \tan^2 \theta_v$$
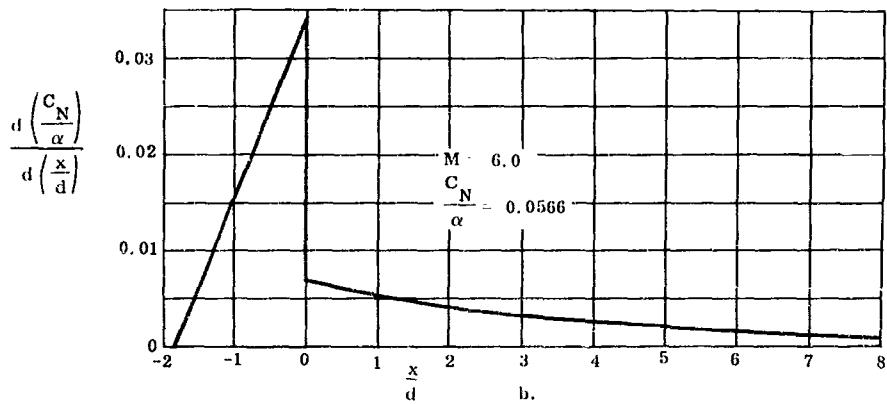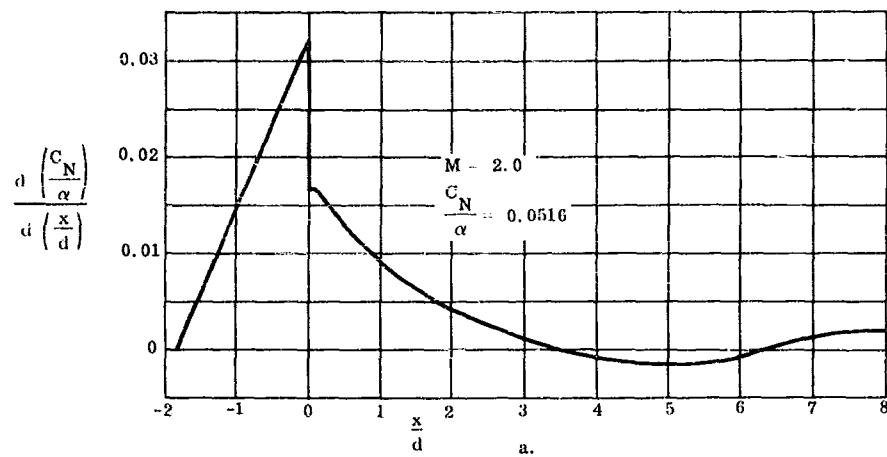
Figure A-42. Distribution of Normal Force Coefficient, Supersonic Flow Regime

A6 REFERENCES FOR APPENDIX A

A-1.   Graham, E. W., "The Forces Produced by Fuel Oscillation in a Rectangular Tank," Douglas Aircraft Co. Report SM-13748, Revised 16 April 1951

A-2.   Lorell, J., "Forces Produced by Fuel Oscillation," Jet Propulsion Laboratory and California Insitute of Technology Progress Report 20-149, October 1951

A-3.   Schmitt, A. F., "Forced Oscillations of a Fluid in a Cylindrical Tank Undergoing Both Translation and Rotation," Convair Reports ZU-7-069 and ZU-7-074, 4 February 1957

A-4.   Bauer, H. F., "Fluid Oscillations in a Circular Cylindrical Tank Due to Bending of Tank Walls," ABMA Report No. DA-TR-3-58, April 1958

A-5.   Reissner, E., "Complementary Energy Procedure for Vibrations of Liquid-Filled Circular Cylindrical Tanks," Space Technology Laboratory Report EM 7-9, GM-TR-203, June 1957

A-6.   Rabinovich, B. I., "Concerning Equations of Elastic Oscillations of Thin-Walled Bars Filled with Liquid Having a Free Surface," Space Technology Laboratory Translation STL-T-RU-19, GM-60-5111-59, June 1960

A-7.   Schmitt, A. F., "Suggested Modification to Fluid Sloshing Analogy for Flexible Missile Studies," Convair Memo AD-338, 20 January 1958

A-8.   Hausrath, A. H., "On Sloshing in Oblate Spheroids " To be Published by Convair-Astronautics

A-9.   Budiansky, B., "Sloshing of Liquids in Circular Canals and Spherical Tanks," Journal of Aeronautical Sciences, March 1960, Vol. 27, No. 3

A-10.   Green, J. W., "Further Remarks on Conical Sloshing," Space Technology Laboratory Report PA/M-553/2, May 1957

A-11.   Harper, J., "Propellant Sloshing in a Conical Tank Undergoing Arbitrary Forced Translation Motion," Convair Report ZU-7-089TN, January 1958

A-12.   Trembath, N. W., "Fluid Sloshing in Tanks of Arbitrary Shape," Ramo-Wooldridge Report GM 45-3-378

A-13.   Berlot, R. R., "Production of Rotation in a Confined Liquid, Through Translational Motion of the Boundaries," Journal of Applied Mechanics, Vol. 81, December 1959

A-14.   Abramson, H. W., and Ransleben, G., "Simulation of Fuel Sloshing Characteristics in Missile Tanks by Use of Small Models," American Rocket Society Journal, July 1960, Vol. 30, No. 7

A-15.   O'Niel, J. P., "Final Report on an Experimental Investigation of Sloshing." Space Technology Laboratory Report TR-59-0000-09960, 4 March 1960

A-16.   Kugler, G. L., "Propellant Sloshing Test for "C" Missile During Second Stage Flight," Convair Report 7A 1386, November 1958

A-17.   Cooper, R. M., and O'Niel, J. P., "Damping Ratios for Sloshing Liquids in a Cylindrical Tank Having a Hemispherically Domed Bottom and Roof: Application to the Able-Star Propellant Tank," Space Technology Laboratory Report STL/TR-59-0000-09780, October 1959

A-18.   McCarty, J. L. and Stephens, D. G., "Investigation of the Natural Frequencies of Fluid in Spherical and Cylindrical Tanks," NASA TND-252, May 1960

A-19.   McCarty, J. L., and Stephens, D. G., "Experimental Investigations of the Natural Frequencies of Liquid in Toroidal Tanks," NASA TND-531, October 1960

A-20.   Case, K. M., and Parkinson, W. C., "The Damping of a Liquid in a Right Circular Cylindrical Tank," Ramo-Wooldridge Corp. Report GM 45-75, September 1956

A-21.   Miles, J. W., "Ring Damping of a Free Surface Oscillation in a Circular Tank," ASME Applied Mechanics Division Paper No. 57-A-31, March 1957

A-22.   Geissler, E. D., "Problems in Attitude Stabilization of Large Guided Missiles," Aero Space Engineering, October 1960

A-23.   Baer, H. H., "Propellant Damping by Fixed-Ring Baffles," Ramo-Wooldridge Report GM-TN-35, September 1956

A-24.   Miles, J. W., "On Free Surface Oscillations in a Rotating Liquid," Space Technology Laboratory Report EM8-18, 18 August 1958

A-25.   Graham, E. W. and Rodreguez, A. M., "The Characteristics of Fuel Motion Which Affect Airplane Dynamics," Douglas Aircraft Co. Report SM-14212

A-26.   Kachigan, K., "Forced Oscillations of a Fluid in a Cylindrical Tank," Convair Report ZU-7-046, 4 October 1956

A-27.   Miles, J. W., "On the Sloshing of Liquid in a Flexible Tank," Journal of Applied Mechanics, Vol. 25, No. 2, June 1958

A-28.   Eulitz, W., "The Sloshing Phenomenon and the Mechanism of a Liquid in Motion in an Oscillating Missile Container," ABMA Report R-DS-31, October 1957

A-29.   Howell, E. and Ehler, F. G., "Experimental Investigation of the Influence of Mechanical Baffles on the Fundamental Sloshing Mode of Water in a Cylindrical Tank," Ramo-Wooldridge Corp. Report GM-TR-69, July 1956

A-30.   Lamb, H., Hydrodynamics, 6th Edition, Cambridge University Press, 1932

A-31.   Lawrence, J. R., Wang, C. J., and Reddy, R. B., "Variational Solution of Fuel Sloshing Modes," Jet Propulsion Laboratory, November 1958

A-32.   Li, T. C., "Liquid Behavior in a Zero-G Field," Convair-Astronautics Report AE60-0682, October 1960

A-33.   Widmayer, E. Jr., and Reese, J. R., "Moment of Inertia and Damping of Fluid in Tanks Undergoing Pitching Oscillation," NASA RM L53E01a, June 1953

A-34.   Scanlan, R. H. and Rosenbaum, R., An Introduction to The Study of Aircraft Vibration and Flutter, The Macmillan Company, 1951, Sections 7:10, 7:11, and 7:12

A-35.   Bisplinghoff, R. L., et al., Aeroelasticity, The Addison-Wesley Publishing Company, Inc., 1955

A-36.   W. C. Pitts, J. N. Nielson, and G. E. Kaatari, "Lift and Center of Pressure of Wing-Body-Tail Combinations at Subsonic, Transonic, and Supersonic Speeds," NACA Report 1307, 1957, Unclassified

A-37.   Laitone, E. V., "Linearized Subsonic Flow Theory About Inclined Bodies of Revolution," Journal of Aeronautical Sciences, Vol. 4, November 1947

A-38.   E. C. Polhamus, "Effect of Nose Shape on Subsonic Aerodynamic Characteristics of a Body of Revolution Having a Fineness Ratio of 10.94," NACA RM L57F25, August 1957, Confidential

A-39.   M. E. Morrison, "Low-Speed Wind Tunnel Tests on 15, 25, 40, and 55 Degree Semi-Vertex Angle Cones to Determine the Support Effects on Force Coefficients," Convair-San Diego Report CVAL 167 B, March 1958, Unclassified

A-40.   S. L. Treon, "The Effect of Nose Shape on the Static Aerodynamic Characteristics of Ballistic-Type Missile Models at Mach Numbers from 0.6 to 1.4," NASA Memo 5-17-59A, May 1959, Confidential

A-41. W. J. Geudtner, "Sharp and Blunted Cone Force Coefficients and Centers of Pressure From Wind Tunnel Tests at Mach Numbers From 0.50 to 4.06," Convair-San Diego Report ZA-7-017, June 1955, Confidential

A-42. R. M. Wakefield, et al., "Transonic Static Aerodynamic Characteristics of a Blunt Cone-Cylinder Body with Flared Afterbodies of Various Angles and Base Areas," NASA TM X-106, December 1959, Confidential

A-43. G. E. Solomon, "Transonic Flow Past Cone-Cylinders," NACA Report 1242, 1955, Unclassified

A-44. A. Ferri, "The Method of Characteristics for the Determination of Supersonic Flow over Bodies of Revolution at Small Angles of Attack," NACA TN 1809, February 1949

A-45. Z. Kopal, "Tables of Supersonic Flow Around Yawing Cones," Massachusetts Institute of Technology Technical Report No. 3, 1947, Unclassified

A-46. A. H. Stone, "On Supersonic Flow Past a Slightly Yawing Cone," Journal of Mathematical Physics, Vol. 27, p. 67, April 1948

A-47. Ames Research Staff, "Equations, Tables, and Charts for Compressible Flow," NACA Report 1135, 1953, Unclassified

A-48. M. D. Van Dyke, "First and Second Order Theory of Supersonic Flow Past Bodies of Revolution," Journal of Aeronautical Sciences, Vol. 18, No. 3, March 1951

A-49. J. W. Huth and L. W. Dhanes, "Normal Force Coefficients for Pointed Bodies of Revolution at Supersonic Speeds," Rand RM-729, 1 December 1951, Confidential

A-50. A. J. Eggers, et al., "The Generalized Shock-Expansion Method and its Application to Bodies Traveling at High Supersonic Airspeeds," Journal of Aeronautical Sciences, Vol. 22, No. 4, April 1955, pp. 231-238

A-51. C. A. Syvertson and D. H. Dennis, "A Second-Order Shock-Expansion Method Applicable to Bodies of Revolution Near Zero Lift," NACA TN 3527, January 1956

A-52. C. A. Syvertson and D. H. Dennis, "A Second-Order Shock-Expansion Method Applicable to Bodies of Revolution Near Zero Lift," NACA Report 1328, 1957, Unclassified

A-53. G. Grimminger and G. B. W. Young, "Lift on Inclined Bodies of Revolution in Hypersonic Flow," Journal of Aeronautical Sciences, Vol. 17, No. 11, November 1950, pp. 675-690

A-54. J. H. Henderson, "Effect of Nose Bluntness on Normal Force, Pitching Moment, and Center of Pressure of Cone-Cylinder and Cone-Cylinder-Frustum Bodies of Revolution at Mach Numbers of 1.50, 2.18, and 4.04," OML Report GR11F, June 1958, Confidential

A-55. R. E. Lavender, "Normal Force, Pitching Moment, and Center of Pressure of Eighty Cone-Cylinder-Frustum Bodies of Revolution at Mach Number 1. 0," OML Report 6R3N3, April 1956, Confidential

A-56. R. E. Lavender, J. H. Henderson, and R. A. Deep, "Normal Force, Pitching Moment, and Center of Pressure of Eighty Cone-Cylinder-Frustum Bodies of Revolution at Mach Number 2.18," OML Report 6R3P, January 1956, Confidential

A-57. J. L. Sims and J. H. Henderson, "Normal Force, Pitching Moment, and Center of Pressure of Eighty Cone-Cylinder-Frustum Bodies of Revolution at Mach Number 2.81," OML Report 6R3N2, March 1956, Confidential

A-58. J. H. Henderson and J. L. Sims, "Normal Force, Pitching Moment, and Center of Pressure of Eighty Cone-Cylinder-Frustum Bodies of Revolution at Mach Number 4.04," OML Report 6R3N1, March 1956, Confidential

A-59.   D. B. Kink and G. T. Chapman, "The Stabilizing Effectiveness of Conical Flares on Bodies With Conical Noses," NASA TM X-30, September 1959, Confidential

A-60.   H. Chaplin and F. J. DeMeritte, "Static Stability and Axial Force Measurements on Cone Cylinders," NAVORD Research Report 178, May 1953, Unclassified

A-61.   D. H. Dennis and B. E. Cunningham, "Forces and Moments on Inclined Bodies at Mach Numbers from 3.0 to 6.3," NACA RMA54E03, 1959

A-62.   R. G. Norell, "Normal Force, Pitching Moment, and Normal Force Distributions of Cone-Cylinders at Supersonic Speeds," Convair-San Diego Report ZA-7-010, April 1954, Confidential

APPENDIX B

SUBSYSTEM TRANSFER FUNCTIONS

B1 INTRODUCTION

The main body of this report presents the equations of motion and approximate transfer functions giving the response of a flexible booster to various inputs. To complete the picture for closed-loop control analysis, this Appendix presents a survey of equations used to represent the various subsystems and components employed in autopilots. A cursory discussion is given of the most important characteristics of several classes of subsystems. The intent is not to provide a complete derivation of equations of motion but rather to describe the characteristics which would affect the analysis of the autopilot-flexible booster transfer functions.

The subsystems to be discussed are divided into four general categories: Sensors, Control Force Generators, Positioning Servos, and Autopilot elements. The general characteristics of each are given to furnish a guide to the data needed to analyze the effect of the individual components on the overall transfer functions. To obtain this data it is usually necessary to resort to detailed analysis, test data, and manufacturer's literature.

B2 SENSORS

A reference input is required for the autopilot and control system. The information furnished by this reference may consist of body angular position, angular rate, and/or acceleration. The reference input may be with respect to an inertial reference or other external references such as angle of attack or local-vertical. The sensors may either be "strapped down" (rigidly attached to the airframe) or mounted on an inertial platform.

Appendix B2 is physically divided into sections dealing with gyros, accelerometers, angle-of-attack meters, and stable platforms. The class of external references which includes horizon scanners, sun seekers, and star trackers is not discussed. In boosters these references, if employed at all, are more for guidance than for control; therefore, their output signals can be filtered to exclude signals in the frequency range of the flexible booster and control system modes.

B2.1 <u>Gyroscopic</u>. The gyroscope consists of a wheel which is spun at a high angular velocity. The most useful characteristic of a gyroscope is its property of maintaining its axis in a fixed direction in inertial space unless acted upon by an external torque.

This characteristic of a gyroscope can be expressed as an angular counterpart of Newton's first law of motion: A body in rotation will continue to rotate about a fixed axis with constant angular speed unless acted upon by an external moment.

The physical concept of a gyroscope can be visualized by imagining a spinning disk supported so as to be free to move in any direction. This disk will remain fixed in space unless a force acts upon it. When one pushes on the disk with a force, F, so as to cause its spin axis to move to the right the axis will actually "precess", i.e., move up or down, depending on which direction the disk is spinning.

This phenomenon can be described mathematically. Consider a momentum vector, H, which points along the axis of spin in accordance with right hand rules; its length is proportional to the magnitude of the angular momentum.
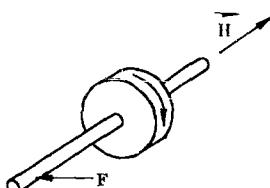
H = I (MOMENT OF INERTIA) $\overline{\Omega}$ (ANGULAR SPIN VELOCITY)

Figure B-1. Gyroscopic Precession

The rate of change of momentum is equal to the applied moment:

$$M = \frac{\overline{dH}}{dt} \text{ inertial.}$$

The rate of change of angular momentum can be expressed in terms of body axis coordinates as:

$$\left(\frac{\overline{dH}}{dt}\right)_{\text{inertial}} = \left(\frac{\overline{dH}}{dt}\right)_{\text{body}} + \overline{\omega}_{\text{body}} \times \overline{H} \qquad .$$

For a rigid gyroscope, $(\overline{dH}/dt)_{\text{body}} = 0$ and the preceding reduces to:

$$M = \overline{\omega} \times \overline{H} \qquad .$$

The preceding can also be written in the common form for the magnitudes as:

$$M = I_{\text{(spin axis)}} \Omega_{\text{(spin axis)}} \omega_{\text{(precession)}}.$$

The spinning wheel can be used in several ways. The simplest way would be to mount it on a suitable set of gimbals and use it as a directional reference (Figure B-2). Used thusly it is referred to as a free gyro. The use of a free gyro, or two-degree-of-freedom gyro, requires that the spinning rotor be mounted in a set of gimbals. The attendant friction and balancing problems usually contribute to drift, thereby limiting the use of this type of gyro to applications where low drift rates and high accuracies are not required. Two symbolic gimbal configurations of this type are shown in Figure B-2. The first configuration is that of a strict free gyro which will provide a two-axes inertial reference. As there are no restraining gimbals in the configuration, the spinning gyro wheel remains fixed in space, and the angle between the wheel gimbal and the frame is the inertial angle. The second configuration illustrated has an added refinement: command orientation capability. This orientation command may be added if the gyro is to be used in a strapped down guidance and control system. When orientation commands are used along with viscous friction about the gimbal the gyro becomes a rate integrating gyro.

B2.1.1 Rate Integrating Gyros. The rate integrating gyro is so named because the resultant effect of a disturbance is to produce a rotation of the gimbal system about the output axis that is proportional to the integral of the input axis rate. This gyro may have either one or two degrees of freedom, although one degree is the most common. A typical configuration, along with a system block diagram for a single-degree-of-freedom rate integrating gyro is given in Figure B-3.

The block diagram indicates output signals from two sources: 1) command torques and 2) input axis rates.

The equation of motion is:

$$Js^2 \theta_o + Fs\theta_o = H\omega_i + K_T E_i \qquad .$$

Then the respective transfer functions are:
(Command Torques)

$$\frac{E_o}{E_i} = \frac{1}{s} \cdot \frac{K_T K_P}{Js + F} \qquad \text{and}$$

(Input Axis Rates)

$$\frac{E_o}{\omega_i} = \frac{1}{s} \cdot \frac{HK_P}{Js + F}$$
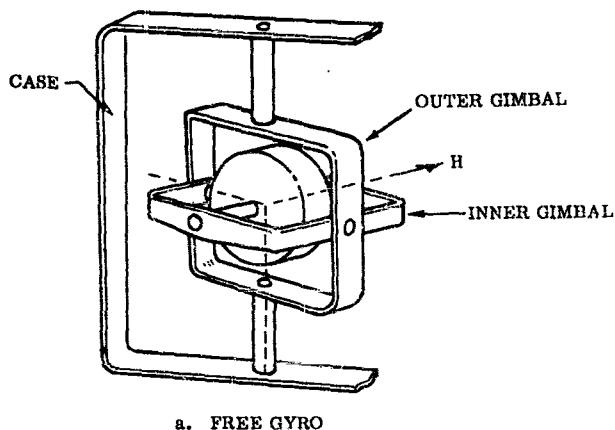
a. FREE GYRO
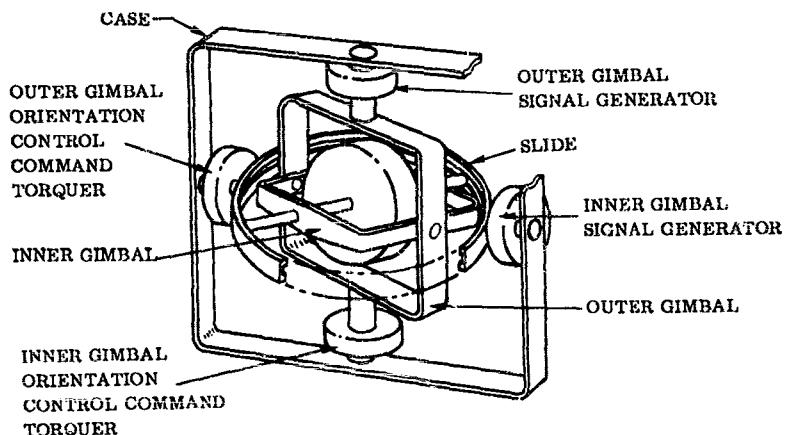
b. TWO-DEGREE OF FREEDOM GYRO

Figure B-2. Schematic Gyro Configurations

where

$$E_o = K_p \Theta_o.$$

The total transfer function is:*

$$E_o = \frac{1}{s} \cdot \frac{K_p/J}{s + F/J} \; (H\omega_1 + K_T E_1)$$

---

*It may be shown that this unit also responds to angular velocities of the case about the output axis (ω_o).

$E_o/\omega_o = K_p/(s + F/J)$, where $E_o = K_p(\Theta - \omega_o/s)$. Since J/F is very small (on the order of 0.005 sec), this coupling term is usually neglected. In addition to the output axis pickup expressed in the preceding equation, the gyro will also sense motion about other than the intended input axis if it is precessed away from its null position (a second order effect).

Figure B-3. Rate Integrating Gyro
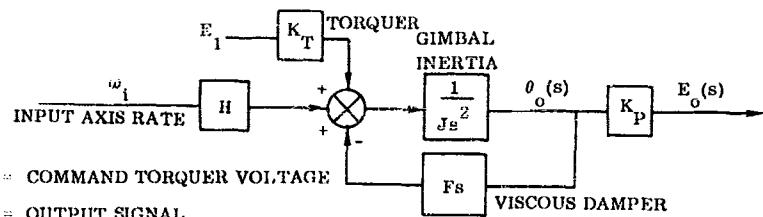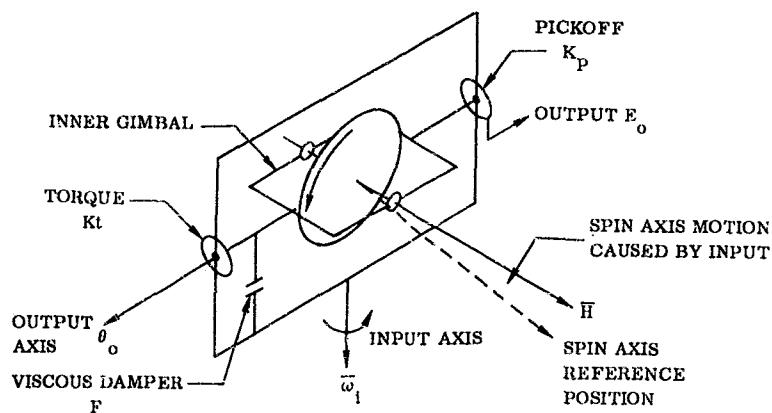
E_i = COMMAND TORQUER VOLTAGE
E_o = OUTPUT SIGNAL
F = VISCOUS FRICTION
H = ANGULAR MOMENTUM
J = GIMBAL INERTIA
K_p = PICKOFF SENSITIVITY
K_T = COMMAND TORQUER GAIN
θ_o = SYSTEM OUTPUT AXIS ANGLE
ω_i = INPUT AXIS RATE

The time constant J/F of the first order lag term is made small by design (order of 0.005 seconds), and hence this factor is usually omitted.

B2.1.2 Rate Gyros. In addition to inertial angular position data it is sometimes desirable to measure the angular rates of the vehicle. For this purpose a rate gyro is used. In a rate gyro the torque necessary to rotate the momentum vector is restrained by a counter torque. This counter torque can come from either a spring or an electrical torque generator. For the case of the spring restraint a block diagram representing the equations of motion and a typical configuration is shown in Figure B-4.

The equation of motion for the rate gyro on Figure B-4 is:

$$Js^2\theta_o + (Fs + K_\theta)\theta_o = H\omega_i \quad .$$

SPIN ANGULAR
VELOCITY

OUTPUT AXIS

ANGULAR DISPLACEMENT
OF H NEEDED TO DEVELOP
SPRING TORQUE

VISCOUS DAMPING

SPRING
RESTRAINT
K_θ

REFERENCE AXIS

$\overline{M}$

$\overline{\omega}$

$\overline{H}$

INPUT AXIS

$\omega_i(s)$

INPUT
RATE
AXIS

K_θ

$\dfrac{1}{Js^2}$

Fs

$\theta_o(s)$

K_p

$E_o(s)$
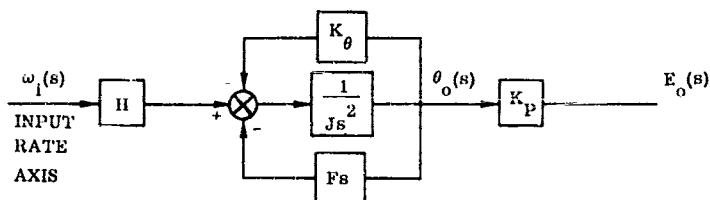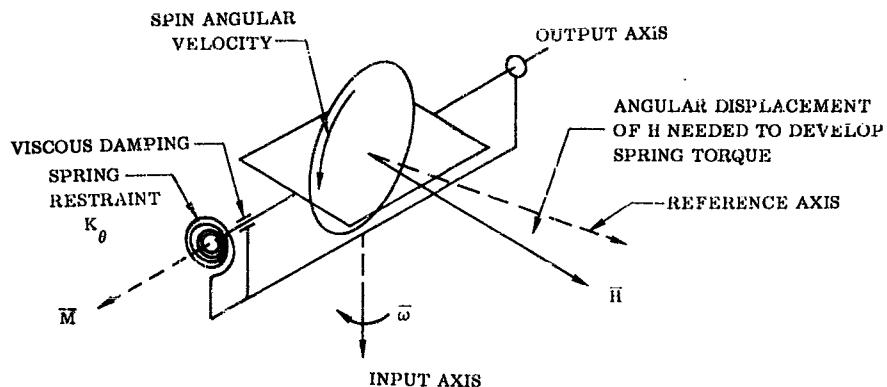
E_o = OUTPUT VOLTAGE

F = VISCOUS FRICTION

H = ANGULAR MOMENTUM

J = GIMBAL INERTIA

K_p = PICKOFF SENSITIVITY

K_θ = SPRING CONSTANT

θ_o = SYSTEM OUTPUT AXIS ANGLE

ω_i = INPUT AXIS RATE

Figure B-4. Rate Gyro

The transfer function then becomes:

$$\frac{E_o}{\omega_i} = \frac{K_p H/J}{s^2 + \dfrac{F}{J}s + \dfrac{K_\theta}{J}}$$

where

$$E_o = K_p \Theta_o \ .$$

The static gain (volts output per unit rate input) is:

$$\frac{K_p H}{K_\theta}$$

and the natural frequency is:

$$\omega = \sqrt{\frac{K_\Theta}{J}} \; .$$

The major factor in the selection of a rate gyro is the relationship between static gain and natural frequency. As the natural frequency is increased the static gain is lowered, and null voltage levels increase. Gyros with a wide range of characteristics are commercially available with frequencies of from 6 to 50 cps and damping ratios of from 0.3 to 2.5 critical damping.

It is also possible to obtain rate information from a rate integrating gyro. This is accomplished by placing a nulling amplifier around the rate integrating gyro. The output of the gyro then becomes proportional to angular rate. As an example, consider the rate integrating gyro of Figure B-3. The transfer function of this gyro is:

$$E_o = \frac{1}{s} \cdot \frac{\dfrac{K_P}{J}}{s + \dfrac{F}{J}} \; (H\,\omega_i + K_T E_i) .$$

Let the feedback or nulling voltage be:

$$E_i = -K_F E_o ;$$

then

$$E_o = \frac{1}{s} \cdot \frac{K_P/J}{s + F/J} \; (H\,\omega_i - K_T K_F E_o) .$$

This reduces to:

$$\frac{E_o}{\omega_i} = \frac{K_P \dfrac{H}{J}}{s^2 + (F/J)\,s + \dfrac{K_T K_F K_P}{J}}$$

which is the input-rate-to-output-signal transfer function.

It can be seen that the electric torque restoring force $(K_T K_F K_P)$ is equivalent to the spring K_Θ in the preceding equation for a spring-restored rate gyro.

The static gain then becomes:

$$\frac{H}{K_T K_F}$$

and the natural frequency is:

$$\omega = \sqrt{\frac{K_T K_F K_P}{J}}$$

The damping of this second order system is dependent upon the feedback gain (and hence frequency) chosen.

B2.2 Accelerometers. The accelerometer provides information as to the inertial motion of a body. Accelerometers can be classified into two major categories: 1) spring-restrained and 2) force-rebalanced. These accelerometers may detect either linear or angular motions, or any combination thereof. Additional uses of acceleration devices such as velocity sensing are also made: this can be done by external integration of the output signal.

B-8

The accelerometers illustrated in this section are fitted with a displacement transducer (shown as a potentiometer) and a spring or electro-magnetic restoring force. Accelerometers manufactured today contain many unique arrangements of mass, restoring element, and output transducer. The combinations are too numerous to describe in detail. A description of the operation of these devices will indicate the nature of the restoring element and transducer; from these the transfer function of the device may be determined. The three simple accelerometers analyzed in the following pages are all equipped with displacement transducers. Some classes of accelerometer-type instruments are equipped with velocity-sensitive output transducers. These transducers change the output characteristics of the device such that the output is proportional to "jerk" (rate of change of acceleration).

The first accelerometer configuration is that of a spring-restrained linear accelerometer, shown schematically in Figure B-5.
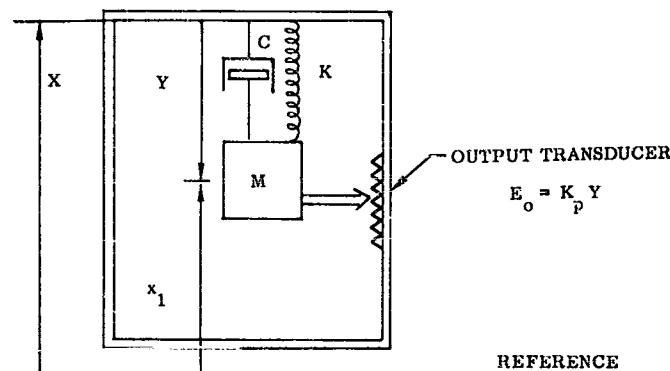
Figure B-5. Line Schematic of Spring Rebalanced Accelerometer

The equation of motion is:

$$-M\ddot{X}_1 + C\dot{Y} + KY = 0.$$

After the following substitutions are made:

$$X_1 = (X - Y)$$

$$E_o = K_p Y.$$

This reduces to the following transfer function:*

$$\frac{E_o}{\ddot{X}} = \frac{K_p}{s^2 + \frac{C}{M}s + \frac{K}{M}}.$$

---

*The use of $\ddot{X}$ for d^2x/dt^2 (acceleration) was admitted in an operational equation to clarify the relationship between the input and output variables.

The static gain (voltage output for a unit steady state acceleration) is:

$$\frac{E_o}{\ddot{X}_{ss}} = \frac{MK_p}{K}$$

The undamped natural frequency is:

$$\omega = \sqrt{\frac{K}{M}}$$

The accelerometer can also be adapted to record linear and/or angular acceleration in all combinations. Consider the accelerometer shown schematically in Figure B-6. The equation of motion for the configuration can be determined by equating the inertial moments and the moments due to the restraints F_Θ and K_Θ, the gimbal spring and damper:

$$\sum M_{\Theta_{(I)}} = M_2 \ell_2 \ddot{X} - M_2 \ell_2^2 \ddot{\Theta} - M_1 \ell_1^2 \ddot{\Theta} - M_1 \ell_1 \ddot{X}$$

$$\sum M_{\Theta_{(B)}} = F_0 (\dot{\Theta} - \dot{\Theta}_i) + K_\Theta (\Theta - \Theta_i),$$

where the quantities F_0 and K_Θ have the units of a torsional damper and spring.
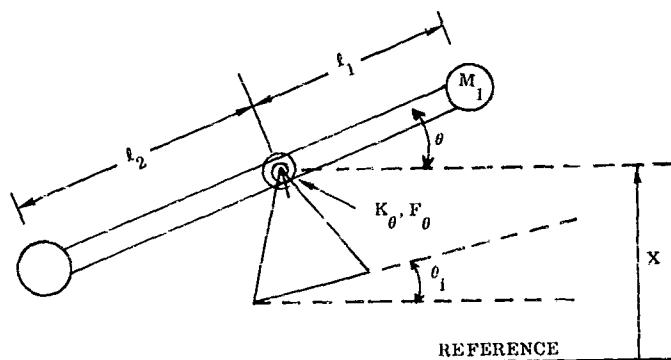
M_1 & M_2 = SEISMIC MASSES

ℓ_1 & ℓ_2 = LEVER ARM OF SEISMIC MASSES

θ = INERTIAL ROTATION OF ARM

θ_i = INPUT ROTATION OF ARM

X = LONGITUDINAL MOTION

K_θ = TORSIONAL SPRING CONSTANT

F_θ = TORSIONAL DAMPER CONSTANT

Figure B-6. Spring Unbalanced Accelerometer Sensitive to Both Longitudinal and Rotational Accelerations

By equating the inertial and base moments, the following transfer function can be obtained:

$$\Theta = \frac{(F_0 s + K_\Theta)\Theta_i + (M_2 \ell_2 - M_1 \ell_1)\ddot{X}}{(M_2 \ell_2^2 + M_1 \ell_1^2)s^2 + F_\Theta s + K_\Theta}$$

To determine the transfer function for the output voltage let

$$E_o = (\Theta_i - \Theta) .$$

Then the following transfer function can be written:

$$E_o = \frac{\left(M_1 \ell_1^2 + M_2 \ell_2^2\right)\ddot{\Theta} + \left(M_1 \ell_1 - M_2 \ell_2\right)\ddot{X}}{\left(M_2 \ell_2^2 + M_1 \ell_1^2\right)s^2 + F_\Theta s + K_0} .$$

If the accelerometer is then placed a distance L from the center of gravity such that:

$$\ddot{X}_a = \ddot{X} + L\ddot{\Theta}_i ,$$

then one can write:

$$E_o = \frac{\left[\left(M_1 \ell_1^2 + M_2 \ell_2^2\right) + L\left(M_1 \ell_1 - M_2 \ell_2\right)\right]\ddot{\Theta} + \left(M_1 \ell_1 - M_2 \ell_2\right)\ddot{X}_a}{\left(M_1 \ell_1^2 + M_2 \ell_2^2\right)s^2 + F_0 s + K_0} .$$

From the preceding it can be demonstrated that by varying the various parameters (M_1, M_2, ℓ_1, ℓ_2 and L) the accelerometer can be made to sense either pure $\ddot{\Theta}_i$, pure $\ddot{X}$ or any combination of $\ddot{X}$ and $\ddot{\Theta}_i$.

B2.2.1 Force-Rebalance Accelerometer. The seismic mass of Figures B-5 and B-6 can be restrained by an external force (usually magnetic) in place of the spring restoring force. Such a configuration would be called a force-rebalance accelerometer. A schematic representation of a force-rebalance accelerometer is presented in Figure B-7.

E_a = FILTER OUTPUT

E_o = OUTPUT SIGNAL

F_{KT} = FORCE DUE TO ERROR SIGNAL

K_A = AMPLIFIER GAIN

K_F = FILTER TRANSFER FUNCTION

K_p = PICKOFF GAIN

K_T = FORCE TRANSDUCER GAIN

X = LONGITUDINAL MOTION OF CASE

X_i = LONGITUDINAL MOTION OF WEIGHT

Y = RELATIVE MOTION OF WEIGHT AND CASE
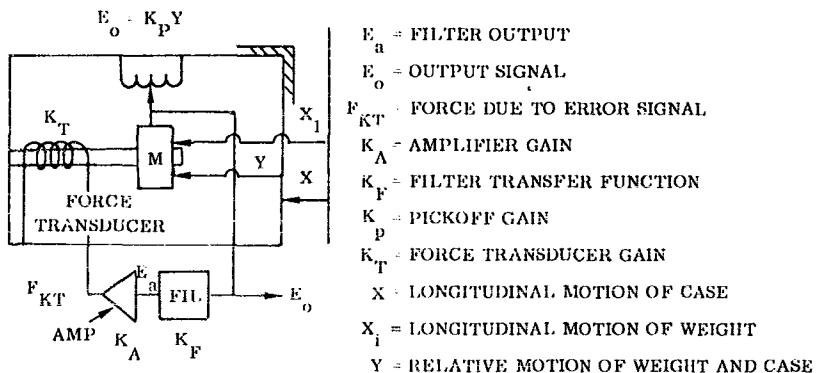
Figure B-7. Line Schematic of a Force Rebalanced Accelerometer

The equation of motion for the seismic mass can be written as follows:

$$M\ddot{X}_1 + F_{KT} = 0$$

where:

$$F_{KT} = K_T K_A K_F K_P Y_1$$

also

$$X_1 = X + Y.$$

The term F_{KT} is the force used to restrain the seismic mass of the force-rebalance accelerometer. The transfer function for the accelerometer then becomes:

$$\frac{E_o}{\ddot{X}} = \frac{-K_P}{s^2 + \dfrac{K_T K_A K_F K_P}{M}} . \tag{B-1}$$

As the preceding transfer function is not damped, the filter characteristics must be altered to provide damping. The filter transfer function, K_F, should be that of a lead network, to provide damping.

A simple lead-lag circuit is representative of the type of compensation that could be used to damp the accelerometer:

$$\frac{E_a}{E_o} = \frac{1 + \tau_a s}{1 + \tau_b s} . \tag{B-2}$$

Substituting Equation B-2 into Equation B-1 gives the following transfer function:

$$\frac{E_o}{\ddot{X}} = \frac{-K_P}{\left(s + \dfrac{K_T K_A K_P \tau_a}{M(1 + \tau_b s)}\right)\left(s + \dfrac{K_T K_A K_P}{M(1 + \tau_b s)}\right)} .$$

This is equivalent to a pair of complex conjugate roots multiplied by a lag-lead dipole. For $\tau_b < \tau_a$ one has:

$$\frac{E_o}{\ddot{X}} = \frac{-K_P}{s^2 + 2\zeta\omega_n s + \omega_n^2} \cdot \frac{1 + \tau_b s}{1 + s/\rho}$$

where ρ is a real root of the denominator. The values of natural frequency and damping are adjusted by choice of τ_a/τ_b and the rebalance loop static gain, $K_P K_T K_A$. The static gain of the force rebalance accelerometer is:

$$\frac{E_o}{\ddot{X}}\bigg|_{ss} = \frac{M}{K_T K_A} .$$

B2.3 <u>Inertial Platform Transfer Functions</u>. In an inertially guided vehicle the dynamic response of an inertial platform can affect the stability of the vehicle short-period modes in several ways. There are two feedback loops in which the dynamic response of the platform may appear. First, it always appears in the guidance loop. Second, if the platform, through gimbal angle pickoffs or a resolver chain, is used as the position reference, the platform dynamics will also appear in the position loop.

The actual platform response is highly nonlinear, even in a "linear" analog rebalanced accelerometer-analog-torqued-gyro platform, because of static friction. The effect of static friction is essentially a reduction in loop gain and an increase in phase lag. The effects are more pronounced at low signal levels, where the platform is usually operating. However, the platform is usually considered to be a "stiff" system and, for frequencies below 10 cps or so, can be linearized without much error.

There are several methods of presenting frequency response information (Bode Plot, Nichols Chart, etc.). Platform manufacturers have adopted these different techniques, as may be seen in Figures B-8, B-9 and B-10.
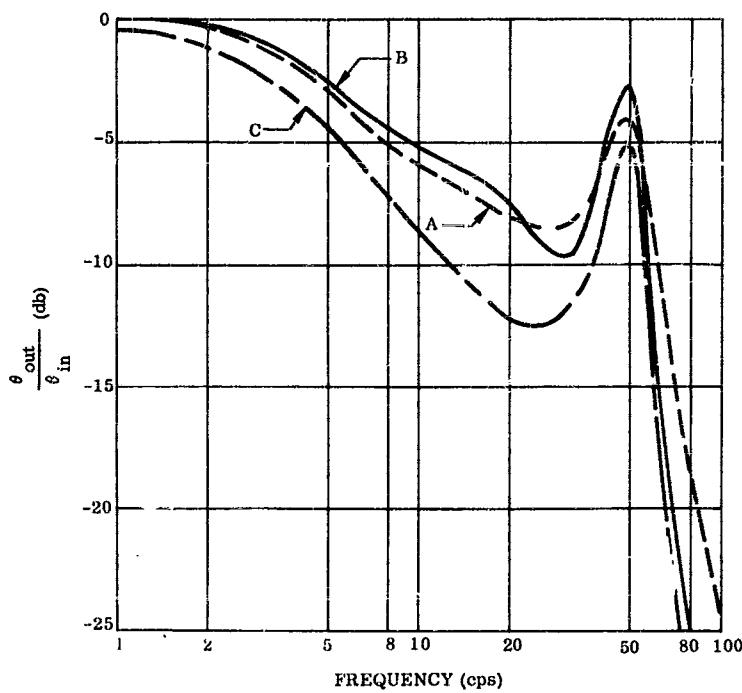
CURVE A J.P.L. SQUARE WAVE RESPONSE   (MANUFACTURER'S DATA)
CURVE B APPROX. SQUARE WAVE RESPONSE ⎫
CURVE C APPROX. SINE WAVE RESPONSE   ⎭ COMPUTER MODEL

Figure B-8. Frequency Response (Bode Plot) Vega Platform

Figure B-8 presents a Bode Plot of the proposed Vega space booster inertial platform's closed-loop response. Curve A is the actual data as received from the manufacturer. It shows "Square Wave Response versus Square Wave (Input) Frequency".

Figure B-9 presents the closed-loop transmissibility of the Arma-Atlas platform. The transmissibility is the angular displacement of the platform in inertial space per angular displacement of the missile in inertial space, versus frequency of the missile angular displacement.

Figure B-10 presents an open-loop Nichol's chart for the Centaur space booster inertial platform's leveling loop as provided by the manufacturer, Minneapolis-Honeywell.

Since this frequency response information is usually available and the actual transfer function is not, an approximation must be developed. Using the Vega platform (Figure B-8) as an example, one method of approximation will be described.
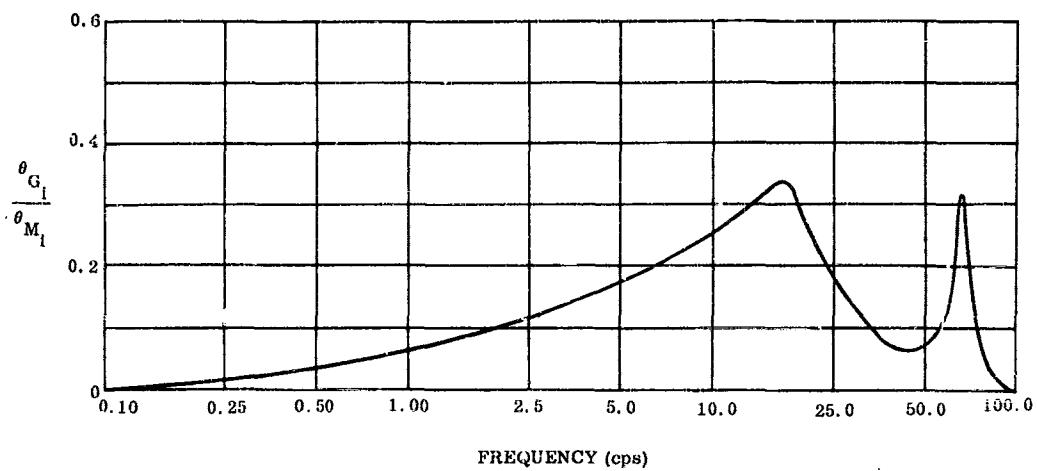
Figure B-9. Transmissibility, Arma Platform
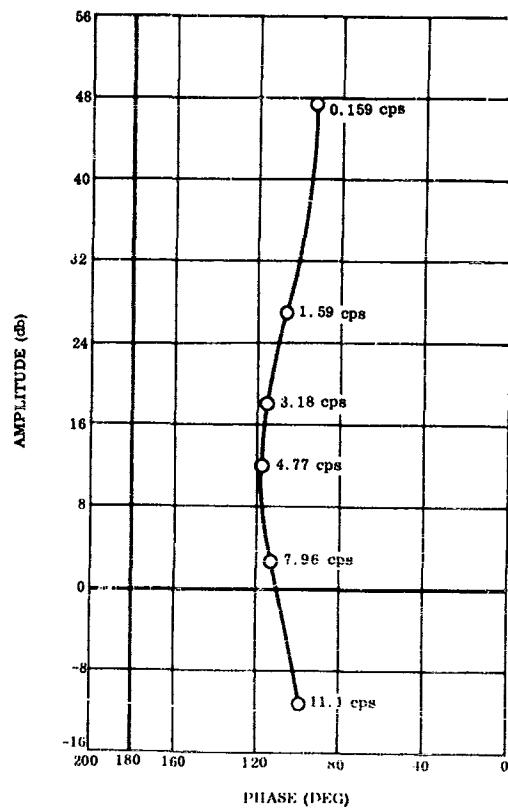
Figure B-10. Nichol's Chart M-H Miniature Platform

Curve A of Figure B-8, as mentioned previously, is the actual data as received from the manufacturer. From experience it was felt that a transfer function of the form:

$$\frac{\theta\text{out}}{\theta\text{in}} = \frac{(\tau_2 s + 1)}{(\tau_1 s + 1)\left(\dfrac{s^2}{\omega_n^2} + \dfrac{2\zeta}{\omega_n} s + 1\right)}$$

would be a good compromise between complexity and accuracy of curve fit. Next, this transfer function was programmed for the analog computer, and the values of τ_1, τ_2, ω_n and ζ were adjusted until a square wave response similar to that required was obtained (curve B of Figure B-8 shows this approximate square-wave response). The sine-wave response of the approximate transfer function was obtained (see curve C of Figure B-8) for comparison purposes.

Once the approximate platform transfer function is obtained, the method of insertion into the feedback loops must be ascertained. Again using the Vega vehicle system as an example (because it uses gimbal angle pick-offs for position reference), the pitch and yaw channel block diagrams of Figure B-11 and B-12 were developed. Figure B-13 shows the coordinate system used in these diagrams. Normally, the bending mode is not included in the position loop, but for the Vega configuration the slope of the first bending mode at the platform position was about ten times the slope at the rate gyro location, and an appreciable first-bending mode component was expected. This should be kept in mind for all vehicles where the position and rate sensors are at different locations, particularly when the position sensors are located in one of the upper stages of a multi-staged vehicle.
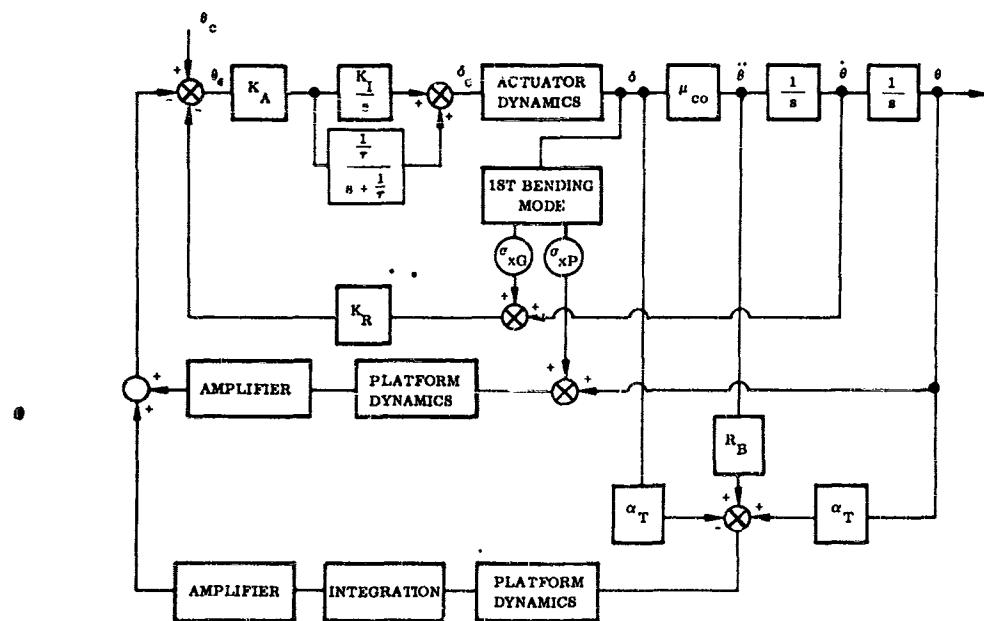

Figure B-11. Pitch Channel
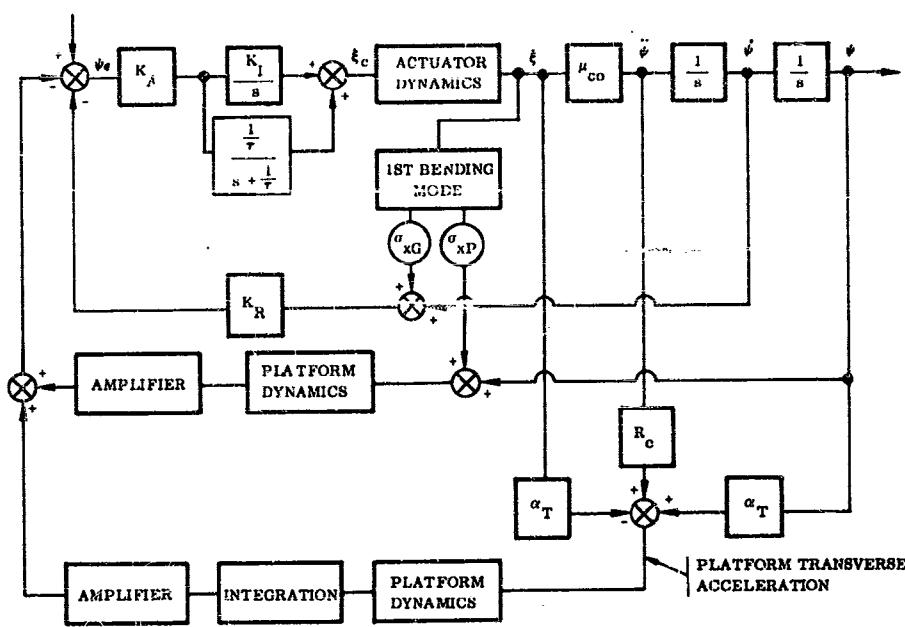
Figure B-12. Yaw Channel
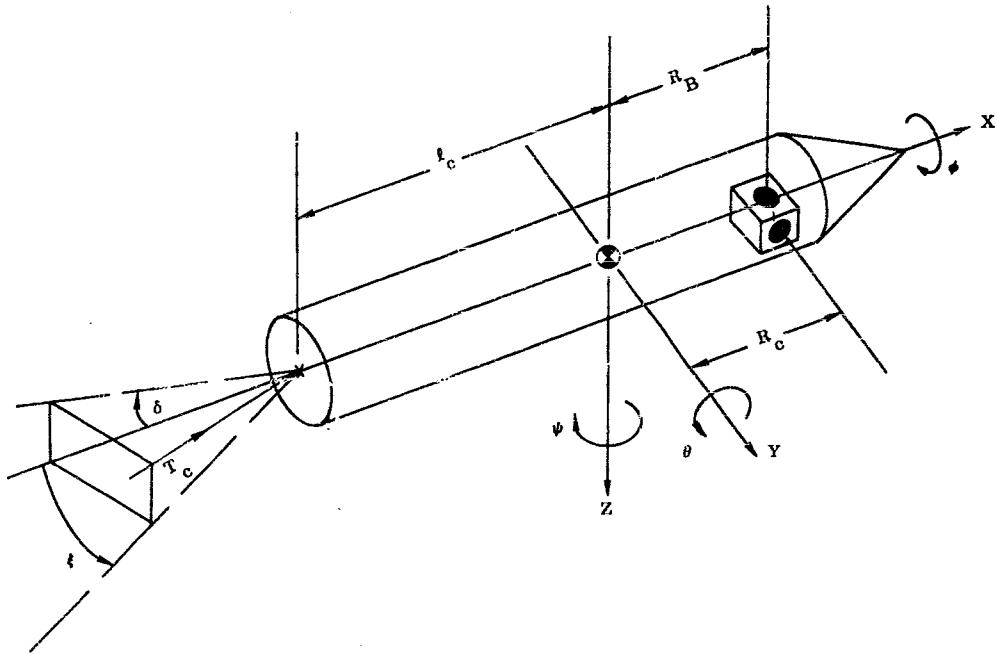
Figure B-13. Coordinate System

B2.4 Dynamics of Angle of Attack Sensors. There are many possible approaches to the problem of measuring angle of attack. Since the list of possible techniques (with variations) is quite long, no attempt will be made here to provide a complete set of descriptions. A good description and primary evaluation of most of the ideas for angle-of-attack measurement is available in Reference B-1. Only a few of the basic approaches have been tried with any success. We will attempt to classify these strictly on the basis of dynamic characteristics, and point out such factors as relative accuracy, reliability, bulk, and complexity.

First, a broad distinction is indicated between systems which sense angle of attack more or less directly and the process of deriving angle of attack by computer mechanization of lift. The latter approach passes essential information through the dynamics of pressure sensors, accelerometers, and a computing process and would be troublesome if good dynamic response is an important consideration. Hence, this treatment of dynamic characteristics will confine itself to methods which are based on direct sensing.

The direct sensing methods can be classified in two general categories -- according to whether or not the sensor is moveable.

With stationary sensors, angle of attack is computed from the pressure sensed by two or more appropriately positioned orifices. The moveable sensor is usually designed to point into the relative wind; angle of attack is derived from its position relative to the airframe. A little used alternate is to measure the aerodynamic forces on a moveable (but restrained) device. This type will not be considered here, since corrections for Mach number, dynamic pressure (q), and side slip angle are tedious and there is no indication in the literature that such a device has been developed and successfully used.

The moveable sensor class can be subdivided into simple weather-vane types and powered null-seeking devices. The two are alike in that angle of attack is read from the position of the sensor. The null-seeking device has a pair of orifices located symmetrically about the reference axis. The sensor is driven by a servo so that pressures on the two orifices are equal.

B2.4.1 Stationary Angle-of-Attack Sensors. If a probe is provided with orifices as indicated in Figure B-14, then one may write:

$$\alpha = K \ \frac{P_U - P_L}{P_T - P_S} \ f(M) f(\beta)$$

where:

β is side slip or the component of relative wind in a plane perpendicular to the plane of α measurement.

M is free stream Mach number.

K is an appropriate constant

and $P_T - P_S$ is the measure of dynamic pressure, q.

The arrangement of Figure B-14b eliminates the need for Mach number and β correction at the expense of sensitivity:

$$\alpha = K \frac{\left(P_{U_2} - P_{L_2}\right)}{\left(P_{U_1} - P_{L_1}\right) - \left(P_{U_2} - P_{L_2}\right)} \ 0 + \frac{\theta}{2} .$$

These equations are developed in Reference B-1.

The important results, where dynamic characteristics are concerned, is that although the need for Mach number and β corrections may be eliminated, there remains a requirement for manipulation of ratios of differential pressures.

With the probe of Figure B-14a, first order dynamic requirements apply only to the measurement of $\frac{P_U - P_L}{q}$. Dynamic pressure, q, and Mach number vary slowly compared to the short period variation of α. The function of β, included in the expression for α, does have short period dynamic characteristics, however. It can be mechanized as a change in gain of the α sensor. This requires the dynamics of a servo in β corrections. The permissible lag will depend upon how much dynamic cross-talk can be allowed.

The transfer function which operates directly on α will depend upon the mechanism of pressure-ratio sensing and the pneumatic characteristics of the probe, lines, and transducer volume.

The most direct approach to pressure-ratio sensing is to drive position transducers directly from bellows volume. This is the easiest way to get good dynamic response. Extreme accuracy cannot be attained with reasonable instrument volume because the measured pressure ratio must be high enough to overcome friction in the system. The performance of currently available sensors indicates that accuracies to ± 0.2 degree (from the pressure sensor only) can be readily obtained. No directly applicable dynamic data are available. The devices of similar construction designed for Mach number measurement indicate that a response equivalent to a first order time lag can be expected. Time constants on the order of 0.01 to 0.02 second should be attainable at moderate to high dynamic pressures. Both response and accuracy deteriorate at low values of q.

Accuracies in sensing α to considerably better than ± 0.2 degree would probably require the use of a servo-driven pressure ratio sensor. Servo-loop dynamics are sensitive to change in q, but are essentially second order.

The transfer function for pneumatic line lag can be closely approximated with a first order time constant:

$$\frac{1}{\tau_\ell s + 1} ,$$

where $\tau_\ell = \dfrac{128\,\mu\ell}{P\,\pi\,D^4}\left[V + \dfrac{V_t}{2}\right]$.
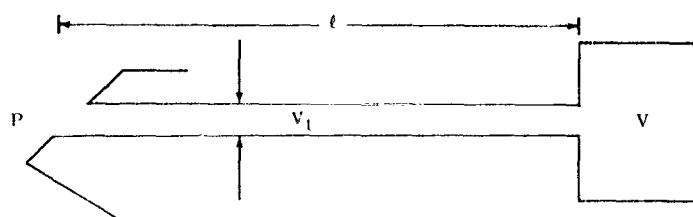
μ = viscosity of air,

P = average pressure in system,

$V_t = \pi\ell D$ = volume of sensing line, and

V = transducer volume.

From this example it is apparent that response is strongly affected by the length of pressure leads and the transducer volume as well as the total pressure.

In addition to this lag there is a transportation time delay which only becomes significant with long pneumatic lines between the sensor and transducer. This delay is simply the time required to propagate sound in air along the length of the tube.

In summary, for the stationary angle-of-attack sensor, one has a transfer function:

$$\frac{\alpha_m}{\alpha} = \frac{K\left[e^{-as}\right]}{(\tau_\ell(P_T)\,s + 1)(\tau_t\,s + 1)}$$

for direct-drive bellows transducers, or:

$$\frac{\alpha_m}{\alpha} = \frac{K\left[e^{-as}\right]}{(\tau_\ell(P_T)\,s + 1)\left[\dfrac{\tau_m}{K_s(q)}\,s^2 + \left(\dfrac{1}{K_s(q)} + K_{\dot\theta}\right)s + 1\right]}$$

when a servo-driven pressure ratio sensor is used. Here:

K	arbitary
a	line transport time delay (usually not significant)
$\tau_\ell(P_T)$	pneumatic line lag (a function of total pressure)
τ_t	time constant of bellows-transducer
τ_m	servo motor-time constant
$K_s(q)$	servo gain, a function of q
$K_{\dot\theta}$	servo rate feedback gain (if used).

B2.4.2 Moveable Sensors. The aerodynamic-vane type sensor is an attractive solution to the angle-of-attack measurement problem because of its simplicity, reliability, and freedom from the necessity for computed corrections. It has one serious drawback of requiring a moveable part (usually fragile) protruding from the airframe. The moveable vane is subject to damage and deformation in handling which could cause errors or complete malfunction. In applications where this characteristic can be tolerated and where extreme accuracy, especially at low Mach number is not required, the moveable vane is probably the simplest and most inexpensive solution.

a.

b.
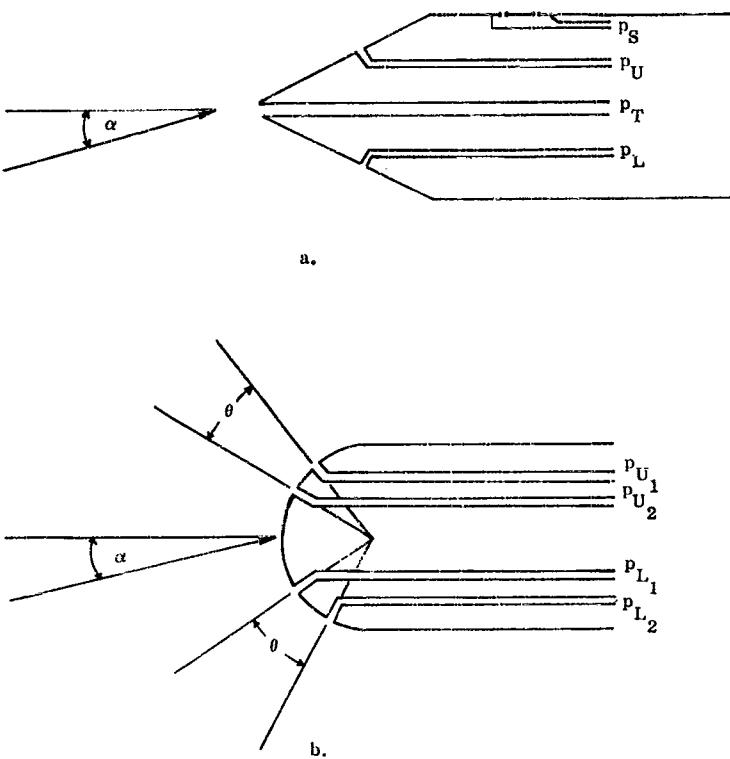
Figure B-14. Stationary Angle-of-Attack Sensors

A straight-forward NASA design of this type of sensor, presented in Reference B-2, will be used in an example to present typical dynamics. It is sketched in Figure B-15.

This particular vane is extremely light-weight; hence it has a very high response and is heavily damped. The ratio $C\ell_{\dot\phi}/C\ell_{\phi}$ is estimated to be about 0.08; this is probably conservative. Inertia is only 10^{-4} lb-in-sec^2, and $C\ell_{\phi}$ is estimated at 2.9/radian. Substitution into the transfer function gives:

$$\frac{\phi}{\alpha} \ (s) = \frac{(0.8\ s + 1)}{(0.1\ s + 1)\ (0.0001\ s + 1)}.$$

Reference B-2 shows accuracies of ±1/4 degree or less at supersonic velocities. Subsonic operation brings upwash errors which can be as high as one degree at a five-degree angle of attack (on a nose probe mount ahead of a lifting surface). The latter is a position error and could be compensated for as a function of Mach number. It is apparent from this example that if static errors in the above range can be tolerated, the vane type sensor provides excellent dynamic response.

When greater accuracy is required the null-seeking, servo-driven moveable sensor may be required. Accuracies with less than ±0.1 degree error are claimed for models currently in use.

$$\frac{\theta}{\alpha}(s) = \frac{\dfrac{Cl_{\dot\phi}}{Cl_\phi}s + 1}{\dfrac{I}{qxACl_\phi}s^2 + \left(\dfrac{Cl_{\dot\phi}}{Cl_\phi} + \dfrac{F(AMPL.)}{qxACl_\phi}\right)s + 1}$$

WHERE:
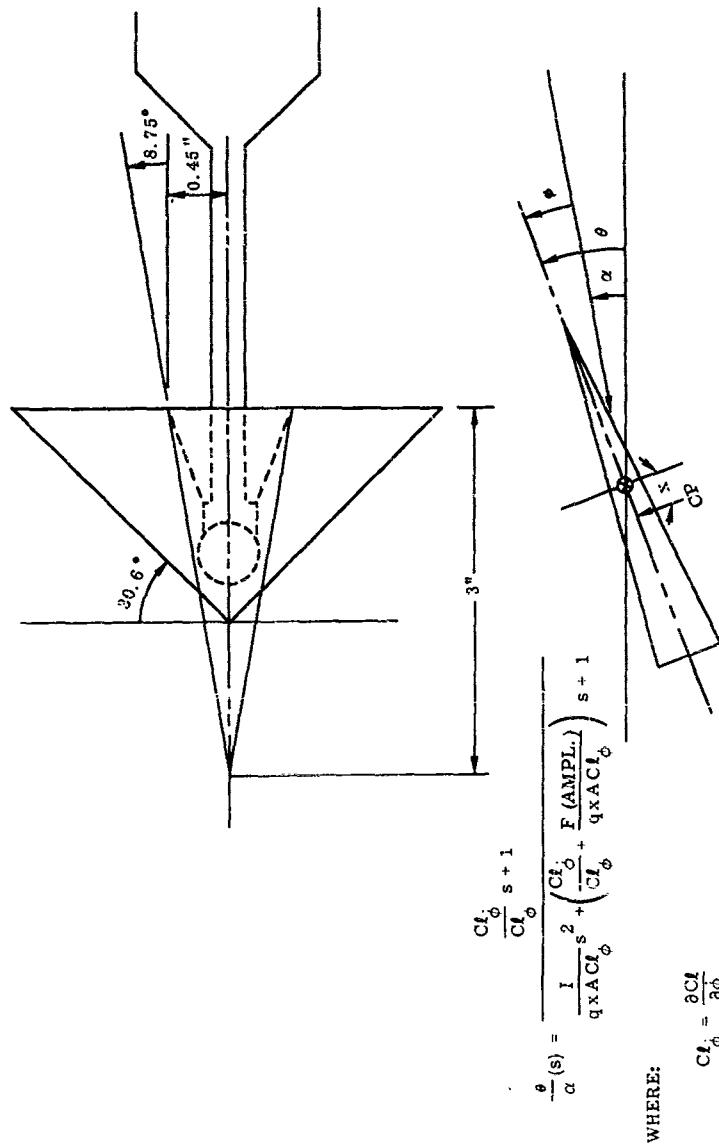
I = MOMENT OF INERTIA ABOUT HINGE POINT

A = REFERENCE AREA

x = DISTANCE FROM CENTER OF PRESSURE (CP) TO HINGE POINT

$Cl_\phi = \dfrac{\partial Cl}{\partial \phi}$

$Cl_{\dot\phi} = \dfrac{\partial Cl}{\partial \dot\phi}$

$F(AMPL.)$ = EFFECTIVE DAMPING FROM FRICTION

Figure B-15. Aerodynamic Vane Type Angle-of-Attack Sensor

Since provisions for moving the sensor require servo motor location near the vane, pneumatic line lags will probably not be significant. The range of the differential pressure sensor need not be large; hence, it can have good dynamic response. The dynamic characteristics of this type of sensor would then be dominated by the characteristics of the servo which drives the null-seeking head. Typically:

$$\frac{\Omega}{\alpha} \, (s) = \cfrac{1}{\dfrac{\tau_1}{K_s} s^2 + \left(\dfrac{1}{K_s} + \tau_0\right) s + 1}$$

where

$K_s(q) =$ total loop gain

$\tau_0 =$ rate feedback time constant (if used)

$\tau_1 =$ servo motor time constant.

K_s varies proportionally with dynamic pressure. Unless some automatic gain scheduling is provided within the servo loop, the servo must be designed with adequate response set by the lowest dynamic pressure to be encountered, and stability determined by the highest.

The transfer function varies from heavily damped, essentially first order response at low q values to highly damped, second order at high q values.

B3 CONTROL ELEMENTS

This section contains a phenomenological discussion of several of the various active configurations that can be used to provide forces for stability and control of booster vehicles. The several properties to be considered will be given a general treatment to familiarize the reader with certain properties of these devices.

These prime-mover devices are grouped into two general categories: aerodynamic and reaction jet (thrust) control.

B3.1 <u>Aerodynamic Control</u>. The aerodynamic forces used for control can be obtained either by configuration (stable aerodynamic booster) or by an active control system (moveable aerodynamic surfaces). The moveable aerodynamic surfaces are the only ones to be considered herein. These surfaces may be further subdivided as to the amount of surface that is moveable, the method of actuation, the position on the vehicle, etc.

The methods to be used for synthesis and analysis of the flexible booster and control system are not affected to any great degree by these differences in the control elements. The major differences occur in the relative importance of the control force, actuation force due to position, and inertial forces. This relative importance may affect the degree of approximation that can be used. The majority of the approximations discussed in Section 4 are based on the premise that the inertial force of the control device (a rocket engine in this case) will be large and the actuation position force nil. For moveable aerodynamic surfaces this situation may be reversed. When this occurs it may be reasonable to approximate the forces produced by the aerodynamic surface by a first-order lag for more complex analyses than would be possible for the gimbaled engine. The force produced by any given surface configuration will be a function of the flight variables, which are dynamic pressure, Mach number, and angle of attack of the surface. This force is derived for several values of angle of attack at various dynamic pressures and Mach numbers. A curve of force versus surface angle can be plotted for various flight times (see Figure B-16).

The force versus surface angle is approximately linear in the region around zero angle of attack. The common technique is to linearize this curve, on the basis of the largest anticipated angle of attack, and then use this linear constant for stability analyses. If this is not possible (due to the nature of the curve), then a describing function analyses will be required (Reference B-3).
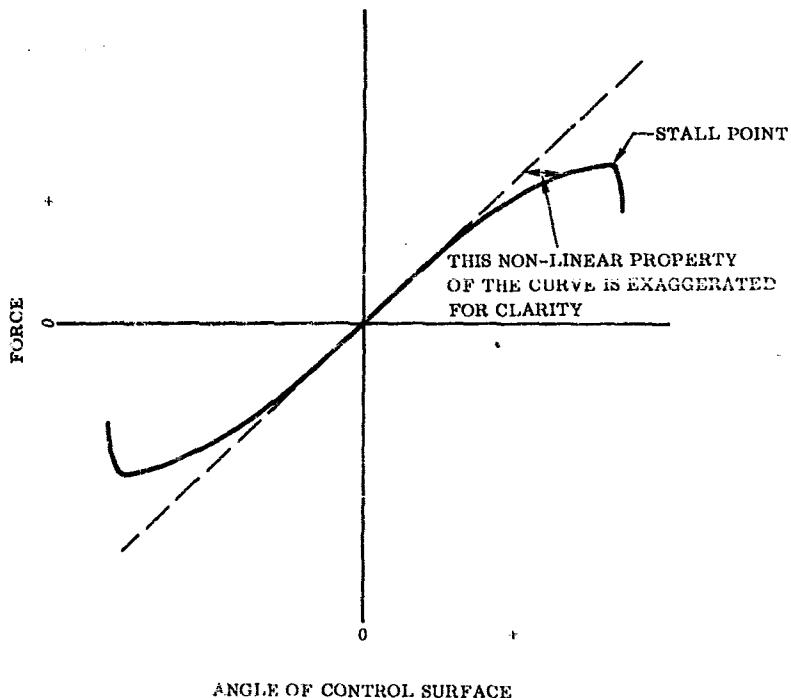
Figure B-16. Typical Plot of Force Versus Control Deflection

B3.2 <u>Thrust Vectoring Schemes.</u> The majority of the present booster vehicles use thrust vectoring for control. Thrust vectoring is used because it allows control during flight conditions when aerodynamic control is not possible — such as immediately after launch and later when the vehicle leaves the sensible atmosphere. As thrust vector forces are more constant than the aerodynamic forces, the synthesis and analysis of the control system will be easier, too. This property may also allow a constant-gain autopilot and control system to be used. The thrust vectoring can be accomplished in several ways, such as gimbaled engines, moveable nozzles, stream deflection, and on-off control.

B3.2.1 <u>Gimbaled Engines.</u> The gimbaled engine is the method which is used currently for large, liquid fueled boost vehicles. Gimbaled engines were presumed in deriving the equations presented in the body of this report (see Section 4). The primary control force for this scheme of control is simple in conception: thrust times the sine of the gimbal angle. The control moment is this force times the lever arm between the gimbal point and the vehicle center of gravity. Certain secondary forces* (gimbal-friction, jet-damping, hose-restraint, thrust-offset, and inertial forces) will have to be considered in the analysis of the control system. The equations of motion are not discussed at this point, as they are covered in detail elsewhere in the report (Subsection 4.3.3 and Appendix B4-2).

B3.2.2 <u>Moveable Nozzles.</u> The major use of the moveable nozzle, as opposed to a moveable (gimbaled) engine, is in the control of solid propellant rocket motors. The thrust-vector deflection is obtained by allowing the nozzle to move through an angle with respect to the rocket motor case (Figure B-17).

---

* These forces are referred to herein as secondary because they are not the forces desired for control. This does not imply necessarily that they are smaller in magnitude than the primary forces.
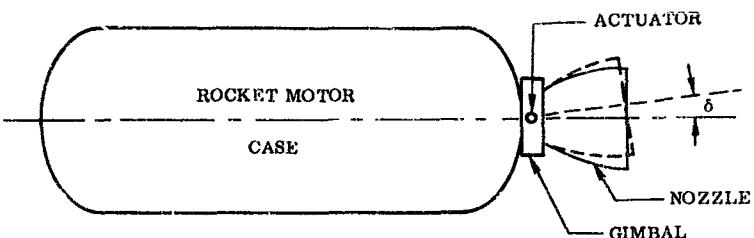
Figure B-17. Solid Propellant Rocket Motor With Movable Nozzle

For the solid propellant rocket with moveable nozzle, the forces are similar to those for the gimbaled engine. The relative importance of the several terms (particularly in the secondary forces) will change, and these changes are reflected in the servo-motor load. The actuator moment necessary to deflect the exhaust stream then becomes significant. This moment is the result of an internal aerodynamic torque and is a function of $\dot{m}v$ (the mass flow and velocity). It is proportional to the sine of the thrust deflection angle. The magnitude of the moment coefficient is dependent upon the geometry and cannot be expressed by a simple general formula. The configuration changes will tend to decrease the inertial forces (due to less mass being gimbaled), while increasing the friction and elastic forces, which must be overcome to move the nozzle. The resulting actuator system is generally satisfactorily approximated by a first order system, even for relatively high frequency mode studies.

The terms "moveable" for nozzles and "gimbaled" for engines are used because the solid propellant nozzles are moved in one plane only, while liquid engines are gimbaled in both the pitch and yaw planes. Although this situation still occurs in practice, there apparently are no insurmountable problems regarding deflection of the solid propellant nozzle in both the pitch and yaw planes.

B3.2.3 **Pivoted Nozzles.** Pivoted nozzles, as opposed to moveable nozzles, will be used herein to denote configurations in which the entire motor case is rotated to produce thrust deflection forces (see Figure B-18 for a typical configuration).

The forces for the pivoted nozzle are identical to those for the gimbaled engine*. The inertial forces are larger than those for the moveable nozzle; this may require the use of a third or higher order actuator servo simulation for the higher mode analyses.

The pivoted nozzle installation offers some unique advantages in combining control capability, along with a performance increment which may be shown to be positive (a gain) for many installations.

B3.2.4 **Stream Deflection Schemes.** The stream deflection schemes considered herein are those where the nozzle is not deflected but the exhaust stream is deflected by some other phenomena to produce a lateral force. The stream deflection can be accomplished by various types of apparatus. These devices can be separated into two general categories: mechanical means and fluid control.

The mechanical apparatus used for stream deflection include such devices as jet vanes, jetevators, full eyelids, single eyelids, spoiler tabs, and split extension nozzles. In addition to the devices for a regular nozzle, a pivoting cowl and laterally displaced spike are used for thrust-vector control of isentropic spike nozzles. A definition of the above mentioned apparatus along with curves of steady state performance are given by P. A. Hunter (Reference B-4). The general result obtained by use of such devices will be similar to that indicated in Figure B-19.

---

* The possible exception is the absense of hose restraint torques for the pivoted nozzle. This is not felt to be significant as the hose restraint torques are usually dropped for gimbaled engines.

SOLID
PROPELLANT
ROCKET MOTOR

PIVOT AXIS

NOZZLE

THRUST

MAIN ROCKET WITH
FIXED NOZZLE
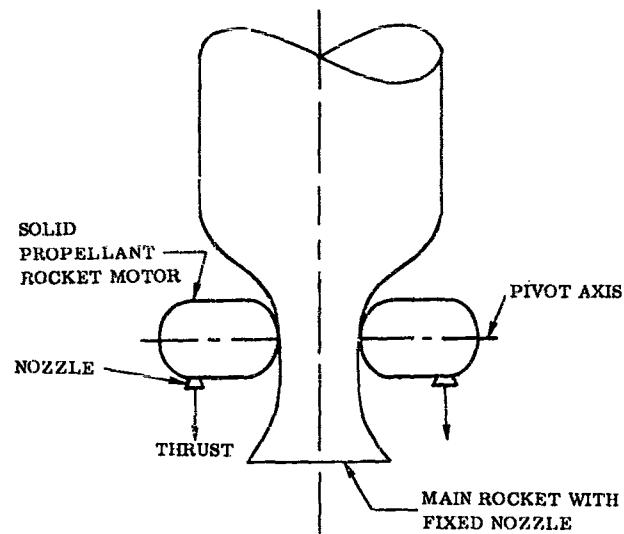
Figure B-18. Pivoted Nozzles Used for Control

Figure B-19 compares two methods of obtaining a lateral force; viz., engine rotation and stream deflection. The base of comparison (the dotted line of Figure B-19) is produced by an engine rotation. This base is compared to forces produced by stream deflection. The comparison is for two engines with initial thrust, F_R. In both cases a lateral force, F_Y or F_Y', is produced. For the engine rotation, $F_Y = F_R \sin \delta$ and $F_X = F_R \cos \delta$. For the stream deflection device an identity, $F_Y' = F_Y$ would result in an F_X' such that $F_X' < F_X$. Restating the preceding in words: The stream deflection will always be less efficient for producing lateral forces than an engine rotation.


STREAM DEFLECTION

ENGINE ROTATION
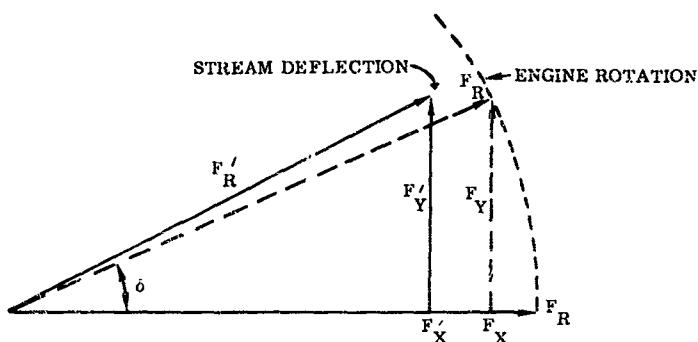
Figure B-19. Typical Vector Diagram of Reaction Control Forces

The stream deflection will be accomplished usually by a light-weight system, compared to the weight of the engine. Therefore, inertial forces will be minor. Thus, the first order approximation:

$$F_Y = \frac{1}{\tau s + 1} \; F_{Y \; command}$$

may be used for most analyses.

The fluid stream can be deflected by injecting a secondary stream of fluid into the exhaust, see Figure B-20 (References B-4 and B-5). This secondary stream has the effect of creating a shock wave which, in turn, causes an effective deflection of the thrust vector, similar to that obtained by gimbaling the engine. Although there are no inertial forces connected with this scheme, the response will be limited by fluid transport lags and valve response characteristics.
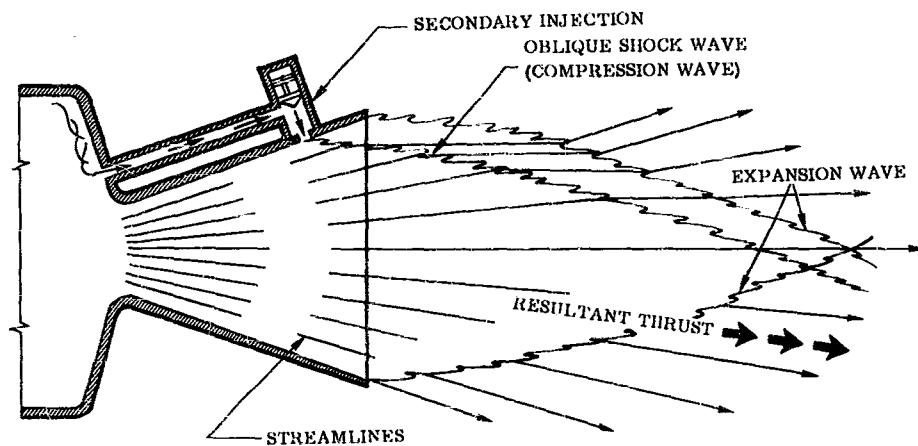

Figure B-20. Oblique Shock Deflection by Chamber Gas Injection Principle

B3.2.5 Variable Thrust Control. An effective thrust deflection can be produced by throttling one or more of the engines in a multiple-engine system. The basic method of control moment is illustrated in Figure B-21.
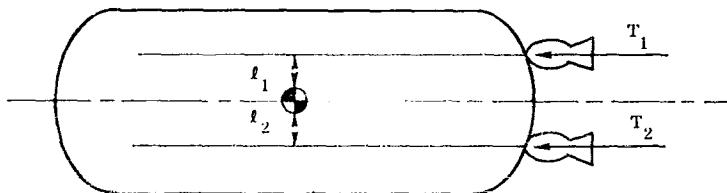

Figure B-21. Schematic for Control by Varying Rocket Engine Thrust

The moment produced about the center of gravity is:

$$\sum M = T_1 \ell_1 - T_2 \ell_2$$

where T_1 — thrust of number 1 engine

ℓ_1 — moment arm of number 1 engine thrust vector about the missile center of gravity. For a command change in thrust, Δt, such that $T_1 = T_{1n} + \Delta t$ and $T_2 = T_{2n} - \Delta t$, one obtains:

$$\sum M = (T_{1n} \ell_1 - T_{2n} \ell_2) + \Delta t (\ell_1 + \ell_2) - \Delta t (\ell_1 + \ell_2).$$

Escher (Reference B-6) presents a scheme for the use of a liquid-propellant rocket engine employing several fixed, differentially throttled thrust-chambers for effecting space vehicle three-axis control.

Although schemes involving throttling of rocket engines have not been used, they do constitute an acceptable method if the lags involved in obtaining the commanded moment can be reduced to a reasonable value.

B3.2.6 <u>On-Off Control.</u> The last method of control to be discussed is that obtained by using auxiliary on-off rocket engines. This usually consists of several fixed chambers firing transverse to the vehicle, singly or in combinations to produce the desired control couples (see Figure B-22). These chambers are controlled by a logic system which usually involves a dead-zone in position and rate. A simulation of the engine thrust characteristics is usually required for autopilot and control system analysis because of the large nonlinearities present. Figure B-23 gives a typical response of a small on-off rocket engine. The initial delay on both rise and decay is caused, to a great extent, by circuitry, valve characteristics, and fluid transportation lags. This lag will vary from two to 100 milliseconds, depending on the engine and control system configuration. The rise time is a function of the propellant and will vary from 30 or more milliseconds for a hydrogen peroxide engine to approximately one millisecond for some hypergolic bipropellant chambers. Because of the strong nonlinear characteristics a limit cycle oscillation will exist, the amplitude and frequency of which must be set by system parameter adjustments.

Auxiliary rockets of this type range in size (thrust levels) from 0.01 pound to about 1,000 pounds. The lower thrust level rockets use cold gas as their working fluid and are not likely to be applied in the control of large boosters; their application is in the realm of space vehicle and satellite control. The larger thrust level rockets use chemical propellants (mono- or bipropellant) to generate hot working gases. These larger rockets may prove feasible for control of some classes of booster vehicles.

B4 POSITIONING SERVO

B4.1 <u>Electrical Actuators.</u> Two approaches to electrical control actuation are commonly available: some form of direct-coupled electrical servo, or a clutch-actuated servo. With both types the more attractive systems (from a cost and weight standpoint, especially for smaller missiles) are highly nonlinear. Typical transfer functions for the linear (or continuous) direct coupled servos are presented, after which the simulation of discontinuous direct coupled types is discussed. Finally, basic characteristics of the extremely nonlinear clutch systems are discussed.

B4.1.1 <u>Direct-Coupled Linear Electrical Servos.</u> Following is a development of the transfer function of the three common types of d-c electrical servos. These are the basic linearized transfer functions of the essential hardware. These characteristics should be taken into account even if nonlinear methods of excitation are used. The transfer functions of the three basic types of d-c servos are essentially the same form -- third order. With a given set of torque and velocity requirements, the armature-controlled motor will usually give the fastest dynamic response. The field-controlled motor provides good economy of control power but lacks inherent damping and is useful only when a slow response can be tolerated. It also is inefficient in overall use of electrical power since high armature current must be maintained regardless of output, for proper control. The field-controlled servo transfer function is included here for completeness. It will probably not be useful for control system actuation.

The servo using a series motor will probably best meet the requirements of the majority of direct-coupled control actuating requirements. It provides the highest stall and low speed torque for a given motor weight.

Transfer functions are developed using the following symbols. Symbols not included in this list are defined by the equation or diagram in which they first appear:

δ – output position

ϕ – flux

τ – rate feedback time constant (gain)

A   – effective load spring constant (aerodynamic load)

F   – effective damping from friction

J   – effective inertia of load and motor

K', K'' – proportionality constants

T   – output torque

V_e – counter e.m.f.

Subscripts

f   – field

a   – armature

The typical armature- or field-controlled servo motor can be represented as in Figure B-24.
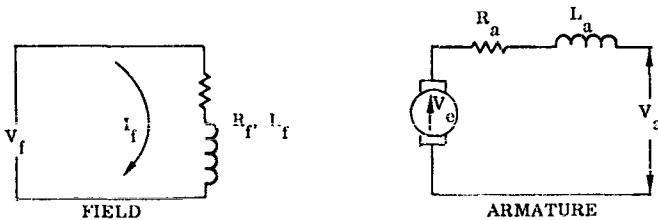

Figure B-24. Schematic of a Typical Armature- or Field-Controlled Servo Motor

where:

$$V_a = V_e + I_a R_a + L_a \frac{dI_a}{dt}$$

$$V_f = I_f R_f + L_f \frac{dI_f}{dt}$$

$$T = K' \phi I_a$$

$$V_e = K'' \phi \dot{\delta}$$

For armature control, V_f is constant (or a permanent magnet field excitation can be used), ϕ is constant, and:

$$T = K_i I_a$$

$$V_e = K_{\dot{\delta}} \dot{\delta}$$

For an inertial, frictional, and aerodynamic spring load:

$$T = J\ddot{\delta} + F\dot{\delta} + A\delta$$

$$V_a = K_{\dot{\delta}}\dot{\delta} + \frac{R_a}{K_i}(J\ddot{\delta} + F\dot{\delta} + A\delta) + \frac{L_a}{K_i}(J\dddot{\delta} + F\ddot{\delta} + A\dot{\delta})$$

$$\frac{\delta}{V_a}(s) = \frac{\dfrac{Ki}{Ra\,A}}{\dfrac{L_a J}{R_a A}s^3 + \left(\dfrac{J}{A} + \dfrac{L_a F}{R_a A}\right)s^2 + \left(\dfrac{K_{\dot{\delta}} K_i}{R_a A} + \dfrac{F}{A} + \dfrac{L_a}{R_a}\right)s + 1}$$

If L_a can be considered negligible, as is usually the case, then

$$\frac{\delta}{V_a}(s) = \frac{\dfrac{K_i}{R_a A}}{\dfrac{J}{A}s^2 + \left(\dfrac{K_{\dot{\delta}} K_i}{R_a A} + \dfrac{F}{A}\right)s + 1} \ .$$

In the servo system of Figure B-25, where the rate feedback represented by τs may or may not be necessary, the overall transfer function of the actuating system becomes:
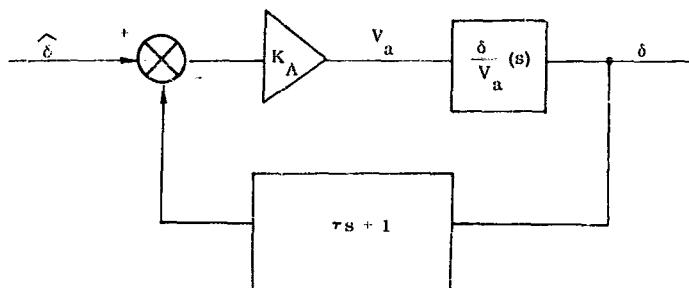

Figure B-25. Use of Electric Servo Motor in Position Servo Loop

$$\frac{\delta}{\hat{\delta}}(s) = \frac{\dfrac{1}{\dfrac{R_a A}{K_A K_i} + 1}}{\dfrac{R_a J}{R_a A + K_A K_i}s^2 + \left(\dfrac{K_{\dot{\delta}} K_i + R_a f + \tau K_A K_i}{R_a A + K_A K_i}\right)s + 1} \ .$$

When aerodynamic loads are small compared to inertial and/or frictional loads:

$$\frac{\delta}{\hat{\delta}}(s) = \frac{1}{\dfrac{R_a J}{K_A K_i}s^2 + \left(\dfrac{K_{\dot{\delta}} K_i + R_a F + \tau K_A K_i}{K_A K_i}\right)s + 1} \ .$$

The Field control circuit is as shown in Figure B-24. This transfer function assumes the armature current, I_a, constant. This implies either that armature resistance, R_a, is large or that the source has a high output impedance. The flux, ϕ, is then proportional to the field current, I_f:

$$V_f = I_f R_f + L_f \frac{dI_f}{dt} \quad , \quad T = K_i I_f$$

$$V_f = \frac{R_f}{K_i} T + \frac{L_f}{K_i} \frac{dT}{dt} \quad .$$

Again

$$T = J\ddot{\delta} + F\dot{\delta} + A\delta \quad .$$

Eliminating T between these last two equations gives:

$$\frac{\delta}{V_f}(s) = \frac{\dfrac{K_i}{R_f A}}{\dfrac{L_f J}{R_f A} s^3 + \left(\dfrac{R_f J + L_f F}{R_f A}\right) s^2 + \left(\dfrac{R_f F + L_f A}{R_f A}\right) s + 1} \quad .$$

The complete servo with rate feedback as in Figure B-25 has the transfer function:

$$\frac{\delta}{\hat{\delta}}(s) = \frac{\dfrac{\dfrac{1}{R_f A}}{\dfrac{K_A K_i} + 1}}{\left(\dfrac{L_f J}{R_f A + K_A K_i}\right)s^3 + \left(\dfrac{R_f J + L_f F}{R_f A + K_A K_i}\right)s^2 + \left(\dfrac{R_f F + L_f A + \tau K_A K_i}{R_f A + K_A K_i}\right)s + 1} \quad .$$

With inertial and frictional loads only, the servo transfer function is:

$$\frac{\delta}{\hat{\delta}}(s) = \frac{1}{\dfrac{L_f J}{K_A K_i}s^3 + \left(\dfrac{L_f F + R_f J}{K_A K_i}\right)s^2 + \left(\dfrac{R_f F + \tau K_A K_i}{K_A K_i}\right)s + 1} \quad .$$

Series motors operate with pronounced nonlinearity.

In the circuit of Figure B-26:
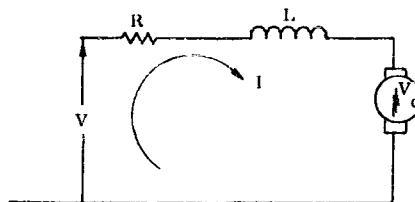
Figure B-26. Schematic of Series Motor

a. $V = RI + L \dfrac{dI}{dt} + V_e \ (\dot{\delta}, I)$

b. $T(I) = k \, \phi(I) \, I$

c. $V_e = (I, \dot{\delta}) = k' \, \phi(I)\dot{\delta}$

$\quad$ for $\phi(I) = k'' \, I$ and where $\begin{cases} k \, k'' = K_1 \\ k'k'' = K_{\dot{\delta}} \end{cases}$;

then

$$T = K_1 I^2 \text{ and } V_e = K_{\dot{\delta}} \, I \, \dot{\delta} \ .$$

To arrive at a transfer function, both b. and c. must be approximated in a linear fashion. If both are assumed linear in a limited range of the torque-speed and torque-current characteristics of the motor,

d., e. $\quad T = K_1 I, \ \dfrac{dT}{d\dot{\delta}} = K_2,$ where K_1 and K_2 are the constants of proportionality. Then:

f. $\quad V = \dfrac{RT}{K_1} + \dfrac{L}{K_1} \dfrac{dT}{dt} + \left[V_e \ (\dot{\delta}) \right] \quad .$

With an inertial, frictional, and spring load:

g. $\quad T = J\ddot{\delta} + F\dot{\delta} + A \delta + \left[K_2 \, \dot{\delta} \right] \ .$

The term $K_2 \, \dot{\delta}$ in g. represents the same physical effect as $V_e \ (\dot{\delta})$ in f., i.e., the change in torque due to changing back-e.m.f. (and hence changing current) accompanying a speed change. Obviously, they are not equivalent if $V_e \ (\dot{\delta})$ is assumed to be a linear function. No claim of superior accuracy is made for the representation of g.; it is used only because the constant K_2 is readily available from the torque-speed curves of the motor. The transfer function is obtained by substituting g. into f. and excluding the term $V_e \ (\dot{\delta})$, since the effect is now accounted for in g.:

$$\frac{\delta}{V} \ (s) = \frac{\dfrac{K_1}{RA}}{\dfrac{LJ}{RA} s^3 + \left(\dfrac{L \, (F + K_2) + RJ}{RA} \right) s^2 + \left(\dfrac{LA + R (F + K_2)}{RA} \right) s + 1}$$

In the control loop of Figure B-27,

$$\frac{\delta}{\hat{\delta}} \ (s) = \frac{\dfrac{K_1 K_A}{RA + K_1 K_A}}{\dfrac{LJ}{RA + K_1 K_A} s^3 + \left[\dfrac{L (F + K_2) + RJ}{RA + K_1 K_A} \right] s^2 + \left[\dfrac{LA + R (F + K_2)}{RA + K_1 K_A} \right] s + 1}$$
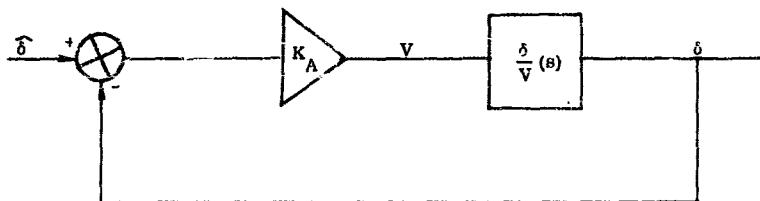
Figure B-27. Series Motor Control Loop

When the load has a negligible spring $(A \longrightarrow O)$,

$$\frac{\delta}{\hat{\delta}}(s) = \frac{1}{\dfrac{LJ}{K_1 K_A} s^3 + \left[\dfrac{L(F + K_2) + RJ}{K_1 K_A}\right] s^2 + \left[\dfrac{R(F + K_2)}{K_1 K_A}\right] s + 1} .$$

Note that this linearizing process involves extreme assumptions of proportionality. The transfer function is good only for small disturbances about a specific operating point. For some applications the series motor, like the armature-controlled motor, can be represented by a transfer function simplified by neglecting L, the combined inductance of field and armature. This assumption should be made with caution, as field induction is likely to be large.

B4.1.2 Clutch-Actuated Systems. Clutch systems can be divided into two classes for purposes of establishing an equivalent transfer function: those designed for continuous control and those intended to be strictly an on-off device. Both types offer the advantages of high load acceleration capability with low control power.

The magnetic powder clutch servo is typical of the continuous control type. Torque transmission by the clutch is near enough to being linear with clutch magnetizing current that the inductive lag is the most significant dynamic feature. Prime mover speed can usually be assumed constant. Thus, this type of clutch servo can be well represented by an inductive lag:

$$\frac{T}{V_{in.}}(s) = \frac{K}{(\tau_c s + 1)} ,$$

where τ_c is determined by the resistance-inductance characteristics of the clutch magnet and the driving source impedance. This time constant can be made quite short. With an inertial and frictional load:

$$T = J\ddot{\Theta} + F\dot{\Theta} ,$$

$$\frac{\Theta}{T}(s) = \frac{1}{F s \left(\dfrac{Js}{F} + 1\right)} , \text{ and}$$

$$\frac{\Theta}{V} = \frac{K}{F s \left(\dfrac{Js}{F} + 1\right) \left(\tau_c s + 1\right)} .$$

Since the friction in the load is likely to be low compared to the inertia, some form of compensation is usually necessary. The transfer function with rate feedback (Figure B-28) becomes:
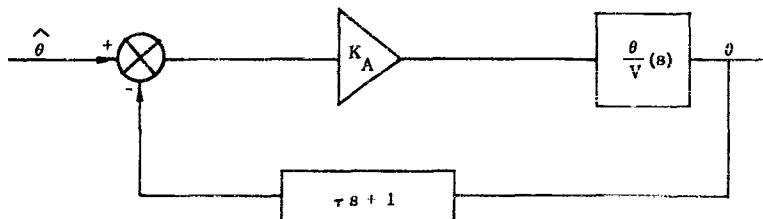

Figure B-28. Magnetic Clutch Servo in a Position Servo Loop

$$\frac{\theta}{\hat{\theta}}(s) = \frac{1}{\dfrac{J\,\tau_c}{K_A K}\,s^3 + \left(\dfrac{J}{KK_A} + \dfrac{\tau_c F}{K_A K}\right)s^2 + \left(\dfrac{F}{K_A K} + \tau\right)s + 1}$$

With the inductive lag, τ_c, negligible, the transfer function becomes:

$$\frac{\theta}{\hat{\theta}}(s) = \frac{1}{\dfrac{J}{K_A K}\,s^2 + \left(\dfrac{F}{KK_A} + \tau\right)s + 1}$$

A second class of clutch servo operates as on-off devices. Performance is quite different from that of an on-off controlled, direct coupled servo. Dynamics of the motor are not involved in the transfer function, as in the case of the continuous clutch control servo, if the motor has sufficient effective inertia (high speed motor driving through a high ratio reduction gear) and develops sufficient torque so that prime mover speed is essentially constant. This is usually the case.

The helical spring clutch is a good example of this type of control (Figure B-29). The spring is rigidly attached to the driven shaft and is wound with low clearance on the driving shaft. Undisturbed, the driving shaft spins freely inside the helical spring. When the free end of the spring is deflected in the direction of shaft rotation, friction between it and the driving shaft causes the spring to wrap suddenly and seize for its full length on the drive shaft. With a high speed drive, this wrapping action takes place very suddenly and almost instantly brings the load to drive shaft speed. Speed of response can be very fast — limited only by the ability of the system to withstand the shock loads imposed. A protective slip clutch can be provided by using the spring clutch principle in reverse. Shock loads can also be reduced by providing flexibility and damping in the driven shaft. This will not influence positioning system stability if position feedback is taken off ahead of the shaft flexibility.

This system cannot be easily represented in terms which are compatible with the usual mathematical description of a system except in a piece-meal fashion. Let it be assumed that the system's own internal stability and smoothness of operation has been achieved by appropriate control over dead space, system hysteresis, drive shaft flexibility, and clutch actuating time lags. These lags, though short compared to the response of the over-all system, might be critical in secondary effects such as clutch and brake chatter. The system then will have a response which is practically instantaneous to any command which is within the limits bounded by the maximum rate of the system (the prime mover speed) and the threshold imposed by the necessary dead space. That is, the system will not respond at all to inputs below its threshold; it will possess a transfer function of unity for inputs above the threshold level.
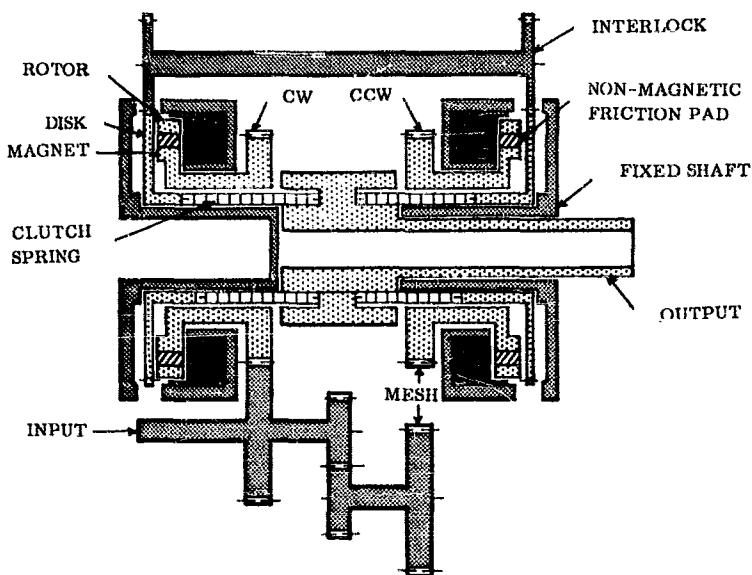
Figure B-29. Simplified Schematic of Spring Clutch Electro-Mechanical Servo

Figure B-30 shows two typical position servo control loops. In one case a brake ("back braking") is applied to the output shaft and load whenever the spring clutch servo is not activated. Thus for error signals within the threshold the output rates are zero and for error signals above the threshold the output rate is the constant servo rate, $\dot{\theta}_c$. When no back braking is applied the system response within the threshold is determined by the nature of the load, as the system "free wheels" (marked as "response undefined" in the figure).

B4.2 Electro-Hydraulic Positioning Servo. The electro-hydraulic engine servo systems for thrust-vector control are usually comprised of a high pressure hydraulic supply (pump), a servo amplifier, a hydraulic actuator, an electro-hydraulic servo valve, and a position transducer. A great many of the systems presently used also include an accumulator which acts as a hydraulic capacitor in the system.

The hydraulic power supplies currently used are of two types. One employs the variable displacement pump whose flow output is controlled by means of a servo sensing the high pressure side of the hydraulic system. A relief valve is also connected from the high pressure side to the low pressure side (hydraulic reservoir) of the system to minimize pressure transients above the operating pressures of the system. For normal operation the relief valve remains closed, opening only when pressures exceed a value overcoming the pre-load on the relief valve. The second type of system uses a fixed displacement pump with a relief valve to maintain the supply pressure within set limits as well as to meet the normal flow requirements. In this second system the relief valve is normally open such that supply pressure and valve opening, which is dependent on supply pressure, maintain flow through the relief valve equal to the flow output of the fixed displacement pump. When there is a flow demand of the system, this flow is accomplished by the relief valve closing down and the supply pressure therefore reducing in value. Excluding nonlinearities of the relief valve, the pressure excursions usually encountered from no flow-to full flow may be anywhere from five to 25 percent of supply pressure depending on the orifice geometry and spring-rate of the relief valve poppet assembly. Also, depending on the design of the relief valve, the reset pressure of the valve may be as low as 80 percent of the cracking pressure.
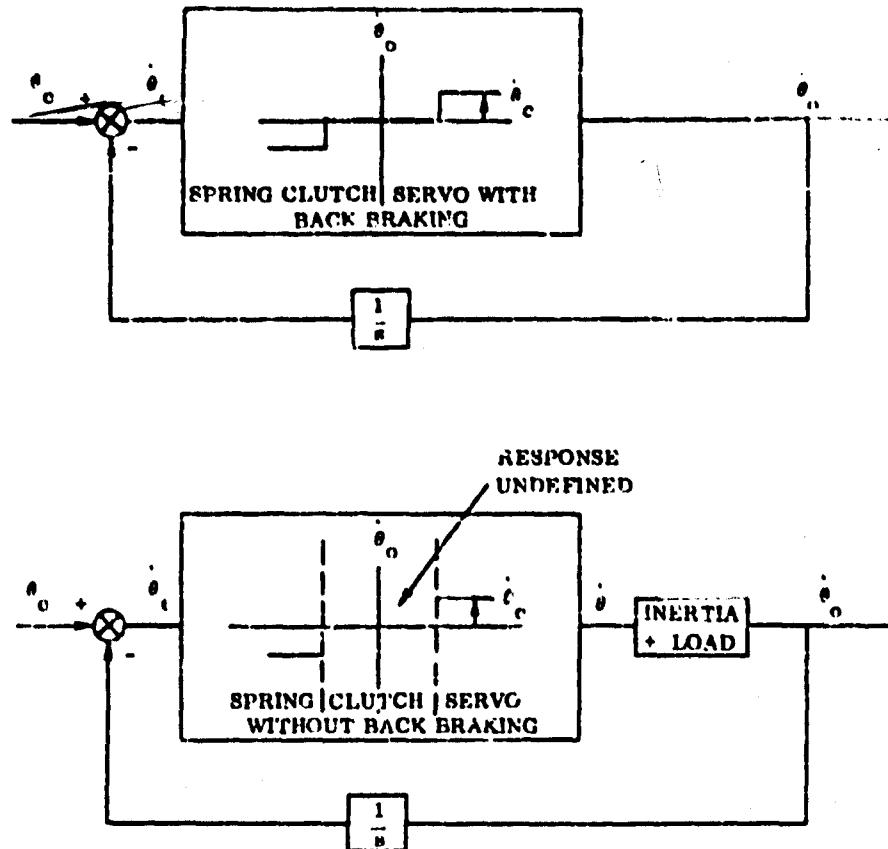
Figure B-30. Typical Response of Spring Clutch Servos Having a Constant Speed Input

In this analysis we shall discount the pump and relief valve dynamics since they both would exhibit a fairly flat frequency response with minimal phase shift within the band-width of the overall engine servo-loop. This being so, supply pressure will be assumed constant, being the value of zero flow demand. This assumption will not hold true for situations which require ignition of engines during flight (e.g., starting). During the thrust rise transients, the hydraulic supply will vary greatly with a marked effect upon the engine servo characteristics. The nature of the hydraulic pressure buildup accompanying engine ignition and of the varied hydraulic power demands is so dependent upon the peculiarities of a given installation as to defy general treatment. Fortunately, this period of off-nominal behavior is very brief and leads to no closed-loop elastic instability.

The electro-hydraulic servo gimballing system is probably one of the most highly (unintentionally) nonlinear in-stallations in a flight control system. A block diagram of a system used as a position servo is shown in Figure B-31. The servo amplifier can be assumed to be linear, as can the feedback transducer, since both are usually designed so that their saturation limits are above those of either the flow limit or actuator stops. The electro-hydraulic servo valve is usually of two basic designs, that of either pressure control or flow control. The flow control valve is the most widely used of the two in thrust vector control of swivelling rocket engines, and is the design that will be analyzed herein. Schematic diagrams of an hydraulic servo valve and a simulated rocket engine position servo are shown in Figures B-32 and B-33; they are taken from Backus (Reference B-7).
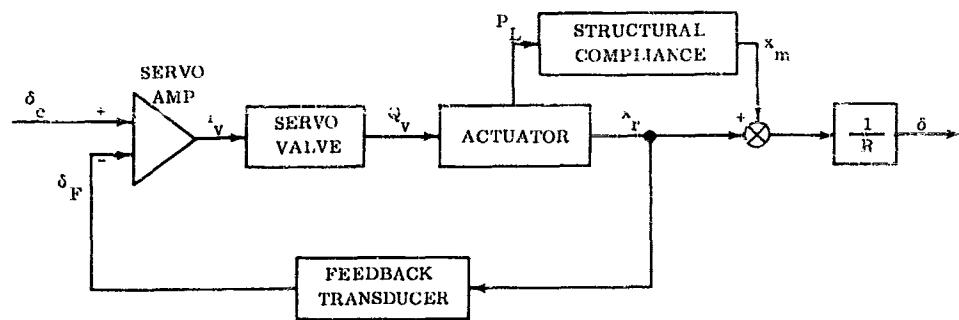
Figure B-31. Simplified Block Diagram of Positioning Servo
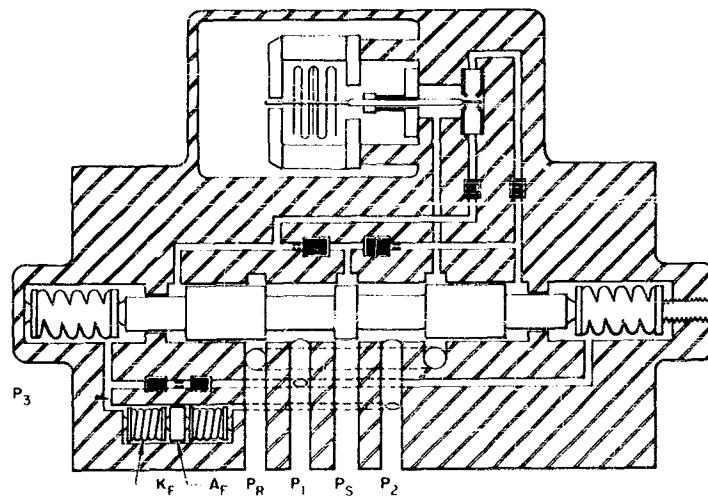
52-7474

Figure B-32. Electrohydraulic Dynamic-Pressure Feedback Servo Valve - Schematic Diagram
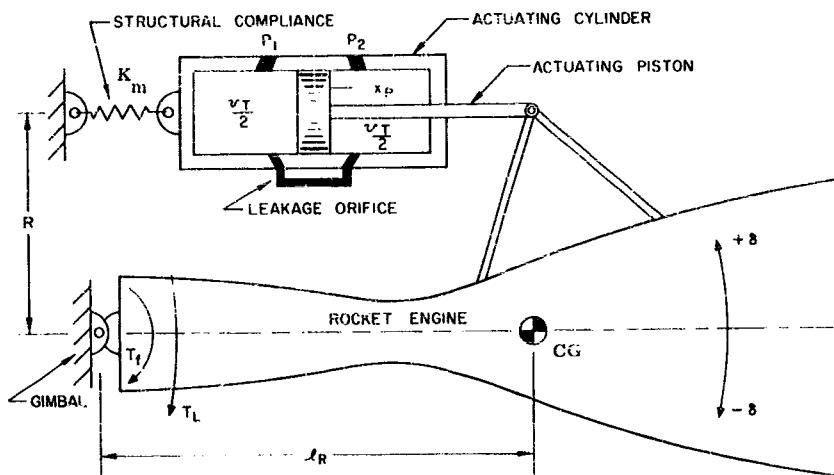
Figure B-33. Gimbaled Rocket Engine Position Servo - Schematic Diagram

B4.2.1 Servo Valve Flow. The basic equations for the system are developed by including the effects of a leakage orifice across the load piston, dynamic pressure feedback to the valve spindle, and load pressure feedback to the valve spindle. Later in the development, equations for each specialized case are obtained by elimination of the nonpertinent terms. The flow of hydraulic fluid, Q_v, from the servo valve into the left half of the actuating cylinder, shown in Figure B-33, is given by:

$$Q_v = \begin{cases} + X_s C_S \sqrt{|P_S - P_1|} & S\,gn\,(P_s - P_1)\,;\ X_s > 0 \\ \\ + X_s C_S \sqrt{|P_1 - P_R|} & S\,gn\,(P_1 - P_R)\,;\ X_s < 0 \end{cases} \tag{B-3}$$

where

$$X_s = \text{displacement of valve spool,}$$
$$\text{assumed positive to the right (ft)}$$

$$C_s = \text{discharge parameter } (\text{ft}^2/\text{sec } \sqrt{\text{lb/ft}^2}\,)$$

$$P_s = \text{supply pressure } (\text{lb/ft}^2)$$

$$P_1 = \text{pressure at point 1 } (\text{lb/ft}^2)$$

$$P_R = \text{reservoir (return) pressure } (\text{lb/ft}^2)$$

$$S\,gn\,Y \quad \text{sign of Y (N.D)}.$$

The discharge parameter, C_s, in general may vary with both the spool displacement and the actuator load pressure.

It may be assumed without serious error that the flow into the left half of the actuating cylinder is equal to the flow out of the right half of the cylinder. From this assumption it can be concluded that:

$$Q_v = \frac{+ X_s C_s}{\sqrt{2}} \quad \sqrt{\left| P_s - P_R + \overline{P_L \ sgn \ X_s} \right|} \quad sgn \left(P_s - P_R + P_L \ sgn \ X_s \right) \quad (B-4)$$

where

$$P_L = \text{load pressure} = P_1 - P_2 \quad (lb/ft^2).$$

The valve spool displacement X_s is assumed to be a linear combination of the valve current, i_v, and the dynamic pressure feedback, P_{13}.

$$C_s X_s = - K_V \ i_{veq} = - K_V \ (i_v + K_s \ P_{13}) \quad (B-5)$$

where

$$K_v = \text{servo valve discharge parameter} \left(\frac{ft^3/sec}{ma \ \sqrt{lb/ft^2}} \right)$$

$$K_s = \text{pressure feedback gain} \quad \left(ma / lb/ft^2 \right).$$

The true valve current, i_v, is directly proportional to the total input voltage to the servo amplifier which, in turn, is equal to the difference between the command signal and the feedback transducer signal.

$$i_v = K_a \left(\delta_c - \delta_F \right) = K_a \ \delta_e \quad (B-6)$$

where

$$K_a = \text{servo amplifier gain} \quad (ma/rad) \quad .$$

Since the feedback transducer is normally built integrally within the actuating cylinder, it measures the displacement of the piston relative to the cylinder and not the actual engine displacement (due to the compliance of the actuator mount and engine). Thus, the feedback transducer output is:

$$\delta_F = \delta - \frac{A}{K_m R} \ P_L \overset{*}{} \quad (B-7)$$

where

$$K_m = \text{actuator structural spring constant (lb/ft)}$$

$$A = \text{piston area (ft}^2)$$

$$R = \text{actuating moment arm (ft)}$$

$$\delta = \text{actual engine position (rad)}$$

$$\delta_F = \text{indicated engine position by feedback transducer (rad)}.$$

---

* If the mount compliance $1/K_m$ is included in the vehicle flexibility when the body bending modes are computed, this compliance correction is expressed as a function of the modal coordinates instead of the load pressure (see Section 4).

B4. 2. 2 <u>Flow Equation</u>. The total flow is the sum of the piston displacement flow, leakage flow and compressibility flow* such that:

$$Q_v = A \dot{x}_r + C_L \sqrt{|P_L|} \; \text{sgn} \; P_L + \frac{V_T}{4B} \dot{P}_L \tag{B-8}$$

where

x_r = relative displacement between piston

   and cylinder = $-R \, \delta_F$ (ft)

C_L = discharge parameter for leakage by-

   pass orifice (ft^3/sec $\sqrt{\text{lb/ft}^2}$)

V_T = total volume of oil in actuating

   cylinder (ft^3)

B = bulk modulus of hydraulic fluid (lb/ft^2).

The total valve flow is:**

$$Q_v = i_{veq} K_v \sqrt{|P_s - P_R + P_L \; \text{sgn} \; i_{veq}|} \; \text{sgn} \; (P_s - P_R + P_L \; \text{sgn} \; i_{veq}) \tag{B-9}$$

where

$$i_{veq} = K_a (\delta_c - \delta_F) + K_s P_{13}$$

$$= K_a (\delta_c - \delta) + \frac{K_a A}{K R_m} P_L + K_s P_{13} \tag{B-10}$$

B4. 2. 3 <u>Dynamic Pressure Feedback</u>. The dynamic pressure feedback, P_{13}, to the servo valve spool is determined by equating the flow through the dynamic pressure feedback (DPF) orifice to the flow due to the velocity of the washout piston, (see Figure B-32).

$$\frac{A_F^2}{K_F} \dot{P}_{32} = C_F \sqrt{|P_{32}|} \; \text{sgn} \; P_{13} \tag{B-11}$$

where

A_F = area of washout piston (ft^2)

K_F = spring constant for washout piston (lb/ft)

C_F = discharge parameter for DPF orifice (ft^3/sec $\sqrt{\text{lb/ft}^2}$)

$P_{32} = P_L - P_{13}$.

---

* If the hydraulic compressibility is accounted for in the body bending modes then in this equation it is omitted by setting $B \longrightarrow \infty$ (see Section 4).

** Equation B-9 represents a typical mathematical expression for flow into a valve as a function of valve current and supply, return, and load pressures. The valve gain, K_v, may itself be a function of these parameters. The relationships must be determined empirically or from the manufacturer's data.

B4.2.4 <u>Actuator Load Pressure</u>. The actuator load pressure is dependent on the dynamic equilibrium of the engine system. (cf. Equation 3-13).

$$T_{L \; servo} = -P_L \; AR = + I_R \; \ddot{\delta} + T_f + T_L \; .$$

(B-12)

I_R is the moment of inertia of the thrust chamber about the swivel point. T_f is the torque due to gimbal friction and can be expressed as a combination of both viscous (C_v) and coulomb (C_B) type friction:

$$T_f = C_v \; \dot{\delta} + C_B \; s \; gn \; \dot{\delta} \; .$$

(B-13)

The torque, T_L, consists of all inertial load torques due to the accelerations of the various body modes (rigid and elastic).

B4.2.5 <u>Describing Functions for Linearized Equations</u>. The equations above constitute a set of simultaneous nonlinear differential equations. Since the system is very nonlinear, it is difficult to solve analytically.

The nonlinearities occur in valve gain, K_v (itself a function of valve current and hydraulic pressures), in the half-power flow functions of hydraulic pressure and in the bearing friction. These nonlinearities must be removed before suitable transfer functions can be written. The method used in linearizing is based on finding equivalent linear terms.

The assumptions which justify a describing function analysis are well met in the elastic coupling stability study application; i. e., the signals of interest are almost purely harmonic, and frequencies other than the primary are greatly attenuated. These conclusions follow because the significant modal roots are very lightly damped, enjoy a suitable frequency separation, and the various modes are coupled but very weakly.

The nonlinear Equations (B-8), (B-9), (B-11) and (B-13) can be linearized as follows:

$$A \; \dot{x}_r = \bar{C}_L \cdot P_L + \frac{V_t}{4B} \; \dot{P}_L = -i_{veq} \; K_v \sqrt{P_s - P_R}$$

(B-14)

$$\frac{A_F^2}{K_F} \left(\dot{P}_L - \dot{P}_{13} \right) = \bar{C}_F \; P_{13}$$

(B-15)

$$T_f = \bar{C}_f \; \dot{\delta}$$

(B-16)

where

$\bar{C}_L$ = equivalent admittance for C_L

$\bar{C}_F$ = equivalent admittance for C_F

$\bar{C}_f$ = equivalent admittance for gimbal friction.

The equivalent admittance, $\bar{C}_L$, $\bar{C}_F$, and $\bar{C}_f$, are both amplitude- and frequency-dependent.

An additional linearization is implied in Equation B-14, whereby the valve gain, K_v, is taken to be a constant. This is an excellent approximation for many commercial flow-compensated values and is further justified (if K_v should vary somewhat) by assuming a mean value for a range of operating conditions. A still more elaborate valve flow model (cf. Equation B-3) could be used if desired.

B4.2.6 Equivalent Admittance. Assume the input signal to a stable nonlinear element to be as follows:

$$X_1 = A_1 \sin \omega t$$

The output signal from the nonlinear element would be periodic, and may be expressed as a Fourier series in the form:

$$X_2 = \sum_n a_n \sin n\omega t + \sum_n b_n \cos n\omega t.$$

The coefficients of the fundamental components are:

$$a_1 = \frac{1}{\pi} \int_{-\pi}^{\pi} X_2 \sin \omega t \quad d\omega t$$

$$b_1 = \frac{1}{\pi} \int_{-\pi}^{\pi} X_2 \cos \omega t \quad d\omega t.$$

By definition, the equivalent admittance (nonlinear gain) is

$$G_{NL} = \frac{X_2}{X_1} \quad \text{where, for the output function, all but the fundamental frequency components}$$

are omitted.

Hence,

$$G_{NL} = \frac{a_1 \sin \omega t + b_1 \cos \omega t}{A_1 \sin \omega t}.$$

$$= \frac{a_1}{A_1} + j \frac{b_1}{A_1}$$

The (j) is used to denote the quadrature component. Since the motion is quasi-harmonic, $j = s/\omega$ and one has:

$$G_{NL} = g_E + \frac{b_E}{\omega} s$$

where

$$g_E = \frac{a_1}{A_1} = \frac{1}{\pi A_1} \int_{-\pi}^{\pi} X_2 \sin \omega t \ d\omega t \qquad (B-17)$$

$$b_E = \frac{b_1}{A_1} = \frac{1}{\pi A_1} \int_{-\pi}^{\pi} X_2 \cos \omega t \ d\omega t . \qquad (B-18)$$

B4.2 7 Gimbal Friction. The nonlinear torque due to viscous and coulomb friction was given as

$$T_f = C_v \dot\delta + C_B \ \text{sgn} \dot\delta .$$

The object is to determine what coefficient $\bar{C}_f$ should be used at a particular amplitude and frequency if the above equation is linearized as follows:

$$T_f = \bar{C}_f \dot\delta \qquad ; \qquad \frac{T_f}{\dot\delta} = \bar{C}_f = G_{NL} .$$

Assuming $\dot{\delta} = \bar{\dot{\delta}} \sin \omega t$, then from Equation (B-17),

$$g_E = \frac{1}{\pi \bar{\dot{\delta}}} \int_{-\pi}^{\pi} \left(C_V \dot{\delta} + C_B \frac{\dot{\delta}}{|\dot{\delta}|} \right) \sin \omega t \; d\omega t$$

$$= \frac{2}{\pi} \int_{0}^{\pi} \left(C_V + \frac{C_B}{\bar{\dot{\delta}} \sin \omega t} \right) \sin^2 \omega t \; d\omega t$$

$$= C_V + \frac{4}{\pi} \frac{C_B}{\omega \bar{\dot{\delta}}} \; . \tag{B-19}$$

Similarly, one finds:

$$b_E = 0$$

Therefore:

$$G_{NL} = \frac{T}{\dot{\delta}} \equiv \bar{C}_f = g_E + \frac{b_E}{\omega} s$$

$$= C_V + \frac{4}{\pi} \frac{C_B}{\bar{\dot{\delta}}} \; .$$

B4.2.8 Orifice Flow.

The Equivalent admittance for flow through the leakage orifice is determined as:

$$\bar{C}_L = \frac{1.11 \; C_L}{\sqrt{\bar{P}_L}} \tag{B-20}$$

where

$\bar{P}_L$ = maximum sinusoidal amplitude of load pressure.

Similarly, the equivalent admittance for flow through the orifice of the dynamic pressure feedback network is:

$$\bar{C}_F = \frac{1.11 \; C_F}{\sqrt{\bar{P}_{13}}} \tag{B-21}$$

where $\bar{P}_{13}$ = maximum sinusoidal amplitude of dynamic pressure feedback

The linearized equations can now be maniuplated as linear differential equations. They are:

$$\tau_F \; \dot{P}_{13} + P_{13} = \tau_F \; \dot{P}_L \tag{B-22}$$

where

$$\tau_F = \frac{A_F^2}{\bar{C}_F K_F} \quad \text{effective time constant of DPF network (seconds)}.$$

$$P_L \; AR = - \bar{C}_f \; \dot{\delta} - T_L \; (t) - I_R \ddot{\delta} \tag{B-23}$$

$$A \dot{x}_r + \bar{C}_L \; P_L + \frac{V_T}{4B} \; \dot{P}_L = - i_{veq} \; K_i \; \sqrt{P_s - P_R}$$

$$i_{veq} = K_a (\delta_c - \delta) + \frac{K_a A}{K_m R} P_L + K_s P_{13} \; .$$

Also,

$$\delta_F = -\frac{x_r}{R} = \delta - \frac{A}{K_m R} P_L \; .$$

A general expression for δ (s) can now be obtained as a function of the commanded engine position, δ_c (s), and the load torque, T_L (s):

$$\delta(s) = \frac{K_c \omega_c^2 (\tau_F s + 1) \delta_c (s) - \frac{1}{I_R} (\tau_F s^2 + K_1 s + K_o) T_L (s)}{(\tau_F s^4 + N_3 s^3 + N_2 s^2 + N_1 s + K_c \omega_c^2)}$$

where

$$\omega_c^2 = \frac{(AR)^2}{I_R \left(\frac{V_T}{4B} + \frac{A^2}{K_M} \right)}$$

$$K_c = \frac{K_a K_v}{A R} \sqrt{P_s - P_R}$$

$$K_1 = \left\{ 1 + \frac{\tau_F \left[\bar{C}_L + K_c \left(\frac{A^2}{K_m} + \frac{A K_s R}{K_a} \right) \right]}{\left(\frac{V_T}{4B} + \frac{A^2}{K_m} \right)} \right\}$$

$$K_o = \frac{1}{\left(\frac{V_T}{4B} + \frac{A^2}{K_m} \right)} \left(\bar{C}_L + \frac{A^2}{K_m} K_c \right) \tag{B-24}$$

$$N_3 = \frac{1}{I_R} \tau_F \bar{C}_f + K_1$$

$$N_2 = \tau_F \omega_c^2 \left(1 + \frac{\bar{C}_f K_s K_c}{K_a AR} \right) + \frac{1}{I_R} \bar{C}_f + K_o \left(1 + \frac{1}{I_R} \tau_F \bar{C}_f \right)$$

$$N_1 = \frac{1}{I_R} \bar{C}_f K_o + \omega_c^2 (1 + \tau_F K_c) \; .$$

A block diagram of the complete electrohydraulic position servo is presented in Figure B-34. Note that in the development of the equations controlled damping by means of both dynamic pressure feedback in the servo valve and a leakage orifice in the piston have been assumed. Special cases of each will be considered now.
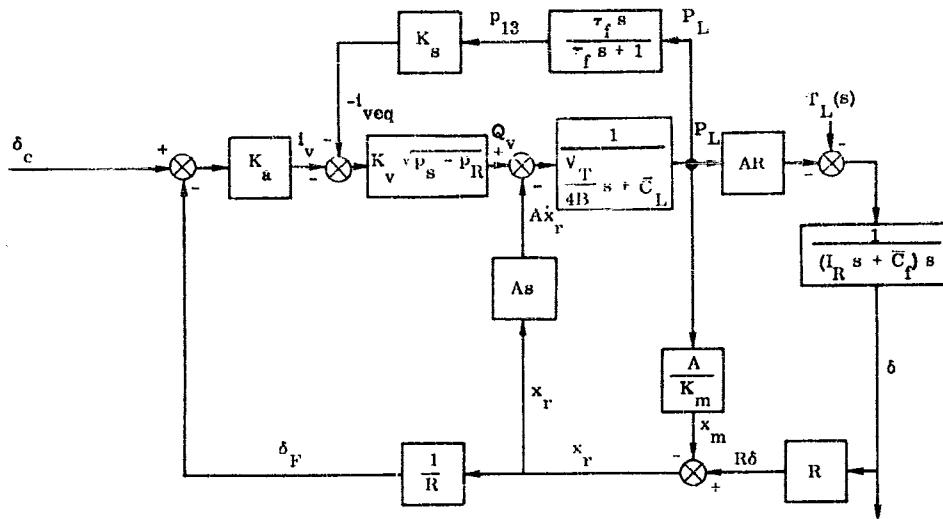
Figure B-34. Block Diagram of Electrohydraulic Swivelled Rocket Engine Position Servo

a. **Leakage Orifice Only.** The describing function for this case is obtained by completely blocking off the dynamic pressure feedback network. That is, let $\tau_F \to 0$ and the result is:

$$\frac{\delta(s)}{\delta_c(s)} = \frac{K_c \omega_c^2 - \frac{1}{I_R}(s + K_0)\frac{T_L(s)}{\delta_c(s)}}{s^3 + \zeta_{cn}\omega_{cn}s^2 + \omega_{cn}^2 s + K_c\omega_c^2} \qquad \text{(B-25)}$$

where K_0 is defined by Equation (B-24) and

$$2\zeta_{cn}\omega_{cn} = K_0 + \frac{1}{I_R}\bar{C}_f$$

$$\omega_{cn}^2 = \omega_c^2 + \frac{1}{I_R}\bar{C}_f K_0 .$$

A simplified first order expression for low frequency application can be obtained by letting $\omega_c \to \infty$:

$$\frac{\delta(s)}{\delta_c(s)} = \frac{K_c}{\left\{\left[1 + \frac{1}{(AR)^2}\bar{C}_f(\bar{C}_L + \frac{A^2}{K_m}K_c)\right]s + K_c\right\}} . \qquad \text{(B-26)}$$

b. **Dynamic Pressure Feedback Only.** The describing function for this case is obtained by blocking the leakage orifice flow, i. e., $\bar{C}_L = 0$.

The result is:

$$\frac{\delta(s)}{\delta_c(s)} = \frac{K_c \, \omega_c^2 \, (\tau_F s + 1) - \frac{1}{I_R} \, (\tau_F s^2 \, K_2 s + K_3) - \frac{T_L(s)}{\delta_c(s)}}{(\tau_F s^4 + N_4 s^3 + N_5 s^2 + N_6 s + K_c \, \omega_c^2)} \tag{B-27}$$

where

$$K_2 = \frac{\tau_F K_c}{\left(\frac{V_T}{4B} + \frac{A^2}{K_m}\right)} \left(\frac{A R^2 K_s}{K_2} + \frac{A^2}{K_m}\right)$$

$$K_3 = \frac{\frac{A^2}{K_m} K_c}{\left(\frac{V_T}{4B} + \frac{A^2}{K_m}\right)}$$

$$N_4 = \frac{1}{I_R} \, \tau_F \, \bar{C}_f + K_2$$

$$N_5 = \frac{1}{I_R} \, \bar{C}_f + \tau_F \, \omega_c^2 \, \left(1 + \frac{\bar{C}_f K_s K_c}{A K_a R}\right) + K_3 \, \left(1 + \tau_F \, \bar{C}_f \, \frac{1}{I_R}\right)$$

$$N_6 = \frac{1}{I_R} \, \bar{C}_f K_3 + \omega_c^2 \, (1 + \tau_F \, K_c)$$

A first order approximation valid at low frequencies is,

$$\frac{\delta(s)}{\delta_c(s)} = \frac{K_c}{\left(1 + \frac{1}{K_m \, R^2} \, \bar{C}_f K_c\right) s + K_c} \tag{B-28}$$

c. <u>Load Pressure Feedback Only</u>. The describing function for this case is obtained by allowing the spring constant, K_F, in the dynamic pressure feedback network to approach zero. The time constant, τ_F, becomes infinite and Equation B-27 reduces to

$$\frac{\delta(s)}{\delta_c(s)} = \frac{K_c \, \omega_c^2 - \frac{1}{I_R} \, (s + K_4) \frac{T_L(s)}{\delta_c(s)}}{(s^3 + N_7 s^2 + N_8 s + K_c \, \omega_c^2)} \tag{B-29}$$

where

$$K_4 = \frac{\left(\dfrac{A K_s K_c R}{K_a} + \dfrac{A^2}{K_m} K_c \right)}{\left(\dfrac{V_T}{4B} + \dfrac{A^2}{K_m} \right)}$$

$$N_7 = \frac{1}{I_R} \bar{C}_F + K_4$$

$$N_8 = \omega_c^2 \left[1 + \frac{\bar{C}_f K_c}{R^2} \left(\frac{K_s R}{K_a A} + \frac{1}{K_m} \right) \right]$$

The first order approximation is:

$$\frac{\delta(s)}{\delta_c(s)} = \frac{K_c}{\left[1 + \dfrac{1}{I_R} \bar{C}_f \left(\dfrac{K_s K_c R}{K_a A} + \dfrac{K_c}{K_m} \right) \right] s + K_c}$$

B4.2.9 <u>Numerical Determination of Equivalent Admittances.</u> The equivalent admittances determined in the foregoing sections require a knowledge of ω, δ, P_L, P_{13} and i_{veq} for their numerical calculation. First, the amplitude, $\bar{\delta}$, at the frequency, ω, of the output is specified. This admits calculation of $\bar{C}_f$ (Equation B-19). Next, it can be assumed that the output load torque disturbance, T_L, is either zero or is of minor importance in determining the amplitude of actuator load pressure. (This restriction can be eliminated in digital routines utilizing frequency response or root-locus techniques by employing an iterative procedure.)

Equation (B-23) is utilized to obtain:

hence,

$$\left. \begin{array}{l} P_L \ (j\omega) = \dfrac{1}{A R} \ (I_R \ \omega^2 - \bar{C}_f \ j\omega) \delta \ (j\omega) \\[20pt] \bar{P}_L = \dfrac{\bar{\delta}}{A R} \ \sqrt{(I_R \ \omega^2)^2 + (\bar{C}_f \ \omega)^2} \end{array} \right\} \qquad\qquad \text{(B-30)}$$

The amplitude of the dynamic pressure feedback, P_{13}, obtained from Equation (B-22) is

$$\tilde{P}_{13} = \frac{\tau_F \omega}{\sqrt{(\tau_F \omega)^2 + 1}} \ \bar{P}_L \qquad\qquad \text{(B-31)}$$

$$\sqrt{\bar{P}_L^2 + \frac{1}{(2 a_F^2 \omega^2)^2}} - \frac{1}{2 a_F^2 \omega^2}$$

where

$$a_F \cdot \frac{A_F^2}{1.11\, C_F K_F} \quad .$$

The amplitude of the equivalent valve current i_{veq} is obtained from Equations B-12 and B-14. Again, T_L is neglected with the result:

$$\bar{i}_{veq} = \frac{K_a}{\omega_c^2 K_c}\, \omega\bar{\delta} \sqrt{\left[\omega_c^2 - \omega^2 + \frac{1}{I_R}\, \frac{\bar{C}_f \bar{C}_L}{\left(\dfrac{V_T}{4B} + \dfrac{A^2}{K_m}\right)} \right]^2 + \omega^2 \left[\frac{1}{I_R}\, \bar{C}_f + \frac{\bar{C}_L}{\left(\dfrac{V_T}{4B} + \dfrac{A^2}{K_m}\right)} \right]^2} \quad .$$

Finally, note that in computing these describing function engine coefficients, the engine amplitude, $\bar{\delta}$, used must be the <u>total</u> control angle, δ', $- \sum_i q_i\,(\, \sigma_{xc}^{(i)} - \sigma_{xt}^{(i)}\,)$ since this is the angle through which the bearing friction couple acts. It is also the angle whose acceleration is related to load pressure, P_L, in computing the leakage and other valve flow linearizations. Thus, in any amplitude-dependent set of roots, the results obtained will be for various values of this total control angle. This property is actually fortuitous, since most actual flight and test data is seen as functions of this same total angle, measured at the engine gimbal.

B4.2.10 <u>Comparison of Results With Test and Analog Simulations</u>. The describing functions presented above can be appraised by comparing their frequency response functions to the corresponding "exact" functions obtained through the solution of the original system of nonlinear differential equations (Equations B-8, -9, -11, -12 and -13). The approximate frequency response can be determined from the calculated describing functions which were obtained by selecting a constant output amplitude (i.e., $\bar{\delta}$ constant), assuming the load torque, $T_L = 0$, and then solving for the complex ratio of output to input, $\left[\delta / \delta_c\right]$ $(j\omega)$.

Since the coefficients of the polynomial in "s" are, in general, both amplitude- and frequency-dependent, the function which results is a "constant output amplitude" frequency response function. This function, in contrast to linear transfer functions, is often heavily dependent upon the amplitude of the output (or input) signal.

The corresponding "exact" frequency responses were obtained by solving the appropriate nonlinear differential equation on an analog computer. Section 6, Paragraph 6.1.1 presents a comparison of data calculated by the two methods. These data represent "constant-output-amplitude" frequency characteristics of a rocket engine position servo system. The servo valve used was a Moog compensated flow control valve. Controlled damping was achieved by a leakage path through the actuator piston. The describing function employed was, therefore, that given by Equation B-25.

APPENDIX B4.3

PNEUMATIC POSITIONING SERVO

SYMBOLS USED IN APPENDIX B4.3

Symbol	Definition	Units
A_h	effective orifice area	$in.^2$
$Ai_{10}(Ai_{20})$	average effective inlet area from extend (retract) side of the cylinder	$in.^2$
$Ae_{10}(Ae_{20})$	average effective exhaust area from extend (retract) side of the cylinder	$in.^2$
$A_1(A_2)$	piston area on extend (retract) side	$in.^2$
C_{pe}	the negative of the partial of the nonlinear flow coefficient, N, with respect to pressure ratio	N.D.
$f(\dot{\delta})$	a generalized friction representation	in.-lbs/rad/sec
g	acceleration due to gravity	368 in./sec/sec
i	valve input	milliamp
I_R	load moment of inertia as seen by the actuator	$lb-in.-sec^2$
K_i	valve input gain	$in.^2/i$
K_M	mounting structure spring constant	lbs/in.
K_R	load spring constant	in.-lbs/radian
m	mass of gas	$lbs-sec^2/in.$
n	polytropic index	N.D.
P	absolute pressure	psi
$P_1(P_2)$	absolute pressure in extend (retract) side of actuator	psi
$P_{10}(P_{20})$	average pressure in extend (retract) side of actuator	psi
P_d	downstream pressure	psi
P_u	upstream pressure	psi
P_L	load pressure ($P_1 - P_2$)	psi
R	length of lever arm	in.
R_g	ideal gas constant (for air) (for most solid propellants)	640 in./°R 900 in./°R
r_{cp}	ratio of downstream to upstream pressure to just give sonic flow in an orifice, 0.53 for most gases	N.D.
s	the Laplace operator	sec^{-1}
T	absolute temperature	°R

SYMBOLS USED IN APPENDIX B4.3 (Continued)

Symbol	Definition	Units
T_T	total torque	in.-lbs
t	time	sec
V	volume	$in.^3$
$V_{10}(V_{20})$	average volume in extend (retract) side of cylinder	$in.^3$
W	weight rate of flow of gas	lbs/sec
$W_{1c}(W_{2c})$	weight rate of flow of gas into the extend (retract) side of the actuator	lbs/sec
$W_{1v}(W_{2v})$	weight rate of flow of gas from the extend (retract) side of the valve	lbs/sec
x	piston displacement	in.
$W_{01}W_{02})$	weight rate of flow of gas from supply part through exhaust part during steady state null position of valve and actuator	N.D.
γ	ratio of specific heats of power fluid	N.D.
β	the change in exhaust area per change in inlet area	N.D.

B4.3.1 Introduction. A type of positioning servo that is becoming more important in missile applications is the pneumatic positioning servo. The pneumatic positioning servo is most often referred to as the "hot gas servo", since a hot gas is often used as the working fluid. The following treatment is not restricted by the temperature of the gas and therefore applies to cold as well as hot gas systems.

Pneumatic systems most often derive their high pressure working fluid from either a high pressure storage bottle (cold gas) or from a gas generator (hot gas). Figures B-35, -36 and -37 picture the three main configurations of pneumatic systems using hot and cold gas. In all three designs it is common practice to exhaust the working fluid overboard, since it is less costly to store a large quantity of high pressure working fluid in the form of solid, liquid, or gas and exhaust it overboard than to include the plumbing and pumps necessary to repressurize and reuse the fluid.

In all of these systems the gas supply pressure down-stream of the regulator may be considered constant. Also, the control valves have resonances which are well above the overall system band width, so one may ignore the higher order valve dynamics.
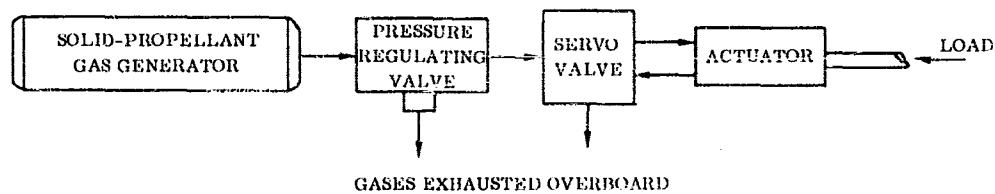
Figure B-35. Solid Propellant Hot Gas System
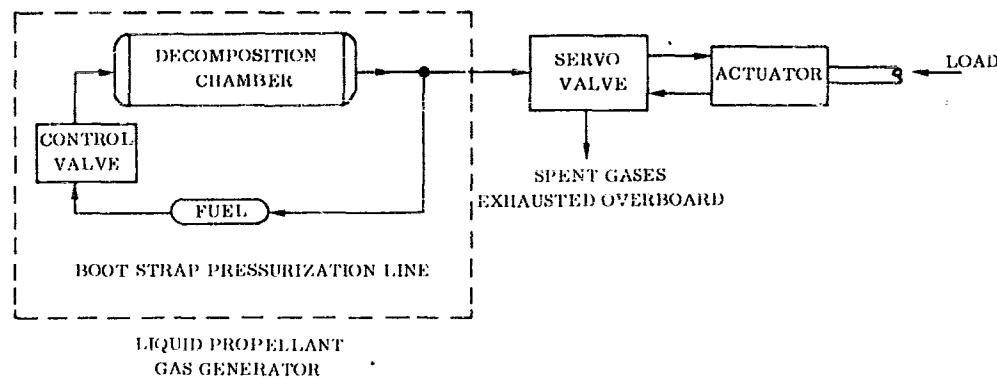
Figure B-36. Liquid Propellant Hot Gas System
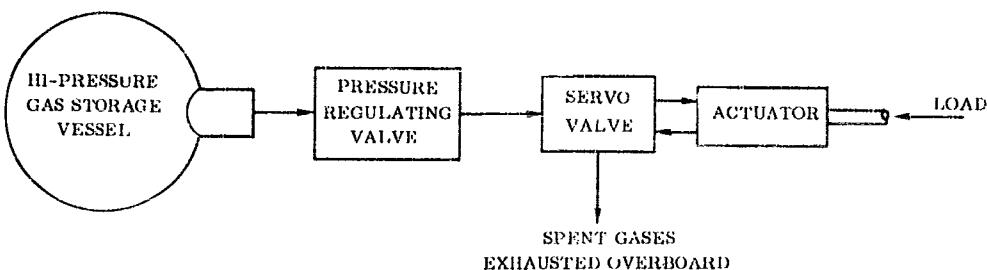
Figure B-37. Stored Gas System

B4.3.2 <u>Analysis.</u> In an analytic treatment of a pneumatic servo the following basic relationships are required:

a. valve current to valve (spool) motion

b. orifice equation - gas flow versus orifice area and pressures

c. piston and cylinder relationship between volume changes, flow and pressure

d. load pressure equations relating piston pressures to load (piston) response.

Herein the first relation is assumed to be a simple proportionality, by neglect of valve dynamics. The second and third relationships are, by the nature of gas laws, highly nonlinear. A small perturbation approach is taken to provide a reasonable linearization. The final relationship follows as practically a definition. Combined, these relationships lead to the desired δ/i_v transfer function of the servo actuator.

B4.3.3 <u>Equations for a Pneumatic Orifice.</u> The weight rate of flow of a gas through an orifice is described by

$$W = N \frac{A_h P_u}{\sqrt{T}} \tag{B-32}$$

Where $N = N(P_d/P_u)$ is the nonlinear flow coefficient for the compressible fluid. This nonlinear coefficient is commonly given for subsonic flow as:

$$\left(\frac{P_d}{P_u} > r_{cp} \right)$$

$$N\left(\frac{P_d}{P_u}\right) = \left(\frac{P_u}{P_d}\right)^{1/\gamma} \sqrt{\frac{2g}{Rg} \cdot \frac{\gamma}{\gamma-1} \left[1 - \left(\frac{P_u}{P_d}\right)^{\frac{\gamma-1}{\gamma}} \right]} \tag{B-33}$$

For supersonic flow the coefficient is:

$$\left(\frac{P_d}{P_u} \leq r_{cp} \right)$$

$$N\left(\frac{P_d}{P_u}\right) \quad r_{cp} \quad .$$

However, a simpler expression for the subsonic flow which gives exactly the same results is:

$$N\left(\frac{P_d}{P_u}\right) = r_{cp}\sqrt{1-\left(\frac{1-r_{cp}\frac{P_u}{P_d}}{1-\frac{P_d}{P_u}}\right)^2} \tag{B-34}$$

Equation (B-32) is not useful for linear analysis. However, the expression can be linearized if it is assumed that the variables are limited to small excursions about their average values:

$$dW = \frac{1}{\sqrt{T}}\left(A_h P_u dN + A_h Nd P_u + P_u Nd A_h\right) \quad . \tag{B-35}$$

The "dN" as it appears in Equation (B-35) is not a useful variable and must be found in other terms:

$$dN\left(\frac{P_d}{P_u}\right) = \frac{\partial N\left(\frac{P_d}{P_u}\right)}{\partial\left(\frac{P_d}{P_u}\right)} \times d\left(\frac{P_d}{P_u}\right)$$

$$= \frac{\partial N\left(\frac{P_d}{P_u}\right)}{\partial\left(\frac{P_d}{P_u}\right)} \times \frac{P_u dP_d - P_d dP_u}{P_u^2} \quad . \tag{B-36}$$

When the partial of the nonlinear flow coefficient with respect to pressure ratio is defined as $-C_{pc}$, Equations (B-35) and (B-36) combine into the following:

$$dW = \frac{1}{\sqrt{T}}\left[-A_h C_{pc} dP_d + \frac{A_h C_{pc} P_d}{P_u} dP_u + A_h Nd P_u + P_u Nd A_h\right]$$

$$dW = \frac{A_h}{\sqrt{T}}\left[\left(\frac{C_{pc} P_d}{P_u} + N\right)dP_u - C_{pc} dP_d + \frac{P_u N}{A_h} dA_h\right] \tag{B-37}$$

Equation (B-37) describes the change in the weight rate of gas flow through a sharp-edged orifice as a function of area and pressure variations (perturbation equation).

B4.3.4 Equation of a Piston and Cylinder. The equation for the state of a volume of gas is:

$$PV = m_g R_g T \quad . \tag{B-38}$$

Differentiation of Equation (B-38) and rearrangement (with $W \equiv \frac{dm_g}{dt}$) yields:

$$\frac{dP}{Pdt} + \frac{dV}{Vdt} = \frac{R_g T}{PV} W + \frac{dT}{Tdt} \quad . \tag{B-39}$$

If the thermodynamic process of the control volume of the cylinder is assumed to be polytropic, the relationship between temperature and pressure is:

$$\frac{P^{\left(\frac{n-1}{n}\right)}}{T} = \text{constant},$$ (B-40)

where n can range from 1.0 for an isothermal process to γ for an adiabatic process. Differentiation of the above yields:

$$\frac{P}{T} \frac{dT}{dt} = \left(1 - \frac{1}{n}\right) \frac{dP}{dt}$$ (B-41)

Combining Equations (B-39) and (B-41) one obtains the relationship for a variable volume:

$$W = \frac{P}{R_g T} \frac{dV}{dt} + \frac{V}{nR_g T} \frac{dP}{dt}$$ (B-42)

The small perturbation approach is taken again. The coefficients of the differential quantities are assumed to be average values over one cycle. The average values are denoted by subscript zeros. The linear approximation to Equation (B-42) becomes:

$$W = \frac{P_o}{R_g T} \frac{dV}{dt} + \frac{V_o}{nR_g T} \frac{dP}{dt}$$ (B-43)

If the variable volume is that of a cylinder and piston, Equation (B-43) becomes:

$$W = \frac{AP_o}{R_g T} \frac{dx}{dt} + \frac{V_o}{nR_g T} \frac{dP}{dt} \ .$$

The equations which describe both sides of the piston-cylinder combination then are written as:

$$W_{1c} = \frac{A_1 P_{10}}{R_g T} \frac{dx}{dt} + \frac{V_{10}}{nR_g T} \frac{dP_1}{dt}$$ (B-44)

$$W_{2c} = \frac{A_2 P_{20}}{R_g T} \frac{dx}{dt} + \frac{V_{20}}{nR_g T} \frac{dP_2}{dt} \ .$$

B4.3.5 Combined Orifice, Valve and Piston Equations. It will be assumed that the system has an open-centered valve (Figure B-38) such that there is always a flow of gas through the valve*. The open-centered valve is the most popular for vehicles with short mission times and is also relatively easy to analyze. A closed-center valve will have the same type of linearized transfer function; the major dynamic difference appears as a lower damping.

---

* The weight rates of flow through the two sides of the system during a steady null position of the valve are:

$$W_{01} = \frac{\gamma_{cp} A_{c10} P_{10}}{\sqrt{T}} = \frac{\gamma_{cp} A_{i10} P_s}{\sqrt{T}} \qquad W_{02} = \frac{\gamma_{cp} A_{c20} P_{20}}{\sqrt{T}} = \frac{\gamma_{cp} A_{i20} P_s}{\sqrt{T}}$$
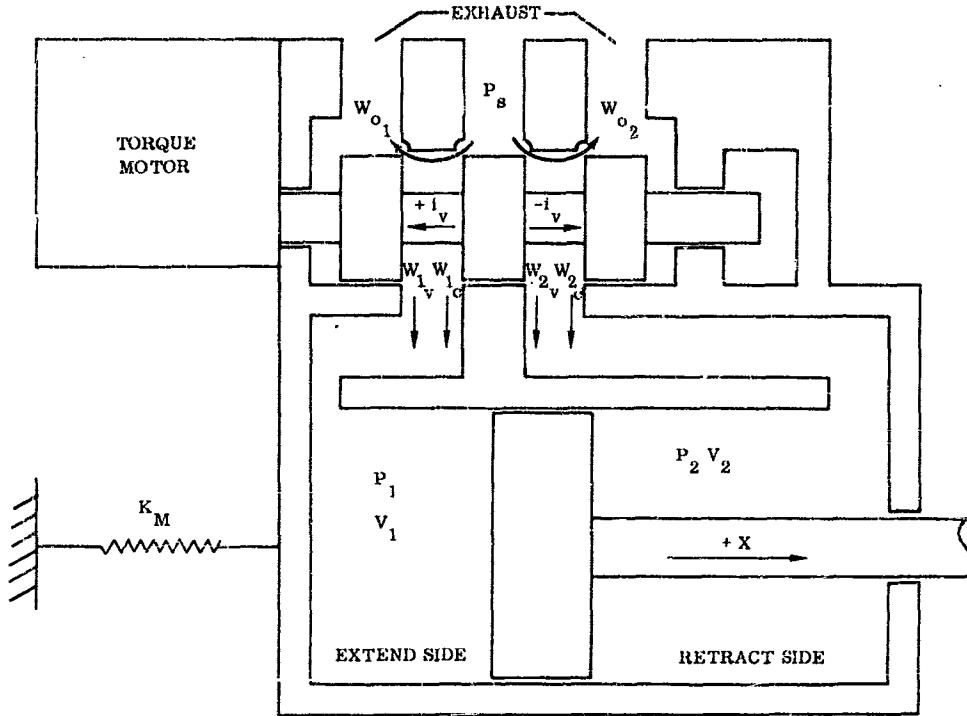
Figure B-38. Pneumatic Positioning Servo-With Open Center Control Valve

If the valve actuating dynamics are negligible, and both inlet and exhaust orifices are choked, the effective flows from the valve can be found from Equation (B-37) to be as follows:

$$W_{1v} = \frac{r_{cp} K_i}{\sqrt{T}} \left[P_s + \beta P_{10} \right] i \quad - \quad \frac{Ae_{10} r_{cp}}{\sqrt{T}} P_1$$

$$W_{2v} = \frac{- r_{cp} K_i}{\sqrt{T}} \left[P_s + \beta P_{20} \right] i \quad - \quad \frac{Ae_{20} r_{cp}}{\sqrt{T}} P_2 \quad .$$

(B-45)

Equations (B-44) and (B-45), when combined, describe the response from valve input to actuator behavior.

$$\frac{r_{cp} K_i}{\sqrt{T}} \left[P_s + \beta P_{10} \right] i = \frac{A_1 P_{10}}{R_g T} \frac{dx}{dt} + \frac{Ae_{10} r_{cp}}{\sqrt{T}} P_1 + \frac{V_{10}}{nR_g T} \frac{dP_1}{dt}$$

(B-46)

$$\frac{- r_{cp} K_i}{\sqrt{T}} \left[P_s + \beta P_{20} \right] i = \frac{- A_2 P_{20}}{R_g T} \frac{dx}{dt} + \frac{Ae_{20} r_{cp}}{\sqrt{T}} P_2 + \frac{V_{20}}{n R_g T} \frac{dP_2}{dt} \quad .$$

It should be noted that numerous assumptions have been made in obtaining Equations (B-46). The temperature of the gas in the actuator may not be the same as the temperature of the valve, but this can be handled by modifying the value of average exhaust area or valve gain appropriately. Leakage across the piston has been neglected, but this is usually minor. Piston leakage or other considerations, such as stabilizing volumes, may be included in the equations by application of Equations (B-37) and (B-43).

The introduction of the following additional assumptions results in a considerably simplified final expression.

$$P_{10} = P_{20}$$

$$A_1 = A_2$$

$$Ae_{10} = Ae_{20}$$

$$V_{10} = V_{20} \quad .$$

Combining Equations (B-46) and incorporating the above results in a single expression for the valve and actuator:

$$\frac{2r_{cp}K_i}{\sqrt{T}}\left[P_s + \beta P_{10}\right] = \frac{2A_1 P_{10}}{R_g T}\frac{dx}{dt} + \frac{Ae_{10}r_{cp}}{\sqrt{T}}P_L + \frac{V_{10}}{nR_g T}\frac{dP_L}{dt} .$$

(B-47)

B4.3.6 Actuator Load Pressure. The total differential force across the actuator must equal the total torque divided by the actuator lever arm.

$$A_1 P_1 - A_2 P_2 = \frac{T_T}{R}$$

(B-48)

Pressure and torque variations about average valves are obtained by taking the total differential of Equation (B-48):

$$A_1 dP_1 - A_2 dP_2 = \frac{\partial T_T}{\partial \delta}\frac{d\delta}{R} + \frac{\partial T_T}{\partial \dot{\delta}}\frac{d\dot{\delta}}{R} + \frac{\partial T_T}{\partial \ddot{\delta}}\frac{d\ddot{\delta}}{R}$$

(B-49)

Equation (B-49) may contain other terms such as the change in torque with respect to normal acceleration, which may or may not be important. It is reasonable to assume that the average velocity and acceleration are zero; so, if the average position is taken as the zero point for δ, the increments of the variables become the variables themselves. The rotational spring constant is, by definition, the partial of torque with respect to angular displacement. The partial of torque with respect to rate will usually consist of a friction term which is a function of rate. As a rule, any viscous damping in the load is so small that it may be neglected. The partial of torque with respect to angular acceleration is the moment of inertia of the load. When these substitutions are made, Equation (B-49) becomes:

$$A_1 P_1 - A_2 P_2 = \frac{K_R}{R}\delta + \frac{f(\dot{\delta})}{R}\dot{\delta} + \frac{I_R}{R}\ddot{\delta} .$$

(B-50)

The friction term, $f(\dot{\delta})$, cannot be linearized for general inputs: it can be studied on a computer or linearized for sinusoidal inputs by means of describing functions. The previous assumptions of a balanced actuator and the linearizing condition of operation about steady state operating points simplifies Equation (B-50) to:

$$A_1 P_L = \frac{K_R}{R}\delta + \frac{f(\dot{\delta})}{R}\dot{\delta} + \frac{I_R}{R}\ddot{\delta} .$$

(B-51)

If the actuator mounting can be described as a simple spring, the load displacement differs from the piston displacement as follows (see Figure B-34):

$$X = R\delta + \frac{A_1 P_L}{K_M}$$ (B-52)

Combining (B-51) and (B-52) gives:

$$K_M \dot{X} = \left[K_M \ddot{R} + \frac{K_R}{R} \right] \dot{\delta} + \frac{f(\dot{\delta})}{R} \dot{\delta} + \frac{1_R}{R} \ddot{\delta}$$ (B-53)

B4.3.7 Combined Transfer Function. The transfer function from valve input to either actuator position or load position can now be obtained by combining Equations (B-47), (B-51) and (B-53). However, the resulting expression is somewhat complicated. A better feel for the various terms can be obtained by investigating the following special case:

$$f(\dot{\delta}) = K_R = 0$$

$$K_M = \infty$$

The resulting expression gives the transfer function from valve input to load displacement of the open-loop servo:

$$\frac{\delta(s)}{i(s)} = \frac{\dfrac{R_g r_{cp} K_i \sqrt{T}\left[P_s + \beta P_{10}\right]}{A_1 P_{10} R}}{s\left[\dfrac{V_{10} 1_R}{2nA_1^2 R^2 P_{10}} s^2 + \dfrac{Ae_{10} r_{cp} 1_R R_g \sqrt{T}}{2 P_{10} R^2 A_1^2} s + 1 \right]}$$ (B-54)

Equation (B-54) indicates a number of basic facts concerning gas servo behavior:

a. The open loop gain is proportional to the square root of the absolute temperature.

b. The open loop natural frequency is not a function of temperature.

c. Some damping is available as a result of the average exhaust area, but this damping is temperature-dependent.

B4.3.8 Final Remarks. The most common form of gas servo has fixed inlet orifices and variable exhaust orifices. Equation (B-54) is not directly applicable to such a valving configuration without a few minor changes. The modification consists of redefining βK_i in terms of the exhaust orifice only and allowing β to approach infinity while K_i approaches zero. However, the value of βK_i is held constant. The net result is that the supply pressure drops out of the expression for gain.

For most applications in a closed-loop position servo, the open loop natural frequency is not sufficiently high with respect to control frequencies that it can be ignored. Some form of the derivative of position is required in the feedback for damping. The resulting closed loop transfer function will be at least third order and probably of even higher order; the principal behavior can be adequately described with a second order equation. In the absence of more detailed information, a second order system with a natural frequency equal to the open loop natural frequency and a damping factor of 0.3 to 0.5 may be used.

B5 AUTOPILOT ELEMENTS

The preceding material in Appendix B discussed certain of the subsystem transfer functions which would be of importance in the analysis of the autopilot and control system for a flexible booster. To be complete this appendix would have to include the peculiar characteristics of such items as the following: amplifiers, power supplies, modulators, demodulators, filter networks, integrators, and various types of feedback transducers which could include linear and angular position, linear rate and tachometer, etc. Of interest might be such nonlinear characteristics as thresholds, limits, nonlinear gain calibration, noise generation (microphonic noise and/or harmonics), etc.

This detailed information will not be presented, for the following reasons. First, these characteristics are usually such that they do not greatly affect the adequacy of most linear analyses. Their effects are usually of a second order nature; therefore, they do not constitute the more important stability effects which are of prime consideration in determining gain and configuration. Second, they are highly specialized topics about which much literature is available, both as to the characteristics themselves and to their treatment analytically. (See References B-8 and B-9 for a more detailed discussion.)

B6 REFERENCES FOR APPENDIX B.

B-1.   Emerson, F. M., "Study of Systems for True Angle-of-Attack Measurement," WADC Technical Report 54-267, May 1955.

B-2.   Mitchell, Jesse L., and Peck, R. F., "An NACA Vane-Type Angle-of-Attack Indicator for Use at Subsonic and Supersonic Speeds," NACA Technical Note 3441, May 1955.

B-3.   Gosgriff, R. L., Nonlinear Control Systems, McGraw-Hill Book Company, Inc., 1958.

B-4.   Hunter, P. A. "An Investigation of the Performance of Various Reaction Control Devices," NASA Memo 2-11-59L, March 1959.

B-5.   Schaefer, R. L., Drewry, D. G., and Wilson, K. C., "Advanced Methods for Trajectory Control of Solid Propellant Rockets," (Unclassified title), Fifth AFBMD-STL Symposium of Ballistic Missile and Space Technology, August 1960. (Confidential Report)

B-6.   Escher, W. J. D., "An Alternate to the Gimbaled Thrust Chamber," Missile Design and Development, April 1960.

B-7.   Backus, F. I., "Describing Functions for Nonlinear Electrohydraulic Gimbaled Rocket-Engine Position Servos, With Application to Closed-Loop Control Systems," Convair-Astronautics Report AE60-0287, 10 June 1960.

B-8.   Gille. J. C. et al., Feedback Control Systems, McGraw-Hill Book Company, Inc., 1959, Chapter 33.

B-9.   Truxal, J. G., Control Engineers' Handbook, McGraw-Hill Book Company, Inc., 1958, Sections 6 through 11 and 17.

APPENDIX C

MISCELLANEOUS TOPICS

C1 THE STABILITY AND CONTROL EFFECTS OF A SPINNING PAYLOAD

Spin stabilization is sometimes used for attitude control of space vehicles. This method of control will hold the vehicle spin axis alignment in inertial space and also minimize the effect of such factors as engine-thrust-vector misalignment, and center-of-gravity offset. The spin-stabilized vehicles by themselves do not fall within the scope of this report because they do not contain active control systems.

In a majority of boost vehicles, the upper stages which are to be spin-stabilized are spun by gas jets just prior to separation of those stages. No lower stage control problem is created thereby. However, for some configurations, spin is applied to the upper stage(s) of multistage booster vehicles before launch; this method of spinning a payload will affect the boost vehicle's stabilization and control system. It is this effect which will be discussed in this section.

The effects of the spinning payload on the boost vehicle are divided into two categories which are: 1) gyroscopic forces and 2) mass unbalance forces.

C1.1 **Gyroscopic Forces.** The gyroscopic forces will be analyzed first. Consider the mode of motion of Figure C-1. The normal modal equation of motion is:

$$\ddot{q}_i + \omega_i^2 \, q_i = \frac{Q_i}{\mathcal{M}_i} \tag{C-1}$$
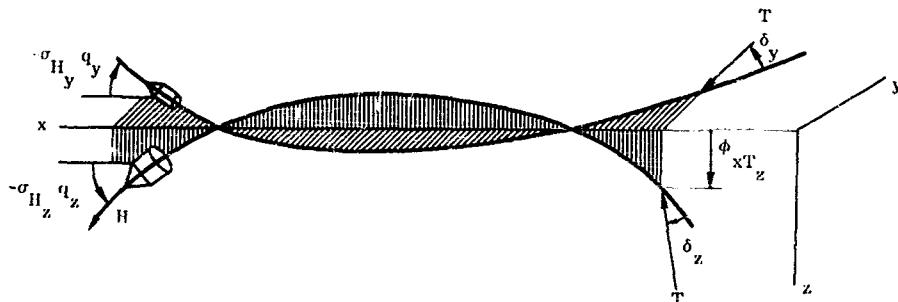
Figure C-1. Schematic of Elastic Booster Vehicle with Spinning Payload

The mode shape is calculated with the "spinning" payload considered as an inert part of the mode; i.e., the mass and the inertial and elastic properties are used for the calculation. This method of treatment assumes that classical normal modes can be applied with sufficient accuracy to yield a usable solution. This assumption will be valid only for small gyroscopic coupling, i.e., a small payload spinning at a relatively slow rate.

For this analysis, the payload is treated as if it were rotating about the vehicle longitudinal axis with an angular momentum, H. The mode generalized forces due to the gyroscopic moments then become:

$$Q^H_Y = -\sigma_{H_Y}^{(i)} \, \omega_{H_Y} \, H \tag{C-2}$$

$$Q^H_Z = + \sigma_{H_Z}^{(i)} \, \omega_{H_Z} \, H.$$

The quantity ω_H, the precession velocity, is:

$$\omega_{H_Y} = -\sigma_{H_Z}^{(i)} \dot{q}_Z \tag{C-3}$$

$$\omega_{H_Z} = -\sigma_{H_Y}^{(i)} \dot{q}_Y .$$

In the following discussion the index "i" is dropped, being understood. The pitch plane (x - z plane) equation then becomes:

$$\ddot{q}_Z + \omega^2 q_Z = \frac{Q_Z}{\mathcal{M}} - \frac{\sigma_H^2 H}{\mathcal{M}} \dot{q}_Y . \tag{C-4}$$

The term σ_H^2, implies a symmetrical vehicle with pitch plane modes identical to those of the yaw plane. If this is not the case then the term, σ_H^2, becomes $\sigma_{H_Z} \sigma_{H_Y}$.

Similarly we can write for the yaw plane:

$$\ddot{q}_Y + \omega^2 q_Y = \frac{Q_Y}{\mathcal{M}} + \frac{\sigma_H^2 H}{\mathcal{M}} \dot{q}_Z . \tag{C-5}$$

The gyroscopic forces have the effect of coupling the pitch and yaw planes. Before examining the effect of this coupling on closed-loop stability through the autopilot, a basic property of the system may be demonstrated from the free-vibration forms of Equations C-4 and C-5. Setting $Q_Y = Q_Z = 0$ one obtains:

$$\left[s^4 + \left(2\omega^2 + \frac{\overline{Q}^2}{\mathcal{M}^2} \right) s^2 + \omega^4 \right] q_Y = 0 \tag{C-6}$$

where

ω = natural frequency original uncoupled elastic modes

$\overline{Q}$ = generalized gyroscopic forcing function $\sigma_H^2 H = \sigma_H^2 I_H \beta_H$ *

β_H = spin velocity.

An identical result is obtained for the generalized coordinate q_Z.

Equation C-6 yields two natural frequencies: one slightly above and one slightly below the original ω (for typical $\overline{Q}/\mathcal{M}$ values). Clearly then, the gyroscopic effect of the spinning payload has been to couple two "artificially uncoupled" modes to produce two new orthogonal modes whose natural frequencies are the solutions of Equation C-6, and whose coupled equations of motion are Equations C-4 and C-5.

To obtain a qualitative feel for the stability effects of the gyroscopic coupling, a simple control system will be added to the equations. The generalized forces will be set equal to the control forces (see Figure C-2):

$$Q_Z = -T\delta_Z \quad \phi_{XT_Z} \tag{C-7}$$

$$Q_Y = -T\delta_Y \quad \phi_{XT_Y} .$$

---

* Note that the units of $\overline{Q}$ are lb/ft/sec.
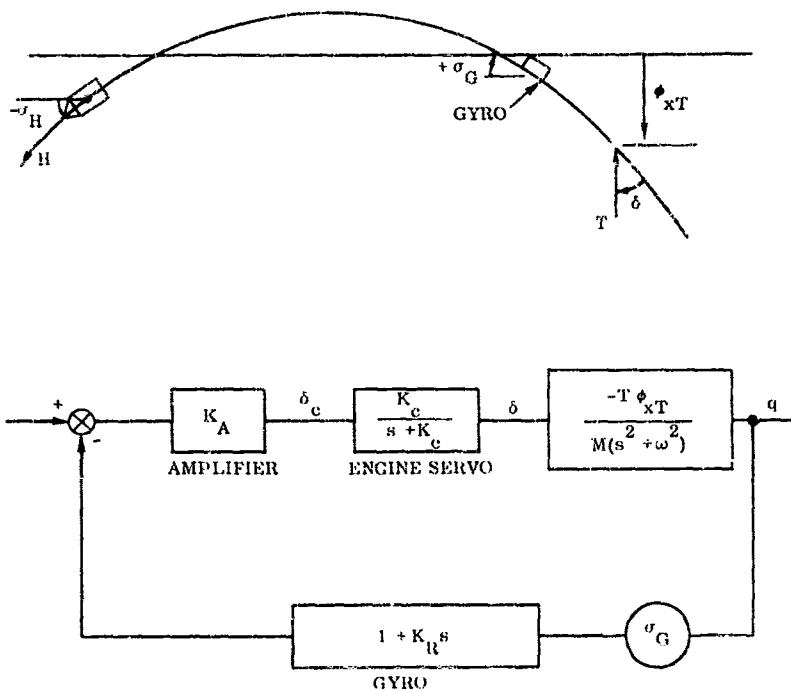
Figure C-2. Bending Mode with Simple Control System Added

The transfer function between modal motion and control engine deflection will be expressed as:

$$\frac{\delta_Z}{q_Z} = \frac{\delta_Y}{q_Y} = K_A G (s) \ *.$$

(C-8)

In a specific case, referring to Figure C-2, G(s) would be given by:

$$G (s) = \frac{\sigma_G K_R K_C \left(s + \frac{1}{K_R} \right)}{s + K_c}$$

Equations C-4 and C-5 may now be written as:

$$\left.
\begin{aligned}
(s^2 + \omega^2) \, q_Y &= - \frac{T K_A G \ \phi_{XT_Y}}{M} q_Y + \frac{\overline{Q}}{M} s \, q_Z \\
(s^2 + \omega^2) \, q_Z &= - \frac{T K_A G \ \phi_{XT_Z}}{M} q_Z - \frac{\overline{Q}}{M} s \, q_Y
\end{aligned}
\right\}$$

---

* A symmetric control is assumed.

or,

$$\left[s^2 + \omega^2 + \frac{TK_A G \phi_{XT}}{\mathcal{M}} \right] q_Y - \frac{\overline{Q}}{\mathcal{M}} s\, q_Z = 0$$

$$\frac{\overline{Q}}{\mathcal{M}} s\, q_Y + \left[s^2 + \omega^2 + \frac{TK_A G \phi_{XT}}{\mathcal{M}} \right] q_Z = 0.$$

(C-9)

The roots of the stability equation (determinant of the coefficients set equal to zero) establish the system's closed-loop stability. As may be seen, these roots are now functions of $\overline{Q}$ (i.e., of $\sigma_H^2 H$) as well as the amplifier gain, K_A. A locus of system roots as a function of $\overline{Q}$ is of great interest and can be readily contructed, as will now be described.

If the autopilot root locus is constructed first without a spinning payload, the operating point roots (roots for nominal amplifier gain K_A) so obtained are the roots of the numerator of the coefficients in square brackets in Equation C-9. The roots of the denominator of this same square bracket coefficient are the roots of all lag terms in the autopilot forward path. Symbolically,

$$\left[s^2 + \omega^2 + \frac{TK_A G \phi_{XT}}{\mathcal{M}} \right] \quad \cdots \quad \left[\frac{(s + r_1)(s + r_2)\ldots(s + r_i)}{(s + P_1)(s + P_2)\ldots(s + P_j)} \right]$$

(C-10)

where the r_i's are closed loop roots (with $\overline{Q} = 0$) and the P_j's are the forward

path poles (K_c, in the case of the example system of Figure C-2).

Now the stability equation from Equation C-9 may be written as:

$$\left[\frac{\pi_i (s + r_i)}{\pi_j (s + P_j)} \right]^2 + \left(\frac{\overline{Q}}{\mathcal{M}} \right)^2 s^2 = 0$$

or

$$1 + \left(\frac{\overline{Q}}{\mathcal{M}} \right)^2 \frac{s^2 \left[\pi_j (s + P_j) \right]^2}{\left[\pi_i (s + r_i) \right]^2} = 0.$$

(C-11)

A root locus may now be drawn for Equation C-11. Figure C-3 shows a typical result. Note that each "open loop" (pole) and zero is doubled. The general property depicted in Figure C-3 is the developing of two bending roots by the gyroscopic payload effect. Note that one of these is less stable than the closed-loop bending root without spin. The loci departing from the double bending pole have been rotated away from a vertical departure; this is a function of whether or not the double servo pole is outside the double servo zero. This property in turn depends upon the sense of σ_G, the bending-mode slope at the gyro station. Hence, the sense of this departure rotation could be reversed in another case.

C1.2 Mass Unbalance. In addition to gyroscopic moments, a mass unbalance on the spinning payload will produce transverse harmonic exciting forces. The effect of these forces can be evaluated with a single plane analysis. This problem is similar in nature to that of the flexible shaft critical speed problem of classical vibration analysis. Consider a payload spinning at an angular velocity, β, and having a mass unbalance, $\overline{M\ell}$ *. The generalized force of Equation C-1 can now be written as:

$$\ddot{q} + \omega^2 q - \frac{Q}{\mathcal{M}} = \frac{\phi_H \beta^2 \overline{M\ell} \sin \beta t}{\mathcal{M}}$$

(C-12)

---

* The mass unbalance is written $M\ell$ where M is the spinning mass and ℓ is the center-of-gravity offset. The term is written $\overline{M\ell}$, as it appears only in Appendix C1; both M and ℓ are used elsewhere in the text with different meanings.
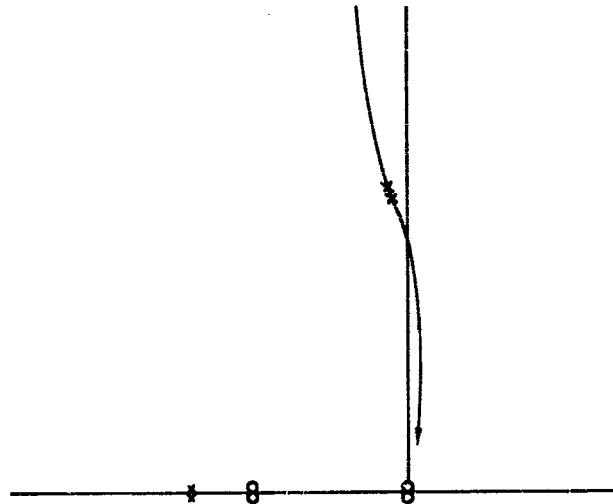
Figure C-3. Typical Locus of Elastic Vehicle System Roots as a Function of Spinning Payload Momentum
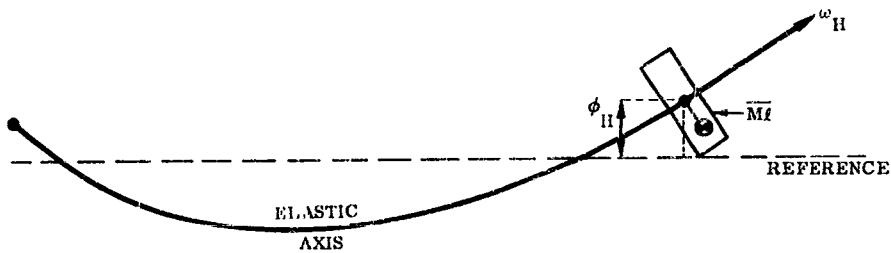

Figure C-4. Mass Unbalance of the Spinning Payload

A particular solution may be obtained by substituting

$$q = b \sin \beta t$$

into Equation C-12:

$$b (-\beta^2 + \omega^2) = \frac{\phi_H''}{)l'}^2 \quad \overline{M\ell} \qquad\qquad b = \frac{\phi_H \overline{M\ell}}{)l} \cdot \frac{1}{\frac{\omega^2}{\beta^2} - 1} \cdot \qquad\qquad (C-13)$$

A counterpart to Equation C-13 with modal damping (ζ) included is:

$$b = \frac{\phi_H \overline{M\ell}}{)l} \cdot \frac{\beta^2}{\sqrt{(\beta^2 - \omega^2)^2 + 4 \zeta^2 \omega^2 \beta^2}} \cdot \qquad\qquad (C-14)$$

In either case (C-13 or C-14), the equation serves to indicate that the mode natural frequency, ω, and the spin frequency, β, should be separated.

The effect of mass unbalance can also be analyzed including a control system. Qualitatively, the same results are obtained, the closed loop system resonant frequencies and damping being but slightly different from the open loop properties.

The coupling which exists between the mass unbalance forces and the autopilot does not affect the system stability. The magnitudes of the vehicle oscillation, $q^i = b \phi x^{(i)}$ become the quantities of interest. The major observation which can be made is that the spin frequency will have to be kept separated from the mode frequency, and/or the payload will have to be carefully balanced. The amplitude of oscillation can then be contained to some desired value.

Maintaining adequate frequency separation between the payload's spin frequency and the booster vehicle's elastic mode frequencies can present a problem. It may not be possible, particularly for the larger boost vehicles, to use a spin frequency below that of the first mode at launch. When this condition arises, the spin frequency will have to be changed during flight; i. e., usually increased to capitalize upon the increase in modal frequency as flight progresses.

C2 SOLID PROPELLANT GRAIN MODES

The solid propellant grain behaves as a visco-elastic solid. This visco-elastic mass must be represented in some manner when the elastic properties of the booster are calculated. The simplest and most straightforward method of accomplishing this is to consider the grain as an inert mass, rigidly attached to the case.

This method of analysis is usually used for the elastic calculations on solid propellant boosters. These calculations are then coupled with tests to evaluate the elastic properties of the booster. This method, while it has several shortcomings, is in wide use and has been found to yield satisfactory results.*

The visco-elastic properties of the grain could be used to provide a more comprehensive analysis of the elastic motion. There are several analytic models which adequately describe the dynamic behavior of the visco-elastic solid (Reference C-1 or C-2). However, it is generally felt that this area of analysis does not need to be considered for study of lateral bending.

There are several reasons why the visco-elastic properties of the solid propellant grain are not used in calculations of the booster elastic properties. First, they are found to be relatively unimportant for booster vehicles having a reasonable slenderness ratio. The grain structure, in response to stress, exhibits a complicated behavior which can be represented as instantaneous elasticity, delayed elasticity, and viscous flow. For small stresses occurring for short times, the properties could be approximated by considering only the instantaneous elasticity. The modulus of elasticity of solid propellant grains currently being used is in the range from 500 to 2000 psi at an ambient temperature of 70-80° F. Thus, the contribution to the bending stiffness is quite small compared at that of the vehicle shell which is commonly referred to as the solid propellant rocket motor case.

A second consideration is the variable nature of the grain properties themselves. The nature of the approximations which can be used for the model to represent the grain would vary depending on the stress level within the grain, frequency of the application of stress, and temperature. The modulus of elasticity is quite temperature-dependent exhibiting a change of roughly a factor of 10 for every 40 degrees F of change in grain temperature. This property alone makes it cumbersome to describe adequately the solid propellant grain motion. This difficulty in analysis along with the relative unimportance of the visco-elastic effects on the mode has prompted most analysts to omit these effects from the model used to describe the lateral elastic motion of the booster. Bending mode tests run by various airframe manufacturers have indicated that these omissions do not affect the adequacy of the calculations. The above should not be taken to imply that the visco-elastic behavior of the solid propellant grain is not important in all problems. It does become quite important under certain conditions, particularly in the analysis of the longitudinal modes.

C3 EFFECT OF MASS FLOW AND INTERNAL DAMPING ON DERIVATIONS OF EQUATIONS OF MOTION

The previous sections have given the derivation of equations for a rocket propelled vehicle, with aerodynamic forces. The equations used are correct under the assumptions made and are as complete as is reasonable. The preceding equations do not, however, include the effects of mass flow within the vehicle, such as occur when the vehicle is expending propellant. The effect of internal damping of the structure was also omitted although it was reintroduced later as an equivalent viscous damping in each normal mode. These quantities lead to velocity-dependent terms in the equations of motion. In this section the equations are re-derived, and an evaluation of the importance of these additional terms is made.

---

* The nonlinear properties resulting from fastening the various components together to assemble the solid propellant booster vehicle are found to produce effects in excess of the grain motion for present configurations.

C3.1 <u>Velocity-Dependent Terms Due to Mass Flow.</u> The following assumptions are used in the analysis of mass flow terms:

a. The resulting force acting on a system depends only on the time rate of change of a body's linear momentum.

b. The forces exerted by two bodies on each other are equal and opposite and act on the line joining them.

c. No matter is created or destroyed within the vehicle.

C3.1.1 <u>Newton's Law.</u> The linear momentum is defined as:

$$\vec{P} = \int_{VOL} \vec{V}\, dm \ .$$

The force is proportional to the rate of change of momentum:

$$F = \frac{d}{dt}\, (\vec{P}) \quad .$$

C3.1.2 <u>Eulerian Coordinates.</u> The equations of motion written with fixed axes could be used to describe the motion of an airframe as a function of time. Due to considerations in calculation of inertial and force data for the airframe, it is expedient to use an Eulerian, or body-fixed, axis system. The equations of motion may then be expressed in terms of quantities measured relative to these axis.

The absolute or inertial rate of change of a vector is expressed in terms of the rates of change of the vector components as resolved in body coordinates and the body coordinate's rotation by

$$\frac{d\vec{G}}{dt}\Bigg|_{inertial} \qquad \frac{d\vec{G}}{dt}\Bigg|_{body} \qquad + \vec{\omega} \times \vec{G}$$

where $\vec{\omega}$ is the angular velocity of the body coordinate system.

To apply the preceding relationships to a flexible vehicle with mass flowing within the system, a very complete derivation must be obtained. One such derivation is given in Reference C-3, and is summarized below.

For a general mass system the velocity of a mass particle, dm, may be expressed as the vector sum:

$$\vec{V} = \dot{\vec{R}}_c + \dot{\vec{\rho}} + \vec{V}_t$$

where

$\vec{R}_c$ = position vector from an inertial origin to the instantaneous mass center of the system which, in turn, is taken as the origin of the body axes.

$\vec{\rho}$ = position vector from the mass center (body axis origin) to a point fixed in the mass system.

$\vec{V}_t$ = velocity of the mass particle, dm, at position $\vec{R}_c + \vec{\rho}$, relative to this fixed point in the mass system - designated as the <u>transport velocity.</u>

Since it will be more convenient to measure $\vec{\rho}$ in the body axis system we write:

$$\dot{\vec{\rho}} = (d\vec{\rho}/dt)_{body} + \vec{\omega} \times \vec{\rho}$$

and hence

$$\vec{V}_t = \dot{\vec{R}}_c + \left(\frac{d\vec{\rho}}{dt}\right)_{body} + \vec{\omega} \times \vec{\rho} + \vec{V}_t \quad .$$

(C-15)*

---

* Subscript "body" will be denoted by "b" hereafter.

C-9

In this equation the first term gives the motion of the mass center (commonly called the center-of-gravity), the second term represents both the effects of center-of-gravity shifts due to mass flows and of elastic motions within the system, the third gives the effect of using a rotating coordinate system, and the fourth represents the particle mass flow within the system.

Now if $(d\rho/dt)_b$ is the velocity of a point fixed in the mass system relative to the mass center, then it is the negative of $(d\vec{r}_c/dt)_b$, the velocity of the mass center relative to the fixed point. The latter expression will be introduced now, since it will be convenient for evaluating the effects of center-of-gravity motion (travel) in a rigid-vehicle body due to propellant expenditure. Thus:

$$\vec{V} = \dot{\vec{R}}_c - \left(\frac{d\vec{r}_c}{dt}\right)_b + \vec{\omega} \times \vec{\rho} + \vec{V}_t \ .$$

We assume $(d\vec{r}_c/dt)_b$ is constant over the system in the following discussion (rigid vehicle)*. If this velocity is integrated over the mass system, the linear momentum becomes:

$$\vec{P} = M\left[\dot{\vec{R}}_c - \left(\frac{d\vec{r}_c}{dt}\right)_b + \vec{V}_i\right] \tag{C-16}$$

where $M = \int_{vol} dm$.

$$V_i = \frac{1}{M} \int_{vol} \vec{V}_t\, dm = \text{average internal mass velocity:}$$

and use has been made of the fact that, by definition, $\int \rho\, dm = 0$.

For angular momentum the corresponding result takes the form:

$$\vec{H}_c = I_c\,\vec{\omega} + \int_{vol} \vec{\rho} \times \vec{V}_t\, dm \tag{C-17}$$

where
$I_c = $ moment of inertia tensor.

$\vec{\omega} = $ angular velocity of body axis with respect to inertial space.

$\vec{\rho} = $ position vector from center of mass to element of mass.

$\vec{V}_t = $ internal transport velocity.

The preceding are now adapted to a mass system representing a vehicle from which mass is being expelled.

---

* This assumption is not necessary in practice, since the elastic modes of a system as commonly computed satisfy the condition

$$\int \left(\frac{dr_c}{dt}\right)_b dm = 0$$

where $(dr_c/dt)_b$ is the velocity due to elastic motions.

Force is equal to the rate of change of momentum of a closed system of particles. In the case of the vehicle it is convenient to write:

$$\vec{F} = \frac{d}{dt}\ \vec{P} - \vec{D}_p\ (t) \tag{C-18}$$

where $\vec{D}_p\ (t)$ is the rate at which linear momentum is being transferred into the system, i.e.,

$$\vec{D}_p\ (t) = -\ \lim_{\Delta t \to 0}\ \frac{\Delta \vec{P}}{\Delta t}\ .$$

The same can be written for angular momentum:

$$\vec{J}_c = \frac{d}{dt}\ \vec{H}_c - \vec{D}_{Hc}\ (t) \tag{C-19}$$

where $\vec{D}_{Hc}\ (t)$ is the rate at which angular momentum is being transferred into the system:

$$\vec{D}_{Hc}\ (t) = -\ \lim_{\Delta t \to 0}\ \frac{\Delta \dot{H}_c}{\Delta t}\ .$$

For linear motion, the result of combining Equations (C-16) and (C-18) is:

$$M\ \ddot{\vec{R}}_c = \vec{F} + \dot{M}\ \left(\vec{V}_e - \vec{V}_i + \vec{\omega} \times \vec{\rho}_e\right) + M\ \frac{d}{dt}\ \left[\left(\frac{d\vec{r}_c}{dt}\right)_b - \vec{V}_i\right]$$

where $\vec{V}_e$ = average exhaust velocity and

     $\vec{\rho}_e$ = vector from mass center to the center of the exhaust.

In the special case of a rigid body:

$$\dot{M} = \frac{d\vec{r}_c}{dt} = \vec{V}_i = 0$$

and the rigid body equation becomes

$$M\ \ddot{\vec{R}}_c = \vec{F}\ .$$

For rotational motion, Equations (C-17) and (C-19) give:

$$\frac{d}{dt}\ \left(\mathbf{I}_c\ \vec{\omega}\right) = \vec{J}_c - \int_{surface} \mu \vec{\rho} \times \vec{V}_t\ ds - \dot{M}\ \vec{\rho}_e \times \left(\frac{d\vec{r}_c}{dt}\right)_b$$

$$- E\ \dot{\vec{\omega}} - \frac{d}{dt}\ \int_{volume} \vec{\rho} \times \vec{V}_t\ dm\ . \tag{C-20}$$

where μ = outward mass flow rate per unit area and

     E = exhaust tensor defined by:

$$\int_{surface} \mu \vec{\rho} \times (\vec{\omega} \times \vec{\rho})ds = E\ \vec{\omega}\ .$$

For a rigid body, $\vec{V}_t = \dot{M} = \mu = E = 0$, and one has:

$$\frac{d}{dt}(I_c \vec{\omega}) = \vec{J}_c .$$

The preceding equations may be used to evaluate the effects of fluid transfer upon the equations of motion of a vehicle. It is first necessary to establish which terms are already included by use of the engine thrust as a force when the equations of motion are written "conventionally". It is shown in Reference C-3 that the rocket engine thrust and rocket thrust torques are given respectively by:

$$\vec{T}_R = \dot{M}(\vec{V}_e - \vec{V}_i) + \vec{F}_P - M\left(\frac{d\vec{V}_i}{dt}\right)_b + \vec{\omega} \times \left[\dot{M}\vec{\rho}_e - M\left(\frac{d\vec{r}_c}{dt}\right)_b - M\vec{V}_i\right] \qquad (C-21)$$

and

$$\vec{J}_R = -\int_{surface} \mu\vec{\rho} \times \vec{V}_t \, ds + \vec{J}_p - \dot{M}\vec{\rho}_e \times \left(\frac{d\vec{r}_c}{dt}\right)_b - \left(\frac{d}{dt}\right)_b \int_{vol} \vec{\rho} \times \vec{V}_t \, dm$$

$$-\left[\left(\frac{dI_c}{dt}\right)_b + E\right]\vec{\omega} - \vec{\omega} \times \int_{vol} \vec{\rho} \times \vec{V}_t \, dm \qquad (C-22)$$

where $\vec{F}_P$ and $\vec{J}_P$ are forces and torques due to environmental back pressure (integral of exhaust pressure minus ambient pressure over the engines' exit planes).

The equation for translational motion, Equation C-19, may be rewritten as:

$$M\ddot{\vec{R}}_c = \vec{F} + \dot{M}(\vec{V}_e - \vec{V}_i + \vec{\omega}\times\vec{\rho}_e) + M\left(\frac{d^2\vec{r}_c}{dt^2}\right)_b + M\vec{\omega} \times \left(\frac{d\vec{r}_c}{dt}\right)_b$$

$$- M\left(\frac{d\vec{V}_i}{dt}\right)_b - M\vec{\omega} \times \vec{V}_i .$$

Using the expression for engine thrust given above and with the observation that

$$\left(\frac{d^2\vec{r}_c}{dt}\right)_b = \left(\frac{d\vec{V}_i}{dt}\right)_b ,$$

this becomes:

$$M\ddot{\vec{R}}_c = \vec{F} + \vec{T}_R + 2M\vec{\omega} \times \left(\frac{d\vec{r}_c}{dt}\right)_b + M\left(\frac{d^2\vec{r}_c}{dt^2}\right)_b . \qquad (C-23)$$

Likewise, for rotation,

$$\frac{d}{dt}(I_C \vec{\omega}) = \vec{J}_c + \vec{J}_R - \left(\frac{dI_C}{dt}\right)_b \vec{\omega} \ . \tag{C-24}$$

In these equations of motion the applied forces and torques are understood now to exclude specifically those effects due to the difference between rocket engine exhaust pressures and the atmospheric back pressure, since these are included in $\vec{T}_R$ and $\vec{J}_R$.

Examining these last equations of motion, it is seen that certain of the effects of mass flow within the vehicle body are reflected as terms involving the products of rates of change of body inertial properties and the body angular rates. In general, these terms are negligibly small and may be safely omitted from the equations of motion, as is done in the main text. The remaining additional term arises from the acceleration of the vehicle mass center relative to the fixed portions of the vehicle. This term, too, is most often safely neglected.

Although the mass flow terms do not significantly affect the motion of the vehicle, considered as a mass system, they could have an effect on the motion of the generalized coordinates (modes) used to represent the elastic motion. The next section will analyze the effect of mass flow and internal damping on the motion of these elastic modes.

C3.2 Velocity-Dependent Terms Due to Damping (Modal Coordinates). The method which is used to calculate the elastic properties (normal modes) is presented in Appendix A4. This method assumes constant coefficients, no mass flow terms, and, also, no internal damping within the structure itself.

The simplifying assumptions made in the derivation of the modes result in elimination of all velocity-dependent terms. The classes of velocity- or pseudovelocity-dependent terms that result in damping fall into three general classes: viscous, coulomb, and structural. These classes of damping will be considered along with the mass flow terms, as both effects lead to velocity-dependent terms which must be accounted for when the modes are calculated.

For a simple spring mass system with a viscous damper the equation of motion is:

$$M\ddot{X} + C_V \dot{X} + KX = F_{external}$$

The viscous damping used here is the simplest form of damping to analyze analytically.

For coulomb damping the preceding equation would be written

$$M\ddot{X} + C_F \frac{\dot{X}}{|\dot{X}|} + KX = F_{external} \ .$$

By use of a describing function to find an equivalent linear gain, one arrives at:

$$M\ddot{X} + \frac{4}{\pi}\frac{C_F}{\omega\bar{X}}\dot{X} + KX = F_{external}$$

where ω is the frequency and $\bar{X}$ is the peak value of X.

For structural damping the forces are usually approximated by a force that opposes the motion and is in phase with the velocity. For simplicity of analysis, and also from a lack of basic knowledge as to the exact nature of damping present, one assumes that the magnitude of the damping is proportional to the elastic restoring force. This force can be represented mathematically by replacing the elastic restoring force term, KX, by the terms $KX(1 + jg_x)$ (see Reference C-4). The constant g_x is the structural damping coefficient. Since, for modal calculations, the motion of the modes is harmonic ($s = j\omega$), the effect of damping can be represented as:

C-13

$$C_{equivalent} = \sqrt{KM} (g_x) = \frac{k}{\omega_n} g_x .$$

The above defines a fixed relationship between amplitude and velocity, which would only hold for harmonic oscillation at the resonant frequency.

C3.3 Velocity-Dependent Terms Due to Mass Flow (Modal Coordinates). Before analyzing the effect of the preceding terms on the calculation of normal modes, the mass flow terms will be analyzed so that the effect of both damping and mass flow terms can be considered.

The first section of this appendix gives the velocity dependent terms for the mass flow in a rigid vehicle. These are shown to be negligibly small in the aggregate over the vehicle. However, this cannot be projected to imply that the mass flow terms will be negligible for each incremental segment of the elastic vehicle. The forces at each segment do indeed exist and their effect must be analyzed to insure adequacy of the assumption used in calculating the modal parameters.

If we consider only the motion normal to the longitudinal axis, the rate of change of momentum (RCM) is equal to the momentum lost, minus momentum leaving, minus the momentum entering, minus the momentum gained, and plus the product of mass times acceleration. Thus, for a descrete element of the beam we can write:

$$m\ddot{q}_{(Y)} + \dot{m}_E \dot{q}_{(Y)} - \dot{m}_E \dot{q}_E + \dot{m}_L \dot{q}_{(Y)} - \dot{m}_L \dot{q}_{(L)} = F_{EX} \qquad (C\text{-}25)$$

Subscripts   E = entering
               L = leaving
               Y = mass station

F_{EX} is the "external" force acting on the beam segment (this will include elastic forces).

For a series solution involving several discrete masses of a flexible vehicle some distribution of velocity between two adjacent masses will have to be provided. The easiest method available is to distribute these such that half the force necessary to transfer the propellant from one segment to the next will be supplied by each segment. Thus, for the ith segment:

$$\dot{m}_E^{(i)} = - \dot{m}_L^{(i)} = - \dot{m}_a$$

where $\dot{M}_a$ is the mass flow rate and the subscript, a, refers to station a, the free surface location of the propellant.

$$\dot{q}_E = \frac{\dot{q}_{(i-1)} + \dot{q}_i}{2}$$

$$\dot{q}_L = \frac{\dot{q}_i + \dot{q}_{(i+1)}}{2} .$$

Thus, one may write:

$$F_{EXi} = m_i \ddot{q}_i \dotfill i < a$$

$$F_{EXa} = m_a \ddot{q}_a + \dot{m}_a \left(\dot{q}_a - \dot{q}_{a+1} \right) \big/ 2 \dotfill i = a$$

$$F_{EXi} = m_i \ddot{q}_i + \dot{m}_a \left(\dot{q}_{i-1} - \dot{q}_{i+1} \right) \big/ 2 \dotfill i > a$$

$$F_{FXt} = m_t \ddot{q}_t + \dot{m}_a \left(\dot{q}_{t-1} + \dot{q}_t \right) \big/ 2 - \dot{m}_a \dot{q}_{t+1} \dotfill i = t ,$$

where (t) refers to the vehicle "tail" or more precisely, the rocket gimbal. The velocity, $\dot{q}_{t+1}$, will be the transverse exhaust velocity component, written hereafter as $\dot{q}_{EX}$.

For multiple propellants:

$$F_{EXi} = m_i \ddot{q}_i + (\dot{m}_a + \dot{m}_b \cdots \dot{m}_n)(\dot{q}_{i+1} - \dot{q}_{i+1})/2,$$

where a, b. . n refer to n propellants carried aboard. The combined equations can be written as follows in a specific case:

$$
\begin{Bmatrix} m_1\ddot{q}_1 \\ m_2\ddot{q}_2 \\ m_3\ddot{q}_3 \\ m_4\ddot{q}_4 \\ m_5\ddot{q}_5 \end{Bmatrix}
+ \dot{m}_a
\begin{bmatrix} 0 & 0 & 0 & 0 & 0 \\ 0 & 1/2 & -1/2 & 0 & 0 \\ 0 & 1/2 & 0 & -1/2 & 0 \\ 0 & 0 & 1/2 & 0 & -1/2 \\ 0 & 0 & 0 & 1/2 & 1/2 \end{bmatrix}
\begin{Bmatrix} \dot{q}_1 \\ \dot{q}_2 \\ \dot{q}_3 \\ \dot{q}_4 \\ \dot{q}_5 \end{Bmatrix}
+
$$

$$
+ \dot{m}_b
\begin{bmatrix} 0 & 0 & 0 & 0 & 0 \\ 0 & 0 & 0 & 0 & 0 \\ 0 & 0 & 1/2 & -1/2 & 0 \\ 0 & 0 & 1/2 & 0 & -1/2 \\ 0 & 0 & 0 & 1/2 & 1/2 \end{bmatrix}
\begin{Bmatrix} \dot{q}_1 \\ \dot{q}_2 \\ \dot{q}_3 \\ \dot{q}_4 \\ \dot{q}_5 \end{Bmatrix}
- (\dot{m}_a + \dot{m}_b)
\begin{Bmatrix} 0 \\ 0 \\ 0 \\ 0 \\ \dot{q}_{EX} \end{Bmatrix}
=
\begin{Bmatrix} F_1 \\ F_2 \\ F_3 \\ F_4 \\ F_5 \end{Bmatrix}
\qquad (C-26)
$$

or in matrix notation abbreviated as:

$$
[m]\,[\ddot{q}] + m_a \begin{bmatrix} 0 & | & 0 \\ \hline 0 & | & 1/2 \end{bmatrix} \{\dot{q}\} + \dot{m}_b \begin{bmatrix} 0 & | & 0 \\ \hline 0 & | & 1/2 \end{bmatrix} \{\dot{q}\} - (\dot{m}_a + \dot{m}_b)\begin{Bmatrix} 0 \\ \hline \dot{q}_{EX} \end{Bmatrix} = \{F\}. \quad (C-27)
$$

The above should be adequate for discussion. A vehicle may contain several propellant tanks; however, it is unlikely that propellant will be consumed from more than two tanks at any given instant.

C3. 4 <u>Equations of Motion With Velocity Dependent Terms.</u> The homogenous equations for an N-degree-of-freedom, lumped-parameter linear system is written as

$$[m]\,\{\ddot{q}\} + [c]\,\{\dot{q}\} + [k]\,\{q\} = 0 \qquad (C-28)$$

where the matrix $[C]$ is also a symmetric matrix. Assume a transformation is made which diagonalizes the inertial and stiffness matrices:

$$\{\eta\} = [\psi] \{q\}$$

such that

$$[M] \{\ddot{\eta}\} + [\psi^{*}] [C] [\psi] \{\dot{\eta}\} + [K] \{\eta\} = 0$$

where

$$[M] = [\psi^{*}] [m] [\psi]$$

$$[K] = [\psi^{*}] [k] [\psi]$$

The system of equations is uncoupled if $[\psi^{*}] [c] [\psi]$ is also a diagonal matrix. Based upon the preceding, Caughey (Reference C-5) shows that a necessary and sufficient condition for a damped system to have classical normal modes is that the damping matrix be diagonalized by the same transformation which uncouples the undamped system. Thus, if the undamped system's normal modes are $[\Phi]$, the damped system will possess these same normal modes if

$$[\Phi^{*}] [c] [\Phi]$$

is a diagonal matrix.

Caughey goes further to show the general conditions on $[C]$ under which these normal modes will diagonalize it. Briefly, these are that in the canonical form of Equation (C-28) (the form wherein the inertial matrix is a unit matrix) the damping matrix must be expressible as a polynomial in the elastic matrix. (This is a generalization of Rayleigh's result that the damping matrix be a linear function of the stiffness matrix.) In the light of this result, the two types of velocity-dependent terms of concern herein may be discussed.

If the structural damping is represented as $C_{EQ} = kg / \omega_{n}$, or its equivalent for a multidegree of freedom system $[C_{EQ}] = \frac{g}{\omega_{n}} [k]$, it is easy to see that the damping matrix will have the required property.

Those velocity-dependent terms from mass flow effects (Equations C-27 or C-28) are somewhat more troublesome, as the contributions to the C_{EQ} matrix are not symmetric. However, the following may be used to reduce the equation to a point where a simplified result is apparent.

Assume for the moment that the equations of motion are to be written from an energy viewpoint. The following potential functions are written.

a. Kinetic energy $1/2 \lfloor \dot{q} \rfloor [M] \{\dot{q}\}$

b. Potential energy $1/2 \lfloor \dot{q} \rfloor [K] \{q\}$

c. Dissipation function $1/2 \lfloor \dot{q} \rfloor [C_{EQ}] \{\dot{q}\}$

where C_{EQ} is the matrix containing the mass flow terms. This nonsymmetric matrix may be divided into symmetric and antisymmetric parts:

$$\left[C_{EQ} \right] = [S] + [A].$$

Referring to Equation C-26 it is seen that the symmetric parts of C_{EQ} come from the main diagonal only, and that the matrix $[S]$ consists of only two terms:

$$\dot{m}_{a/2} \quad \text{at the free surface}$$

and $\quad \dot{m}_{a/2} \quad$ at the gimbal* .

These symmetric matrix elements cannot be shown to satisfy Caughey's criterion (above) and hence will affect the modal calculations. However, two points of view may be adopted: they may be considered as small effects (which they are) and be neglected, or they may be treated as additional motion-dependent external forces in solution of the nonhomogenous equations.

Finally, we note that

$$\lfloor \dot{q} \rfloor \quad [A] \quad \{\dot{q}\} = 0$$

if $[A]$ is (as postulated) an antisymmetric matrix with a null (zero) main diagonal.

This appendix has analyzed the effect of velocity-dependent terms on the derivation and use of classical normal modes. The analysis indicated that the mode calculations can be accomplished with the velocity-dependent terms due to structural damping and mass flow excluded and that their effects may be added later, during the autopilot and control system analysis, to the mode itself. This result is in agreement with the methods presented in the body of the report.

C4 LONGITUDINAL MOTION TERMS IN SYSTEM EQUATIONS

It is often assumed by those working in the field that, based upon the restriction of small modal deflections, the booster masses deflect and applied forces act only in a lateral direction. Subsequently, the majority of modal calculations and generalized forces applied to the mode are arrived at by assuming rotation and lateral translation, but no longitudinal translation of either masses or applied forces. On the surface this approximation may appear to be a good one, but this is not always the case. It is hoped that the following example may contribute some insight to the problem and indicate what approximations, if any, may be made.

First, assume a uniform free-free beam of constant stiffness and mass distribution over its entire length. A Force, T, is applied and fixed to the end of the beam, such that the force rotates and translates with the end of the beam; i.e., it has the identical slope and deflection as the end of the beam. Figure C-5 represents the deflected beam and applied force, T.
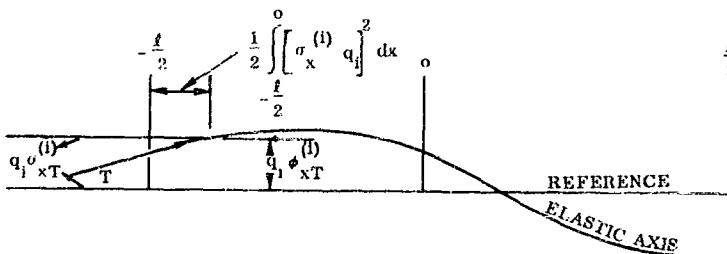
Figure C-5. Schematic of Uniform Free Beam Deflecting Under a Thrust Force

* The other flow term involving q exhaust is treated as a thrust term in writing the nonhomogenous system equations of motion.

For small deflections, and therefore small angular rotations, the work done by the force, F, in a deflection, q_i, is to be computed.

$$WORK = \text{lateral work} + \text{longitudinal work*}$$

$$= + \int_0^{q_i} T \; \sigma_{XT}^{(i)} \; q_i \; \left(\varphi_{XT}^{(i)} \; dq_i \right) + T \; 1/2 \int_{-\ell/2}^0 \left(\sigma_{XT}^{(i)} \; q_i \right)^2 dx \; .$$

If the deflections and slopes are known only at regular intervals (Δx) over the vehicle length, the longitudinal work may be approximated by numerical integration. For the uniform beam the work is:

$$WORK = 1/2 \; T \; \sigma_{XT}^{(i)} \; \varphi_{XT}^{(i)} \; q_i^2 + 1/2 \; T \; \Delta x \sum_{\ell/2}^{\ell} \sigma_x^{(i)^2} \; q_i^2$$

If we compare the longitudinal work to the lateral work by means of the ratio, R_W, for various modal deflections, q_i, it is found that the value of the ratio increases from a value of one for the rigid body pitching mode to a value of 3.08 for the fifth bending mode. Since the longitudinal and lateral work are of opposite sign for all modes, they tend to oppose each other. Thus, there is zero work done due to rigid-body pitching. The following chart gives a comparison of the ratio of longitudinal work to lateral work for the various modes.

$$R_W = \frac{\Delta x \sum_{\ell/2}^{\ell} \sigma_x^{(i)^2}}{\sigma_{XT}^{(i)} \; \varphi_{XT}^{(i)}}$$

MODE	R_W
Pitching	1
Plunging	Undefined
1st Bending	1.35
2nd Bending	1.77
3rd Bending	2.24
4th Bending	2.50
5th Bending	3.08

These ratios were obtained using data from Bishop and Johnson (Reference C-6). The numerical integration was performed using intervals equal to 2 percent of the overall length.

Although this is only a cursory look at the problem, it may be deduced that the omission of the longitudinal generalized force ($T \; \Delta x \sum \sigma_x^{(i)^2} \; q_i$) and the lateral generalized force ($T \; \sigma_{XT}^{(i)} \; \varphi_{XT}^{(i)} \; q_i$) is a good approximation for the lower body-bending modes of the booster. For the higher order bending modes, where

---

* Since the beam has a uniform mass distribution, the center of mass will be the longitudinal elastic center. Also, this integral uses the expression

$$\int (ds - dx) \approx 1/2 \int \left(\frac{dy}{dx} \right)^2 dx \; .$$

this approximation is not good, the bending mode calculations themselves may be in significant error since the inertial loads due to the longitudinal motion are not usually included in the calculation of the bending modes.

When analyses of the higher order bending modes are required at greater accuracy, it is desirable that the bending mode calculations allow for the longitudinal inertial loads and that the longitudinal generalized forces be included in these analyses.

In deriving the equations of motion for the flexible booster vehicle (Section 3) the only work done by the rocket thrust on each mode is taken as due to the inclination of this thrust vector with respect to the elastic axis at the gimbal; i.e. ($\sigma_{Xe}^{(i)}$ - $\sigma_{XT}^{(i)}$) q_i T is the component permitted to do work. In this way, the remaining work terms, as discussed above, are assumed to be self-cancelling and are therefore omitted.

C5 DYNAMICS OF A NONCOMMANDED ENGINE

The arrangement on the booster vehicle may be such as to have engines which, while firing and capable of elastic motion, are not being utilized for control, at least at the time-instant being analyzed. As these rocket engines have thrust, there will be nonconservative forces connected with any elastic motion that the engine executes. Thus, the elastic motions represented by modes may couple through these noncommanded engines, as well as the autopilot and control system (see Paragraph 4.3.2.5).

The analysis of the coupling through noncommanded engines will be outlined in this section. The same equations are used for this coupling as were used in the analysis of load torque feedback, T_{L_k}, for the commanded engine.

The equation of motion for the rocket engine, as given in Paragraph 4.3.3, is:

$$\delta_k' = \frac{-\sum_{j=1} \left[\left(M_R \ell_R \phi_{XT}^{(j)} - I_R \sigma_{Xe}^{(j)} \right) s^2 - \bar{C}_f \left(\sigma_{Xe}^{(j)} - \sigma_{XT}^{(j)} \right) s \right] q_j + \dfrac{K_c R^2 \delta c}{\bar{C}_L / A^2}}{I_R \left\{ s^2 + \dfrac{1}{I_R} \left[\bar{C}_f + \dfrac{A^2 R^2}{\bar{C}_L} \right] s + \dfrac{K_c R^2 A^2}{I_R \bar{C}_L} \right\}} \tag{C-29}$$

The equation for mode motion resulting from the preceding engine deflection is given in Paragraph 4.3.2.1.

$$q_j = \frac{-\sum_{k=1}^{M} K_{jk} \left(s + z_{j_{TWD_k}} \right)\left(s + \bar{z}_{j_{TWD_k}} \right) \delta_k' + Q_j}{M_j \left(s^2 + 2\xi_j' \omega_j' s + \omega_j'^2 \right)} \tag{C-30}$$

where the Q_j's are additional generalized force inputs from nonorthogonal modes.

The block diagram, Figure C-6, shows one mode and two engines - one with both command and load torque feedback and the other having only load-torque feedback. The engine servos must be linearized by means of describing functions; these relationships are amplitude-dependent. Hence, the relationship between the relative motion of the different engines considered must be determined by an iterative procedure. To establish the total transfer function of the mode, including coupling through the noncommanded engines, the following procedure may be used.

a. An amplitude of commanded engine motion $|\delta_1|$ is chosen. For this amplitude the describing function coefficients for engine number 1 are evaluated for use in Equation C-29.

b. Using Equation C-29 (the δ_c / q_j transfer function of the autopilot is presumed known) and the equation:

$$\delta_k = \delta_k' - \left(\sigma_{Xe}^{(j)} - \sigma_{XT}^{(j)} \right) q_j , \tag{C-31}$$
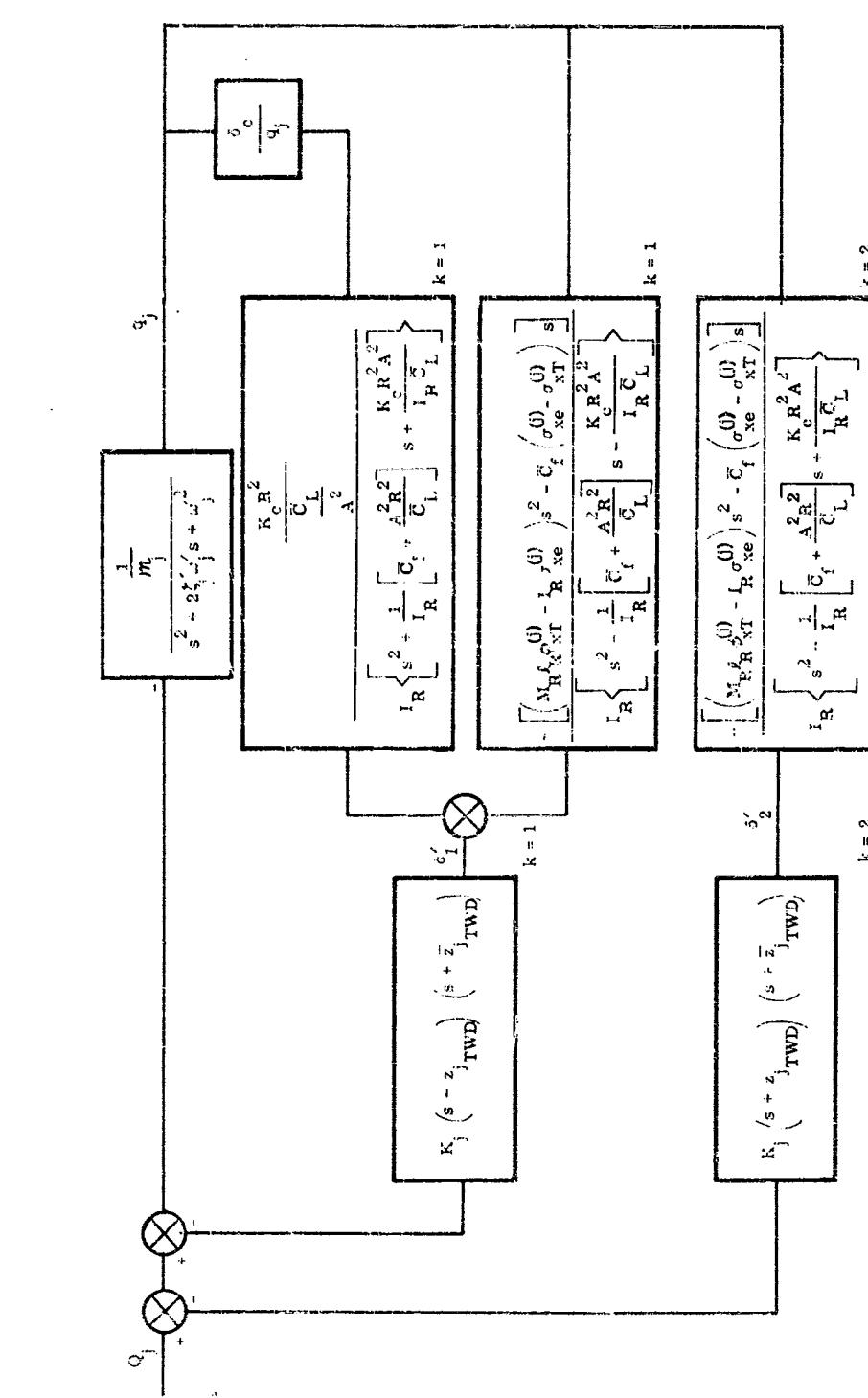
Figure C-5. Block Diagram of Elastic Mode With Load Torque Feedback

q_j is found. This evaluation is made for $s = j\omega'_j$, where ω'_j is the open loop modal frequency.

c. The passive engine (number 2) amplitude, $|\delta_2|$, is next estimated from Equation C-31 by using as a first trial $\delta'_2{}_{(1)} = 0$, i.e., $|\delta_2|_{(1)} = - \left| \left(\sigma_{Xe}^{(j)} - \sigma_{XT}^{(j)} \right) q_j \right|$.

d. Using this trial value of δ_2 the describing function coefficients for Equation C-29 (as applied to engine number 2) are evaluated.

e. Equation C-29 is now solved for δ'_2, using the value of q_j previously obtained (step b, above). This value of q_j is held constant in this and succeeding steps.

f. With this value of δ'_2 a new trial value of δ_2 is obtained from Equation C-31 and steps d - f are repeated iteratively to converge on the final value of δ'_2. The test for convergence should be applied to both δ_2 and δ'_2.

The transfer function can now be evaluated as to the effect of the load torque feedback. The results of this feedback have been analyzed for a particular engine and are shown in Figure C-7. This figure shows the locus of the vector which represents the motion of a bending mode's open loop pole due to this feedback. From this it can be seen that the load torque feedback produces a destabilizing effect (moves pole towards right) for $\omega < \omega_{TWD}$, and a stabilizing effect for $\omega > \omega_{TWD}$, where ω_{TWD} is the familiar "Tail-Wags-Dog" frequency.

$$\omega_{TWD} \sqrt{\frac{T}{M_R \ell - \left(\frac{\theta}{\omega} \middle/ \phi \right)_{XT}}}$$
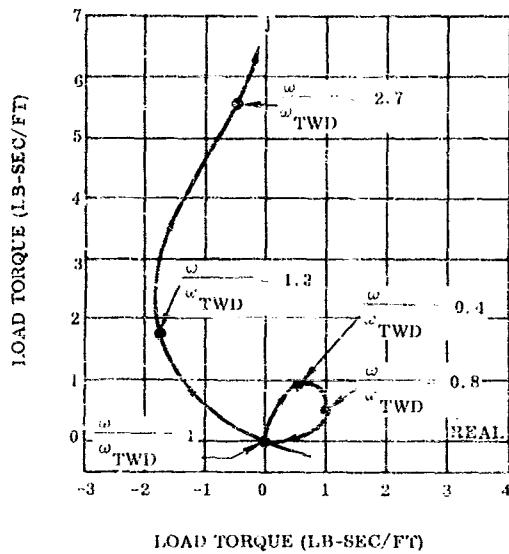
Figure C-7. Influence of Load Torque Feedback on the Effective Mode Open Loop Bending Pole

It should be noted that the above result is not completely general, since it depends upon sense (sign) and relative magnitudes of elastic modal deflections at the aft end. For some very high frequency modes the reversed effect is occasionally found (see Section 5).

C6 REFERENCES FOR APPENDIX C

C-1.   J. T. Bergen, Visco-elasticity Phenomenological Aspects, Academic Press, 1960

C-2.   D. R. Bland, Theory of Linear Visco-elasticity, Pergamon Press, 1960

C-3.   J. A. Thorp and R. C. Hutchinson, "The Dynamics of Rocket-Powered Vehicles," Massachusetts Institute of Technology Report R-206, February 1959

C-4.   R. H. Scanlan and R. Rosenbaum, Introduction to the Study of Aircraft Vibration and Flutter, The Macmillan Company, New York, 1951

C-5.   T. K. Caughey, "Classical Normal Modes in Damped Linear Systems," Journal of Applied Mechanics, June 1960

C-6.   R. Bishop and D. Johnson, Vibration Analysis Tables, Cambridge University Press, 1956

Unclassified

Convair-Astronautics, San Diego, Calif.
APPROXIMATE TRANSFER FUNCTIONS FOR
FLEXIBLE-BOOSTER-AND-AUTOPILOT
ANALYSIS, by D. R. Lukens, A. F. Schmitt,
and G. T. Broucek. April 1961. 310 p. (incl.
167 p. Appendix) incl. illus. tables, 92 refs.
(Proj. 8219; Task 82158) (WADD TR-61-S3)
(Contract AF 33 (616)-7037)
Unclassified report

Results of an analysis of flexible boosters having
autopilot control are summarized. Simplifica-
tions and approximations are presented, along
with derivations of many of the equations.

(over)

1. Flexible-Booster-Autopilot-Control Problems
2. Transfer Functions
3. Synthesis and Analysis Methods
4. Aeroelasticity
5. Control Systems
6. Guided Missile Boosters (Hyper-velocity Vehicles)

Unclassified

Unclassified

7. Propellant Sloshing
8. Servo-Elastic Coupling
9. Servomechanisms

Results indicate that accurate solutions to most
nonwinged booster problems can be achieved by
simple root-locus techniques involving linearized
equations. Methods and equations for a more
comprehensive analysis are also provided.

The methods of synthesis and analysis embody
three major limitations: 1) use of a linear air-
frame, 2) use of small, rigid aerodynamic sur-
faces, and 3) a simple quasi-steady-state model
representation of the aerodynamics.

Appendices contain methods of development of
parameters and material necessary for prelimi-
nary analysis of vehicles.

Unclassified